University of Stuttgart
Germany

Malte
Sauerwein

Simulation of Coupled Transfer and Transport Phenomena in Multi-Phase Materials with Application to Polymer Gels

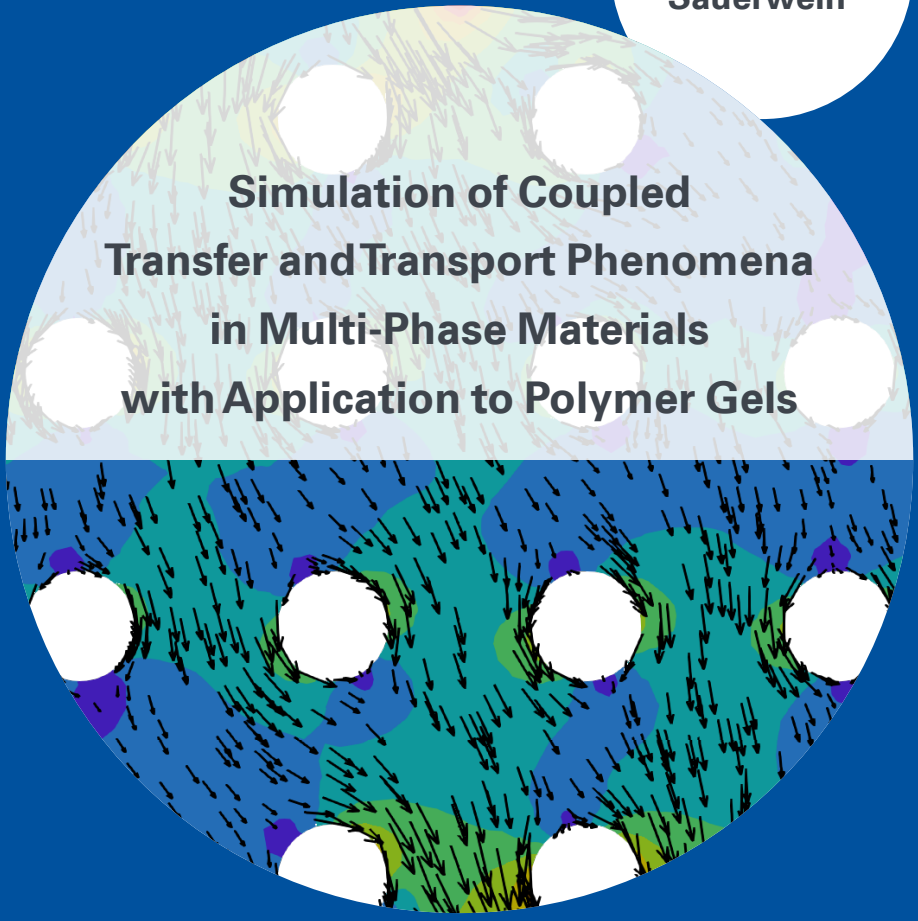

7

Publication series of the
Institute of Applied Mechanics (IAM)

Simulation of Coupled Transfer and Transport Phenomena in Multi-Phase Materials with Application to Polymer Gels

Von der Fakultät Bau- und Umweltingenieurwissenschaften
der Universität Stuttgart zur Erlangung der Würde
eines Doktor-Ingenieurs (Dr.-Ing.)
genehmigte Abhandlung

vorgelegt von

Malte Ferry Sauerwein

aus
Bochum

Hauptberichter:	Prof. Dr.-Ing. Holger Steeb
Mitberichter:	Prof. Lynn Schreyer
	Prof. Matti Ristinmaa

Tag der mündlichen Prüfung: 29. März 2021

Institut für Mechanik (Bauwesen) der Universität Stuttgart
Lehrstuhl für Kontinuumsmechanik
Prof. Dr.-Ing. H. Steeb
2021

Publication series of the Institute of Applied Mechanics (IAM), Volume 7
Institute of Applied Mechanics
University of Stuttgart, Germany, 2021

© Malte Sauerwein
Institute of Applied Mechanics (CE)
Chair of Continuum Mechanics
University of Stuttgart
Pfaffenwaldring 7
70569 Stuttgart, Germany

ISBN 978 – 3 – 937399 – 55 – 3
(D 93 – Dissertation, Universität Stuttgart)

Acknowledgements

The content of this doctoral thesis was carried out during the years 2015 and 2020 when I was a research assistant at the Institute of Applied Mechanics (Civil Engineering), Chair of Continuum Mechanics, at the University of Stuttgart. This work would not have been possible without the help and wisdom of numerous people, whom I would like to express my deepest gratitude.

First of all, I would like to sincerely thank Professor Holger Steeb for giving me the opportunity to conduct the work presented here. His broad expertise together with his open-mindedness were for me the perfect source for new inspiration and motivation. I enjoyed the past years working together with him and I am especially thankful for the freedom he gave me to develop my research interests in certain fields. At the same time, there was a continuous support and the willingness to discuss new ideas whenever I needed it. I also thank Professor Lynn Schreyer, not only for evaluating my thesis, but also for the fruitful discussions we had at conferences. Since her works on Hybrid Mixture Theory are the first papers I read as PhD student, she had by no doubt an enormous impact on my research career. I also thank my third examiner Professor Matti Ristinmaa. Since I was following his publications and his research group for a long time, I was honored that he evaluated my thesis.

I spent my first year as PhD student at the Ruhr University Bochum. In this regard, I would like to thank my office-mate and friend Dennis Wingender for the countless discussions about mechanics and numerical implementations. I will always remember playing table tennis with him in the conference room after a long day of exam corrections. I am thankful for the great and friendly atmosphere, which I experienced at the Ruhr-University Bochum, but later also at the University of Stuttgart. During my employment as research assistant, some of the colleagues became close friends. At this point, I would like to thank Marlon Suditsch for his enormous support during the preparation of my PhD defense and of course for being a great skate buddy. I thank Patrick Schröder for his support for any IT and programming issue, but also for being my partner in crime when it comes to the monthly bicycle demonstration Critical Mass. I also thank Matthias Ruf, Patrick Schmidt and Dr.-Ing. Arndt Wagner, Dominik Fauser and Nadine Kijanski for the great times we spent together at conferences, workshops and of course at the Bauigelfest. Furthermore, I want to thank Lukas Eurich, David Krach, Daniel Rostan, Josef Katzmann, Dongwon Lee, Alixa Sonntag, Samaneh Vahid Dastjerdi, Paul Voland, Dr.-Ing. Maria Camila Osorno Tejada and Dr.-Ing. Rakulan Sivanesapillai. I owe special thanks to Christine Klee for her support in all administrative regards.

My special thanks go to my wonderful parents and my brother for their continuous support during all phases of my PhD. Finally, I would like to thank my partner Erika for her support and understanding even in exhausting situations. You have the talent to ask the right questions and put me back on track. I can always rely on you.

Stuttgart, May 2021 Malte Sauerwein

Contents

Deutschsprachige Zusammenfassung

Motivation

Die Verwendung von Polymeren als Bestandteil fluidgesättigter poröser Materialien hat innerhalb der vergangenen Jahre stark an Bedeutung gewonnen. Polymere, die sich im Porenraum der Festkörpermatrix befinden, können in Abhängigkeit ihrer spezifischen Eigenschaften mit dem Porenfluid sowie mit dem Festkörper wechselwirken. Hierdurch kommt es zu Änderungen der makroskopischen Eigenschaften des gesamten porösen Materials, wobei insbesondere Transportprozesse innerhalb des Porenraums davon betroffen sind.

Eine weitverbreitete Anwendungsmöglichkeit wasserlöslicher Polymere findet sich innerhalb der Erdöltechnik. Beim sogenannten Polymer Flooding (frei übersetzt: Polymerflutung) werden Polymerlösungen in Speichergesteine geringer Permeabilität injiziert. Die Polymerlösung breitet sich im Porenraum aus und transportiert das eingeschlossene Öl in Richtung der Produktionsbohrung. Die Polymerlösung besitzt eine höhere Viskosität im Vergleich zu Wasser, was eine erhöhte Mobilisierung des eingelagerten Öls mit sich bringt. Als Resultat kann eine deutliche Effizienzsteigerung hinsichtlich der Ölförderung erreicht werden.

Um den Transport der Lösung sowie die damit einhergehenden Wechselwirkungen mit der Festkörpermatrix vorherzusagen, ist eine herausfordernde jedoch notwendige Aufgabe zur erfolgreichen Umsetzung von Polymer Flooding Projekten auf der Feldskala. Während der Infiltration der Polymerlösung in das poröse Gestein lagert sich ein Teil der fluidisierten Polymerpartikel am Festkörperskelett an, sodass die Polymerkonzentration zu einer örtlich sowie zeitlich veränderlichen Größe wird. Darüber hinaus verursacht die Anlagerung von Polymeren an den Festkörper morphologische Änderungen des Porenraums. Auf der Makroskala resultiert hieraus eine Abnahme der intrinsischen Permeabilität. Als Konsequenz ist zu beobachten, dass bei konstanter Injektionsrate (Flussrate der Lösung) eine Erhöhung des Injektionsdrucks mit steigender Anlagerung auftritt. Numerische Simulationen basierend auf einer konsistenten kontinuumsmechanischen Modellierung ermöglichen ein Verständnis der komplexen Zusammenhänge, wodurch der Zugang zur Prozessoptimierung eröffnet wird.

Abseits der Erdöltechnik werden quellfähige Polymere zur Bindung der freien Porenflüssigkeit innerhalb poröser Medien verwendet. Aufgrund ihrer Eigenschaften werden diese Polymere auch als Superabsorbierende Polymere (SAP) bezeichnet. Aus chemischer Sicht sind SAP vernetzte Polyelektrolyte, die mit der Absorption von wässrigen Lösungen zu Hydrogelen anquellen. Seit der Entwicklung von Procter & Gamble im Jahr 1957 bis heute, werden SAP wegen ihrer schnellen Absorptionsrate und der hohen Quellungskapazität hauptsächlich für Hygieneprodukte verwendet [160]. Während der vergangenen Jahre wurden erhebliche Fortschritte bezüglich der charakteristischen Polymereigenschaften erzielt. Im Speziellen konnten die Absorptionsraten sowie

die Quellungskapazitäten deutlich gesteigert werden. Aus diesem Grund haben SAP in unterschiedlichen industriellen Sektoren an Bedeutung gewonnen, was vor allem die Nutzung innerhalb poröser Materialien betrifft.

In jüngerer Vergangenheit konnten innovative Baustoffe entwickelt werden, in denen SAP zur adaptiven Steuerung der freien Porenflüssigkeit eingesetzt wurden. Vor diesem Hintergrund ist die Entwicklung eines Verpressmörtels zu erwähnen, der durch den Einsatz von SAP einen Großteil des freien Porenwassers durch Hydrogele binden kann, sodass sich eine schnelle Aushärtung des Mörtels erzielen lässt. Zuverlässige Modelle zur Erfassung der zeitabhängigen Flüssigkeitsaufnahme innerhalb des Porenraums stellen demnach die notwendige Basis zur Entwicklung effektiver Rheologiemodelle dar.

Es kann zusammengefasst werden, dass Polymere innerhalb fluidgesättigter poröser Medien bei unterschiedlichen Anwendungsmöglichkeiten zu einer maßgeblichen Veränderung der makroskopischen Eigenschaften führen können. Die Interaktionen der Polymere mit der Festkörpermatrix sowie mit dem Porenfluid unterscheiden sich aus physikalischer Sicht stark, jedoch lassen sich Anlagerungs-/Ablösungsprozesse sowie Absorptions-/Desorptions-prozesse innerhalb einer kontinuumsmechanischen Modellierung allgemein durch den Massenaustausch der beteiligten Phasen beschreiben.

Stand der Forschung, Vorgehensweise und Zielsetzung

Das Ziel der vorliegenden Arbeit ist die makroskopischen Modellierung poröser Materialien, die eine Sättigung des Porenraums mit einer Porenflüssigkeit sowie einem Polymer aufweisen. Im Fokus der Untersuchung sind die vielfältigen komplexen Prozesse, die innerhalb des Porenraums stattfinden und durch die Anwesenheit des Polymers induziert werden. Wie bereits zuvor erwähnt, ist es möglich die effektiven Eigenschaften poröser Materialien durch den Einsatz von Polymeren zu modifizieren. Hierbei werden die Anforderungen an die Modellierung in drei übergeordnete Kategorien unterteilt:

- Kontrolle der freien Porenflüssigkeit innerhalb des Festkörperskeletts,
- Anlagerung der Polymere an die Festkörpermatrix,
- Fließverhalten von Polymerlösungen durch die poröse Matrix.

Innerhalb der Literatur sind Fortschritte auf allen Bereichen zu verzeichnen. Allerdings existiert nach Kenntnisstand des Autors kein Mehrphasenmodell zur systematischen Beschreibung der gekoppelten Prozesse innerhalb des Porenraums. Demnach wird in der vorliegenden Arbeit ein Mehrphasenmodell entwickelt, welches aus einer porösen Festkörper-matrix, einer Porenflüssigkeit und einem Porengel besteht.

Aus praktischer Sicht ist die genaue Erfassung aller geometrischen Informationen sowie die Beschreibung aller physio-chemischen Prozesse auf der Mikroskala nicht umsetzbar. Aus diesem Grund wird in der vorliegenden Arbeit eine makroskopische Modellformulierung auf Basis der Hybrid Mixture Theory (HMT) (frei übersetzt: Hybri-

de Mischungstheorie) gewählt [20, 21], die eine homogenisierte Beschreibung der Mikrostruktur ermöglicht. Die Entwicklung makroskopischer Konstitutivmodelle ist schließlich für die effektive Modellierung der oben genannten Phänomene notwendig. Vor diesem Hintergrund wird im Folgenden ein Literaturüberblick hinsichtlich der unterschiedlichen Modellanforderungen gegeben.

Zunächst wird ein Überblick bezüglich der Literatur gegeben, in der der Flüssigkeitsaustausch von Polymeren betrachtet wird. Polymere, die in der Lage sind Flüssigkeiten zu absorbieren und zu binden, wurden bereits seit den frühen Arbeiten von Flory [53], Flory & Rehner [55], Huggins [71] und Flory & Rehner [56] untersucht. Diese Klasse von Polymeren wird auch als Hydrogel bezeichnet. Durch die Weiterentwicklung dieser Polymere hin zu geladenen Hydrogelen, auch bekannt als Superabsorbierende Polymere (SAP), sind weitaus höhere Quellungsgrade zu erreichen. In der Literatur finden sich verschiedene Ansätze zur Modellbeschreibung der Triebkräfte hinter der Absorption. Demnach entwickelte die Gruppe um Huyghe & Janssen [74, 76] und Wilson *et al.* [164] ein Mehrphasenmodell zur Beschreibung geladener poröser Materialien, die aus einer geladenen Festkörpermatrix bestehen, welche mit einem Porenfluid und mobilen Ionen gesättigt ist. Die Ladung der mobilen Ionen im Porenraum befindet sich im Gleichgewicht mit der geladenen Festkörperphase, sodass das gesamte Material auf makroskopischer Ebene ladungsneutral ist. Da fixierte Ladungen mit der Festkörpermatrix verbunden sind, existiert eine Konzentrationsdifferenz zwischen Ionen innerhalb des Gels und Ionen in einem Umgebungsfluid. Zur Abschwächung der Konzentrationsdifferenz wird schließlich Flüssigkeit vom Gel absorbiert. Auf diesem Modellierungsansatz baut ebenso das Mehrphasenmodell von Acartürk [2] auf, was zur Beschreibung elektroaktiver, quellfähiger poröser Materialien entwickelt wurde. In diesem Modellansatz tauscht das poröse Medium Porenfluid mit dem Umgebungsfluid über die Phasengrenze aus. D. h., die Quellung des Materials wird über die Randbedingungen des porösen Materials bestimmt. Es ist zu erwähnen, dass ein solches Mehrphasenmodell zur Modellierung von Quellprozessen in Zusammenhang mit geladenen Hydrogelen, jedoch auch von biologischem Gewebe herangezogen werden kann, da das Konzept der fixierten Ladungen ebenso ein weithin anerkannter Modellierungsansatz innerhalb der Biomechanik darstellt [164].

Ähnliche kontinuumsbasierte Modelle zur Beschreibung geladener Hydrogele wurden von English *et al.* [51] und Yang *et al.* [165] entwickelt. Im Unterschied zu den oben genannten Modellen wurde das umgebende Porenfluid explizit in der Modellierung berücksichtigt. Die Triebkräfte für den Transport von Flüssigkeiten und Ionen wurden abgeleitet aus zuvor postulierten thermodynamischen Potentialen. Neben der Ionenkonzentration fand auch der Einfluss des pH-Werts der äußeren Flüssigkeit hinsichtlich der Absorptionseigenschaften Berücksichtigung. Es ist zu erwähnen, dass geladene Hydrogele nicht ausschließlich sensitiv auf die chemische Zusammensetzung des Umgebungsfluids reagieren, d. h. Ionenkonzentration oder pH-Wert, sondern auch auf Temperaturänderungen [36] oder elektrische Felder [2]. Durch die reversible Quellung eignen sich geladene Hydrogele ferner auch als Sensoren für komplexe Anwendungen [93].

Direkte Modellierungsansätze von Hydrogelen, die als chemische Aktuatoren oder zur

medizinischen Wirkstoffabgabe genutzt werden, finden sich zahlreich innerhalb der Literatur. Zwar erlangt die Nutzung von SAP als Zusatzstoff in Betonmischungen seit einigen Jahren an Bedeutung, jedoch gibt es nur wenige kontinuumsbasierte Modellierungsansätze zur Beschreibung des Flüssigkeitsaustauschs von Hydrogelen innerhalb poröser Materialien. In diesem Zusammenhang ist zu erwähnen, dass Viejo *et al.* [158] ein mesoskopisches Modell einer mit SAP modifizierten Betonmatrix entwickelte. Ferner ist in Hinblick auf aktuelle Forschungsthemen bezüglich SAP modifizierter Betonmischungen auf den RILEM Forschungsbericht [106] zu verweisen, welcher eine umfassende Übersicht der Entwicklungen aufzeigt.

Das Hauptziel zur Nutzung von SAP ist die Kontrolle des ungebundenen Porenwassers innerhalb von Betonmischungen [105, 106]. Wasser wird zum einen für die Hydratation der Zementphase benötigt, hat aber auch einen maßgeblichen Einfluss auf die rheologischen Eigenschaften des Betons. Da einige Anwendungen eine gute Verarbeitbarkeit der frischen Betonmischung erfordern, ist ein hoher Wasseranteil innerhalb der Mischung von großer Bedeutung, um beispielsweise eine Pumpfähigkeit im frischen Zustand zu ermöglichen. Durch Hinzugabe von SAP kann die Menge des freien Porenwasser über die Zeit kontrolliert werden [107, 130]. Darüber hinaus wurde der Einfluss von SAP auf die mechanischen Eigenschaften von Beton experimentell untersucht [28, 106–108, 111, 117].

Da SAP nicht nur die Möglichkeit besitzen Wasser aufzunehmen, sondern auch kontrolliert an die Umgebung abzugeben, erlangten SAP bei der Vermeidung von Schrumpfrissen in Betonstrukturen besondere Aufmerksamkeit [79, 80, 104]. In diesem Kontext werden SAP der Mischung hinzugefügt, um zusätzliches Porenwasser zu speichern, das über einen längeren Zeitraum an die Zementphase abgegeben wird. Durch die kontinuierliche Hydratation wird die volumetrische Dehnung während der Aushärtung verringert, was insbesondere bei ultrahochfestem Beton (UHPC) einen entscheidenden Vorteil bringt [13, 42, 65, 107, 111, 128, 130, 132, 138, 174].

Auf der Mikroskala führt das Aufquellen von SAP Partikeln zu einer Reduzierung der effektiven Porosität der Festkörpermatrix, sodass sich die intrinsische Permeabilität verringert. Der Fluidtransport wird demnach durch aufgequollene SAP beeinflusst [159, 160]. Dieser sogenannte Gelblockingeffekt wird ausgenutzt, um Risse innerhalb der Betonmatrix abzudichten [89, 137, 139]. Es ist anzumerken, dass selbstheilende poröse Materialien durch den Einsatz von SAP ebenso in anderen Branchen praktische Relevanz erreicht haben. Czupryna [43] entwickelte eine innovative, selbstdichtende Kabelummantelung für Stromkabel. Das Eindringen von Wasser bei Beschädigung der Kabelummantelung kann auch dann verhindert werden, wenn die äußere Schicht Risse aufweist. Hierzu wird ein trockenes SAP Granulat dem Matrixmaterial der Kabelummantelung beigemischt. Im Falle der Schädigung der äußeren Kabelschicht dringt Wasser in die Struktur ein und initialisiert eine Quellung der trockenen SAP Partikel innerhalb der Matrix. Die angequollenen Hydrogele bilden eine Wasserbarriere und schützen somit den Kern des Kabels vor Wasserkontakt.

Auf der einen Seite finden sich innerhalb der Literatur zahlreichen kontinuumsbasierte Modelle zur Beschreibung geladener Hydrogele, auf der anderen Seite existieren rein experimentelle Untersuchungen zum Flüssigkeitsaustausch zwischen Hydroge-

len und Porenfluid innerhalb poröser Baustoffe. Aus diesem Anlass wird in der vorliegenden Arbeit ein kontinuumsmechanisches Mehrphasenmodell entwickelt, dass die Polymere innerhalb des Porenraums als Bestandteil eines porösen Materials betrachtet. Hieraus resultiert, dass die Flüssigkeitsaufnahme der Hydrogele nicht durch einen Fluss über die Phasengrenze Hydrogel-Porenfluid bestimmt ist, wie in Modellen von Acartürk [2], Huyghe & Janssen [76] und Yu *et al.* [168], sondern über lokale Massenaustauschterme in den entsprechenden Massenbilanzen. Kontinuumsbasierte Mischungsmodelle unter Berücksichtigung von Massenaustauschtermen wurden zuvor von einigen Wissenschaftlern hinsichtlich unterschiedlicher Anwendungen entwickelt. Alexandersson *et al.* [8], Alexandersson & Ristinmaa [9] und Askfelt *et al.* [12] entwickelten ein Mehrphasen- und Mehrkomponentenmodell basierend auf der HMT zur Simulation thermo-hydro-mechanischer Kopplungen innerhalb von Kartonage. Ristinmaa *et al.* [119] benutzte denselben theoretischen Rahmen zur Beschreibung eines allgemeinen thermo-plastischen porösen Materials mit besonderer Berücksichtigung des Transports und des Massenaustauschs. Kinematik und Massenaustausch sind hierbei über eine multiplikative Zerlegung des Deformationsgradienten gekoppelt. Loret *et al.* [100, 101] und Gajo & Loret [59] entwickelten ein Mehrphasenmodell für quellfähiges Tongestein. Die Kopplung zwischen Massenaustausch und Deformation repräsentieren hier chemisch-induzierte Volumenänderungen auf der Makroskala. Darüber hinaus wurden Wachstumsprozesse in porösen Medien, wie die Remodellierung weichen Gewebes [118, 143] oder das Tumorwachstum [10, 11, 35], durch Massenaustauschterme innerhalb kontinuumsbasierter Mischungstheorien modelliert.

Neben der Steuerung der freien Porenflüssigkeit innerhalb des Porenraums, stellt die Polymeranlagerung an das Festkörperskelett, bedingt durch die Infiltration einer Polymerlösung, die zweite Modellanforderung dar. Durch die Polymeranlagerung reduziert sich die Polymerkonzentration der Lösung, was bezogen auf eine Anwendung im Polymer Flooding ein negative Wirkung hätte – die Viskosität der injizierten Lösung und somit die Mobilisierung der Ölphase nehmen ab. Ferner verlangsamt die Anlagerung von Polymeren die Ausbreitungsgeschwindigkeit der Konzentrationsfront im Porenraum. Aus wirtschaftlicher Sicht verursacht eine hohe Polymeranlagerung erhöhte Kosten, da ein Anteil des Polymers im Porenraum verloren geht [172]. Eine genaue Kenntnis der Polymeranlagerung ist demnach von großer Bedeutung für die erfolgreiche Umsetzung von Polymer Flooding Projekten.

Al-Hajri *et al.* [7], Idahosa *et al.* [77], Zhang & Seright [173] und Zhang [172] führten zur quantitativen Charakterisierung von Polymeranlagerungen Laborexperimente an Bohrkernen durch, sogenannte Core Flooding Experimente (frei übersetzt: Kernflutung). Hierbei wird eine Polymerlösung mit konstanter Flussrate in einen porösen Bohrkern injiziert, wobei die Polymerkonzentration am austretenden Ende des Kerns gemessen wird. Die hieraus erhaltenen Durchbruchskurven der Polymerkonzentration werden üblicherweise über das injizierte Porenvolumen aufgetragen. Das angelagerte Polymervolumen lässt sich schlussendlich anhand dieser Durchbruchskurven bestimmen. Es ist zu erwähnen, dass eine solche Abschätzung eine gemittelte Aussage über den Bohrkern beschreibt. Es konnte in unabhängigen experimentellen Studien von Al-Hajri *et al.* [7], Idahosa *et al.* [77], Zhang & Seright [173] und Zhang [172] gezeigt wer-

den, dass die maximale Polymeranlagerung mit steigender Injektionsrate wächst. Dieser Aspekt spielt vor dem Hintergrund der Wirtschaftlichkeit des gesamten Polymer Flooding Projekts eine entscheidende Rolle und muss demnach berücksichtigt werden.

Es ist innerhalb der Literatur eine weit verbreitete Annahme, dass der Anlagerungsprozess durch drei Mechanismen getrieben wird [6, 172]. Chemo-physikalische Kräfte verursachen die Adsorption von Polymeren auf der Oberfläche des Festkörperskeletts. Diese Triebkräfte resultieren primär aus van der Waals-Kräften, Wasserstoffbrückenbindungen sowie elektrostatischen Wechselwirkungen [113, 131, 141]. Ferner sind die wirkenden Kräfte bestrebt die Oberflächenenergie durch die Polymeranlagerung zu reduzieren [44]. In Abhängigkeit der Morphologie des Porenraums und der Größe der Polymermoleküle, können fluidisierte Polymere an kleinen Poren aufgehalten werden. Ein dritter Mechanismus, welcher auch als Hydrodynamic Retention (frei übersetzt: hydrodynamische Anlagerung) bekannt ist, lässt sich auf die Geschwindigkeitsverteilung im Porenraum zurückführen. Insbesondere bei höheren Injektionsraten verursachen hydrodynamische Kräfte die Anlagerung von Polymeren an das Festkörperskelett [6]. Mit zunehmender Polymeranlagerung geht eine Morphologieänderung des Porenraums einher, was sich durch eine Reduktion der Permeabilität bemerkbar macht. Folglich ist ein Anstieg der Injektionsdruckdifferenz bei kontinuierlicher Injektionsflussrate zu beobachten.

Zwar konnte in experimentellen Untersuchungen herausgefunden werden, dass sich die Polymeranlagerung hinsichtlich unterschiedlicher Mechanismen aufspalten lässt, trotzdem wird innerhalb der Literatur fast ausschließlich die gesamte Polymeranlagerung über Adsorptions-Isothermen modelliert [39]. Bereits Dawson & Lantz [45] postulierte, dass die Polymeranlagerung an eine Langmuir-Isotherme angepasst werden kann, ungeachtet der Tatsache, dass die Isotherme ursprünglich für rein reversible Adsorptionsprozesse hergeleitet wurde [98]. Durch die Modellierung der Anlagerung über eine Isotherme wird impliziert, dass dieser Prozess instantan erfolgt. Fundamentale Kritik an der Nutzung der Langmuir-Isothermen wird beispielsweise von Zhang [172] geäußert. Die Polymeranlagerung an das Festkörperskelett ist zum größten Teil irreversibel, sodass eine Anwendung der Langmuir-Isothermen auf theoretischer Basis prinzipiell nicht gerechtfertigt ist. In der vorliegenden Arbeit, wird der Anlagerungsprozess als dynamischer Massenaustausch zwischen fluidisierten und angelagerten Polymeren modelliert. Hierbei wird a priori zwischen irreversibler und reversibler Anlagerung unterschieden. Ähnliche kontinuumsbasierte Modelle wurden bereits von Tiraferri *et al.* [147], Tosco & Sethi [151] und Tosco *et al.* [149] entwickelt, um Infiltrationsprozesse von fluidisierten Mikro- und Nanopartikeln in porösen Medien zu simulieren. Basierend auf diesen Arbeiten wird hier ein vergleichbares dynamisches Modell gewählt, was schließlich an experimentell ermittelte Durchbruchskurven angepasst wird.

Der Massenaustausch spielt bei der Formulierung des Mehrphasenmodells eine essentielle Rolle. Die zwei zuvor genannten Phänomene, d. h. Absorption/Desorption sowie Anlagerung/Ablösung, sind Wechselwirkungen zwischen dem Polymer und dem Porenfluid bzw. dem Polymer und der Festkörpermatrix. Diese Interaktionen werden im Mehrphasenmodell effektiv durch Massenaustauschterme innerhalb der zugehörigen Massenbilanzen beschrieben und sind demnach auf natürliche Weise in die kontinu-

umsbasierte Mischungstheorie eingebettet.

Um die Ausbreitung der Polymerlösung innerhalb des Porenraums abbilden zu können, ist eine makroskopische Modellierung der Polymerlösung hinsichtlich der tatsächlichen Rheologie essentiell. Newtonische Flüssigkeitsströmungen durch poröse Materialien werden üblicherweise durch das Darcy-Gesetz beschrieben. In diesem Falls ist die Scherspannung des Fluids proportional zur Scherrate, während die dynamische Viskosität die Proportionalitätskonstante darstellt. Im Gegensatz dazu kann beobachtet werden, dass das Verhalten von Polymerlösungen im Allgemeinen nichtnewtonischer Natur ist, sodass kein linearer Zusammenhang zwischen dem Druckgradienten und der Flussrate vorliegt. Die in situ Viskosität des Fluids wird hierbei zu einer Funktion der Scherrate.

Viele Polymerlösungen zeigen in rheologischen Messungen ein scherverdünnendes (strukturviskoses) Fließverhalten. In diesem Zusammenhang wurden analytische und empirische Rheologiemodelle entwickelt, die das scherratenabhängige Verhalten abbilden können. Die Modellierung der Viskosität über ein Potenzgesetz, sowie komplexere Modelle, wie z. B. das Carreau-, Ellis- oder Cross-Modell, finden vielfach Anwendung innerhalb der Literatur [29, 150, 171]. Es konnte jedoch experimentell gezeigt werden, dass die Rheologie von Polymerlösungen, die durch poröse Medien fließen, maßgeblich von der intrinsischen Rheologie abweicht [170]. Zamani *et al.* [170] postulierte, dass der Unterschied durch die komplexe Geometrie des porösen Mediums hervorgerufen wird. Unter dem Einfluss hoher Injektionsraten konnten Delshad *et al.* [46] und Najafabadi *et al.* [110] beobachten, dass sich einige Polymerlösungen innerhalb poröser Medien scherverdickend (dilatant) verhalten. Interessanterweise wurden dieselben Polymerlösungen in rheologischen Messungen als scherverdünnend (strukturviskos) charakterisiert. Dieser Effekt wird mit dem viskoelastischen Charakter von Polymerlösungen in Verbindung gebracht, der sich durch die geometrischen Restriktionen im Porenraum bemerkbar macht [142]. Es ist anzumerken, dass dieses Phänomen in Sochi [140] ausführlich diskutiert wurde.

Um die in situ Viskosität mit der intrinsischen Viskosität in Verbindung zu bringen, wurde ein konstitutiver Zusammenhang zwischen der effektiven Scherrate und der lokalen Filtergeschwindigkeit entwickelt. Die effektive Scherrate ist innerhalb der makroskopischen Modellierung nicht direkt zugänglich, da sie die Scherrate repräsentiert, die innerhalb des ortsaufgelösten Porenraums zu erwarten wäre. Für ein regelmäßiges poröses Medium bestehend aus Röhren, konnte diese Beziehung durch Lösen der Navier-Stokes-Gleichung jedoch analytisch hergeleitet werden. Um diesen Zusammenhang zwischen Mikro- und Makroskala auch auf realistische Porenskelette zu übertragen, wurde ein zusätzlicher empirischer Parameter eingefügt, der demnach experimentell bestimmt werden muss. Zamani *et al.* [170] untersuchte mittels direkter numerischer Simulationen den konstitutiven Zusammenhang anhand realistischer Mikrostrukturen aus CT-Daten. Es ist zu erwähnen, dass das konstitutive Konzept der effektiven Scherrate von zahlreichen Autoren benutzt wurde, um die scherratenabhängige Rheologie von Polymerlösungen makroskopisch abbilden zu können [41, 69, 99, 115, 151].

In der vorliegenden Arbeit wird ein Mehrphasenmodell formuliert, dass die Anforderungen der zuvor genannten Anwendungen auf makroskopischer Ebene umsetzt. In

diesem Zusammenhang spielt die Entwicklung von Massenaustauschtermen eine entscheidende Rolle, um die spezifischen Interaktionen effektiv zu erfassen. Um schließlich die gekoppelten Prozesse numerisch abzubilden, ist es notwendig die Bilanzgleichungen des Systems, welche üblicherweise durch gekoppelte partielle Differentialgleichungen beschrieben sind, zu lösen. Hierfür werden die schwachen Formen örtlich sowie zeitlich diskretisiert und anschließend mit Hilfe der Finiten Elemente Methode (FEM) gelöst. Ziel dieser Arbeit ist schlussendlich die Entwicklung eines vielseitigen Materialmodells zur Berechnung komplexer Interaktionen in gesättigten porösen Medien, die über Massenaustauschterme gesteuert werden.

Gliederung der Arbeit

Die Grundlagen der kontinuumsbasierten Mischungstheorie werden in **Kapitel 2** eingeführt. Zu Beginn wird eine historische Einordnung der Entwicklung moderner Mischungstheorien gegeben. Nach der Einführung grundlegender Größen und Definitionen wird die Kinematik innerhalb der HMT diskutiert. Demnach wird die Mischung betrachtet als eine Überlagerung mehrerer Kontinua, was zu der unabhängigen Formulierung von Bilanzgleichungen für jedes Kontinuum führt. Hierbei spiegeln geeignete Austauschterme in den Bilanzgleichungen die Interaktionen zwischen Phasen und Komponenten auf konstitutiver Ebene wider. Der zweite Hauptsatz der Thermodynamik wird schließlich in Form der Entropieungleichung für das isotherme Mehrphasen- und Mehrkomponenten-Modell formuliert.

Geladene Hydrogele werden in der vorliegenden Arbeit als ein Bestandteil eines Mehrphasenmaterials betrachtet. Die Konstitutivmodellierung der reversiblen Flüssigkeitsaufnahme wird allerdings isoliert in **Kapitel 3** diskutiert, um die komplexen chemophysikalischen Triebkräfte im Detail erklären zu können. In diesem Kapitel liegt der Fokus auf der Herleitung der thermodynamischen Grundlagen geladener Hydrogele. Es werden etablierte Modelle zur Beschreibung der Triebkräfte hinter der Absorption sowie Desorption von Flüssigkeiten erläutert.

In **Kapitel 4** wird das allgemeine Modell bezüglich der Phasen- und Komponentenzusammensetzung spezifiziert. Das Modell besteht demnach aus einem Festkörperskelett, wobei der Porenraum gleichzeitig mit einer wässrigen Porenflüssigkeit sowie einem Gel gefüllt ist. Einerseits berücksichtigt das Modell die Anlagerung des Gels an das Festkörperskelett, wobei anderseits gleichzeitig Absorptions- und Desorptionsprozesse als Wechselwirkung zwischen Gel und Porenflüssigkeit berücksichtigt werden. Diese komplexen Prozesse innerhalb des Porenraums werden im makroskopischen Kontinuumsmodell durch Massenaustauschterme erfasst. Im Folgenden wird die Entropieungleichung an die gewählte Modellkomposition adaptiert und ausgewertet. Bei der Auswertung werden Resultate bezüglich der thermodynamischen Modellierung von Hydrogelen genutzt. Das Resultat liefert konstitutive Beziehungen, die im thermodynamischen Gleichgewicht gelten müssen, sowie zusätzliche Terme, die für die Dissipation innerhalb des Materials verantwortlich sind. Der dissipative Anteil liefert Nahe des Gleichgewichts thermodynamisch konsistente Formen für die Sicker- und Diffusions-

geschwindigkeiten sowie für die Massenaustauschterme. Das komplexe Mehrphasenmodell stellt ein übergeordnetes sogenanntes Mastermodell dar. Im weiteren Verlauf der Arbeit wird dieses Modell systematisch reduziert, sodass unterschiedliche Modelleigenschaften isoliert und unabhängig von einander untersucht werden können.

In Hinblick auf die zuvor erwähnte Modellreduktion, liegt in **Kapitel 5** der Fokus auf der Simulation des Absorptions-/Desorptionsprozesses. Hierbei werden Hydrogele untersucht, die in Kontakt mit einer Salzlösung stehen. Vor dem Hintergrund experimenteller Untersuchungen, wird die dynamische Flüssigkeitsaufnahme von Hydrogelen bestimmt. Mithilfe der experimentellen Ergebnisse werden die Modellparameter innerhalb der konstitutiven Modellierung kalibriert. Ferner wird ein Modell zur Beschreibung der Dynamik des Massenaustauschs entwickelt, was ebenso an die experimentellen Daten angepasst wird. Durch die Einführung des postulierten Modells, wird der notwendige Umfang experimenteller Daten zur Modellkalibrierung reduziert. Das entwickelte Modell kann mit hoher Genauigkeit die in Experimenten beobachtete reversible Flüssigkeitsaufnahme abbilden. Es ist hier zu erwähnen, dass die maßgeblichen Ergebnisse aus diesem Kapitel bereits in [124] veröffentlicht wurden.

In **Kapitel 6** wird das Mastermodell bezüglich einer zweiten Variante reduziert. Hierbei liegt der Fokus auf dem Transport und der Infiltration von Polymerlösungen innerhalb poröser Medien. Zur Vereinfachung wird der Massenaustausch zwischen Porenflüssigkeit und Gel innerhalb des Modells ausgeschlossen, wobei die Anlagerung von Polymeren an das Festkörperskelett berücksichtigt wird. Die Kopplungseffekte zwischen der Polymeranlagerung, dem nichtnewtonischen Fließverhalten der Polymerlösung sowie die Entwicklung der Permeabilität infolge von Anlagerungen, werden kontinuumsmechanisch modelliert. Das Ziel ist die numerische Untersuchung des Infiltrationsprozesses mit Hilfe der Finiten Elemente Methode. Hierzu werden die notwendigen Bilanzgleichungen in schwacher Form dargestellt und das Anfangsrandwertproblem allgemein formuliert.

Als nächstes wird ein kleinskaliges Polymer Flooding Experiment simuliert, wobei das Kontinuumsmodell mit Hilfe von Literaturdaten kalibriert wird. Neben der Polymeranlagerung wird die Entwicklung der Permeabilität sowie die nichtnewtonische Rheologie diskutiert. Das Mehrphasenmodell ist in der Lage die injektionsratenabhängige Polymeranlagerung sowie Viskositätsänderungen abzubilden. Das kalibrierte Materialmodell wird schließlich exemplarisch auf ein komplexeres Anfangsrandwertproblem angewandt und die Modelleigenschaften und Kopplungen vor dem Hintergrund heterogener Geschwindigkeitsverteilungen analysiert.

Die Resultate der vorliegenden Arbeit sind in **Kapitel 7** zusammengefasst. Des Weiteren werden zusätzlicher Modellierungsansätze sowie offene Fragestellungen diskutiert.

Nomenclature

Conventions

General conventions

$(\cdot)$		placeholder for arbitrary quantity
$\delta(\cdot)$		test function of primary unknown
$\mathrm{d}(\cdot)$	or $\partial(\cdot)$	differential or partial derivative operator

Index and suffix conventions

$\dot{(\cdot)} = \mathrm{d}(\cdot)/\mathrm{d}t$	total time derivative with respect to the overall mixture φ
$(\cdot)'_{\alpha}$	material time derivative following the motion of a phase φ^{α}
$(\cdot)'_{\alpha_j}$	material time derivative following the motion of a species φ^{α_j}
$\partial_t(\cdot) = \partial(\cdot)/\partial t$	local time derivative
$(\cdot)_m$	molar quantity
$(\cdot)_e$	electromagnetic quantity
$\hat{(\cdot)}^{\alpha_j}, \hat{(\cdot)}^{\alpha}$	total production term of species φ^{α_j} (or phase φ^{α})
$\hat{(\cdot)}^{\alpha_j}_{\beta}, \hat{(\cdot)}^{\alpha}_{\beta}$	production of $\hat{(\cdot)}^{\alpha_j}$ (or $\hat{(\cdot)}^{\alpha}$) due to interaction with phase φ^{β}
$(\cdot)_0$	initial value
$\lvert(\cdot)\rvert$	absolute value
$(\cdot)^T$	transpose of a quantity
$(\cdot)_{rev}$	reversible part of $(\cdot)$
$(\cdot)_{irr}$	irreversible part of $(\cdot)$
$(\cdot)_a$	attachment quantity
$(\cdot)_d$	detachment quantity
$\bar{(\cdot)}$	specified boundary condition
$\bar{(\cdot)}_{in}$	boundary condition at injection boundary
$\bar{(\cdot)}_{out}$	boundary condition at outlet boundary
$(\cdot)_{PM}$	quantity related to Power Model
$(\cdot)_{CM}$	quantity related to Carreau Model
$(\cdot)_{ECM}$	quantity related to Extended Carreau Model
$a_{(\cdot)}, b_{(\cdot)}, c_{(\cdot)}, d_{(\cdot)}$	fitting coefficients corresponding to empirical function $(\cdot)$

Symbols

Greek letters

Symbol	Unit	Description
α		phase identifier: S: solid skeleton, L: polymer solution, K: intrinsic solid, A: attached polymer gel, G: fluidized polymer gel, F: liquid, fA: absorbed solution (attached), sA: polymer chains (attached), fG: absorbed solution (free), sG: polymer chains (free)
α_r	[−]	scaling factor (Metropolis-Hastings algorithm)
α_{pm}	[−]	shift factor in constitutive porous media shear rate
β	[−]	scaling exponent in permeability and density production function
β_{rev}, β_{irr}	[−]	formation damage coefficient
β_{ECM}	[−]	model parameter in Extended Carreau Model
Γ		domain boundary
Γ_D		Dirichlet boundary
Γ_N		Neumann boundary
Γ^j	[mol/(m^3 s)]	molar density production function
Γ_0^j	[mol/(m^3 s)]	molar density production coefficient
γ^{α_j}	[−]	activity coefficient
$\gamma^{\alpha_\pm}$	[−]	average activity coefficient of dissolved ions
$\dot{\gamma}_{pm}$	[1/s]	porous media shear rate
$\dot{\gamma}_{bulk}$	[1/s]	bulk (intrinsic) shear rate
$\dot{\gamma}_p$	[1/s]	general shear rate in pipe model
$\dot{\gamma}_{p,eff}$	[1/s]	shear rate in pipe model due to power-law fluid
$\Delta\mu^j, \Delta\mu^j_{ion}, \Delta\mu^w_{mix}, \Delta\mu^w_{elast}$	[J/kg]	mass specific chemical potential difference
$\varepsilon^{\alpha_j}, \varepsilon^\alpha, \varepsilon$	[J/kg]	mass specific internal energy
$\hat{\varepsilon}^\alpha, \hat{\varepsilon}^{\alpha_j}, \hat{\varepsilon}_r^{\alpha_j}, \hat{\varepsilon}_a^{\alpha_j}$	[J/(m^3 s)]	energy production
$\boldsymbol{\varepsilon}_S$	[−]	linearized strain tensor

$\zeta^{\alpha_j}, \zeta^{\alpha}$	[1/(J m^3 s)]	total mass transfer rate
$\zeta^{\alpha}_{\beta}, \zeta^{\alpha_j}_{\beta}$	[1/(J m^3 s)]	mass transfer rate from φ^{β} to φ^{α} (or φ^{α_j})
$\hat{\eta}^{\alpha_j}_r, \hat{\eta}^{\alpha_j}_a, \hat{\eta}^{\alpha}_r$	[J/(K m^3 s)]	intra- and inter-phase entropy production
$\eta^{\alpha_j}, \eta^{\alpha}$	[J/(K kg s)]	mass specific entropy
Θ	[–]	random number between 0 and 1 (Metropolis-Hastings algorithm)
κ	[–]	ratio between fixed charges and cross-linking density
$\mathbf{\Lambda}^{\alpha}_r$	[J/kg]	Lagrange multiplier
$\hat{\Lambda}^{\alpha_j}, \hat{\Lambda}^{\alpha}, \hat{\Lambda}$	[J/(K m^3 s)]	entropy production
λ	[–]	isotropic stretch
λ_i	[–]	principal stretch in $\mathbf{e}_i$-direction
λ_{eff}	[N/m^2]	effective 1. Lamé parameter
$\lambda^{\alpha}, \lambda^{\alpha_j}$	[J/kg]	Lagrange multiplier
λ^{α}_e	[J/C]	electric potential (Lagrange multiplier)
$\lambda_{a,k}$	[1/m]	filtration coefficient of k-th active site
λ_{CM}	[–]	model parameter in Carreau Model
$\Delta\mu^i_e$	[J/kg]	mass specific chemical potential difference due to electro-neutrality
$\tilde{\mu}^{\alpha_j}$	[J/kg]	relative mass specific chemical potential
μ^{α_j}	[J/kg]	absolute mass specific chemical potential
$\mu^{\alpha_j}_m$	[J/mol]	absolute molar chemical potential
μ^{α_N}	[J/kg]	mass specific reference chemical potential
$\mu^j_{m,0}$	[J/mol]	molar chemical potential under reference conditions
μ_{eff}	[N/m^2]	effective 2. Lamé parameter
$\mu^{\alpha R}$	[Pa s]	effective dynamic viscosity of phase φ^{α}
$\mu_{p,eff}$	[Pa s]	dynamic viscosity in pipe model due to power-law fluid
μ_{newton}	[Pa s]	dynamic viscosity of Newtonian fluid
μ_{bulk}	[Pa s]	bulk (intrinsic) viscosity
μ_0	[Pa s]	Newtonian plateau viscosity for low shear rate (Carreau Model)
μ_∞	[Pa s]	Newtonian plateau viscosity for high shear rate (Carreau Model)
μ_{ECM}	[Pa s]	model parameter in Extended Carreau Model
ν	[mol/m^3]	intrinsic cross-linking density
ν_{eff}	[–]	effective Poisson ratio

ξ_{A_i}	[–]	indicator function in stair-case function
ρ, ρ^{α}	[kg/m^3]	partial (apparent) density
ρ^{α_j}	[kg/m^3]	concentration/density of species
$\rho^{\alpha R}$	[kg/m^3]	effective (true) density
$\rho_m^{\alpha_j}$	[mol/m^3]	molar concentration/density of species
$\hat{\rho}^{\alpha}, \hat{\rho}^{\alpha_j}, \hat{\rho}_a^{\alpha_j}, \hat{\rho}_r^{\alpha_j}$	[kg/(m^{3}s)]	density production
$\rho_e^{\alpha_j}, \rho_e^{\alpha}$	[C/m^3]	charge density
$\rho^{sG_{fc}}$	[kg/m^3]	intrinsic Fixed Charge Density (FCD)
$\rho_m^{sG_{fc}}$	[mol/m^3]	intrinsic molar Fixed Charge Density (FCD)
$\rho_m^{G_{fc}}$	[mol/m^3]	molar Fixed Charge Density (FCD) of the hydrogel
$\tilde{\rho}_i^{F_s}$	[mol/(m^3)]	i-th salt concentration in stair-case function
$\sigma_{\eta}, \sigma_{\eta}^{\alpha_j}, \sigma_{\eta}^{\alpha}$	[J/(K kg s)]	mass specific external entropy supply
$\boldsymbol{\sigma}_{ac}$		vector of standard deviations (Metropolis-Hastings algorithm)
$\sigma, \sigma_{i,pro}$		standard deviation (Metropolis-Hastings algorithm)
σ^2		error variance (Metropolis-Hastings algorithm)
τ^j	[s]	characteristic swelling time
$\tau^w, \tau_{abs}^w, \tau_{des}^w, \bar{\tau}_{abs}^w, \bar{\tau}_{des}^w$	[s]	characteristic swelling time for water
τ_{eff}	[N/m^2]	effective shear stress
τ_{rz}	[N/m^2]	shear stress in pipe model
$\boldsymbol{\phi}_{\eta}^{\alpha_j}, \boldsymbol{\phi}_{\eta}^{\alpha}$	[J/(K m^3 s)]	entropy flux
ϕ	[–]	polymer volume fraction
ϕ^f	[–]	solvent volume fraction in gel (lattice model)
ϕ^p	[–]	polymer volume fraction in gel (lattice model)
$\varphi^{\alpha}, \varphi^{\alpha_j}$		phase and species
$\boldsymbol{\chi}_{\alpha}$	[m]	motion function
χ	[–]	Flory-Huggins interaction parameter
$\Psi, \Psi^{\alpha}, \Psi^{\alpha_j}$	[J/kg]	mass specific Helmholtz free energy
$\Psi_{ion}^{\alpha}, \Psi_{mix}^{\alpha}, \Psi_{elast}^{\alpha}$	[J/kg]	mass specific Helmholtz free energy corresponding to physical phenomena
Ψ_{tor}	[–]	tortuosity of porous media
$\boldsymbol{\psi}_{\eta}, \boldsymbol{\psi}_{\eta}^{\alpha}, \boldsymbol{\psi}_{\eta}^{\alpha_j}$	[J/(Km^{3}s)]	entropy efflux
ψ^w	[–]	cumulated activity coefficient of water

$\psi^{\pm}$	[–]	cumulated activity coefficient of mobile ions
$\psi_{a,k}$	[–]	attachment function of k-th active site
Ω		domain

Latin letters

Symbol	Unit	Description
A_i		i-th time interval in stair-case function
A_{eq}	[m^2]	pipe's equivalent cross sectional area
A_{cross}	[m^2]	cross section area of core (core flooding)
a^{α_j}	[–]	activity
$\mathrm{d}a$	[m^2]	current area element
$\mathbf{b}^{\alpha_j}, \mathbf{b}^{\alpha}, \mathbf{b}$	[$\mathrm{m/s}^2$]	mass specific body force
C_{KC}	[–]	Kozeny-Carman coefficient
C_{PM}	[Pa s]	model parameter in Power Model
c^{α_j}	[–]	mass fraction
$\tilde{c}_i^{F_s}$	[–]	i-th salt mass fraction in stair-case function
$\mathbf{D}_{\alpha}$	[1/s]	rate of deformation tensor
$\mathbf{D}^{\alpha_j}$	[s]	diffusivity tensor
D^G	[m^2/s]	dispersion coefficient of polymer gel
$\tilde{D}^G$	[m^2/s]	artificial dispersion coefficient
$D, \bar{D}, D_{\lambda}, \bar{D}_{eq}, \bar{D}_{dis}, \bar{D}_{ex}$	[$\mathrm{W/m}^3$]	rate of energy dissipation per unit volume
$\mathbf{d}$		model prediction (Metropolis-Hastings algorithm)
$\mathbf{d}^{obs}$		averaged observation vector (Metropolis-Hastings algorithm)
d_{eff}	[m]	effective particle diameter
d_{grain}	[m]	average grain diameter
d_{sq}	[m]	diameter of holes in IBVP
$\mathbf{E}_S$	[–]	Green-Lagrange strain tensor
E_{eff}	[Pa]	effective Young's modulus
$\mathbf{e}_i$	[–]	basis vector of orthonormal coordinate system
$\mathbf{F}_{\alpha}$	[–]	deformation gradient
F	[C/mol]	Faraday constant
$\mathbf{g}$		forward operator (Metropolis-Hastings algorithm)
G^{α}	[J/kg]	mass specific Gibbs free energy

G_m^α	[J/mol]	molar Gibbs free energy
$G_{m,mix}^\alpha, G_{m,elast}^\alpha, G_{m,ion}^\alpha$	[J/mol]	molar Gibbs free energy corresponding to physical origin
$\Delta G_{m,mix}^\alpha$	[J/mol]	change in molar Gibbs free energy due to mixing
$\Delta H_{m,mix}^\alpha$	[J/mol]	molar mixing enthalpie
h_{core}, h_{sq}	[m]	geometric dimension in IBVP
h_1, h_2, h_3	[m]	spatial expansions of a finite element in three dimensions
i		ion identifier: $+$: positive ions, $-$: negative ions
$\boldsymbol{j}^{\alpha_j}$	[kg/(m^2 s)]	diffusive flux of species φ^{α_j}
j		species identifier: m: monomer, w: water, i: mobile ions, fc: fixed charges, s: salt
$\mathbf{K}^S$	[m^2]	intrinsic permeability tensor
$K^\alpha, K^{\alpha_j}, K_\beta^{\alpha_j}$	[J/m^3]	kinetic energy contribution
K_{PM}	[–]	model parameter in Power Model
K_{PM}^*	[–]	calibrated model parameter in Power Model
$\mathbf{k}$		model parameter vector (Metropolis-Hastings algorithm)
$\mathbf{k}_{old}$		previous model parameter vector (Metropolis-Hastings algorithm)
$\mathbf{k}_{new}$		new candidate for model parameter vector (Metropolis-Hastings algorithm)
$\mathbf{k}_0$		model parameter vector of initial guesses (Metropolis-Hastings algorithm)
Δk_j		perturbation of j-th parameter (Metropolis-Hastings algorithm)
k^{sG}	[m^2]	isotropic permeability of polymer network
k_0^{sG}	[m^2]	constant in swelling-dependent permeability function
k^S	[m^2]	isotropic permeability
k_0^S	[m^2]	intrinsic permeability of solid skeleton without any polymer retention

$k_{d,k}$	[1/s]	detachment rate of k-th active site
$k_{a,k}$	[1/s]	attachment rate of k-th active site
$\mathbf{L}_{\alpha_j}, \mathbf{L}_{\alpha}, \mathbf{L}$	[1/s]	spatial velocity gradient
L_p	[m]	pipe length
l	[m]	length
M^L	[m^3 s/kg]	isotropic mobility coefficient
M_m^j	[kg/mol]	molar mass of species
m^{obs}	[–]	number of data points (Metropolis-Hastings algorithm)
$m, m^{\alpha}, m^{\alpha_j}$	[kg]	mass of mixture, phase and species
$\mathrm{d}m, \mathrm{d}m^{\alpha}, \mathrm{d}m^{\alpha_j}$	[kg]	local mass element
N	[–]	abstract number of species in phase
N_m^j	[–]	number of molecules (lattice model)
N_A	[–]	Avogadro's number: $6.02214076 \times 10^{23}$
N_m^f	[–]	number of solvent molecules (lattice model)
N_m^p	[–]	number of polymer molecules (lattice model)
N_{deb}	[–]	Deborah number
$\mathbf{n}$	[–]	normal vector on boundary
n^{α}	[–]	volume fraction
$n_m^{\alpha_j}$	[mol]	molar amount of substance
n	[–]	number of intervals in stair-case function
$n_{k,crit}^A$	[–]	critical volume fraction of φ^A at k-th active site
$n_{rev,eq}^A$	[–]	equilibrium volume fraction of reversibly captured particles
n_{rev}^A	[–]	volume fraction of reversible attached polymer gel
n_{irr}^A	[–]	volume fraction of irreversible attached polymer gel
n_{PM}	[–]	model parameter in Power Model
n_{CM}	[–]	model parameter in Carreau Model
n_{ECM}	[–]	model parameter in Extended Carreau Model
n_{PM}^*	[–]	calibrated model parameter in Power Model
n^L	[–]	effective porosity
$\hat{n}^{\alpha}$	[1/s]	volume production
$\mathrm{d}n_m^{\alpha}, \mathrm{d}n_m^{\alpha_j}$	[mol]	local molar mass element

P	[–]	probability density
PVI	[–]	Pore Volumes Injected (PVI)
PV	[m^3]	pore volume
Pe	[–]	Péclet number
$\tilde{Pe}$	[–]	computational Péclet number (mesh-dependent)
p	[$\mathrm{N/m}^2$]	hydraulic pressure (Lagrange multiplier)
p^α, p^{α_j}	[$\mathrm{N/m}^2$]	partial pressure
$\hat{\mathbf{p}}^\alpha, \hat{\mathbf{p}}^{\alpha_j}, \hat{\mathbf{p}}_r^{\alpha_j}, \hat{\mathbf{p}}_a^{\alpha_j}$	[$\mathrm{N/m}^3$]	momentum production
$p_e^{\alpha_j}$	[$\mathrm{N/m}^2$]	electrostatic pressure
p_d	[–]	parameter in Donnan equation
$\bar{p}_{out}$	[$\mathrm{N/m}^2$]	pressure at outlet boundary (boundary condition)
$\bar{p}_{in}$	[$\mathrm{N/m}^2$]	injection pressure (boundary condition)
$\bar{p}_{in,max}$	[$\mathrm{N/m}^2$]	plateau value in ramp function $\bar{p}_{in}$ (boundary condition)
Δp	[$\mathrm{N/m}^2$]	differential pressure
Δp_{post}	[$\mathrm{N/m}^2$]	differential pressure during water flooding after polymer injection
Δp_{pre}	[$\mathrm{N/m}^2$]	differential pressure during water flooding prior to polymer injection
Q	[m^3/s]	volumetric flow rate
Q_p	[m^3/s]	general volumetric flow rate through pipe
$Q_{p,PM}$	[m^3/s]	volumetric flow rate through pipe (power-law fluid model)
$Q_{p,newton}$	[m^3/s]	volumetric flow rate through pipe (Newtonian fluid model)
$Q_{polymer}$	[m^3/s]	injected flow rate during polymer flooding
Q_{pre}	[m^3/s]	injected flow rate of water flood prior to polymer injection
Q_{post}	[m^3/s]	injected flow rate of water flood after polymer injection
Q_{static}	[m^3/s]	low injection flow rate (static retention)
$\mathrm{d}Q_e^{\alpha_j}$	[C]	infinitesimal charge of species φ^{α_j}
$\mathbf{q}_{static}$	[$\mathrm{m/s}$]	Darcy velocity due to low injection flow rate
$\mathbf{q}_T, \mathbf{q}_T^\alpha, \mathbf{q}_T^{\alpha_j}$	[$\mathrm{J}/(\mathrm{m}^3\,\mathrm{s})$]	heat influx vector (convection)
$\mathbf{q}, \mathbf{q}^\alpha$	[$\mathrm{m/s}$]	Darcy velocity
$\Delta\mathbf{q}^\alpha$	[$\mathrm{m/s}$]	dispersive flux per unit area, $\alpha = \{F, G\}$
q	[–]	mass specific degree of swelling

q_v	[−]	volumetric degree of swelling
q_d	[−]	parameter in Donnan equation
q_{free}, q_{att}	[−]	mass specific degree of swelling of fluidized and attached hydrogel
q_0	[−]	initial degree of swelling
q^∞	[−]	Equilibrium Degree of Swelling (EDS)
$\bar{q}$	[m/s]	volumetric solution flux per unit area (boundary condition)
$\bar{q}_{in}$	[m/s]	injection flux per unit area (boundary condition)
$\Delta\bar{q}^G$	[m/s]	dispersive flux per unit area (boundary condition)
$\mathbf{R}^\alpha$	[kg/(m^3 s)]	resistance tensor (seepage flow)
$\mathbf{R}^{\alpha_j}$	[kg/(m^3 s)]	resistance tensor (diffusive flow)
$\mathbf{R}^{\alpha L}, \mathbf{R}^{GS}$	[kg/(m^3 s)]	resistance tensor (dispersive flow)
R	[J/(K mol)]	universal gas constant: 8.314 J/(K mol)
R_{eq}	[m]	equivalent tube radius
R_j	[J/(K kg)]	specific gas constant of species φ^{α_j}
R_p	[m]	pipe radius
RRF	[−]	Residual Resistance Factor (RRF)
RF	[−]	Resistance Factor (RF)
Re	[−]	Reynolds number
$\mathbf{r}$		vector of search radii (Metropolis-Hastings algorithm)
$r^{\alpha_j}, r^\alpha, r$	[J/(kg s)]	mass specific external heat supply (radiation)
r_m	[−]	number of monomers per polymer chain (lattice model)
r_p	[m]	radial coordinate in cylinder coordinate system
SSQ		Sum of Squares
$\Delta S^\alpha_{m,mix}$	[J/(K mol)]	molar mixing entropy
$\bar{s}^G_{in,max}$	[−]	saturation in polymer flood (boundary condition)
$\bar{s}^G_{in}$	[−]	injected polymer saturation (boundary condition)
s^α	[−]	saturation, $\alpha = \{G, F\}$
$\mathbf{T}, \mathbf{T}^\alpha, \mathbf{T}^{\alpha_j}$	[N/m^2]	Cauchy stress tensor
$\mathbf{T}^\alpha_R$	[N/m^2]	Reynolds-like stress tensor

$\mathbf{T}_E^{\alpha}$	[N/m^2]	partial effective stress tensor
$\mathbf{I}$	[–]	second order identity tensor
$T, T^{\alpha}, T^{\alpha_j}$	[K]	absolute thermodynamic temperature
$\mathbf{t}$	[N/m^2]	total traction vector
t	[s]	time
t^*	[s]	threshold time
$\mathbf{u}_S$	[m]	solid phase displacement vector
V^{α}	[m^3]	volume of mixture
V	[m^3]	volume of phase
$\tilde{V}_m^{\alpha_j}$	[mol/m^3]	partial molar volume
$\mathbf{v}, \mathbf{v}_{\alpha}, \mathbf{v}_{\alpha_j}$	[m/s]	velocity
$\mathbf{v}_{\alpha\beta}$	[m/s]	relative velocity between φ^{α} and φ^{β}
$\mathbf{v}_{\alpha S}$	[m/s]	seepage velocity
v_z	[m/s]	velocity in axial direction (pipe model)
$\mathrm{d}v, \mathrm{d}v^{\alpha}$	[m^3]	current volume element
$\mathrm{d}v_0^G$	[m^3]	initial infinitesimal volume of hydrogel
$\mathbf{W}_{\alpha}$	[1/s]	spin tensor
$\mathbf{w}_{\alpha_j}$	[m/s]	diffusion velocity
W	[–]	mass specific polymer attachment ratio
$\mathbf{w}_{\alpha}$	[m/s]	relative velocity
$\mathbf{X}_{\alpha}$	[m]	position vector (reference configuration)
$\mathbf{x}$	[m]	position vector (current configuration)
$x_m^{\alpha_j}$	[–]	molar fraction
$\mathbf{y}$		solution vector (Metropolis-Hastings algorithm)
$\mathbf{y}_0$		vector of initial conditions
z_p	[m]	axial coordinate in cylinder coordinate system
z^{α_j}	[–]	charge number of species φ^{α_j} (valence)

Calligraphic letters

Symbol	Description
$\mathcal{B}_t$	abstract body at time t
$\mathcal{N}$	normal distribution
$\mathcal{O}$	origin of a coordinate system
$\mathcal{P}$	material point
$\mathcal{Q}$	set of model parameters
$\mathcal{Q}_{red}$	reduced set of model parameters

$\mathcal{U}$	uniform distribution

Acronyms

Symbol	Description
CM	Carreau Model
DPR	Disproportionate Permeability Reduction
ECM	Extended Carreau Model
EDS	Equilibrium Degree of Swelling
FCD	Fixed Charge Density
HMT	Hybrid Mixture Theory
KDE	Kernel Density Estimation
ODE	Ordinary Differential Equation
PM	Power Model
RVE	Representative Volume Element
RPM	Relative Permeability Modifier
RF	Resistance Factor
RRF	Residual Resistance Factor
SAP	Superabsorbent Polymer
TM	Theory of Mixtures
VIF	Viscosity Increase Factor

Chapter 1:
Introduction and overview

1.1 Motivation

The use of polymers in fluid-saturated porous media has increased in relevance during the last years. Polymers, which exist in the pore space of a solid skeleton, are able to interact depending on their specific properties with the pore fluid as well as with the solid. The interactions cause changes in the macroscopic behavior of the overall porous medium, especially transport processes within the pore space.

A widely-established application of water-soluble polymers can be find in petroleum engineering. During polymer flooding a polymer solution is injected into low permeable reservoir rocks. The polymer solution propagates through the pore space and transports the trapped oil towards the production well. Relative to water, the polymer solution has a much higher viscosity, improving the mobility of oil. An increased efficiency of the oil production is the result.

Predicting the transport of the solution as well as the accompanied interactions with the solid matrix are a challenging but necessary task for the successful realization of polymer flooding projects on the field scale. During the infiltration of the polymer solution into the porous media, a part of the fluidized polymer particles are captured by the solid skeleton, such that the polymer concentration varies in time and space. In addition, the polymer attachment to the solid skeleton causes a change in pore space morphology. On the macroscale, the intrinsic permeability decreases. As a consequence, it can be observed that a constant injection rate (flow rate of solution) results in a rising injection pressure when the attachment increases. Numerical simulations based on a consistent thermodynamic modeling support the understanding of the complex phenomena. In addition, the simulations are viewed as the basis for the process optimization.

Besides petroleum engineering, swellable polymers are used for binding pore liquid within the porous media. Due to the special characteristics of these polymers, they are also termed Superabsorbent Polymers (SAP). From a chemical point of view, SAPs are cross-linked polyelectrolytes, which are able to absorb large amounts of aqueous liquid, while transforming to a hydrogel. Since their development by Procter & Gamble in 1957 until today, SAPs are used because its high absorption dynamics and the high swelling capacity mainly for hygienic products [160]. During the recent years, tremendous progress has been obtained with respect to the characteristic polymer properties. In particular, the absorption rates as well as the swelling capacities have been improved significantly. Due to this reason, SAPs gained in importance in different industrial sectors, which affects especially the use in porous media.

Most recently, innovative building materials were developed based on SAPs for the adaptive control of the free pore liquid. Against this background, the development of a grouting mortar should be mentioned, which is able to bind high amounts of its

free pore water, which ultimately leads to a faster hardening. Reliable models for the capturing of the time-dependent liquid absorption within the pore space are therefore the basis for the development of effective rheology models.

It can be concluded that polymers within fluid-saturated porous media can be designed to have a wide variety of macroscopic properties appropriate for different practical applications. The interactions between polymer and solid skeleton as well as polymer and pore liquid, differentiate strongly from a physical point of view. However, attachment/detachment as well as absorption/desorption processes can be implemented in a continuum mechanical modeling approach through mass exchange terms of the involved phases.

1.2 State of the art, scope and aims

The aim of the thesis is the macroscopic modeling of porous materials, which are simultaneously saturated with a pore liquid and a polymer gel. The focus of this study is to investigate the diverse and complex processes that are induced by the presence of polymers in the pores. As already mentioned, it is possible to modify the effective properties of the porous media through the addition of polymers to the pore space. Here, the requirements towards the modeling are classified into three main categories:

- controlling the free pore liquid within the solid skeleton,
- polymer attachment to the solid matrix,
- rheology of polymer solution flow through porous media.

Progress in all areas is reported in the literature. However, according to the author's knowledge, there does not exist a multi-phase model for the systematic description of all coupled processes in the pore space. To this end, a multi-phase model is developed in this thesis, which consists of a porous solid matrix, a pore liquid and a pore gel.

From a practical point of view, capturing all geometric information form the microstructure as well as the description of all chemo-physical processes is not manageable. Due to this reason, a macroscopic modeling approach based on the Hybrid Mixture Theory (HMT) is chosen [20, 21], which results in a (statistical) homogenized description of the microstructure. The development of macroscopic constitutive models is finally necessary for the effective modeling of the previously mentioned phenomena. Against this background, a literature review with respect to the essential modeling aspects is given in the following.

An overview of the literature, which deals with liquid exchange by polymers is covered. Polymers, which are able absorb and bind aqueous solutions, were studied since the early works of Flory [53], Flory & Rehner [55], Huggins [71] and Flory & Rehner [56]. This special class of polymers is also known as hydrogels. Further development of these polymers towards charged hydrogels, also called Superabsorbent polymers (SAP), led to significant higher swelling degrees. Different modeling approaches of the driving

forces behind liquid absorption can be found in the literature. Therefore, the group around Huyghe & Janssen [74, 76] and Wilson *et al.* [164] developed a multi-phase model to describe charged porous media, which are composed of a charged solid skeleton, while the pore space is saturated with a pore liquid and mobile ions. Herein, the charges of mobile ions in the pore space are in equilibrium with the charged solid skeleton, such that the overall material is charge-neutral. Since fixed charges are attached to the solid skeleton, an ion concentration difference exists between the absorbed and the surrounding solution. Based on this modeling approach, Acartürk [2] developed a multi-phase material for the description of electro-active, swellable porous media. In this modeling approach, the porous medium exchanges pore liquid with the surrounding solution over the phase boundary. To put it differently, the swelling of the material is determined through the boundary conditions of the overall material. It is worth mentioning that such a model can be used to model swelling of charged hydrogels, but also biological tissues, since the concept of fixed charges is also a widely-accepted modeling approach in biomechanics [164].

Similar continuum-based models for the description of charged hydrogels are developed by English *et al.* [51] and Yang *et al.* [165]. In contrast to the previously mentioned models, the surrounding pore liquid was integrated in the model. The driving forces behind liquid and ion transport were derived from previously postulated thermodynamic potentials. Besides the ion concentration, the influence of the surrounding solution's pH-value on the absorption characteristics was considered. It is worth mentioning that charged hydrogels does not only react sensitive towards the pore fluid chemistry of the surrounding solution, e. g. the chemical composition or the pH-value, but also on temperature changes [36] or external electrical fields [2]. Through the reversible swelling, charged hydrogels are suitable for the application as sensors in complex applications [93].

Direct modeling approaches for hydrogels, which are used for sensors or for drug delivery applications can be found numerous in the literature. The use of SAPs as chemical admixture for concrete has recently attained more attention, however, modeling approaches towards the simulation of liquid exchange of hydrogels in porous media are rare. In this context, it is worth mentioning that Viejo *et al.* [158] developed a mesoscopic model for modified concrete with SAPs. Furthermore, the RILEM report [106] gives an excellent overview of the developments and current research topics regarding to SAP modified concrete mixtures.

The main objective of using SAPs is to gain control of free water in concrete mixtures [105, 106]. On the one hand, water is necessary for the hydration process of the cement phase, besides this, the amount of free water has a tremendous effect on the rheological properties of concrete. Some applications require a sufficient workability of fresh mixtures, which is realized through a high water content. Through the addition of SAPs it is possible to control the amount of free pore water over time and, in turn, the rheology to a certain extent [107, 130]. In addition, the influence of SAPs on the mechanical properties of concrete was widely studied through experiments [28, 106–108, 111, 117].

Besides liquid absorption, SAPs are also able to release captured liquid to the surrounding. To this end, SAPs also gained attention in connection with the avoiding of auto-

geneous shrinkage [105, 106]. In this context, SAPs are added to the mixture to store additional pore water, which is released over a long time span to the cement phase. Through the controlled and continuous hydration, volumetric shrinkage during the hardening can be reduced, which is especially of great importance in connection with Ultra High Performance Concrete (UHPC) [13, 42, 65, 107, 111, 128, 130, 132, 138, 174].

On the microscale, swelling of SAPs results in a reduction of the effective porosity of the solid matrix, such that the intrinsic permeability decreases. As a consequence, fluid transport through the porous matrix is affected by the swollen SAP particles [159, 160]. This effect is also known as gel blocking and can be exploited for the sealing of cracks in concrete constructions [89, 137, 139]. It is worth noting that applications of self-healing porous materials based on the SAPs can also be found in different industrial sectors. Czupryna [43] developed an innovative, self-sealing cable sheath for power cables. Penetration of water due to damage of the cable sheath can be avoided even when the outer layer is fractured. For this purpose, a dry SAP granulate is added to the matrix material of the cable sheath. In case of damage of the cable sheath, water penetrates into the structure and initializes swelling of the embedded SAPs within the matrix. The swollen hydrogels form a water barrier and protect the cable core from water contact.

On the one hand, numerous continuum-based models for the simulation of charged hydrogels can be found in the literature, while on the other hand, purely experimental studies of liquid absorption by hydrogels within construction materials are reported in the literature. Due to this reason, a continuum-based multi-phase model will be developed in the present thesis, which treats the polymers within the pore space as a part of a porous material. Following this, the liquid absorption of hydrogels will not be represented through flow across the phase boundary hydrogel-pore liquid, as in models by Acartürk [2], Huyghe & Janssen [76] and Yu *et al.* [168], but through local mass exchange terms in the corresponding mass balances. Such macroscopic mixture models accounting for mass exchange in porous media were derived by many researchers for various applications. Alexandersson *et al.* [8], Alexandersson & Ristinmaa [9] and Askfelt *et al.* [12] used a multi-phase and multi-species approach based on the HMT to describe the thermo-hydro-mechanical coupling in paperboard. Ristinmaa *et al.* [119] used the same theoretical framework for developing a general model for a thermo-plastic material with a particular focus on transport and mass exchange. Kinematics and mass exchange are coupled by using a multiplicative split of the deformation gradient in a mass conserving and non-conserving part. Loret *et al.* [100, 101] and Gajo & Loret [59] established a mixture-based model to describe chemically active expansive clays. The coupling between mass exchange and deformation represents chemical swelling and shrinking on the macroscale. In addition, growth processes in biomechanics, i. e. remodeling of soft tissue and tumor growth, were also modeled through mass exchange terms within continuum-based mixture theories [10, 11, 35, 118, 143].

Besides controlling the free pore liquid within the pore space, polymer attachment to the solid skeleton, induced by the infiltration of a polymer solution, denotes the second key requirement towards the modeling approach. Polymer attachment causes a reduction of the solution's polymer concentration, which has a negative effect in case of polymer flooding – the viscosity of the injected solution and therefore the mobility of

the oil phase reduce significantly. Furthermore, the attachment slows down the propagation of the concentration front in the pore space. From an economic point of view, the polymer attachment leads to higher costs, because a part of the injected polymer gets lost in the pore space [172]. Precise knowledge of the polymer attachment process is therefore of great importance for the successful realization of polymer flooding projects.

Al-Hajri *et al.* [7], Idahosa *et al.* [77], Zhang & Seright [173] and Zhang [172] carried out small-scale laboratory experiments, so-called core flooding experiments, for the purpose of characterizing the polymer attachment in a quantitative manner. In these studies the polymer solution is injected with a constant flow rate into a porous core, while the polymer concentration at the exiting end of the core is measured. The resulting breakthrough curves of the polymer concentration are usually plotted over the injected pore volume, while the attached polymer volume is finally estimated from these curves. It is worth mentioning that such estimation is an averaged statement with respect to the core volume. It was shown in independent experimental studies of Al-Hajri *et al.* [7], Idahosa *et al.* [77], Zhang & Seright [173] and Zhang [172] that the maximum amount of polymer attachment rises with increasing injection rate. This aspect plays also an important role against the background of the economic efficiency of the whole polymer flooding project and has to be taken into consideration.

It is well-reported throughout the literature that the polymer attachment process is essentially driven by three distinct mechanisms [6, 172]. Chemo-physical forces cause the adsorption of polymers on the surface of the solid skeleton. This driving force results primary from van der Waals-forces, hydrogen bonding as well as electrostatic interaction forces [113, 131, 141]. Furthermore, the acting forces strive to reduce the surface energy through the coverage of the rock surface [44]. With respect to the pore space morphology and the size of the polymer molecules, fluidized polymers can be trapped at small pores. The third mechanism, which is also known as hydrodynamic retention, is related to the velocity field at the pore scale. Especially at high injection flow rates, hydrodynamic forces cause the attachment of polymer particles to the solid skeleton [6]. Through increasing polymer attachment, the morphology of the pore space is changed, which in turn results in a reduction of the permeability. As a consequence, an increase in injection pressure difference at constant injection flow rate can be observed.

Experimental studies discovered that polymer attachment can be decomposed into different mechanisms, however, polymer attachment in the literature was almost always modeled through adsorption-isotherms [39]. Dawson & Lantz [45] already postulated that polymer adsorption can be fitted to Langmuir-isotherms irrespective the fact that the isotherm was originally derived for purely reversible adsorption processes [98]. Through modeling the attachment with an isotherm, it is implicitly assumed that the attachment process occurs instantaneous. Fundamental criticism of using Langmuir-isotherms in this context was expressed by Zhang [172]. The polymer attachment to the solid skeleton is for the most part irreversible, such that an application of the Langmuir-isotherm is not justified on a theoretical basis. In the present work, the attachment process is modeled as a dynamic mass exchange between fluidized and attached polymer. In this context, it is a priori distinguished between reversible and irreversible attach-

ment. Similar continuum-based models were derived by Tiraferri *et al.* [147], Tosco & Sethi [151] and Tosco *et al.* [149] in order to simulate infiltration processes of fluidized micro- and nano-particles into porous media. Based on these works, a dynamic model is chosen, which will be finally calibrated to experimental breakthrough curves.

The mass exchange plays a fundamental role in the formulation of the multi-phase material model. The two previously mentioned phenomena, i. e. absorption/desorption and attachment/detachment, are interactions between polymer and pore liquid and polymer and solid skeleton, respectively. These interactions are treated in the multi-phase model through mass exchange terms in the corresponding mass balances and are therefore naturally implemented in the continuum-based mixture theory.

In order to simulate the propagation of the polymer solution within the pore space, a macroscopic rheology model for the polymer solution needs to be derived first. Newtonian fluid flow through porous media is usually modeled through Darcy's law. In this case, the shear stress of the fluid is proportional to the shear rate, while the dynamic viscosity is the proportionality constant. In contrast, polymer solutions show generally non-Newtonian flow behavior, such that the linear relation between pressure gradient and flow rate is no longer valid. The in situ viscosity of the fluid becomes therefore a function of the shear rate.

Many polymer solutions show in rheological measurements a shear-thinning (pseudo-plastic) behavior. In this context, analytical and empirical rheology models were developed, which can mimic the shear-rate dependent viscosity. Power-law, as well as more complex models, e. g. the Careau-, Ellis, or Cross-model, are frequently used in the literature to describe the rheology of polymer solutions [29, 150, 171]. However, experiments revealed that the rheology of polymer solutions, which are flowing through porous media, significantly deviate from its intrinsic rheology [170]. Zamani *et al.* [170] postulated that the difference is caused by the influence of the complex porous media geometry. By applying high injection rates, Delshad *et al.* [46] and Najafabadi *et al.* [110] were able to show that many polymer solutions exhibit shear-thickening (dilatant) behavior in porous media. This is interesting because the same polymer solutions showed a purely shear-thinning flow behavior in rheological measurements of the bulk fluids. This effect is associated with the visco-elastic character of most polymer solutions, which becomes noticeable through the geometric restrictions caused by the pore space [142]. It is worth mentioning, that this phenomena is extensively discussed by Sochi [140].

To relate the in situ viscosity to the bulk viscosity, a constitutive model between the effective shear rate and the local filter velocity is developed. The effective shear rate is not accessible for the macroscopic modeling, since it represents the shear rate, which is expected in the spatially-resolved pore space. For a regular porous medium consisting of capillary tubes, this relation was derived analytically by solving the Navier-Stokes equation. To transfer this connection between micro- and macroscale to realistic porous media geometries, an empirical parameter is added to the (analytic) constitutive relation. Therefore, this parameter needs to be determined through experiments. Zamani *et al.* [170] investigated the constitutive behavior by using direct numerical simulations for realistic microstructures obtained from CT-data. The concept of the effective shear

rate is widely-used throughout the literature to model the shear rate-dependent rheology on a macroscopic level [41, 69, 99, 115, 151].

In this thesis, a macroscopic multi-phase model is developed, which implements the requirements stemming from the previously mentioned applications. The development of mass exchange terms are essential for capturing the specific interactions in an effective manner. To simulate the coupled processes numerically, it is necessary to solve the system's governing equations, which are usually described through partial differential equations (PDEs). To this end, the weak forms of the PDEs are discretized in space and time and solved with the Finite Element Method (FEM). The aim of this thesis is finally the development of a versatile material model for the calculation of complex interactions in fluid-saturated porous media, which are controlled through mass exchange terms.

1.3 Outline of the thesis

The fundamentals of a continuum-based mixture theory are introduced in **chapter 2**. It starts with a brief historical classification and the development of modern mixture theories. After introducing fundamental quantities and definitions, the kinematics within the HMT are discussed. Viewing the mixture as a composition of superimposed continua, leads to the independent formulation of balance equations, while proper exchange terms represent the multi-phase and multi-species interactions in a constitutive manner. The second law of thermodynamics is finally expressed as the entropy inequality for the isothermal multi-phase and multi-species model.

Charged hydrogels are treated in this manuscript as a phase in a multi-phase material. For reasons of clarity, the complex phenomena connected to charged hydrogels are discussed in **chapter 3** in the absence of any porous material. In this chapter, the focus is on the derivation of the thermodynamic foundations of charged hydrogels. The aim of this chapter is the derivation of the driving forces for charged hydrogels with respect to the microstructure. Thermodynamic models from the literature are briefly summarized and three different contributions to the driving force of hydrogel swelling are identified.

In **chapter 4** the general model composition into phases and species is specified. The model consists of a solid skeleton, while the pore space is simultaneously filled with an aqueous pore liquid and a polymer gel. On the one hand, the model accounts for polymer attachment to the solid skeleton, while on the other hand, absorption and desorption of pore liquid by the polymer gel is incorporated. These complex processes within the pore space are expressed in the macroscopic continuum-based model through mass exchange terms. In the following, the entropy inequality is adapted to the chosen model decomposition and will be evaluated. By exploiting the entropy inequality, results with respect to the thermodynamic modeling of charged hydrogels are used. The result yields constitutive relations, which are valid in equilibrium as well as additional expressions, which are responsible for the dissipation within the material. The dissipative contribution provides for near-equilibrium conditions thermodynamic-consistent

forms for the seepage and diffusion velocities as well as for the mass exchange terms. The complex multi-phase model is treated as a master model. In the further course of the work, this model is systematically reduced, such that different model capabilities can be investigated isolated and independent from each other.

With respect to the previously mentioned model reduction, the focus in **chapter 5** is on simulating absorption/desorption processes. In this context, hydrogels are investigated, which are in contact with saline solutions. Against the background of experimental investigations, the dynamic liquid exchange is investigated. With the aid of the experimental results, the model parameters within the constitutive models are calibrated. Furthermore, a constitutive model for the description of the absorption/desorption dynamics is developed and is also calibrated to the experimental data. Through the introduction of the postulated model, the necessary amount of experimental data for model calibration is reduced significantly. The developed model can mimic the reversible liquid absorption with high precision. It is worth mentioning that the results presented in this chapter were already published in [124].

In **chapter 6** the master model will be reduced to obtain a second model variant. Here, the focus is on the transport and infiltration of polymer solutions through porous media. For simplicity, the polymer gel does not exchange mass with the pore liquid, while on the other hand, polymer attachment of the fluidized polymer to the solid skeleton is taken into consideration. The coupling effects between polymer attachment, non-Newtonian suspension rheology and the evolution of the permeability due to the attachment processes, are modeled. The aim of the model is the numerical investigation of the infiltration process by using the FEM. For this purpose, the necessary balance equations are derived in weak form and an initial boundary value problem is formulated in a general manner. In the following, a small-scale polymer flooding experiment is simulated, while the continuum-model is calibrated with data from the literature. Besides the polymer attachment, the development of the permeability as well as the non-Newtonian rheology are discussed. The multi-phase model is able to portray the injection rate-dependent polymer attachment and the effective polymer solution viscosity. The calibrated material model is subsequently applied to a more complex initial boundary value problem. The model capabilities are analyzed against the background of the induced heterogeneous seepage velocity distribution.

The results obtained in the manuscript are summarized in **chapter 7**. In addition, further modeling approaches as well as open questions are discussed.

Chapter 2:
Theoretical fundamentals of mixture theory

In a microscopic description of a multi-phase material, phases can be distinguished, such that each material point can be uniquely assigned to a specific phase. However, capturing all geometric information from the micro-structure is a tremendous task and from a practical point of view not manageable for engineering applications. Against this background, the Hybrid Mixture Theory (HMT) is used as a macroscopic continuum-based approach for materials with complex microstructure. The fundamentals of the HMT are introduced in a general fashion within this chapter. The chapter starts with the definition of basic quantities, which are accounting for the composition of the mixture. Next, the kinematic relations of multi-phase and multi-species materials are briefly introduced. Subsequently, balance equations for mass, linear momentum, energy and entropy are presented in local form. In the last part of the chapter, the entropy inequality is derived in a general manner. The exploitation of the entropy inequality, which enables one to formulate thermodynamic-consistent constitutive models, will be carried out in chapter 4 after specifying the model composition and its expected material behavior.

2.1 Preliminaries

The classical Theory of Mixtures (TM) was established by Bowen [32], Truesdell & Toupin [152] and provides a macroscopic description of miscible mixtures. The mixture is viewed as a single phase composed of miscible species. To this end, the TM does not include any geometrical information from the microstructure. For the purpose of modeling immiscible mixtures, for instance solid-fluid mixtures, Hassanizadeh & Gray [66, 67] combined the classical TM with the concept of volume fractions. This approach is later referred to as Hybrid Mixture Theory (HMT) [20, 21]. According to the HMT, the overall material is treated as a mixture of immiscible phases, while each phase is still treated as a miscible mixture of species. In contrast to a microscopic approach, the HMT leads to a continuous description of the material by applying a superposition of the different phases and species at the material point. A similar mixture theory, which incorporates volume fractions in the classical TM, was developed by de Boer [30, 31] and Ehlers & Bluhm [49] and is termed the Theory of Porous Media (TPM). In contrast to the HMT, phases and species are not distinguished a priori, such that all components are treated immiscible and are therefore associated with its individual (constituent) volume. However, this approach does not lead to a straightforward introduction of miscible components, such as dissolved ions, since its intrinsic volume is by definition not accessible.

Throughout this manuscript, the HMT is used for modeling multi-phase and multi-species materials, while the chemical composition of phases is accounted for by using a

multi-species framework. Following the idea proposed by Singh *et al.* [134, 135], a general and flexible description of multi-species phases can be obtained by assuming that each phase contains the same set of N species, where some may be at zero concentration. According to the HMT framework, the overall mixture φ is composed of K phases φ^α, while each phase is composed of N miscible species φ^{α_j}. Finally, the composition of the mixture is represented through

$$\varphi = \bigcup_\alpha \varphi^\alpha \quad \text{and} \quad \varphi^\alpha = \bigcup_j \varphi^{\alpha_j} \,. \tag{2.1}$$

Following that, the infinitesimal volume element which φ^α occupies, is denoted by $\mathrm{d}v^\alpha$, such that the phase volume is obtained by integration over the body $\mathcal{B}$ to

$$V^\alpha = \int_{\mathcal{B}} \mathrm{d}v^\alpha \,. \tag{2.2}$$

For a mixture of immiscible phases, the mixture's volume is given by a summation over the phases

$$V = \int_{\mathcal{B}} \mathrm{d}v = \sum_\alpha V^\alpha \,, \tag{2.3}$$

where $\mathrm{d}v$ denotes the infinitesimal volume element of the mixture.

Therefore, volume fractions for each phase are defined, while the saturation condition imposes an algebraic constraint [14, 49]

$$n^\alpha = \frac{\mathrm{d}v^\alpha}{\mathrm{d}v} \,; \qquad \sum_\alpha n^\alpha = 1 \,. \tag{2.4}$$

In order to account for the composition of the phases, the mass of the species is related to the volume of its corresponding phase, whereas summing over the species yields to the effective (true) phase density

$$\rho^{\alpha_j} = \frac{\mathrm{d}m^{\alpha_j}}{\mathrm{d}v^\alpha} \,; \qquad \rho^{\alpha R} = \frac{\mathrm{d}m^\alpha}{\mathrm{d}v^\alpha} = \sum_j \rho^{\alpha_j} \,. \tag{2.5}$$

ρ^{α_j} is the mass concentration of a component in a mixture and can also be denoted as the density of a component in a multi-species phase. Note that the partial density $\rho^\alpha = \mathrm{d}m^\alpha/\mathrm{d}v$ relates the mass of a phase to the volume of the overall mixture and can be expressed through $\rho^\alpha = n^\alpha \rho^{\alpha R}$. Finally, the density of the mixture calculates to $\rho = \sum_\alpha \rho^\alpha$. Mass fractions relating the mass of a species φ^{α_j} to the mass of the phase φ^α are consequently given by

$$c^{\alpha_j} = \frac{\mathrm{d}m^{\alpha_j}}{\mathrm{d}m^\alpha} = \frac{\rho^{\alpha_j}}{\rho^{\alpha R}} \,; \qquad \sum_j c^{\alpha_j} = 1 \,, \tag{2.6}$$

where the constraint reflects an interdependence of this quantity. Note in passing that throughout this contribution c^{α_j} is for convenience expressed as mass percentage $[\mathrm{m}\%]$.

In order to describe chemical reactions, it is more useful to switch from mass-based ρ^{α_j} to molar concentrations $\rho_m^{\alpha_j}$ by

$$\rho_m^{\alpha_j} = \frac{\mathrm{d}n_m^{\alpha_j}}{\mathrm{d}v^{\alpha}}\,; \qquad \rho_m^{\alpha R} = \frac{\mathrm{d}n_m^{\alpha}}{\mathrm{d}v^{\alpha}} = \sum_j \rho_m^{\alpha_j}\,, \tag{2.7}$$

where $n_m^{\alpha_j}$ denotes the number of moles of species φ^{α_j} and $\rho_m^{\alpha R}$ is the effective (true) molar phase density. Note that quantities expressing a molar measure in this manuscript are denoted by $(\,\cdot\,)_m$. By introducing the molar mass of a species through $M_m^j = \mathrm{d}m^j/\mathrm{d}n_m^j$, molar concentrations are linked to its mass-based counterpart through

$$\rho_m^{\alpha_j} = \frac{\rho^{\alpha_j}}{M_m^j}\,, \tag{2.8}$$

while the molar mass is a constant species' property.

The partial molar volume measures the change in volume of a multi-species phase φ^{α} due to a change in amount of substance of φ^{α_j} and is consequently defined through

$$\tilde{V}_m^{\alpha_j} = \frac{\partial V^{\alpha}}{\partial n_m^{\alpha_j}}\,. \tag{2.9}$$

Following this idea, the volume of a multi-species phase reads

$$V^{\alpha} = \sum_j n_m^{\alpha_j} \tilde{V}_m^{\alpha_j}\,. \tag{2.10}$$

For the sake of completeness, molar fractions are defined through

$$x_m^{\alpha_j} = \frac{\mathrm{d}n_m^{\alpha_j}}{\mathrm{d}n_m^{\alpha}} = \frac{\rho_m^{\alpha_j}}{\rho_m^{\alpha R}}\,; \qquad \sum_j x_m^{\alpha_j} = 1\,. \tag{2.11}$$

In this particular framework, species are able to carry a charge, therefore, the charge density $\rho_e^{\alpha_j}$ will be defined as

$$\rho_e^{\alpha_j} = \frac{\mathrm{d}Q_e^{\alpha_j}}{\mathrm{d}v^{\alpha}}\,, \tag{2.12}$$

where $Q_e^{\alpha_j}$ portrays the absolute charge of the species φ^{α_j}. Note that $(\,\cdot\,)_e$ denotes an electrical quantity in this manuscript. The charge and mass density are related through

$$\rho_e^{\alpha_j} = \frac{z^{\alpha_j} F}{M_m^j} \rho^{\alpha_j} = z^{\alpha_j} F \rho_m^{\alpha_j}\,, \tag{2.13}$$

herein, z^{α_j} denotes the charge number of a species (valence), while F is the Faraday constant.

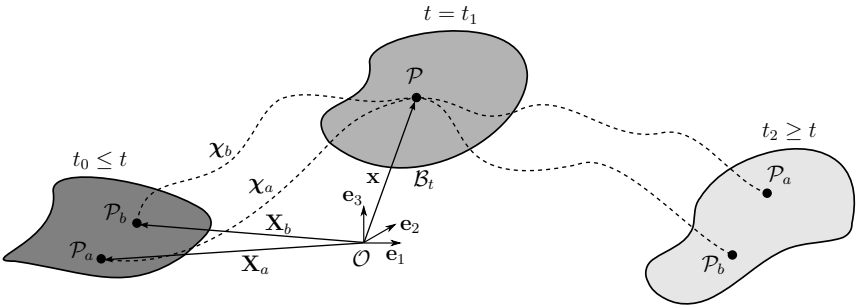

Figure 2.1: *Kinematics in the Hybrid Mixture Theory.*

2.2 Kinematic relations

A body $\mathcal{B}_t$ is defined as a collection of particles at the current time t (Figure 2.1). The position vector $\mathbf{x}$ points at a material point $\mathcal{P}(\mathbf{x}, t)$ within the body, whereas each particular material point simultaneously posses contributions from each phase. In addition, it is assumed that each phase exhibits its own motion function $\boldsymbol{\chi}_\alpha$

$$\mathbf{x} = \boldsymbol{\chi}_\alpha(\mathbf{X}_\alpha, t)\,. \tag{2.14}$$

Thus, any material point in the current configuration $t = t_1$ has an unique reference position $\mathbf{X}_\alpha$ at time t_0. Therefore, the inverse motion function is uniquely defined by

$$\mathbf{X}_\alpha = (\boldsymbol{\chi}_\alpha)^{-1}(\mathbf{x}, t)\,. \tag{2.15}$$

A material filament $\mathrm{d}\mathbf{X}_\alpha$ in the reference configuration is transformed to $\mathrm{d}\mathbf{x}$ in the current configuration by

$$\mathrm{d}\mathbf{x} = \mathbf{F}_\alpha \cdot \mathrm{d}\mathbf{X}_\alpha\,, \tag{2.16}$$

where $\mathbf{F}_\alpha$ denotes the deformation gradient of phase φ^α and can be calculated similar to single-phase continuum mechanics by

$$\mathbf{F}_\alpha = \frac{\partial \boldsymbol{\chi}_\alpha}{\partial \mathbf{X}_\alpha} = \mathrm{Grad}_\alpha\, \boldsymbol{\chi}_\alpha\,. \tag{2.17}$$

Herein, Grad_α denotes the gradient with respect to the reference configuration of phase φ^α. $\mathbf{F}_\alpha$ carries an infinitesimal undeformed material fiber $\mathrm{d}\mathbf{X}_\alpha$ of φ^α into $\mathrm{d}\mathbf{x}$ in the deformed configuration.

The mixture's velocity is defined as the barycentric velocity of the weighted phase velocities according to

$$\mathbf{v} = \frac{1}{\rho} \sum_\alpha n^\alpha \rho^{\alpha R} \mathbf{v}_\alpha\,. \tag{2.18}$$

Phase velocities $\mathbf{v}_\alpha$ relative to the mixture defining the relative velocity $\mathbf{w}_\alpha$

$$\mathbf{w}_\alpha = \mathbf{v}_\alpha - \mathbf{v}\,, \tag{2.19}$$

where the constraint

$$\sum_{\alpha} n^{\alpha} \rho^{\alpha R} \mathbf{w}_{\alpha} = \mathbf{0} \tag{2.20}$$

arises as a natural consequence. In analogy, the phase velocity can be expressed through the species velocity $\mathbf{v}_{\alpha_j}$ by

$$\mathbf{v}_{\alpha} = \frac{1}{\rho^{\alpha}} \sum_{j} n^{\alpha} \rho^{\alpha_j} \mathbf{v}_{\alpha} = \sum_{j} c^{\alpha_j} \mathbf{v}_{\alpha_j} \,. \tag{2.21}$$

Furthermore, diffusion velocities of species $\mathbf{w}_{\alpha_j}$ are denoted by

$$\mathbf{w}_{\alpha_j} = \mathbf{v}_{\alpha_j} - \mathbf{v}_{\alpha} \,, \tag{2.22}$$

where the constraint

$$\sum_{j} \rho^{\alpha_j} \mathbf{w}_{\alpha_j} = \mathbf{0} \tag{2.23}$$

represents the counterpart to (2.20). In addition, relative velocities between two phases are given by

$$\mathbf{v}_{\alpha\beta} = \mathbf{v}_{\alpha} - \mathbf{v}_{\beta} \tag{2.24}$$

and termed seepage velocities in this work when φ^{β} denotes the solid phase, i. e. $\beta = S$. Note that the solid phase displacement is given with respect to the reference configuration by $\mathbf{u}_S = \mathbf{x} - \mathbf{X}_S$ and therefore in a Lagrangian setting. In contrast, seepage velocities are measured relative to the solid skeleton, while diffusion velocities are given with respect to the corresponding (moving) phase. Hence, seepage and diffusive flows are described in a so-called modified Eulerian framework.

The spatial velocity gradient for φ^{α} is defined by

$$\mathbf{L}_{\alpha} = \frac{\partial \mathbf{v}_{\alpha}}{\partial \mathbf{x}} = \operatorname{grad} \mathbf{v}_{\alpha} \tag{2.25}$$

and can be additively splitted into its symmetric and skew-symmetric part by

$$\mathbf{L}_{\alpha} = \mathbf{D}_{\alpha} + \mathbf{W}_{\alpha} \,, \tag{2.26}$$

where standard tensor calculus are used to write

$$\mathbf{D}_{\alpha} = \frac{1}{2}(\mathbf{L}_{\alpha} + \mathbf{L}_{\alpha}^{T}) \quad \text{and} \quad \mathbf{W}_{\alpha} = \frac{1}{2}(\mathbf{L}_{\alpha} - \mathbf{L}_{\alpha}^{T}) \,. \tag{2.27}$$

In analogy to (2.25), the spatial velocity gradient for species φ^{α_j} is defined by

$$\mathbf{L}_{\alpha_j} = \frac{\partial \mathbf{v}_{\alpha_j}}{\partial \mathbf{x}} = \operatorname{grad} \mathbf{v}_{\alpha_j} \,. \tag{2.28}$$

The spatial velocity gradient of the mixture is defined through

$$\mathbf{L} = \frac{\partial \mathbf{v}}{\partial \mathbf{x}} = \operatorname{grad} \mathbf{v} \,. \tag{2.29}$$

In the following, $(\bullet)'_{\alpha_j}$, $(\bullet)'_{\alpha}$ and $\dot{(\bullet)}$ respectively denote the material time derivative of a field variable $(\bullet)$ with respect to the motion of a species, a phase and the overall mixture, namely

$$(\bullet)'_{\alpha_j} = \frac{\partial(\bullet)}{\partial t} + \operatorname{grad}(\bullet)\cdot\mathbf{v}_{\alpha_j}\,; \quad (\bullet)'_{\alpha} = \frac{\partial(\bullet)}{\partial t} + \operatorname{grad}(\bullet)\cdot\mathbf{v}_{\alpha}\,; \quad \dot{(\bullet)} = \frac{\partial(\bullet)}{\partial t} + \operatorname{grad}(\bullet)\cdot\mathbf{v}\,. \tag{2.30}$$

2.3 Balance equations

Next, the governing equations for the multi-phase and multi-species system are postulated in local form. Species are able to interact with each other within a phase, which will be captured by considering *intra-phase* exchange terms. As a restriction, the total intra-phase production terms have to vanish when summed over all species within a phase. Besides interactions among species within a phase, interactions across the phase boundaries are accounted for by *inter-phase* exchange terms. The total production terms on the phase level have to vanish when summed over the phases.

Note that the production terms in the balance equations of mixture theory represent interactions on the constituent but also on the species level. In the literature, different representations of the production terms are presented, where different treatments trace back to the intention if one focuses on describing the *causes* or *effects* of the interactions. In terms of the mass exchange, [8, 9, 12, 24, 119] chose a notation which indicates the origin of the mass gain. Therefore, the density production to a specific species is on the one hand split into intra- and inter-phase mass exchange, while on the other hand the notation distinguishes explicitly between the phases which have a contribution in the mass exchange. On the contrary, a particular production term can also be viewed as an effective quantity (cf. [49, 118, 143]), which reflects the total gain or loss due to the interaction with all other phases.

In this manuscript, a notation is chosen which distinguishes between intra- and inter-phase exchange terms, while in addition, the inter-phase exchange terms are resolved to account explicitly for the individual phase interactions. Following this idea, intra-phase exchange terms are expressed through $\hat{(\bullet)}_a^{\alpha_j}$, while the inter-phase exchange terms on the species and phase level read

$$\hat{(\bullet)}_r^{\alpha_j} = \sum_{\beta\neq\alpha} \hat{(\bullet)}_\beta^{\alpha_j} \quad \text{and} \quad \hat{(\bullet)}_r^{\alpha} = \hat{(\bullet)}^{\alpha} = \sum_{\beta\neq\alpha} \hat{(\bullet)}_\beta^{\alpha}\,. \tag{2.31}$$

Herein, $\hat{(\bullet)}_\beta^{\alpha_j}$ and $\hat{(\bullet)}_\beta^{\alpha}$ denote the production of $(\bullet)^{\alpha_j}$ and $(\bullet)^{\alpha}$ due to the interaction with phase φ^β, respectively.

Conservation of mass The conservation of mass is formulated on the species and phase level by

$$(n^\alpha \rho^{\alpha_j})'_{\alpha_j} + n^\alpha \rho^{\alpha_j} \operatorname{div}(\mathbf{v}_{\alpha_j}) = \hat{\rho}_a^{\alpha_j} + \hat{\rho}_r^{\alpha_j}\,, \tag{2.32}$$

$$(n^\alpha \rho^{\alpha R})'_{\alpha} + n^\alpha \rho^{\alpha R} \operatorname{div}(\mathbf{v}_{\alpha}) = \hat{\rho}^{\alpha}\,, \tag{2.33}$$

herein, $\hat{\rho}_a^{\alpha_j}$ and $\hat{\rho}_r^{\alpha_j}$ represent the density production of φ^{α_j} due to chemical reactions among the species and inter-phase mass transfer, respectively, whereas $\hat{\rho}^\alpha$ is the total density production of the phase. The restrictions for intra and inter-phase mass exchange are respectively given by

$$\sum_j \hat{\rho}_a^{\alpha_j} = 0\,; \qquad \sum_\alpha \hat{\rho}^\alpha = 0\,. \tag{2.34}$$

Furthermore, summing over the species yields the relation between species and their corresponding phase

$$\hat{\rho}^\alpha = \sum_j \hat{\rho}_r^{\alpha_j}\,. \tag{2.35}$$

Summing over the phases leads finally to the well-known mass balance equation in classical continuum mechanics

$$\dot{\rho} + \rho \operatorname{div} \mathbf{v} = 0\,. \tag{2.36}$$

Linear momentum balance It is here a priori assumed that the partial Cauchy stress tensors for species $\mathbf{T}^{\alpha_j}$ and phases $\mathbf{T}^\alpha$ are symmetric, i. e. $\mathbf{T}^{\alpha_j} = (\mathbf{T}^{\alpha_j})^T$ and $\mathbf{T}^\alpha = (\mathbf{T}^\alpha)^T$. The linear momentum balances for phases and species are than given by

$$n^\alpha \rho^{\alpha_j} (\mathbf{v}_{\alpha_j})'_{\alpha_j} - \operatorname{div} \mathbf{T}^{\alpha_j} - n^\alpha \rho^{\alpha_j} \mathbf{b}^{\alpha_j} = \hat{\mathbf{p}}_a^{\alpha_j} + \hat{\mathbf{p}}_r^{\alpha_j}\,, \tag{2.37}$$

$$n^\alpha \rho^{\alpha R} (\mathbf{v}_\alpha)'_\alpha - \operatorname{div} \mathbf{T}^\alpha - n^\alpha \rho^{\alpha R} \mathbf{b}^\alpha = \hat{\mathbf{p}}^\alpha\,. \tag{2.38}$$

On the species level, momentum interactions among species in the same phase $\hat{\mathbf{p}}_a^{\alpha_j}$ and inter-phase momentum exchange $\hat{\mathbf{p}}_r^{\alpha_j}$ are accounted for. The volumetric forces on the phase level are linked to the species level through $\rho^\alpha \mathbf{b}^\alpha = \sum_j n^\alpha \rho^{\alpha_j} \mathbf{b}^{\alpha_j}$. Restrictions for the total intra- and inter-phase momentum exchange terms read

$$\sum_j (\hat{\mathbf{p}}_a^{\alpha_j} + \hat{\rho}_a^{\alpha_j} \mathbf{v}_{\alpha_j}) = \mathbf{0}\,; \qquad \sum_\alpha (\hat{\mathbf{p}}^\alpha + \hat{\rho}^\alpha \mathbf{v}_\alpha) = \mathbf{0}\,. \tag{2.39}$$

Herein, the second contribution in both equations accounts for the momentum exchange due to mass transfer. Again, relations between species and their bulk counterparts can be derived by summing (2.37) over the species, which leads to expressions for the partial Cauchy stresses $\mathbf{T}^\alpha$ and the direct momentum production $\hat{\mathbf{p}}^\alpha$ of an arbitrary phase φ^α to

$$\mathbf{T}^\alpha = \sum_j (\mathbf{T}^{\alpha_j} - n^\alpha \rho^{\alpha_j} \mathbf{w}_{\alpha_j} \otimes \mathbf{w}_{\alpha_j})\,, \tag{2.40}$$

$$\hat{\mathbf{p}}^\alpha = \sum_j (\hat{\mathbf{p}}_r^{\alpha_j} + \hat{\rho}_r^{\alpha_j} \mathbf{w}_{\alpha_j})\,. \tag{2.41}$$

Summing (2.38) over the phases leads to the classical form of the local momentum balance for single-phase continua

$$\rho\, \dot{\mathbf{v}} - \operatorname{div} \mathbf{T} - \rho \mathbf{b} = \mathbf{0}\,, \tag{2.42}$$

from which the total stress tensor as well as the body force vector compute to

$$\mathbf{T} = \sum_{\alpha}(\mathbf{T}^{\alpha} - n^{\alpha}\rho^{\alpha R}\mathbf{w}_{\alpha}\otimes\mathbf{w}_{\alpha})\,, \tag{2.43}$$

$$\rho\,\mathbf{b} = \sum_{\alpha}\rho^{\alpha}\mathbf{b}^{\alpha}\,. \tag{2.44}$$

Conservation of charges In the absence of any external electrical field, the charges are balanced on the species and on the phase level through

$$(n^{\alpha}\rho_e^{\alpha_j})'_{\alpha_j} + n^{\alpha}\rho_e^{\alpha_j}\operatorname{div}\mathbf{v}_{\alpha_j} = \hat{\rho}_e^{\alpha_j}\,, \tag{2.45}$$

$$(n^{\alpha}\rho_e^{\alpha})'_{\alpha} + n^{\alpha}\rho_e^{\alpha}\mathbf{v}_{\alpha} = \hat{\rho}_e^{\alpha}\,, \tag{2.46}$$

where $\hat{\rho}_e^{\alpha_j}$ denotes the total charge production, which can be written as [2]

$$\hat{\rho}_e^{\alpha_j} = \frac{z^{\alpha_j}F}{M_m^j}(\hat{\rho}_a^{\alpha_j} + \hat{\rho}_r^{\alpha_j})\,, \tag{2.47}$$

while direct charge production, i. e. the charge production which does not stem from mass exchange, has been neglected a priori. Summing (2.45) over the charged species corresponding to the phase φ^{α} leads to

$$\hat{\rho}_e^{\alpha} = \sum_j \hat{\rho}_e^{\alpha_j}\,. \tag{2.48}$$

In the framework presented in this manuscript, the charge balance equations are the only governing equation stemming from electrostatics since it is assumed that there is neither an external electric nor a magnetic field.

Conservation of energy The conservation of energy represents the *first law of thermodynamics* and balances the internal energy [16]. The internal energy for a species ε^{α_j} and for a phase ε^{α} are respectively governed by

$$n^{\alpha}\rho^{\alpha_j}(\varepsilon^{\alpha_j})'_{\alpha_j} - \mathbf{T}^{\alpha_j} : \mathbf{L}_{\alpha_j} - \operatorname{div}(\mathbf{q}_T^{\alpha_j}) - n^{\alpha}\rho^{\alpha_j}r^{\alpha_j} = \hat{\varepsilon}_a^{\alpha_j} + \hat{\varepsilon}_r^{\alpha_j}\,, \tag{2.49}$$

$$n^{\alpha}\rho^{\alpha}(\varepsilon^{\alpha})'_{\alpha} - \mathbf{T}^{\alpha} : \mathbf{L}_{\alpha} - \operatorname{div}(\mathbf{q}_T^{\alpha}) - n^{\alpha}\rho^{\alpha}r^{\alpha} = \hat{\varepsilon}^{\alpha}\,. \tag{2.50}$$

Herein, $\hat{\varepsilon}_a^{\alpha_j}$ and $\hat{\varepsilon}_r^{\alpha_j}$ represent the direct energy gain of φ^{α_j} due to species within the same phase and due to inter-phase energy gain from different phases. In addition, $\hat{\varepsilon}^{\alpha}$ is the total energy production of the phase. The restrictions for intra- and inter-phase energy gain are respectively given by

$$\sum_j\left[\hat{\varepsilon}_a^{\alpha_j} + \hat{\mathbf{p}}_a^{\alpha_j}\cdot\mathbf{v}_{\alpha_j} + \hat{\rho}_a^{\alpha_j}\left(\varepsilon^{\alpha_j} + \frac{1}{2}\mathbf{v}_{\alpha_j}\cdot\mathbf{v}_{\alpha_j}\right)\right] = 0\,, \tag{2.51}$$

$$\sum_{\alpha}\left[\hat{\varepsilon}_r^{\alpha_j} + \hat{\mathbf{p}}_r^{\alpha_j}\cdot\mathbf{v}_{\alpha_j} + \hat{\rho}_r^{\alpha_j}\left(\varepsilon^{\alpha_j} + \frac{1}{2}\mathbf{v}_{\alpha_j}\cdot\mathbf{v}_{\alpha_j}\right)\right] = 0\,. \tag{2.52}$$

The species heat flux $\mathbf{q}_T^{\alpha_j}$ and the external heat supply r^{α_j} are related to the phase level through

$$\mathbf{q}_T^{\alpha} = \sum_j \left(\mathbf{q}_T^{\alpha_j} - n^{\alpha}\rho^{\alpha_j}\varepsilon^{\alpha_j}\mathbf{w}_{\alpha_j}\right) \quad \text{and} \quad \rho^{\alpha} r^{\alpha} = \sum_j n^{\alpha}\rho^{\alpha_j} r^{\alpha_j} \,. \tag{2.53}$$

Furthermore, summing over the species yields the relation between species and their corresponding phase

$$\hat{\varepsilon}^{\alpha} = \sum_j \left[\hat{\varepsilon}_r^{\alpha_j} + \hat{\mathbf{p}}_r^{\alpha_j} \cdot \mathbf{v}_{\alpha_j} + \hat{\rho}_r^{\alpha_j}\left(\varepsilon^{\alpha_j} + \frac{1}{2}\mathbf{v}_{\alpha_j} \cdot \mathbf{v}_{\alpha_j}\right)\right] , \tag{2.54}$$

$$\rho^{\alpha}\varepsilon^{\alpha} = \sum_j n^{\alpha}\rho^{\alpha_j}\left(\varepsilon^{\alpha_j} + \frac{1}{2}\mathbf{v}_{\alpha_j} \cdot \mathbf{v}_{\alpha_j}\right) . \tag{2.55}$$

The local energy balance of the mixture is obtained by summing (2.62) over the phases to

$$\rho\,\dot{\varepsilon} - \mathbf{T} : \mathbf{L} - \operatorname{div}\mathbf{q}_T - \rho\, r = 0 \,, \tag{2.56}$$

where the following relations are recovered between the mixture and its phases

$$\rho\,\varepsilon = \sum_{\alpha} \rho^{\alpha}\left(\varepsilon^{\alpha} + \frac{1}{2}\mathbf{v}_{\alpha} \cdot \mathbf{v}_{\alpha}\right) , \tag{2.57}$$

$$\mathbf{q}_T = \sum_{\alpha} \left(\mathbf{q}_T^{\alpha} - \rho^{\alpha}\varepsilon^{\alpha}\mathbf{w}_{\alpha}\right) , \tag{2.58}$$

$$\rho\, r = \sum_{\alpha} \rho^{\alpha} r^{\alpha} \,. \tag{2.59}$$

Entropy balance The *second law of thermodynamics* dictates that the net production of entropy of the overall mixture is always non-negative. To represent the time rate of the entropy in an equality, the direct entropy production on the species level is introduced through $\hat{\Lambda}^{\alpha_j}$ and linked to the phase and mixture levels by

$$\hat{\Lambda} = \sum_{\alpha} \hat{\Lambda}^{\alpha} = \sum_{\alpha}\sum_j \hat{\Lambda}^{\alpha_j} \geq 0 \,. \tag{2.60}$$

Note that the direct entropy production denotes the portion of the entropy production which does not originate from intra- or inter-phase exchange. The entropy balance is given on the species and phase level by

$$n^{\alpha}\rho^{\alpha_j}(\eta^{\alpha_j})'_{\alpha_j} - \operatorname{div}\left(\boldsymbol{\phi}_{\eta}^{\alpha_j}\right) - n^{\alpha}\rho^{\alpha_j}\sigma_{\eta}^{\alpha_j} = \hat{\eta}_a^{\alpha_j} + \hat{\eta}_r^{\alpha_j} + \hat{\Lambda}^{\alpha_j} \,, \tag{2.61}$$

$$n^{\alpha}\rho^{\alpha}(\eta^{\alpha})'_{\alpha} - \operatorname{div}\left(\boldsymbol{\phi}_{\eta}^{\alpha}\right) - n^{\alpha}\rho^{\alpha R}\sigma_{\eta}^{\alpha} = \hat{\eta}^{\alpha} + \hat{\Lambda}^{\alpha} \,, \tag{2.62}$$

where $\hat{\eta}_a^{\alpha_j}$ and $\hat{\eta}_r^{\alpha_j}$ represent the entropy production due to intra-phase and inter-phase exchange, respectively, and $\hat{\eta}^{\alpha}$ is the total entropy production due to inter-phase exchange on the phase-level. The entropy flux $\boldsymbol{\phi}_{\eta}^{\alpha_j}$ and the entropy supply $\sigma_{\eta}^{\alpha_j}$ on the species-level are linked to the phase level through

$$\boldsymbol{\phi}_{\eta}^{\alpha} = \sum_j \left(\boldsymbol{\phi}_{\eta}^{\alpha_j} - n^{\alpha}\rho^{\alpha_j}\eta^{\alpha_j}\mathbf{w}_{\alpha_j}\right) \quad \text{and} \quad n^{\alpha}\rho^{\alpha R}\sigma_{\eta}^{\alpha} = \sum_j n^{\alpha}\rho^{\alpha_j}\sigma_{\eta}^{\alpha_j} \,. \tag{2.63}$$

Since the direct entropy production has been introduced through (2.60), the restrictions for the inter-phase entropy exchange terms are derived to

$$\sum_j (\hat{\eta}_a^{\alpha_j} + \hat{\rho}_a^{\alpha_j} \eta^{\alpha_j}) = 0\,, \tag{2.64}$$

$$\sum_\alpha (\hat{\eta}_r^{\alpha_j} + \hat{\rho}_r^{\alpha_j} \eta^{\alpha_j}) = 0\,. \tag{2.65}$$

Next, the entropy flux $\phi_\eta^{\alpha_j}$ and the entropy supply $\sigma_\eta^{\alpha_j}$ are substituted by the well-established constitutive assumptions [143]

$$\sigma_\eta^{\alpha_j} = \frac{r^{\alpha_j}}{T} \quad \text{and} \quad \boldsymbol{\phi}^{\alpha_j} = \frac{\mathbf{q}_T^{\alpha_j}}{T}\,, \tag{2.66}$$

where furthermore thermal-equilibrium, i. e. $T^{\alpha_j} = T^\alpha = T$, between the species is postulated.
Substituting the energy balance (2.49) in the entropy balance (2.61) and summing over species and phases leads finally to an expression for the entropy production of the overall medium $\hat{\Lambda}$. When thermal effects are neglected one obtains the Clausius-Duhem inequality for a multi-phase and multi-species material by

$$\begin{aligned} \hat{\Lambda} T = \sum_\alpha \sum_j \hat{\Lambda}^{\alpha_j} T = \sum_\alpha \sum_j \Big(& - n^\alpha \rho^{\alpha_j} (\Psi^{\alpha_j})'_{\alpha_j} \\ & + \mathbf{T}^{\alpha_j} : \mathbf{L}_{\alpha_j} - (\hat{\mathbf{p}}_a^{\alpha_j} + \hat{\mathbf{p}}_r^{\alpha_j}) \cdot \mathbf{v}_{\alpha_j} \\ & - (\hat{\rho}_a^{\alpha_j} + \hat{\rho}_r^{\alpha_j}) \frac{1}{2} \mathbf{v}_{\alpha_j} \cdot \mathbf{v}_{\alpha_j} - (\hat{\rho}_a^{\alpha_j} + \hat{\rho}_r^{\alpha_j}) \Psi^{\alpha_j} \Big) \geq 0\,. \end{aligned} \tag{2.67}$$

Herein, the Legendre transformation of the Helmholtz free energy $\Psi^{\alpha_j} = \varepsilon^{\alpha_j} - T\eta^{\alpha_j}$ has been exploited.

Dissipation inequality The mass-based Helmholtz free energy of the mixture Ψ is respectively linked to the Helmholtz free energy on the phase and species level through

$$\rho \Psi = \sum_\alpha \rho^\alpha \Psi^\alpha = \sum_\alpha \sum_j n^\alpha \rho^{\alpha_j} \Psi^{\alpha_j}\,. \tag{2.68}$$

Finally, the entropy inequality for the multi-phase and multi-species system under isothermal conditions reads

$$\begin{aligned} D \;=\; & \sum_\alpha \Big(- n^\alpha \rho^\alpha (\Psi^\alpha)'_\alpha \\ & + \Big[\mathbf{T}^\alpha + \sum_j n^\alpha \rho^{\alpha_j} \mathbf{w}_{\alpha_j} \otimes \mathbf{w}_{\alpha_j} \Big] : \mathbf{L}_\alpha + \sum_j \Big[\mathbf{T}^{\alpha_j} - n^\alpha \rho^{\alpha_j} \Psi^{\alpha_j} \mathbf{I} \Big] : \operatorname{grad} \mathbf{w}_{\alpha_j} \\ & - \sum_j \Big[\operatorname{grad} (n^\alpha \rho^{\alpha_j} \Psi^{\alpha_j}) + \hat{\mathbf{p}}_r^{\alpha_j} + \hat{\mathbf{p}}_a^{\alpha_j} \Big] \cdot \mathbf{w}_{\alpha_j} \\ & - \sum_j \Big[\hat{\rho}_r^{\alpha_j} + \hat{\rho}_a^{\alpha_j} \Big] \frac{1}{2} \mathbf{w}_{\alpha_j} \cdot \mathbf{w}_{\alpha_j} - \hat{\mathbf{p}}^\alpha \cdot \mathbf{w}_\alpha - \hat{\rho}^\alpha \Big[\frac{1}{2} \mathbf{w}_\alpha \cdot \mathbf{w}_\alpha + \Psi^\alpha \Big] \Big) \geq 0\,. \end{aligned} \tag{2.69}$$

Here $\mathbf{I}$ denotes the second order identity tensor. A detailed derivation and discussion were carried out in the literature [22, 23].

Chapter 3:
Thermodynamic theory of charged hydrogels

In the previous chapter, the fundamentals of multiphasic material modeling were introduced in a general fashion. The HMT will be adapted to a chemical active porous material in the next chapter. Since charged hydrogels are an essential component of the overall material under consideration, the thermodynamic fundamentals of charged hydrogels are discussed in this chapter. Here, the attention is focused on a special type of charged hydrogel, namely a Superabsorbent Polymer (SAP). SAPs are cross-linked polyelectrolytes, which are able to absorb high amounts of aqueous solution by forming a hydrogel. The aim of this chapter is the derivation of the driving forces for charged hydrogels with respect to the microstructure. Thermodynamic models are briefly summarized and three different contributions to the driving force of hydrogel swelling are identified.

3.1 Microstructure of charged hydrogels

The ability of a charged hydrogel to absorb large amounts of aqueous solution is driven by the microstructure of the gel. A micromodel of a charged hydrogel in contact with an electrolyte is shown in Figure 3.1. The bi-phasic model is displayed for two points in

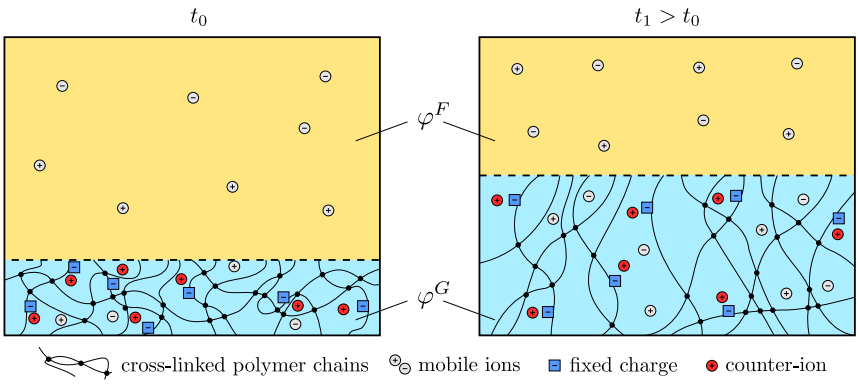

Figure 3.1: *Evolution of the microscopic hydrogel model due to mass exchange. The ambient pore fluid chemistry, i. e. the ion concentration, is chosen such that mass absorption by the hydrogel occurs from t_0 to t_1. The hydrogel is a mixture of absorbed solution and polymer chains, while fixed charges are attached to the polymer network. Counter-ions are trapped by electro-static forces in the gel to maintain electro-neutrality. In addition, mobile ions are present in both the pore fluid and in the absorbed solution.*

time (t_0 and t_1) to emphasize the fact that mass transfer has been occurred in this time span. The total volume, i. e. the sum of the hydrogel and fluid volume, is assumed to be constant with respect to time, such that the inter-phase mass exchange is isochoric.

According to the previously derived HMT framework, the system φ is treated as an immiscible mixture composed of the hydrogel φ^G and the surrounding electrolyte φ^F. More precisely, the hydrogel phase is a porous material, which is itself composed of two phases, namely a hydrophilic polymer network φ^{sG} and an absorbed solution φ^{fG}, i. e. $\varphi^G = \varphi^{sG} \cup \varphi^{fG}$. In the case of charged hydrogels, the multi-species framework of the HMT accounts here for the immiscible phase compositions.

Following this idea, the polymer network is composed of monomer φ^{sG_m} and fixed charges $\varphi^{sG_{fc}}$ attached to the polymer chains, which can not leave the gel. Furthermore, the surrounding and the absorbed solution are mixtures of water φ^{α_w} and mobile charged ions φ^{α_i}, where $\alpha \in \{F, fG\}$. Note that φ^{α_i} is a placeholder which refers to a positive ion φ^{α_+} or a negative one denoted as φ^{α_-}. In addition, $\sum(\bullet)^{\alpha_i}$ is used as abbreviation for $(\bullet)^{\alpha_+} + (\bullet)^{\alpha_-}$ in this contribution, where $(\bullet)^{\alpha_i}$ refers to an arbitrary quantity related to a mobile ion in φ^{α}. To maintain electro-neutrality of the gel, i. e. $\rho_e^G = n^{fG}(\rho_e^{fG_+} + \rho_e^{fG_-}) + n^{sG}\rho^{sG_{fc}} = 0$, a sufficient amount of counter-ions are trapped in the gel structure by electro-static forces. This results in an ion concentration difference between the absorbed and the surrounding solution. Since the polymer network is not able to release the fixed charges, the hydrogel has the tendency to absorb water to dilute the ion concentration difference. The cross-linked polymer network prevents the gel from dissolving in the surrounding fluid and therefore counteracts the volumetric expansion.

Mass- and volume-based degree of swelling On the macroscale, the current state of swelling can be quantified by a volume- or mass-based degree of swelling respectively given by

$$q_v = \frac{\mathrm{d}v^G}{\mathrm{d}v^{sG}} = \frac{\mathrm{d}v^{fG} + \mathrm{d}v^{sG}}{\mathrm{d}v^{sG}} \quad \text{and} \quad q = \frac{\mathrm{d}m^G}{\mathrm{d}m^{sG}} = \frac{\mathrm{d}m^{fG} + \mathrm{d}m^{sG}}{\mathrm{d}m^{sG}}\,. \tag{3.1}$$

However, the polymer volume fraction ϕ is frequently used in the constitutive modeling of hydrogels and is therefore introduced here as

$$\phi = \frac{\mathrm{d}v^{sG}}{\mathrm{d}v^G} = q_v^{-1}\,. \tag{3.2}$$

By using the intrinsic polymer and absorbed solution densities, the mass-based degree of swelling can be expressed in terms of the polymer volume fraction to

$$q = 1 + \frac{\rho^{fGR}}{\rho^{sGR}}\frac{1-\phi}{\phi}\,. \tag{3.3}$$

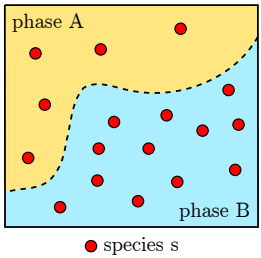

Figure 3.2: *A simple two phase model.*

3.2 Gibbs free energy and chemical potentials

The molar-based Gibbs free energy for an ideal phase φ^α is sufficiently described by the phase temperature T^α, partial pressure p^α and its composition $n_m^{\alpha_j}$ through

$$G_m^\alpha = G_m^\alpha(T^\alpha, p^\alpha, n_m^{\alpha_1}, \cdots, n_m^{\alpha_N})\,, \tag{3.4}$$

where it has been assumed that the phase is an immiscible mixture of N species. In classical thermodynamics, the extensive state variable $n_m^{\alpha_j}$ is used in favor of the molar concentration $\rho_m^{\alpha_j}$, an intensive state variable. It is worth mentioning that the values of $n_m^{\alpha_j}$ are independent for all N species, which is in contrast to the definition of the intensive measure $\rho_m^{\alpha_j}$. In general, the Gibbs free energy accounts for the thermal, mechanical and chemical energy of a phase. Total equilibrium of the phase is therefore mathematically expressed through the vanishing total derivative of the Gibbs free energy, i. e.

$$\mathrm{d}G_m^\alpha = \frac{\partial G_m^\alpha}{\partial T^\alpha}\Big|_{p^\alpha, n^{\alpha_j}} \mathrm{d}T^\alpha + \frac{\partial G_m^\alpha}{\partial p^\alpha}\Big|_{T^\alpha, n^{\alpha_j}} \mathrm{d}p^\alpha + \sum_j \frac{\partial G_m^\alpha}{\partial n_m^{\alpha_j}}\Big|_{T^\alpha, p^\alpha, n^{\alpha_{k\neq j}}} \mathrm{d}n_m^{\alpha_j} = 0\,. \tag{3.5}$$

Here, the molar-based chemical potential of φ^{α_j} is introduced through

$$\mu_m^{\alpha_j} = \frac{\partial G_m^\alpha}{\partial n_m^{\alpha_j}}\Big|_{T^\alpha, p^\alpha, n_m^{\alpha_{k\neq j}}}\,, \tag{3.6}$$

which denotes the change in free Gibbs energy by adding one mole of substance $n_m^{\alpha_j}$ to φ^α, while the pressure, temperature and remaining phase composition are held constant.

The chemical potential and the relation to mass transfer is observed in the following in an exemplary fashion. A simple material consisting of two phases φ^A and φ^B is assumed, while a species φ^{α_s} exists in both phases, cf. Figure 3.2. Under the assumption of thermal and mechanical equilibrium, the change in Gibbs free energy of the system reads

$$\mathrm{d}G_m = \mathrm{d}G_m^A + \mathrm{d}G_m^B = (\mu_m^{A_s} - \mu_m^{B_s})\mathrm{d}n_m^{A_s}\,, \tag{3.7}$$

where the relation $\mathrm{d}n_m^{B_s} = -\mathrm{d}n_m^{A_s}$ holds for a closed system. The following three possible cases are distinguished with respect to the chemical potentials

$$\mu_m^{B_s} > \mu_m^{A_s}, \text{transfer from: } B \rightarrow A\,, \tag{3.8}$$
$$\mu_m^{B_s} < \mu_m^{A_s}, \text{transfer from: } A \rightarrow B\,, \tag{3.9}$$
$$\mu_m^{B_s} = \mu_m^{A_s}, \text{equilibrium}\,. \tag{3.10}$$

Therefore, the chemical potential difference characterizes the direction of the mass transfer process. However, it is important to emphasize that it does not contain any information about the kinetics of the mass exchange.

3.3 Driving forces for hydrogel swelling

The Gibbs free energy of the hydrogel G_m^G is assumed as a superposition of three contributions [160]

$$G_m^G = G_{m,mix}^G + G_{m,elast}^G + G_{m,ion}^G\,, \tag{3.11}$$

while the corresponding processes on the microscale are identified to:

- the mixing of polymer chains and absorbed solvent $G_{m,mix}^G$,
- the entropy elasticity of the network caused by volumetric expansion $G_{m,elast}^G$,
- and the ionic contribution due to fixed charges $G_{m,ion}^G$.

Similar studies of competing phenomena were performed by English *et al.* [51] and Horkay *et al.* [70]. In equilibrium, the chemical potential differences for both water and mobile ions vanish, namely

$$\Delta\mu_m^w = \mu_m^{G_w} - \mu_m^{F_w} = 0\,, \tag{3.12}$$
$$\Delta\mu_m^i = \mu_m^{G_i} - \mu_m^{F_i} = 0 \quad \forall i \in \{+,-\}\,. \tag{3.13}$$

In the following, chemical potential differences are deduced from the additive split (3.11), while appropriate constitutive models on the basis of microstructural considerations and results obtained in polymer physics needs to be derived first.

3.3.1 Ionic contribution

The enormous water uptake of charged hydrogels is mainly related to the ion concentration difference between the surrounding and the absorbed solution. This effect is known as Donnan osmosis and can be explained with the aid of a membrane model, cf. Figure 3.3. The absorbed solution φ^{fG} is in contact with the surrounding solution φ^F, separated by a semi-permeable membrane. The membrane is permeable for water φ^{α_w} and mobile ions φ^{α_i} but impermeable for fixed charges. To this end, the membrane in the model description accounts for the fact that the fixed charges are attached to the polymer chains.

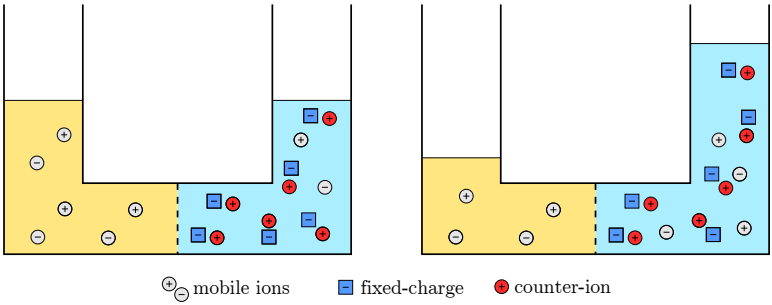

Figure 3.3: *Donnan osmosis of electrolytic solutions with fixed charges (cf. [75]).*

The individual electro-neutrality condition of the surrounding solution φ^F and the hydrogel φ^G, yields to restrictions towards the concentrations, namely

$$\sum \rho_e^{F_i} = \rho_m^{F_+} z^{F_+} + \rho_m^{F_-} z^{F_-} = 0\,, \tag{3.14}$$

$$\sum \rho_e^{G_i} + \rho_e^{G_{fc}} = (1-\phi)(\rho_m^{fG_+} z^{fG_+} + \rho_m^{fG_-} z^{fG_-}) + \phi \rho_m^{sG_{fc}} z^{fc} = 0\,. \tag{3.15}$$

Based on the mathematical form of mixtures of ideal gases, the chemical potential of a solved species in solution is given by

$$\mu_{m,ion}^{\alpha_j} = \mu_{m,0}^{j} + RT \ln(a^{\alpha_j})\,, \tag{3.16}$$

where $\mu_{m,0}^{j}$ is the chemical potential of the pure substance under reference conditions, i. e. standard pressure and standard temperature, while a^{α_j} in the second term denotes the activity of species φ^{α_j}. According to thermodynamics [16], the activities are usually multiplicatively splitted in an activity coefficient γ^{α_j} and a molar fraction $x_m^{\alpha_j}$ to

$$a^{\alpha_j} = \gamma^{\alpha_j}\, x_m^{\alpha_j} = \gamma^{\alpha_j}\, \frac{\rho_m^{\alpha_j}}{\rho_m^{\alpha R}}\,. \tag{3.17}$$

Note in passing that the activity as well as the activity coefficient are dimensionless quantities. In the theory of ideal mixtures, the activity of a solved species coincides with its corresponding molar fraction. In contrast, the activity coefficient introduced for real solutions accounts for deviations from the ideal behavior of infinite dilute solutions. Against this background, it is reasonable to call the activities *effective concentrations*. The chemical potential differences for all species which are able to pass the membrane has to vanish in equilibrium, such that

$$\mu_{m,ion}^{fG_w} = \mu_{m,ion}^{F_w}\,, \tag{3.18a}$$

$$\mu_{m,ion}^{fG_+} = \mu_{m,ion}^{F_+}\,, \tag{3.18b}$$

$$\mu_{m,ion}^{fG_-} = \mu_{m,ion}^{F_-}\,. \tag{3.18c}$$

Driving force for water transfer The ionic contribution of the chemical potential of water is identified with the chemical potential difference across the membrane

$$\Delta\mu^w_{m,ion} = \mu^{fG_w}_m - \mu^{F_w}_m = RT \ln\left(\psi^w \frac{\rho^{fG_w}_m}{\rho^{F_w}_m}\right) \quad \text{with} \quad \psi^w = \frac{\gamma^{fG_w}}{\gamma^{F_w}}\,, \tag{3.19}$$

while $\rho^{fGR}_m = \rho^{FR}_m$ has been assumed in the derivation. Herein, ψ^w accounts for both the non-ideal behavior of absorbed as well as free water and will therefore be called cumulated activity coefficient. By using the charge neutrality conditions for the hydrogel (3.15) and the surrounding solution (3.14), respectively, together with (2.7) enables one to express the molar concentrations of water through

$$\rho^{fG_w}_m = \rho^{fGR}_m - \rho^{fG_-}_m \left(1 + \frac{\left|z^{fG_-}\right|}{z^{fG_+}}\right) - \frac{\phi}{1-\phi}\,\rho^{sG_{fc}}_m \frac{\left|z^{fc}\right|}{z^{fG_+}}\,, \tag{3.20}$$

$$\rho^{F_w}_m = \rho^{FR}_m - \rho^{F_-}_m \left(1 + \frac{\left|z^{F_-}\right|}{z^{F_+}}\right). \tag{3.21}$$

Note that $\Delta\mu^w_{m,ion}$ refers to the driving force for swelling of a soluble (not cross-linked) charged polymer network. In case of deionized water in the surrounding liquid ($\rho^{F_-}_m = \rho^{F_+}_m = 0$), infinite swelling of the polymer network is expected from a theoretical point of view, i. e. the polymer network dissolves in the solution. On the contrary, in a cross-linked network, the polymer is prevented from dissolving.

The chemical potential difference $\Delta\mu^w_{m,ion}$ can be linearized for dilute electrolytic solutions to

$$\Delta\mu^w_{m,ion} = \mu^{fG_w}_{m,ion} - \mu^{F_w}_{m,ion} = -RT\tilde{V}^w_m \sum_i \left(\rho^{fG_i}_m - \rho^{F_i}_m\right) + RT \ln \psi^w\,, \tag{3.22}$$

where the logarithmic term has been approximated by $\ln(1-x) \approx -x$ and the molar phase densities are related by $\rho^{fGR}_m = \rho^{FR}_m \approx (\tilde{V}^w_m)^{-1}$.

Donnan equilibrium Ion equilibrium between absorbed and surrounding solution, which is also known as Donnan equilibrium [164], is frequently assumed in the modeling of charged hydrated media. Herein, electro-chemical equilibrium for mobile ions, which are able to pass the membrane, is instantaneously reached, such that chemical potential differences for positive and negative ions are identified with (3.18b) and (3.18c), respectively.

By using the constitutive forms of the chemical potentials for real solutions (3.16) and the multiplicative split of the activity (3.17), yields the following expressions for the ion

concentrations within the gel

$$\rho_m^{fG_-} = -\frac{p_d}{2} + \sqrt{\left(\frac{p_d}{2}\right)^2 + q_d}\,, \tag{3.23}$$

$$\rho_m^{fG_+} = \frac{p_d}{2} + \sqrt{\left(\frac{p_d}{2}\right)^2 + q_d}\,, \tag{3.24}$$

$$\text{with} \quad p_d = \frac{\phi}{1-\phi}\rho_m^{sG_{fc}}\frac{z^{fc}}{z^{fG_-}}, \quad q_d = \left(\frac{\rho_m^{F_s}}{\psi^{\pm}}\right)^2 \frac{z^{F_-}}{z^{F_+}}\frac{z^{fG_+}}{z^{fG_-}}\,,$$

$$\psi^{\pm} = \frac{\gamma^{fG_\pm}}{\gamma^{F_\pm}} = \left(\frac{\gamma^{fG_+}\gamma^{fG_-}}{\gamma^{F_+}\gamma^{F_-}}\right)^{1/2}. \tag{3.25}$$

For reasons of convenience, the average activity coefficient $\gamma^{\alpha_\pm}$ has been introduced, whereas $\psi^{\pm}$ is defined in analogy to ψ^{w} (3.19) and accounts here for the activity of mobile ions in both phases, i. e. it is the cumulated activity coefficient of ions.

Remark on salt concentration: The salt concentration is generally defined through

$$\rho^{\alpha_s} = \rho^{\alpha_+} + \rho^{\alpha_-}\,, \tag{3.26}$$

while in the absence of fixed charges, the charge-neutrality imposes the restriction

$$z^{\alpha_-}\rho_m^{\alpha_-} + z^{\alpha_+}\rho_m^{\alpha_+} = 0\,. \tag{3.27}$$

A conversion to molar concentrations yields finally to the molar salt concentration for an arbitrary salt

$$\rho_m^{\alpha_s} = \frac{M_m^- + \frac{|z^{\alpha_-}|}{z^{\alpha_+}}M_m^+}{M_m^s}\rho_m^{\alpha_-}\,, \tag{3.28}$$

where the molar mass of salt is given by $M_m^s = M_m^- + M_m^+$.

3.3.2 Mixing contribution

In the early 1940s, Flory [53] and Huggins [71] developed independently mathematical models based on statistical thermodynamics to derive the free energy due to mixing in polymer gels. The theory is later termed the Flory-Huggins theory and is widely used in polymer chemistry. The Gibbs free energy of mixing polymer chains and absorbed solution is formally given by

$$\Delta G_{m,mix}^G = G_m^G - G_m^{sG} - G_m^{fG}\,. \tag{3.29}$$

Starting point of the derivation is then the reformulation of the free mixing energy to

$$\Delta G_{m,mix}^G = \Delta H_{m,mix}^G - T\Delta S_{m,mix}^G\,, \tag{3.30}$$

by using the Legendre transformation. Herein, $\Delta H_{m,mix}^G$ and $\Delta S_{m,mix}^G$ are the change in enthalpie and entropy of the hydrogel due to mixing, respectively. Based on a lattice model, which describes the mixing of polymer chains and solvent molecules (cf.

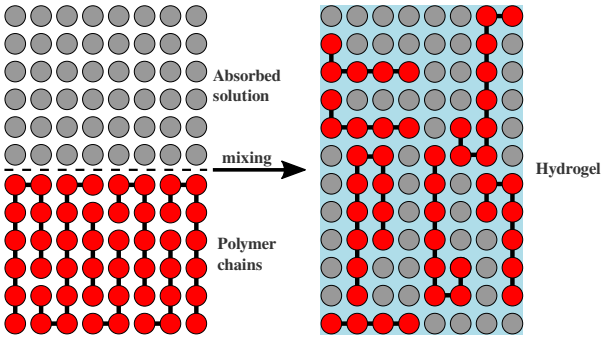

Figure 3.4: *Schematic sketch of the lattice model based on the Flory-Huggins theory. In the hydrogel the absorbed solution and the polymer chains are mixed.*

Figure 3.4), expressions for $\Delta H^G_{m,mix}$ and $\Delta S^G_{m,mix}$ are derived. Each lattice site is either occupied by a monomer molecule or a solvent one, such that the total number of lattice sites reads $N^f_m + r_m N^p_m$. N^f_m denotes the number of solvent molecules, while N^p_m is the number of polymer molecules and r_m is the number of monomers per polymer chain. According to the lattice model, the volume fractions for the solvent ϕ^f and the polymer ϕ^p are introduced through

$$\phi^f = \frac{n^f_m}{n^f_m + r_m\, n^p_m} \quad \text{and} \quad \phi^p = \frac{r_m\, n^p_m}{n^f_m + r_m\, n^p_m}\,, \tag{3.31}$$

where n^f_m, n^p_m denote the amount of substance in moles for the solvent and polymer, respectively.[1] Furthermore, the Avogadro constant N_A is used to convert the number of molecules to the amount of substance by $n^j_m = N^j_m / N_A$.

Without given further details concerning the derivation, the free energy of mixing is derived by applying concepts of statistical thermodynamics finally to

$$\Delta G^G_{m,mix} = RT(n^f_m \ln(\phi^f) + n^p_m \ln(\phi^p) + n^f_m \phi^p \chi)\,. \tag{3.32}$$

Herein, χ is termed the Flory-Huggins interaction parameter [53, 55, 56, 71]. Note that Safronov *et al.* [121] studied the Flory-Huggins interaction parameter for weakly cross-linked hydrogels with respect to the degree of ionization of the polymer network. By assuming dilute aqueous solutions, the amount of substance of absorbed solution is approximated through $n^f_m \approx n^{G_w}_m$, such that chemical potential of absorbed water becomes

$$\Delta \mu^{G_w}_{m,mix} = \frac{\partial \Delta G^G_{m,mix}}{\partial n^{G_w}_m}\bigg|_{n^p_m} = RT(\ln(1-\phi) + \phi + \chi\,\phi^2)\,. \tag{3.33}$$

[1] Note that the volume fractions of solution ϕ^f and polymer ϕ^p are here derived from the lattice model and not from a continuum model. The results obtained in polymer chemistry, i. e. the chemical potential differences, will be later carefully correlated to the continuum scale.

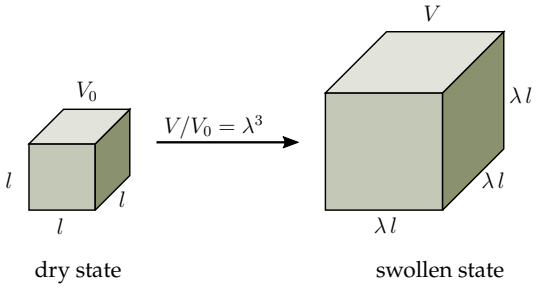

Figure 3.5: *Isotropic hydrogel expansion.*

In the derivation, high degrees of polymerization ($r_m \to \infty$) have been assumed [159]. Furthermore, the polymer volume fraction ϕ^p derived from the lattice model has been substituted by ϕ, the continuum-based definition (3.2).

3.3.3 Elastic contribution

From Figure 3.1 can be deduced that due to the expansion of the network, the polymer chains are forced to orientate in a rather parallel fashion, which in turn reduces the configuration entropy. Since the polymer network tends to maximize its entropy, elastic reset forces are induced by the volumetric expansion. In the pioneering works by Flory & Rehner [55, 56], the structural entropy elasticity was derived from an elementary tetrahedral cell of a three-dimensional cross-linked network. Note that in the derivation of the entropy elasticity, the notation from the lattice model will be used.

In case of unrestricted, isotropic swelling (cf. Figure 3.5), the principal stretches of the hydrogel λ_i are equal in each direction, such that

$$\lambda_1 = \lambda_2 = \lambda_3 = \left(\frac{\mathrm{d}v^G}{\mathrm{d}v_0^G}\right)^{1/3}, \tag{3.34}$$

where $\mathrm{d}v_0^G$ is the initial, dry volume of the hydrogel, i. e. $\mathrm{d}v^G/\mathrm{d}v_0^G = (\phi^p)^{-1}$. The elastic part of the Gibbs free energy due to isotropic volumetric expansion is given in its simplest form by

$$\Delta G^G_{m,elast} = \frac{3}{2} R T n^p_m \left((\phi^p)^{-2/3} - 1\right). \tag{3.35}$$

In the derivation, affine network deformations have been assumed [160]. Note that Cai & Suo [36] used a more sophisticated elastic energy function based on Flory [54] to model anisotropic deformation during swelling. Exploiting again the approximation for dilute aqueous solutions, i. e. $n^f_m \approx n^{G_w}_m$, the chemical potential difference due to entropy elasticity is formally derived by

$$\Delta\mu^{G_w}_{m,elast} = \frac{\partial \Delta G^G_{m,elast}}{\partial n^{G_w}_m} = \frac{\partial \Delta G^G_{m,elast}}{\partial \phi^p}\frac{\partial \phi^p}{\partial n^{G_w}_m} \quad \text{with} \quad \frac{\partial \phi^p}{\partial n^{G_w}_m} \approx -\frac{(\phi^p)^2 \tilde{V}^w_m}{\mathrm{d}v_0^G}. \tag{3.36}$$

Finally, the continuum-based chemical potential is obtained through

$$\Delta\mu_{elast}^{G_w} = RT\tilde{V}_m^w \nu\, \phi^{1/3}\,. \tag{3.37}$$

Herein, the polymer volume fraction ϕ^p has been again substituted by ϕ and the intrinsic cross-linking density of the hydrogel network ν has been introduced.

Chapter 4:
Constitutive setting of multi-phase materials subjected to internal mass exchange

The decomposition of the mixture model into phases and species is a crucial step, which depends on the microstructure of the material but also on the processes under consideration. To discuss a decomposition against the background of the HMT, a meaningful separation into phases and species is necessary. In this modeling approach, a generic porous material is presented, while the pore space is simultaneously filled with a hydrogel and an aqueous pore liquid. In the previous chapter, the relevant processes occurring in charged hydrated polymers have been discussed and will also be taken into account in the following.

4.1 Adaption of the general Hybrid Mixture Theory

4.1.1 Composition of the mixture

Before the specific decomposition is described in detail, it should mentioned that the decomposition into phases is performed across three (phase) levels. By increasing the phase level, the complexity of the model rises, which is in turn necessary to describe more sophisticated processes, for instance inter-phase mass exchange. In Figure 4.1 a possible decomposition of the overall mixture is presented. The processes in the material, which are taken into consideration are summarized as follows:

- flow of a polymer solution φ^L through a porous skeleton φ^S (**phase level I**),
- polymer solution composed of fluidized polymer gel φ^G and pore liquid φ^F (**phase level II**),
- solid skeleton represented as conjunction of an intrinsic granular solid φ^K and attached polymer gel φ^A (**phase level II**),
- attached and fluidized polymer gel both treated as hydrogel, which are therefore composed of polymer chains (attached φ^{sA}, free φ^{sG}) and absorbed solution (attached φ^{fA}, free φ^{fG}) (**phase level III**),
- polymer chains, absorbed solution and pore liquid are (miscible) multi-species phases of charged and non-charged species φ^{α_j} (**species level**).

The overall mixture can be viewed as a bi-phasic material on **phase level I** consisting of a solid skeleton φ^S and a polymer solution φ^L. A continuum model on this scale is able to model hydrodynamic fluid flow through non-reactive porous media. On **phase level**

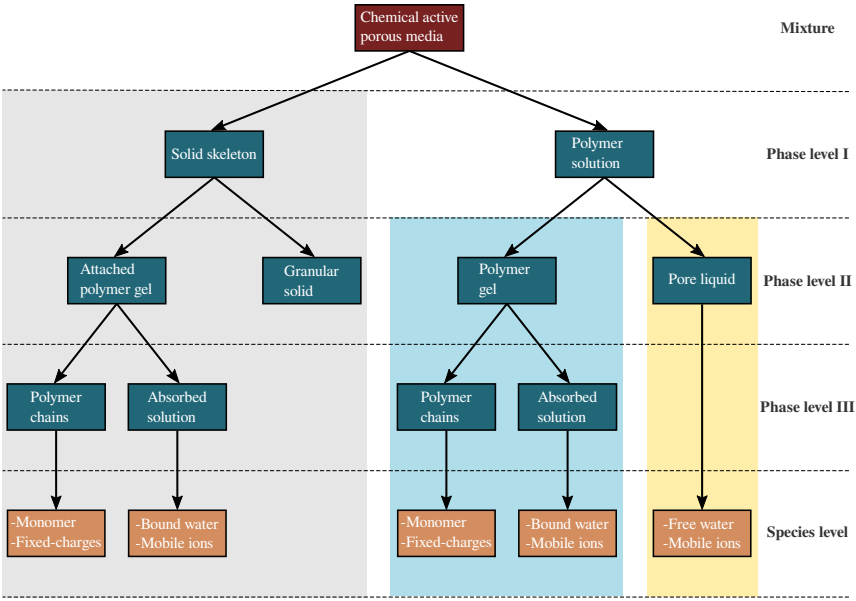

Figure 4.1: *Decomposition of the chemical active porous media model.*

II, it is on the one hand assumed that the polymer solution consists of polymer gel φ^G and pore liquid φ^F, while on the other hand, polymer attachment to the solid skeleton is incorporated. To this end, the solid skeleton is no longer a chemical inert phase, it rather consists of a granular solid φ^K and attached polymer gel φ^A. The continuum model based on **phase level II** is able to describe complex reversible and irreversible polymer attachment processes in porous media. Finally, **phase level III** is invented to account for the structure of hydrogels. The polymer gel, attached to the solid skeleton or as a part of the polymer solution, is individually decomposed into polymer chains and absorbed solution. The definition of three phase levels has been performed with respect to the expected material behavior and allows a clear representation of the complex material. Further model simplifications will be performed in a systematic way throughout this manuscript in order to focus on specific constitutive implications of the model.

4.1.2 Specific kinematic relations

One of the most fundamental concepts of the continuum mixture theory is that each phase exhibits its own motion function $\boldsymbol{\chi}_\alpha$, cf. chapter 2.2. However, according to the expected material behavior, it is assumed that the solid skeleton φ^S, the polymer gel φ^G and the pore liquid φ^F are the only kinematically independent phases and are termed *primary phases*. In contrast, the *subordinated phases* exhibit respectively the motion func-

tion of its primary phase. Following this idea, the colored rectangles in Figure 4.1 are grouping phases with the same motion function. For reasons of convenience, the model decomposition into phases is given by:

- mixture: $\varphi = \varphi^S \cup \varphi^L$
- polymer solution: $\varphi^L = \varphi^F \cup \varphi^G$
- solid skeleton: $\varphi^S = \varphi^K \cup \varphi^A$
- polymer gel (free): $\varphi^G = \varphi^{fG} \cup \varphi^{sG}$
- polymer gel (attached): $\varphi^A = \varphi^{fA} \cup \varphi^{sA}$

The model composition in terms of volume fractions is visualized in Figure 4.2. The inner circle represents phase level I, while II and III are represented by the circular rings, respectively. With the aid of the graphical representation, the saturation condition for the mixture can be easily written to

$$\begin{aligned} \sum_{\alpha} n^{\alpha} &= n^S + n^L = n^K + n^A + n^G + n^F \\ &= n^K + n^{fA} + n^{sA} + n^{fG} + n^{sG} + n^F = 1 \,. \end{aligned} \tag{4.1}$$

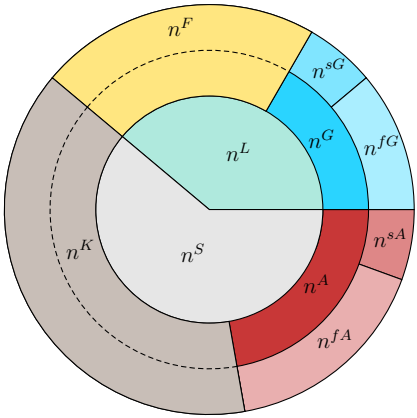

Figure 4.2: *Volume fractions of the mixture model.*

In addition, the multi-species decomposition follows from the previously introduced microstructure of charged hydrogels (cf. chapter 3.1) to:

- pore liquid: $\varphi^F = \varphi^{F_w} \cup \varphi^{F_+} \cup \varphi^{F_-}$
- polymer chains (free): $\varphi^{sG} = \varphi^{sG_{fc}} \cup \varphi^{sG_m}$

- absorbed solution (free): $\varphi^{fG} = \varphi^{fG_w} \cup \varphi^{fG_+} \cup \varphi^{fG_-}$
- polymer chains (attached): $\varphi^{sA} = \varphi^{sA_{fc}} \cup \varphi^{sA_m}$
- absorbed solution (attached): $\varphi^{fA} = \varphi^{fA_w} \cup \varphi^{fA_+} \cup \varphi^{fA_-}$

4.1.3 Inter-phase mass exchange

Chemical reactions among species within the same phase are a priori neglected from the model, such that intra-phase mass exchange vanishes, i. e. $\hat{\rho}_a^{\alpha_j} = 0$. For the material under consideration, inter-phase mass exchange occurs among the solid skeleton φ^S, the polymer gel φ^G and the pore liquid φ^F. On the species level, mass is by assumption exchanged exclusively between the same species. Herein, $\hat{\rho}_\beta^{\alpha_j}$ denotes the mass gain of φ^{α_j} due to the transfer from φ^β. As a consequence, the same amount of mass is lost from φ^{β_j} due to the exchange with φ^α. To this end, the inter-phase mass exchange is restricted through $\hat{\rho}_\beta^{\alpha_j} = -\hat{\rho}_\alpha^{\beta_j}$. In addition, mass exchange terms on the species level can be further subdivided into

$$\hat{\rho}^{S_j} = \hat{\rho}_G^{S_j} + \hat{\rho}_F^{S_j}\,, \quad \hat{\rho}^{G_j} = \hat{\rho}_F^{G_j} - \hat{\rho}_G^{S_j}\,, \quad \hat{\rho}^{F_j} = -\hat{\rho}_F^{G_j} - \hat{\rho}_F^{S_j}\,, \tag{4.2}$$

where (2.31) has been used in the derivation. From a physical point of view, three processes with respect to the inter-phase mass exchange terms are distinguished:

1. absorption and desorption of pore liquid by the free hydrogel:

$$\hat{\rho}_F^G = \hat{\rho}_F^{fG}\,, \tag{4.3}$$

2. absorption and desorption of pore liquid by the attached hydrogel:

$$\hat{\rho}_F^S = \hat{\rho}_F^A = \hat{\rho}_F^{fA}\,, \tag{4.4}$$

3. attachment and detachment of fluidized hydrogel to the solid skeleton:

$$\hat{\rho}_G^S = \hat{\rho}_{sG}^{sA} + \hat{\rho}_{fG}^{fA} = \hat{\rho}_G^A\,. \tag{4.5}$$

The internal mass exchange is finally governed by $\hat{\rho}_F^{fG_j}$, $\hat{\rho}_F^{fA_j}$ and $\hat{\rho}_G^A$, while from a physical point of view, the nature of the density production $\hat{\rho}_F^{fA}$ is similar to $\hat{\rho}_F^{fG}$.

4.1.4 Suitable quantities expressing mass exchange

For the purpose of the constitutive modeling of polymer capture mechanisms in porous media, the amount of attached polymer is defined with regard to the intrinsic skeleton as

$$W = \frac{\mathrm{d}m^A}{\mathrm{d}m^K} = \frac{\rho^A}{\rho^K}\,. \tag{4.6}$$

The time derivative with respect to the solid calculates formally to

$$(W)'_S = \frac{(\rho^A)'_S \rho^K - \rho^A (\rho^K)'_S}{(\rho^K)^2} = \frac{\hat{\rho}^A}{\rho^K}\,, \tag{4.7}$$

where the mass balance equation (2.33) has been used in the derivation. The total attachment rate (4.7) will be later used for the exploitation of the entropy inequality. Herein, $\hat{\rho}^A$ denotes the net density production to the solid skeleton and can be therefore divided into $\hat{\rho}^A = \hat{\rho}^A_G + \hat{\rho}^A_F$.

By assuming that the polymer gel is treated as a hydrogel, the (mass-based) degree of swelling measures the current state of the hydrogel, cf. (3.1). Following this idea, the degree of swelling can be independently introduced here for the free and attached hydrogel respectively through

$$q_{free} = \frac{\mathrm{d}m^G}{\mathrm{d}m^{sG}} = \frac{\rho^G}{\rho^{sG}} \quad \text{and} \quad q_{att} = \frac{\mathrm{d}m^A}{\mathrm{d}m^{sA}} = \frac{\rho^A}{\rho^{sA}}\,. \tag{4.8}$$

The time derivatives are expressed by

$$(q_{free})'_G = \frac{(\rho^G)'_G \rho^{sG} - \rho^G (\rho^{sG})'_G}{(\rho^{sG})^2} = \frac{\hat{\rho}^{fG}_F}{\rho^{sG}}\,, \tag{4.9a}$$

$$(q_{att})'_S = \frac{(\rho^A)'_S \rho^{sA} - \rho^A (\rho^{sA})'_S}{(\rho^{sA})^2} = \frac{\hat{\rho}^{fA}_F}{\rho^{sA}}\,, \tag{4.9b}$$

where use has been made of

$$\hat{\rho}^{fA}_G = -\hat{\rho}^{fG}_S \quad \text{and} \quad \hat{\rho}^{sA}_G = -\hat{\rho}^{sG}_S\,. \tag{4.10}$$

The time rate of the degrees of swelling (4.9a) and (4.9b) exclusively changes due to liquid absorption/desorption as expected.

The attached and fluidized hydrogels are in contact with the same pore liquid, such that the degree of swelling is assumed to be equal, i. e. $q_{att} = q_{free}$. As a consequence, the mass supply rates in (4.9a) and (4.9b) are than related through

$$\hat{\rho}^{fA}_F = \frac{\rho^{sA}}{\rho^{sG}} \hat{\rho}^{fG}_F\,. \tag{4.11}$$

Furthermore assuming $\hat{\rho}^{fG}_F \approx \hat{\rho}^{fG_w}_F$, leads to

$$(q_{free})'_G = \frac{\hat{\rho}^{fG_w}_F}{\rho^{sGR}} \quad \text{and} \quad (q_{att})'_S = \frac{\hat{\rho}^{fA_w}_F}{\rho^{sAR}}\,. \tag{4.12}$$

4.1.5 Helmholtz free energy dependencies

Based on the expected material behavior, dependencies of the Helmholtz free energies are in mixture theories usually postulated for each phase. According to the proposed

model decomposition, an admissible split of the mixture's Helmholtz free energy is given by

$$\rho\Psi = \rho^S\Psi^S + \rho^G\Psi^G + \rho^F\Psi^F\,, \tag{4.13}$$

where the free energies Ψ^S, Ψ^G and Ψ^F correspond to the kinematically independent phases. In addition, the free energies can be further decomposed to

$$\rho^S\Psi^S = \underbrace{\rho^{sA}\Psi^{sA} + \rho^{fA}\Psi^{fA}}_{=\rho^A\Psi^A} + \rho^K\Psi^K\,, \tag{4.14}$$

$$\rho^G\Psi^G = \underbrace{\rho^{sG}\Psi^{sG} + \rho^{fG}\Psi^{fG}}_{=\rho^G\Psi^G}\,. \tag{4.15}$$

In the derivation of the Helmholtz free energies, material incompressibility of each phase is assumed, such that the intrinsic phase density is constant, i. e. $(\rho^{\alpha R})'_\alpha = 0$. The Helmholtz free energy of the liquid solution φ^F depends on its chemical composition through

$$\Psi^F = \Psi^F(c^{F_1}, \ldots, c^{F_{N-1}})\,. \tag{4.16}$$

Note in passing that the composition is fully described by $N-1$ mass fractions.

From a chemical point of view, the absorbed solution φ^{fG} is similar to the pore liquid φ^F, such that its free Helmholtz energy dependencies are given by

$$\Psi^{fG} = \Psi^{fG}(c^{fG_1}, \ldots, c^{fG_{N-1}})\,. \tag{4.17}$$

In addition, the influence of the cross-linked polymer network is captured separately in

$$\Psi^{sG} = \Psi^{sG}(q_{free})\,, \tag{4.18}$$

while q_{free} accounts for the current state of swelling, i. e. the amount of absorbed solution. Finally, the Helmholtz free energy of the gel is given by

$$\Psi^G = \Psi^G(c^{fG_1}, \ldots, c^{fG_{N-1}}, q_{free})\,. \tag{4.19}$$

In the absence of any attached polymer gel, the free energy of the elastic granular solid matrix depends exclusively on the solid deformation and reads

$$\Psi^K_{(1)} = \Psi^K_{(1)}(\mathbf{E}_S)\,, \tag{4.20}$$

where the Green-Lagrange strain tensor $\mathbf{E}_S = 1/2(\mathbf{F}_S^T \cdot \mathbf{F}_S - \mathbf{I})$ has been chosen as an appropriate strain measure. However, in the case of polymer capture onto the granular solid surface, the additional free energy term

$$\Psi^K_{(2)} = \Psi^K_{(2)}(W) \tag{4.21}$$

is proposed, which leads to $\Psi^K = \Psi^K_{(1)} + \Psi^K_{(2)}$. By finally assuming that the attached polymer gel is a charged hydrogel, the Helmholtz free energy of the attached polymer gel is composed of Ψ^{fA} and Ψ^{sA} in analogy to (4.17) and (4.18) through

$$\Psi^{fA} = \Psi^{fA}(c^{fA_1}, \ldots, c^{fA_{N-1}}) \quad \text{and} \quad \Psi^{sA} = \Psi^{sA}(q_{att})\,. \tag{4.22}$$

The attached polymer exhibits the same motion as the intrinsic solid skeleton, however, it is a priori assumed that the induced partial stress tensor $\mathbf{T}^A$ has an insignificant contribution to the mixture's total stress state. This assumption is justified by expecting thin polymer adsorption films on the solid skeleton.

Taking all contributions into consideration, the dependencies of the Helmholtz free energy Ψ^S can be written as

$$\Psi^S = \Psi^S(\mathbf{E}_S, W, c^{fA_1}, \dots, c^{fA_{N-1}}, q_{att})\,. \tag{4.23}$$

Next, total differentials of the Helmholtz free energies are necessary for the investigation of the entropy inequality and are given in the following:

$$\begin{aligned}
\rho^S(\Psi^S)'_S &= \rho^K(\Psi^K)'_S + \rho^{fA}(\Psi^{fA})'_S + \rho^{sA}(\Psi^{sA})'_S \\
&= \rho^K\Big(\mathbf{F}_S \cdot \frac{\partial \Psi^K}{\partial \mathbf{E}_S} \cdot (\mathbf{F}_S)^T : \mathbf{D}_S + \frac{\partial \Psi^K}{\partial W}\frac{\hat{\rho}^A}{\rho^K}\Big) \\
&\quad + \rho^{fA}\Big(\frac{\partial \Psi^{fA}}{\partial c^{fA_1}}(c^{fA_1})'_S + \dots + \frac{\partial \Psi^{fA}}{\partial c^{fA_{N-1}}}(c^{fA_{N-1}})'_S\Big) \\
&\quad + \rho^{sA}\Big(\frac{\partial \Psi^{sA}}{\partial q_{att}}\frac{\hat{\rho}_F^{fA}}{\rho^{sA}}\Big)\,,
\end{aligned} \tag{4.24}$$

$$\rho^F(\Psi^F)'_F = \rho^F\Big(\frac{\partial \Psi^F}{\partial c^{F_1}}(c^{F_1})'_F + \dots + \frac{\partial \Psi^F}{\partial c^{F_{N-1}}}(c^{F_{N-1}})'_F\Big)\,, \tag{4.25}$$

$$\begin{aligned}
\rho^G(\Psi^G)'_G &= \rho^{fG}(\Psi^{fG})'_G + \rho^{sG}(\Psi^{sG})'_G \\
&= \rho^{fG}\Big(\frac{\partial \Psi^{fG}}{\partial c^{fG_1}}(c^{fG_1})'_G + \dots + \frac{\partial \Psi^{fG}}{\partial c^{fG_{N-1}}}(c^{fG_{N-1}})'_G\Big) \\
&\quad + \rho^{sG}\Big(\frac{\partial \Psi^{sG}}{\partial q_{free}}\frac{\hat{\rho}_F^{fG}}{\rho^{sG}}\Big)\,.
\end{aligned} \tag{4.26}$$

In the derivation of (4.24), the derivative related to the Green-Lagrange strain tensor $\mathbf{E}_S$ has been reformulated to

$$\rho^K \frac{\partial \Psi^K}{\partial \mathbf{E}_S} : (\mathbf{E}_S)'_S = \rho^S \mathbf{F}_S \cdot \frac{\partial \Psi^K}{\partial \mathbf{E}_S} \cdot (\mathbf{F}_S)^T : \mathbf{D}_S\,.$$

In addition, use has been made of (4.7), (4.9b) and (4.9a) to rewrite the time derivatives of W, q_{att} and q_{free} in a more suitable way for the exploitation of the entropy inequality.

4.2 Specific entropy inequality

The dissipation inequality of the specific multi-phase and multi-species model is deduced from the general dissipation inequality (2.69) and is given by

$$\begin{aligned} D = \sum_{\alpha} \Big\{ & - \rho^{\alpha} (\Psi^{\alpha})'_{\alpha} \\ & + \mathbf{D}_{\alpha} : \Big[\mathbf{T}^{\alpha} + \sum_{j} n^{\alpha} \rho^{\alpha_j} \mathbf{w}_{\alpha_j} \otimes \mathbf{w}_{\alpha_j} \Big] \\ & + \sum_{j} \operatorname{grad} \mathbf{w}_{\alpha_j} : \Big[\mathbf{T}^{\alpha_j} - n^{\alpha} \rho^{\alpha_j} \Psi^{\alpha_j} \mathbf{I} \Big] \\ & - \sum_{j} \mathbf{w}_{\alpha_j} \cdot \Big[\operatorname{grad} (n^{\alpha} \rho^{\alpha_j} \Psi^{\alpha_j}) + \hat{\mathbf{p}}^{\alpha_j} \Big] \\ & - \mathbf{v}_{\alpha S} \cdot \hat{\mathbf{p}}^{\alpha} \\ & - \sum_{j} \hat{\rho}^{\alpha_j} \Big[(\Psi^{\alpha} + \frac{1}{2} (\mathbf{v}_{\alpha S} \cdot \mathbf{v}_{\alpha S} + \mathbf{w}_{\alpha_j} \cdot \mathbf{w}_{\alpha_j})) - (\Psi^{S} + \frac{1}{2} \mathbf{w}_{S_j} \cdot \mathbf{w}_{S_j}) \Big] \Big\} \geq 0 \,, \end{aligned} \tag{4.27}$$

where the (direct) momentum exchange terms have been merged according to

$$\hat{\mathbf{p}}^{\alpha_j} = \hat{\mathbf{p}}_a^{\alpha_j} + \hat{\mathbf{p}}_r^{\alpha_j} \,; \qquad \hat{\mathbf{p}}^{\alpha} = \hat{\mathbf{p}}_r^{\alpha_j} \,. \tag{4.28}$$

The time rate of the algebraic saturation condition (2.4) is given by

$$\sum_{\alpha} (n^{\alpha})'_S = 0 = (n^G)'_G + (n^S)'_S + (n^F)'_F - \operatorname{grad} n^G \cdot \mathbf{v}_{GS} - \operatorname{grad} n^F \cdot \mathbf{v}_{FS} \tag{4.29}$$

and will be added in connection with the Lagrange multiplier p to the entropy inequality. In analogy, the time rate of the charge-neutrality condition for each phase (2.48) is expressed through

$$\sum_{j} (n^{\alpha} \rho_e^{\alpha_j})'_S = 0 = -\operatorname{div} \Big(\sum_{j} n^{\alpha} \rho_e^{\alpha_j} \mathbf{w}_{\alpha_j} \Big) + \sum_{j} \hat{\rho}_e^{\alpha_j} \tag{4.30}$$

and imposes an additional restriction on the system. Finally, the charge balances for each individual phase will also be added to the entropy inequality through the Lagrange multiplier λ_e^{α}. Note that the charge neutrality of the overall medium could be additionally used to restrict the entropy inequality, which is not done here since the overall charge neutrality is just a combination of the charge neutrality of the individual phases. Thus, adding a redundant restriction does not lead to more physical insights towards the model. The Lagrange multipliers p and λ_e^{α} cannot be identified by the exploitation of the entropy inequality but can be calculated from the boundary conditions. The extended entropy inequality is divided into

$$\bar{D} = D + D_{\lambda} \,, \tag{4.31}$$

where the second part D_λ contains the added restrictions and corresponding Lagrange multipliers:

$$\begin{aligned} D_\lambda = \sum_\alpha \Big\{ & \lambda^\alpha \Big[\rho^{\alpha R} (n^\alpha)'_\alpha + n^\alpha \rho^{\alpha R} \mathrm{div}\,(\mathbf{v}_\alpha) - \hat{\rho}^\alpha \Big] \\ & + \sum_j \lambda^{\alpha_j} \Big[n^\alpha \rho^{\alpha R} (c^{\alpha_j})'_\alpha + \mathrm{div}\,(n^\alpha \rho^{\alpha_j} \mathbf{w}_{\alpha_j}) - \hat{\rho}^{\alpha_j} + c^{\alpha_j} \hat{\rho}^\alpha \Big] \\ & + \sum_j \mathbf{\Lambda}^\alpha_r : \Big[\mathrm{grad}\,(n^\alpha \rho^{\alpha_j} \mathbf{w}_{\alpha_j}) \Big] \\ & - p \Big[(n^\alpha)'_\alpha - \mathrm{grad}\, n^\alpha \cdot \mathbf{v}_\alpha s \Big] \\ & + \sum_j \lambda^\alpha_e \frac{z^{\alpha_j} F}{M^j_m} \Big[\mathrm{div}\left(n^\alpha \rho^{\alpha_j} \mathbf{w}_{\alpha_j} \right) - \hat{\rho}^{\alpha_j} \Big] \Big\} . \end{aligned} \tag{4.32}$$

The first and second row in (4.32) accounting for the mass balances of the (incompressible) phases and for the concentration balances, respectively. Since the mass fractions are coupled by the constraint (2.6), $N-1$ concentration balances per phase can be formulated independently. In addition, the divergence of the constraint related to the diffusive velocities (2.23) is used in the following row. Finally, the material time derivative of the saturation condition (2.4) and the individual charge-neutrality of each phase are weakly enforced. It is anticipated that the Lagrange multipliers λ^α_e and p can not be identified by exploiting the entropy inequality, cf. [2, 76, 90]. In this work, the specific dissipation inequality will be evaluated according to the Liu-Müller method [94, 95].

4.3 Evaluation of the entropy inequality

The entropy inequality $\bar{D}$ can be divided into a non-dissipative $\bar{D}_{eq}$ and a dissipative contribution $\bar{D}_{dis}$, whereas the first one has to vanish in equilibrium and will be used to identify the Lagrange multipliers and equilibrium variables. The equilibrium contributions are summarized to

$$\begin{aligned} \bar{D}_{eq} = \sum_\alpha \Big\{ & (n^\alpha)'_\alpha [-p + \rho^{\alpha R} \lambda^\alpha] \\ & + \mathbf{D}_\alpha : \Big[\mathbf{T}^\alpha + \sum_j n^\alpha \rho^{\alpha_j} \mathbf{w}_{\alpha_j} \otimes \mathbf{w}_{\alpha_j} + n^\alpha \rho^{\alpha R} \lambda^\alpha \mathbf{I} - n^\alpha \rho^{\alpha R} \mathbf{F}_\alpha \cdot \frac{\partial \Psi^\alpha}{\partial \mathbf{E}_\alpha} \cdot \mathbf{F}^T_\alpha \Big] \\ & + \sum_j (c^{\alpha_j})'_\alpha \Big[n^\alpha \rho^{\alpha R} \lambda^{\alpha_j} - n^\alpha \rho^{\alpha R} \frac{\partial \Psi^\alpha}{\partial c^{\alpha_j}} \Big] \\ & + \sum_j \mathrm{grad}\, \mathbf{w}_{\alpha_j} : \Big[\mathbf{T}^{\alpha_j} - n^\alpha \rho^{\alpha_j} \mathbf{I} \Psi^{\alpha_j} + \lambda^{\alpha_j} \mathbf{I} + \mathbf{\Lambda}^\alpha_r + \lambda^\alpha_e \frac{z^{\alpha_j} F}{M^j_m} \mathbf{I} \Big] \Big\} = 0 . \end{aligned} \tag{4.33}$$

4.3.1 Equilibrium contribution

The exploitation of the entropy inequality according to the Liu-Müller method [94, 95] leads to constitutive restrictions, which are derived here for equilibrium as well as near equilibrium conditions. Starting with the equilibrium conditions, (4.33) is evaluated according to the following structure

$$\sum_{\alpha} \Big\{ (n^{\alpha})'_{\alpha} \underbrace{[\dots]}_{=0} + \mathbf{D}_{\alpha} : \underbrace{[\dots]}_{=\mathbf{0}} + \sum_{j} (c^{\alpha_j})'_{\alpha} \underbrace{[\dots]}_{=0} + \sum_{j} \operatorname{grad} \mathbf{w}_{\alpha_j} : \underbrace{[\dots]}_{=\mathbf{0}} \Big\} = 0 \,. \tag{4.34}$$

The derivative of the Helmholtz free energies with respect to the mass fraction of a species is defined as *relative* chemical potential and given by

$$\lambda^{\alpha_j} = \tilde{\mu}^{\alpha_j} := \frac{\partial \Psi^{\alpha}}{\partial c^{\alpha_j}} \,. \tag{4.35}$$

Bennethum *et al.* [24] emphasized that mass fractions in mixture theory are intensive state variables and therefore coupled through the constraint (2.6). As the name suggests, relative chemical potentials in a mixture refer to a reference chemical potential μ^{α_N}. Thus, the following relation holds

$$\tilde{\mu}^{\alpha_j} = \mu^{\alpha_j} - \mu^{\alpha_N} \,, \tag{4.36}$$

where μ^{α_j} denotes the *absolute* chemical potential of φ^{α_j}. Note that the chemical potential of the N-th species is arbitrary set as the reference chemical potential.

Here, in a fully incompressible mixture, the Lagrange multiplier p appears as an additional unknown, which needs to be calculated from the boundary conditions [49]. Therefore, the Lagrange multipliers λ^{α} are identified to

$$\lambda^{\alpha} = \frac{p}{\rho^{\alpha R}} \,. \tag{4.37}$$

Furthermore, the partial stress tensors compute to

$$\mathbf{T}^{\alpha} = -n^{\alpha} p^{\alpha} \mathbf{I} - \mathbf{T}^{\alpha}_{R} + \mathbf{T}^{\alpha}_{E} \,, \tag{4.38}$$

where the effective partial stress tensor $\mathbf{T}^{\alpha}_{E}$, the Reynolds stress tensor $\mathbf{T}^{\alpha}_{R}$ and partial pressure p^{α} are respectively given by

$$\mathbf{T}^{\alpha}_{E} = \begin{cases} \rho^{S} \mathbf{F}_{S} \cdot \frac{\partial \Psi^{S}}{\partial \mathbf{E}_{S}} \cdot (\mathbf{F}_{S})^{T} & \text{if } \alpha = S \\ \mathbf{0} & \text{if } \alpha \neq S \end{cases} , \tag{4.39}$$

$$\mathbf{T}^{\alpha}_{R} = \sum_{j} n^{\alpha} \rho^{\alpha_j} \mathbf{w}_{\alpha_j} \otimes \mathbf{w}_{\alpha_j} \,, \tag{4.40}$$

$$p^{\alpha} = \lambda^{\alpha} \rho^{\alpha R} = p \,. \tag{4.41}$$

In fluid mechanics, a similar expression to $\mathbf{T}^{\alpha}_{R}$ occurs under the investigation of turbulent flow in single-phase media; the diffusion velocities $\mathbf{w}_{\alpha_j}$ are comparable to the

deviation from the mean velocity of the (turbulent) flow [49, 119]. Since the diffusion velocities are relatively small in many engineering applications, the contribution $\mathbf{T}_R^\alpha$ to the partial stress is usually negligible. Due to the assumed constitutive dependencies in the Helmholtz energies (4.16) and (4.19), the effective stress tensors for the liquid and the fluidized polymer phase vanish, i. e. $\mathbf{T}_E^F = \mathbf{T}_E^G = \mathbf{0}$.

The last term in the entropy inequality leads to the identification of the partial stress tensors in terms of the species by

$$\mathbf{T}^{\alpha_j} = n^\alpha \rho^{\alpha_j} \mathbf{I}\Big(\Psi^{\alpha_j} - \lambda^{\alpha_j} - \lambda_e^\alpha \frac{z^{\alpha_j} F}{M_m^j}\Big) - n^\alpha \rho^{\alpha_j} \mathbf{\Lambda}_r^\alpha \,. \tag{4.42}$$

The tensor-valued Lagrange multiplier $\mathbf{\Lambda}_r^\alpha$ can be identified by summing (4.42) over the species, such that the following relationship occurs:

$$\mathbf{\Lambda}_r^\alpha = \Big(\Psi^\alpha - \sum_j c^{\alpha_j} \lambda^{\alpha_j}\Big)\mathbf{I} - \frac{1}{n^\alpha \rho^{\alpha R}} \mathbf{T}^\alpha \tag{4.43}$$

$$= \Big(\Psi^\alpha + \frac{p^\alpha}{\rho^{\alpha R}} - \sum_j c^{\alpha_j} \lambda^{\alpha_j}\Big)\mathbf{I} - \frac{1}{n^\alpha \rho^{\alpha R}} \mathbf{T}_E^\alpha \,, \tag{4.44}$$

where the partial stress tensor $\mathbf{T}^\alpha$ has been substituted. Next, the (mass-based) Gibbs free energy G^α is introduced as the weighted sum of the absolute chemical potentials [21]

$$G^\alpha := \sum_j c^{\alpha_j} \mu^{\alpha_j} = \Psi^\alpha + \frac{p^\alpha}{\rho^{\alpha R}} \,. \tag{4.45}$$

Substituting (4.45) in (4.44) and using the relation between absolute and relative chemical potentials (4.36), leads to the general form of the Lagrange multiplier

$$\mathbf{\Lambda}_r^\alpha = \begin{cases} \mu^{S_N}\mathbf{I} - \frac{1}{\rho^S}\mathbf{T}_E^S, & \text{for } \alpha = S \\ \mu^{\alpha_N}\mathbf{I}, & \text{for } \alpha \neq S \end{cases} . \tag{4.46}$$

In case of vanishing effective stress, i. e. $\mathbf{T}_E^\alpha = \mathbf{0}$, $\mathbf{\Lambda}_r^\alpha$ reduces to the (scalar-valued) relative chemical potential μ^{α_N}. Note that the partial pressures and the chemical potentials are related through the definition of the Gibbs free energy $\mu^{\alpha_j} = \Psi^{\alpha_j} + \frac{p^{\alpha_j}}{\rho^{\alpha_j}}$. In general, the species stress tensor reads

$$\mathbf{T}^{\alpha_j} = -n^\alpha (p^{\alpha_j} + \underbrace{\rho^{\alpha_j} \lambda_e^\alpha \frac{z^{\alpha_j} F}{M_m^j}}_{:= p_e^{\alpha_j}}) + c^{\alpha_j} \mathbf{T}_E^\alpha \,, \tag{4.47}$$

where $p_e^{\alpha_j}$ denotes the electrostatic pressure acting on a charged species. In the derivation, the additional split of the partial pressures $p^\alpha = \sum_j p^{\alpha_j}$ has been exploited. Note in passing that this split resembles Dalton's law, which was initially defined for a mixture of non-reacting gases [16], but can now be deduced from the entropy inequality. On the phase level, the sum of electrostatic pressures, i. e. $\sum_j p_e^{\alpha_j} = 0$, vanishes, which is a consequence of the electro-neutrality assumption postulated on the phase level.

Remark on material compressible phases: It is worth noting that in case of a material compressible phase, its thermodynamic partial pressure p^α can be deduced from the entropy inequality, such that the following expression occurs in the exploitation:

$$(\rho^{\alpha R})'_\alpha \underbrace{(n^\alpha \lambda^\alpha - n^\alpha \rho^{\alpha R} \frac{\partial \Psi^\alpha}{\partial \rho^{\alpha R}})}_{=0} = 0\,. \tag{4.48}$$

Finally the thermodynamic pressure derived from the Helmholtz free energy becomes

$$\lambda^\alpha = \rho^{\alpha R} \frac{\partial \Psi^\alpha}{\partial \rho^{\alpha R}} \rightarrow p^\alpha = (\rho^{\alpha R})^2 \frac{\partial \Psi^\alpha}{\partial \rho^{\alpha R}}\,, \tag{4.49}$$

where the definition (4.41) have been used.

4.3.2 Dissipative contribution

The dissipative contribution of the entropy inequality $\bar{D}_{dis}$ represents the total dissipation in the material and is therefore restricted to be non-negative:

$$\begin{aligned}
\bar{D}_{dis} = \sum_\alpha \Big\{ & - \mathbf{v}_{\alpha S} \cdot [\hat{\mathbf{p}}^\alpha - p \operatorname{grad} n^\alpha] \\
& - \sum_j \mathbf{w}_{\alpha_j} \cdot \Big[\operatorname{grad}(n^\alpha \rho^{\alpha_j} \Psi^{\alpha_j}) + \hat{\mathbf{p}}^{\alpha_j} - \operatorname{grad}(n^\alpha \rho^{\alpha_j}) \Big(\lambda^{\alpha_j} + \lambda_e^\alpha \frac{z^{\alpha_j} F}{M_m^j} \Big) \\
& - \mathbf{\Lambda}_r^\alpha \cdot \operatorname{grad}(n^\alpha \rho^{\alpha_j}) \Big] \\
& - \sum_j \hat{\rho}^{\alpha_j} \Big[\Psi^\alpha + \frac{1}{2} (\mathbf{v}_{\alpha S} \cdot \mathbf{v}_{\alpha S} + \mathbf{w}_{\alpha_j} \cdot \mathbf{w}_{\alpha_j}) + \lambda^\alpha \\
& + \lambda^{\alpha_j} (1 - c^{\alpha_j}) + \lambda_e^\alpha \frac{z^{\alpha_j} F}{M_m^j} \Big] \Big\} - \bar{D}_{ex} \geq 0
\end{aligned} \tag{4.50}$$

$$\text{with} \quad \bar{D}_{ex} = \frac{\partial \Psi^K}{\partial W} (\hat{\rho}_G^A + \hat{\rho}_F^A) + \frac{\partial \Psi^{sA}}{\partial q_{att}} \hat{\rho}_F^{fA} + \frac{\Psi^{sG}}{\partial q_{free}} \hat{\rho}_F^{fG}\,. \tag{4.51}$$

To simplify the evaluation of the entropy inequality, it is assumed that each contribution in (4.50) related to $\{\mathbf{w}_{\alpha_j}, \mathbf{v}_{\alpha_S}, \hat{\rho}_\beta^{\alpha_j}\}$ has to be non-negative independently. This additional restriction is not derived on a theoretical basis. However, it enables one to evaluate (4.50) by using the following structure:

$$\bar{D}_{dis} = \sum_\alpha \Big\{ \underbrace{(\mathbf{v}_{\alpha S} \cdot [\ldots])}_{\geq 0} + \sum_j \underbrace{\mathbf{w}_{\alpha_j} \cdot [\ldots]}_{\geq 0} + \sum_j \sum_{\beta \neq \alpha} \underbrace{\hat{\rho}_\beta^{\alpha_j} [\ldots])}_{\geq 0} \Big\} \geq 0\,. \tag{4.52}$$

Diffusion in multi-species phases The dissipation in the material due to the diffusion of species φ^{α_j} is represented by

$$- \mathbf{w}_{\alpha_j} \cdot \Big[\operatorname{grad}(n^\alpha \rho^{\alpha_j} \Psi^{\alpha_j}) + \hat{\mathbf{p}}^{\alpha_j} - \operatorname{grad}(n^\alpha \rho^{\alpha_j}) \Big(\lambda^{\alpha_j} + \lambda_e^\alpha \frac{z^{\alpha_j} F}{M_m^j} \Big) - \mathbf{\Lambda}_r^\alpha \cdot \operatorname{grad}(n^\alpha \rho^{\alpha_j}) \Big] \geq 0\,, \tag{4.53}$$

while the momentum interaction on the species level is derived from the momentum equation (2.38) to

$$\hat{\mathbf{p}}^{\alpha_j} = \underbrace{n^\alpha \rho^{\alpha_j} (\mathbf{v}_{\alpha_j})'_{\alpha_j}}_{\approx \mathbf{0}} - \operatorname{div} \mathbf{T}^{\alpha_j} - n^\alpha \rho^{\alpha_j} \mathbf{b}^{\alpha_j} . \tag{4.54}$$

Substituting (4.54), the identified Lagrange multipliers (4.35), (4.37), (4.46) and the species stress tensor (4.47) in (4.53) yields to

$$- \mathbf{w}_{\alpha_j} \cdot \Big[n^\alpha \rho^{\alpha_j} \operatorname{div} \Big(\mu^{\alpha_j} \mathbf{I} + \lambda_e^\alpha \frac{z^{\alpha_j} F}{M_m^j} \mathbf{I} - \frac{1}{n^\alpha \rho^{\alpha R}} \mathbf{T}_E^\alpha \Big) - n^\alpha \rho^{\alpha_j} \mathbf{b}^{\alpha_j} \Big] \geq 0 . \tag{4.55}$$

Note that inertia forces has been neglected in the linear momentum interaction (4.54).

Seepage relative to solid skeleton The dissipation in the material caused by the seepage velocity $\mathbf{v}_{\alpha S}$ is given through

$$- \mathbf{v}_{\alpha S} \cdot [\hat{\mathbf{p}}^\alpha - p \operatorname{grad} n^\alpha] \geq 0 , \tag{4.56}$$

where the momentum interaction on the phase level is again derived by the corresponding momentum balance to

$$\hat{\mathbf{p}}^\alpha = \underbrace{n^\alpha \rho^{\alpha R} (\mathbf{v}_\alpha)'_\alpha}_{\approx \mathbf{0}} - \operatorname{div} \mathbf{T}^\alpha - n^\alpha \rho^{\alpha R} \mathbf{b}^\alpha . \tag{4.57}$$

Substituting the momentum exchange term (4.57) into (4.56) and using the definition of the partial stress tensor (4.38) yields

$$- \mathbf{v}_{\alpha S} \cdot (n^\alpha \operatorname{grad} p - \operatorname{div} \mathbf{T}_E^\alpha - n^\alpha \rho^{\alpha R} \mathbf{b}^\alpha) \geq 0 . \tag{4.58}$$

Note that inertia and Reynolds-like forces are neglected in (4.57).

Inter-phase mass transfer Collecting the dissipative parts of the entropy inequality corresponding exclusively to mass exchange gives

$$\sum_\alpha \sum_j \Big\{ - \hat{\rho}^{\alpha_j} \Big[\mu^{\alpha_j} + \lambda_e^\alpha \frac{z^{\alpha_j} F}{M_m^j} + K^{\alpha_j} \Big] \Big\} - \bar{D}_e x \geq 0 , \tag{4.59}$$

while the Gibbs free energy (4.45), the identified Lagrange multipliers (4.35), (4.37), (4.46) and the relation between absolute and relative chemical potentials (4.36) have been used. In addition, the second order velocity terms are lumped into

$$K^{\alpha_j} = \frac{1}{2} (\mathbf{v}_{\alpha S} \cdot \mathbf{v}_{\alpha S} + \mathbf{w}_{\alpha_j} \cdot \mathbf{w}_{\alpha_j}) . \tag{4.60}$$

Next, the dissipation due to mass exchange (4.51) is substituted. Assuming again that each contribution is non-zero, leads to

$$-\hat{\rho}_{fG}^{fA_j}\Big[\frac{\partial\Psi^K}{\partial W}+\Delta\mu_{fG}^{fA_j}+\Delta K_{fG}^{fA_j}+\frac{F}{M_m^j}(\lambda_e^A\, z^{A_j}-\lambda_e^G\, z^{G_j})\Big]\geq 0\,, \tag{4.61a}$$

$$-\hat{\rho}_{sG}^{sA_j}\Big[\frac{\partial\Psi^K}{\partial W}+\Delta\mu_{sG}^{sA_j}+\Delta K_{sG}^{sA_j}+\frac{F}{M_m^j}(\lambda_e^A\, z^{A_j}-\lambda_e^G\, z^{G_j})\Big]\geq 0\,, \tag{4.61b}$$

$$-\hat{\rho}_{F}^{fA_j}\Big[\frac{\partial\Psi^K}{\partial W}+\frac{\partial\Psi^{sA}}{\partial q_{att}}+\Delta\mu_{F}^{fA_j}+\Delta K_{F}^{fA_j}+\frac{F}{M_m^j}(\lambda_e^A\, z^{A_j}-\lambda_e^F\, z^{F_j})\Big]\geq 0\,, \tag{4.61c}$$

$$-\hat{\rho}_{F}^{fG_j}\Big[\frac{\partial\Psi^{sG}}{\partial q_{free}}+\Delta\mu_{F}^{fG_j}+\Delta K_{F}^{fG_j}+\frac{F}{M_m^j}(\lambda_e^G\, z^{G_j}-\lambda_e^F\, z^{F_j})\Big]\geq 0\,, \tag{4.61d}$$

where $\Delta(\,\cdot\,)_{\beta}^{\alpha_j}=(\,\cdot\,)^{\alpha_j}-(\,\cdot\,)^{\beta_j}$ is used for convenience in the derivation.

4.3.3 Near-equilibrium results

The dissipative contributions in the entropy inequality are approximated by a linear Taylor series expansion for near-equilibrium conditions, cf. [25].

Fick's law Linearizing (4.55) near-equilibrium provides a possible form for the diffusion velocity

$$\mathbf{w}_{\alpha_j}=-(\mathbf{R}^{\alpha_j})^{-1}\cdot\Big[n^{\alpha}\rho^{\alpha_j}\mathrm{div}\,\Big(\mu^{\alpha_j}\mathbf{I}+\lambda_e^{\alpha}\frac{z^{\alpha_j}F}{M_m^j}\mathbf{I}-\frac{1}{n^{\alpha}\rho^{\alpha R}}\mathbf{T}_E^{\alpha}\Big)-n^{\alpha}\rho^{\alpha_j}\mathbf{b}^{\alpha_j}\Big]\,, \tag{4.62}$$

herein, $\mathbf{R}^{\alpha_j}$ represents the resistance tensor with respect to diffusion and must be a positive-definite, second order tensor to satisfy the entropy inequality. The diffusion velocity is driven by four contributions. The gradient of absolute chemical potential represents here a classical concentration-dependent influence, while in case of a charged species, the gradient of the electrical potential acts additionally on the the species. By assuming external body forces, i. e. gravitation forces in most cases, a third contribution to the diffusion velocity is added naturally. Finally, the influence of the partial effective stress can be neglected for $\alpha\neq S$ according to (4.39). A Fick's type diffusion flux is obtained by

$$\mathbf{j}^{\alpha_j}=-n^{\alpha}\rho^{\alpha_j}\mathbf{w}_{\alpha_j}=-\mathbf{D}^{\alpha_j}\cdot\Big[\mathrm{grad}\,\Big(\mu^{\alpha_j}+\lambda_e^{\alpha}\frac{z^{\alpha_j}F}{M_m^j}\Big)-\mathbf{b}^{\alpha_j}\Big]\,, \tag{4.63}$$

where $\mathbf{D}^{\alpha_j}$ denotes the diffusion tensor.

Darcy's law The seepage velocities relative to the solid skeleton can be respectively obtained by linearizing (4.58) to

$$\mathbf{v}_{\alpha S}=-(\mathbf{R}^{\alpha})^{-1}\cdot\Big(n^{\alpha}\mathrm{grad}\,p-n^{\alpha}\rho^{\alpha R}\mathbf{b}^{\alpha}\Big)\,, \tag{4.64}$$

where $\mathbf{R}^\alpha$ denotes the resistance tensor with respect to seepage flow and must be again a positive-definite, second order tensor. With respect to the small characteristic length in porous media, the friction force div $\mathbf{T}_E^\alpha$ has an insignificant impact in comparison to the flow-induced (viscous) momentum production $\hat{\mathbf{p}}^\alpha$ and is therefore neglected from (4.64) [49, 125].

Darcy's law is recovered by specifying $\mathbf{R}^\alpha$ in (4.64), such that

$$\mathbf{q}^\alpha = n^\alpha \mathbf{v}_{\alpha S} = -\frac{\mathbf{K}^S}{\mu^{\alpha R}} \cdot (\operatorname{grad} p - \rho^{\alpha R} \mathbf{b}^\alpha) \tag{4.65}$$

is obtained. The Darcy velocity $\mathbf{q}^\alpha$ is driven by the pressure gradient and body forces stemming for instance from gravitation, while $\mathbf{K}^S$ and $\mu^{\alpha R}$ denote the intrinsic permeability tensor of the solid skeleton and the effective dynamic viscosity.

Mass transfer Following the same procedure, the density production terms are obtained from (4.61a)–(4.61d) to

$$\hat{\rho}_{fG}^{fA_j} = -\zeta_{fG_j}^{fA_j}\Big[\frac{\partial \Psi^K}{\partial W} + \Delta\mu_{fG}^{fA_j} + \Delta K_{fG}^{fA_j} + \frac{F}{M_m^j}(\lambda_e^A z^{A_j} - \lambda_e^G z^{G_j})\Big], \tag{4.66}$$

$$\hat{\rho}_{sG}^{sA_j} = -\zeta_{sG}^{sA_j}\Big[\frac{\partial \Psi^K}{\partial W} + \Delta\mu_{sG}^{sA_j} + \Delta K_{sG}^{sA_j} + \frac{F}{M_m^j}(\lambda_e^A z^{A_j} - \lambda_e^G z^{G_j})\Big], \tag{4.67}$$

$$\hat{\rho}_{F}^{fA_j} = -\zeta_{F}^{fA_j}\Big[\frac{\partial \Psi^K}{\partial W} + \frac{\partial \Psi^{sA}}{\partial q_{att}} + \Delta\mu_{F}^{fA_j} + \Delta K_{F}^{S_j} + \frac{F}{M_m^j}(\lambda_e^A z^{A_j} - \lambda_e^F z^{F_j})\Big], \tag{4.68}$$

$$\hat{\rho}_{F}^{fG_j} = -\zeta_{F}^{fG_j}\Big[\frac{\partial \Psi^{sG}}{\partial q_{free}} + \Delta\mu_{F}^{fG_j} + \Delta K_{F}^{fG_j} + \frac{F}{M_m^j}(\lambda_e^G z^{G_j} - \lambda_e^F z^{F_j})\Big]. \tag{4.69}$$

The entropy inequality requires that $\zeta_\beta^{\alpha_j}$ is a positive scalar. It should also be pointed out that the coefficients stemming from the linearizing procedure do not have to be constant neither in time nor in space; they can also be isotropic functions of the set of all equilibrium process variables. The polymer attachment of fluidized gel to the solid skeleton is consequently given by the sum

$$\hat{\rho}_G^A = \sum_j (\hat{\rho}_{fG}^{fA_j} + \hat{\rho}_{sG}^{sA_j}). \tag{4.70}$$

Modeling the polymer gel φ^G as a single-phase consisting of no miscible species, (4.70) reduces to

$$\hat{\rho}_G^A = -\zeta_G^A\Big[\frac{\partial \Psi^K}{\partial W} - \frac{1}{2}\mathbf{v}_{GS} \cdot \mathbf{v}_{GS}\Big]. \tag{4.71}$$

Chapter 5:
Hydrogel swelling in electrolytic solutions

5.1 Three-phase model with reversible mass transfer

Modeling of absorption and desorption processes of hydrogel particles embedded within the pore space of a porous skeleton are the subject of the current chapter. To this end, attachment processes of polymer gel to the surface of the granular matrix are neglected from the general mixture model represented in Figure 4.1. The reduced model is represented through the decomposition in Figure 5.1.

The systematically reduced mixture model consists of a (granular) solid skeleton φ^S, an aqueous pore fluid φ^F and hydrated SAP particles φ^G (cf. Figure 5.2a). Note that the hydrogel phase φ^G is further subdivided into polymer chains φ^{sG} and absorbed solution φ^{fG}. A similar idea concerning an enriched phase composition was followed by Pierce *et al.* [116] for modeling cartilage. The multi-phase model is concluded by the

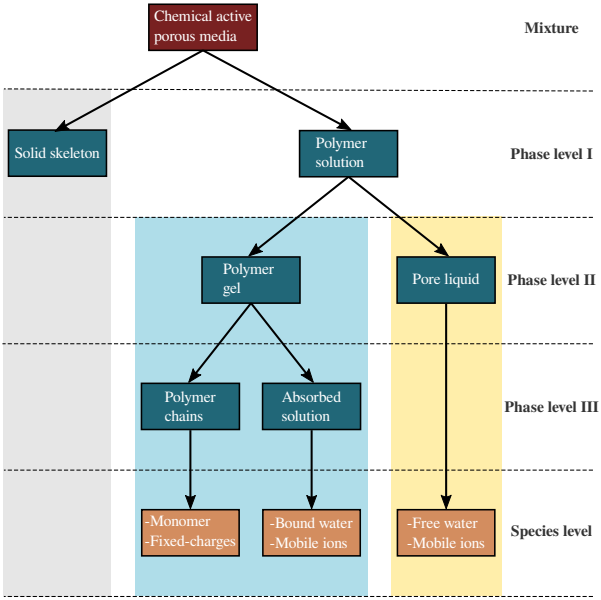

Figure 5.1: *Decomposition of the chemical active porous media model: Modeling absorption and desorption processes in porous media.*

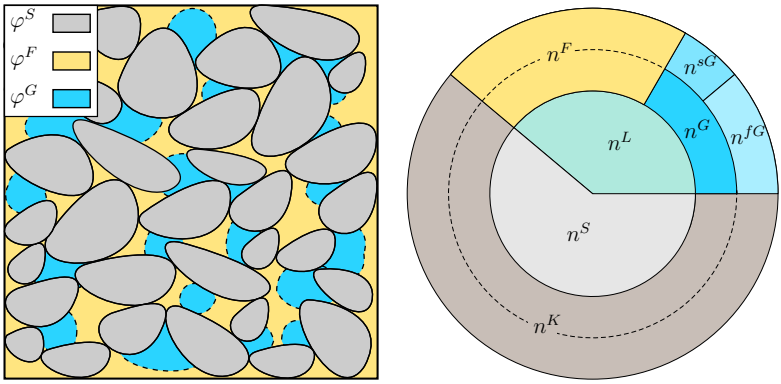

(a) Representative Volume Element (RVE) **(b)** Volume fractions of the three-phase model

Figure 5.2: *Volume fractions of the three-phase model.*

following representation of phases and species

$$\varphi = \{\varphi^S \cup \varphi^F \cup \varphi^G\} \quad \Rightarrow \quad \left\{\varphi^S \cup \{\varphi^{F_w}, \varphi^{F_i}\} \cup \{\varphi^{fG_w}, \varphi^{fG_i}, \varphi^{sG_m}, \varphi^{sG_{fc}}\}\right\}.$$

Since $\varphi^G = \varphi^{fG} \cup \varphi^{sG}$ is assumed, the additive split $n^G = n^{fG} + n^{sG}$ is used here.

The microstructure of the mixture model is smeared out to a continuum representation, cf. Figure 5.2. Volume fractions for each phase are introduced through (2.4), while the specific saturation condition becomes

$$\sum_\alpha n^\alpha = n^S + n^F + \underbrace{n^{sG} + n^{fG}}_{n^G} = 1\,. \tag{5.1}$$

The polymer saturation s^G, which denotes the volume of φ^G with respect to the pore volume, reads

$$s^G = \frac{n^G}{n^G + n^F}\,; \quad s^G + s^F = 1\,, \tag{5.2}$$

while s^F is consequently the fluid saturation. The proposed framework allows the definition of the (solid) polymer volume fraction ϕ with respect to the current hydrogel volume, cf. (3.2).

The molar Fixed Charge Density (FCD) $\rho_m^{G_{fc}} = \phi^s \rho_m^{sG_{fc}}$ is introduced to account for the charges attached to the hydrogel. Here, $\rho_m^{sG_{fc}}$ is the intrinsic FCD of the polymer network. It is a priori assumed that the charge-neutrality condition holds individually for the fluid as well as for the hydrogel phase, i. e.

$$\sum_j \rho_e^{\alpha_j} = 0\,, \quad \alpha \in \{F, G\}\,. \tag{5.3}$$

However, Wilson *et al.* [164] realized that deviations from the charge-neutrality condition result in very strong electrical forces, which tend to equilibrate the system in approximately one nano-second.

5.1.1 Governing equations

In this chapter, the focus is on the constitutive modeling and calibration of the time-dependent inter-phase mass exchange between the polymer and the pore fluid. The mass exchange is locally governed through the density production terms in the corresponding mass balance equations (cf. (2.32) and (2.33)). On the microscale, polymer particles are able to absorb aqueous pore fluid and expand within the pore space of the porous media. In addition, it is a priori assumed in the present modeling approach, that the geometrical constrictions dictated by the pore space morphology are not influencing the local volumetric polymer expansion. This assumption is physically-motivated by expecting a low gel saturation s^G within the pore space. As a consequence, the solid skeleton does not counteract the volumetric expansion of the polymer. In essence, the local mass exchange has no influence on the current total stress state. The total stress in the mixture stems exclusively from externally applied loads, which are not interacting with the internal mass transfer by assumption. Note in passing that Alexandersson *et al.* [8] introduced a generic interaction pressure in order to account for the mechanical interaction between an expanding phase embedded in a porous structure. In this context, a constitutive model for the interaction pressure has to be developed in accordance to experimental observations. An evolving interaction pressure during mass transfer induces solid deformations on the macroscale, which can be measured in an appropriate experimental setting. Note that an interaction pressure is not taken into consideration in this study but can be added without major changes to the modeling framework.

In the following course of this chapter, experimental investigations towards the time-dependent absorption and desorption behavior are carried out with respect to the pore fluid chemistry, i. e. the salt concentration. The experimentally observed absorption/desorption dynamics resemble the local inter-phase mass exchange at the material point in the continuum model. To this end, the results will be used in the further course to determine the local inter-phase mass transfer terms in the mixture model. Therefore, the spatially-resolved mass and charge balance equations are reduced to local evolution equations defined at the material point in order to mimic the experimental setting. It is of great importance to emphasize that the presented multi-phase material is generally affected by non-local transport processes, such as the seepage flow of the fluid relative to the solid skeleton or the diffusion of salt relative to the pore fluid. Moreover, the solid skeleton is able to deform due to externally applied loads. However, setting homogeneous initial conditions as well as homogeneous boundary conditions to the governing equations, results in vanishing gradients in terms of hydraulic pressure, concentration, volume fraction and displacement across the mixture, such that the governing equations degenerate to a local problem formulation, which matches the investigated experimental setup. In this context, the momentum balance of the mixture

is a priori fulfilled, while the overall mixture is in a stress-free state.[1] Through the precise choice of boundary conditions, the problem formulation reduces to an initial value problem, such that the spatially-resolved equations degenerate to a set of Ordinary Differential Equations (ODEs) in time.

Next, balance equations are formulated for the volume fractions, the concentration of the species and the FCD based on the summarized set of model assumptions give by:

- material incompressible phases: $\partial_t(\rho^{\alpha R}) = 0$,
- no seepage flows relative to solid skeleton: $\mathbf{v}_{\alpha S} = \mathbf{0}$,
- rigid solid skeleton, i. e. no solid displacement: $\mathbf{u}_S = \mathbf{0}$,
- no diffusion of species: $\mathbf{w}_{\alpha_j} = \mathbf{0}$,
- molar charges of mobile ions are given by $z^{\alpha+} = z^+ = 1$ and $z^{\alpha-} = z^- = -1$,
- instantaneous charge-neutrality for hydrogel and pore fluid, cf. (5.3) .

Finally, the multi-phase model is governed through the following set of evolution equations:

$$\partial_t\left(n^G\right) = \frac{\hat{\rho}^{fG}}{\rho^{GR}} - \frac{n^G}{\rho^{GR}}\partial_t(\rho^{GR})\,, \tag{5.4}$$

$$\partial_t\left(\rho^{GR}\right) = \left(\rho^{sGR} - \rho^{fGR}\right)\partial_t(\phi)\,, \tag{5.5}$$

$$\partial_t\left(\phi\right) = -\frac{\hat{\rho}^{fG}\phi^2}{n^{sG}\rho^{fGR}}\,, \tag{5.6}$$

$$\partial_t\left(\rho_m^{F_i}\right) = -\frac{1}{n^F}\left(\hat{\rho}_m^{fG_i} - \rho_m^{F_i}\frac{\hat{\rho}^{fG}}{\rho^{FR}}\right) \quad \forall\, i \in \{+,-\}\,, \tag{5.7}$$

$$\partial_t\left(\rho_m^{fG_i}\right) = \frac{1}{n^{fG}}\left(\hat{\rho}_m^{fG_i} - \rho_m^{fG_i}\frac{\hat{\rho}^{fG}}{\rho^{fGR}}\right) \quad \forall\, i \in \{+,-\}\,. \tag{5.8}$$

Herein, $\hat{\rho}^{fG}$ denotes the density production of the absorbed fluid, which is equal to the density production of the overall hydrogel phase $\hat{\rho}^G$. In addition, the density production is formally given by the additive split $\hat{\rho}^{fG} = \hat{\rho}^{fG_w} + \sum \hat{\rho}^{fG_i}$. Its molar-based counterpart, which is more intuitive for the transfer of ions, calculates to $\hat{\rho}_m^{fG_j} = \hat{\rho}^{fG_j}/M_m^j$. Note in passing that the density production terms for the pore fluid are defined in analogy. The ODE system is closed by providing the initial conditions $\mathbf{y}_0 = [n_0^G, \rho_0^{GR}, \phi_0, \rho_{m,0}^{F_+}, \rho_{m,0}^{F_-}, \rho_{m,0}^{fG_+}, \rho_{m,0}^{fG_-}]^T$ as well as the constitutive functions for $\hat{\rho}^{fG_w}$, $\hat{\rho}^{fG_+}$ and $\hat{\rho}^{fG_-}$. Since mass transfer occurs exclusively between species which are present in both the absorbed solution and the pore fluid, the following restriction arises $\hat{\rho}^{F_j} = -\hat{\rho}^{fG_j}$. To this end, it is a priori assumed

[1] Note that the results from the evaluation of the entropy inequality for multi-phase systems have been used [123]. To this end, the seepage and diffusion velocity are expressed through Darcy- and Fick-type laws, respectively. Choosing boundary conditions such that pressure and concentration gradients are vanishing throughout the mixture, leads to vanishing seepage and diffusion velocities in turn.

that chemical reactions among species within a phase, i. e. intra-phase exchange, are excluded.

Due to the assumed incompressibility of the mixture, i. e. $\rho^{\alpha R} = \rho_0^{\alpha R} = \text{const.}\ \forall\, \alpha \in \{S, F, sG, fG\}$, the mass balance equation for the hydrogel phase reduces to the volume balance (5.4). However, an evolution equation for the intrinsic hydrogel density is still given by (5.5), in order to account for density changes caused by inter-phase mass transfer. It is worth mentioning that (5.5) is not a constitutive assumption, it is rather a compatibility condition which has to be satisfied for incompressible phases. Furthermore, (5.6) balances the relative polymer volume fraction, while the concentration of ions in the absorbed fluid and in the pore fluid are governed by (5.7) and (5.8), respectively.

Since the solid phase is not involved in the phase transition, the solid volume fraction does not evolve in time. Furthermore, the remaining volume fraction of the pore fluid can be derived from the saturation condition (5.1) to

$$n^F = 1 - n^G - n^S\,. \tag{5.9}$$

Besides the governing equations (5.4) - (5.8), the charged species are subjected to the charge-neutrality condition (5.3). Assuming monovalent ions in the pore fluid (e. g. NaCl $\rightarrow$ Na^+Cl^-; KCl $\rightarrow$ K^+Cl^-) and negatively fixed charges attached to the polymer chains, lead finally to the following restrictions

$$\sum \rho_e^{F_i} = \rho_m^{F_+} - \rho_m^{F_-} = 0\,, \tag{5.10}$$

$$\sum \rho_e^{G_i} + \rho_e^{G_{fc}} = (1-\phi)(\rho_m^{fG_+} - \rho_m^{fG_-}) - \phi\rho_m^{sG_{fc}} = 0\,. \tag{5.11}$$

The valence of the fixed charges z^{fc} is set to a value of -1 in order to mimic the polarity, while the strength of the fixed charges is given explicitly by its molar concentration $\rho_m^{sG_{fc}}$. The charge-neutrality condition on the phase level places a restriction on the molar concentrations of ions in the hydrogel and in the pore fluid according to

$$\partial_t(\rho_m^{F_s}) = -\frac{1}{n^F}\left(\frac{\sum \hat{\rho}_m^{G_i}}{2} - \frac{\hat{\rho}^{fG}}{\rho^{FR}}\rho_m^{F_s}\right)\,, \tag{5.12}$$

$$\partial_t(\rho_m^{fG_s}) = \frac{1}{n^{fG}}\left(\frac{\sum \hat{\rho}_m^{fG_i}}{2} - \frac{\hat{\rho}^{fG}}{\rho^{fGR}}\rho_m^{fG_s}\right)\,. \tag{5.13}$$

Herein, $\rho_m^{\alpha_s}$ is defined as the molar salt concentration. In the absence of fixed charges, $\rho_m^{F_s} = \rho_m^{F_i}$ holds, while within the charged hydrogel phase, the molar concentrations of mobile ions are unevenly distributed. To this end, $\rho_m^{fG_+}$ is subdivided into counter- and mobile ions, cf. Figure 3.1. The salt concentration within the absorbed fluid is further given by $\rho_m^{fG_s} = \rho_m^{fG_-}$. Finally, the ODE system reduces by substituting (5.7) and (5.8) with the evolution equations (5.12) and (5.13), whereas the salt concentrations $\rho_{m,0}^{fG_s}$ and $\rho_{m,0}^{F_s}$ are used as initial conditions.

5.1.2 Constitutive modeling of mass transfer

Inter-phase mass exchange between the same species, namely water and mobile ions, is incorporated in the modeling approach. However, the enormous mass uptake of the hydrogel per unit time is mainly given due to the transfer of water. To this end, the following simplification $\hat{\rho}^{fG} \approx \hat{\rho}^{fG_w}$ has been made, since $\hat{\rho}^{fG_i} \ll \hat{\rho}^{fG_w}$ is reasonably assumed. A thermodynamic-consistent form of the the density production $\hat{\rho}^{fG_j}$ has been derived by exploiting the entropy inequality. Next, the result presented by (4.69) is compared to well-established constitutive models in polymer chemistry.

Driving force: Chemical potential difference The chemical potential difference $\Delta\mu^w$, i. e. the driving force for mass transfer of water, is derived from the Helmholtz free energies of the subsystem hydrogel-pore-fluid [51, 159]. According to the literature on ionic gels [50], the driving force is usually viewed as a superposition of three distinct chemo-physical phenomena:

- the mixing and interaction of polymer chains and absorbed solvent $\Delta\mu^w_{m,mix}$,
- the entropy elasticity of the network caused by volumetric expansion $\Delta\mu^w_{m,elast}$,
- and the ionic contribution due to the ion concentration difference between absorbed solution and pore fluid $\Delta\mu^w_{m,ion}$.

The first two contributions are governed by the theory of ideal elastomeric gels introduced by Flory & Rehner [55, 56], while the latter one refers to the Donnan theory [164], which was initially derived for electrolytic solutions rather than ionic gels. Note that a brief overview of the thermodynamic fundamentals of charged hydrogels can be found in chapter 3. Finally, the total molar-based chemical potential difference of water is given by

$$\Delta\mu^w_m = \underbrace{RT(\ln(1-\phi)+\phi+\chi\,\phi^2)}_{\Delta\mu^w_{m,mix}} + \underbrace{RT\tilde{V}^w_m\nu\,(\phi)^{1/3}}_{\Delta\mu^w_{m,elast}} + \underbrace{RT\ln\left(\frac{a^{fG_w}}{a^{F_w}}\right)}_{\Delta\mu^w_{m,ion}}. \tag{5.14}$$

In case of charged hydrogels, the ionic contribution is typically responsible for the enormous water uptake, while in contrast, the elastic expansion (entropy elasticity) counteracts further solvent absorption. In addition, the mixing contribution shows only a significant impact to the total chemical potential difference for little swelling. The equilibrium state is reached when the sum of all contributions vanishes.

In the chosen model representation, mobile ions are solved in both the pore fluid and the absorbed solution of the hydrogel, cf. Figure 3.1. By assuming that the ionic solutions are sufficiently dilute, the driving force for ion transfer can be represented through

$$\Delta\mu^i_m = RT\ln\left(\frac{a^{fG_i}}{a^{F_i}}\right). \tag{5.15}$$

By using the charge neutrality conditions for the hydrogel (3.15) and the pore fluid (3.14), together with (2.7), enables one to express the molar concentrations of water through

$$\rho_m^{fG_w} = \rho_m^{fGR} - 2\,\rho_m^{fG_s} - \frac{\phi}{1-\phi}\,\rho_m^{sG_{fc}}\,, \tag{5.16}$$

$$\rho_m^{F_w} = \rho_m^{FR} - 2\,\rho_m^{F_s}\,. \tag{5.17}$$

Next, the transfer of ions is analyzed in more detail. To maintain charge-neutrality of the multi-species phases, the transfer of positively and negatively charged ions occurs always together. To this end, (5.15) has been substituted in (5.20) and summed over i, which leads to

$$\sum \hat{\rho}_m^{G_i} = -\zeta^i RT \ln\left(\frac{a^{G_+}a^{G_-}}{a^{F_+}a^{F_-}}\right). \tag{5.18}$$

Herein, the (molar) transfer rates of ions are chosen according to $\zeta^+ = \zeta^- = \zeta^i$. Inserting the ion activity coefficients (3.17) leads finally to

$$\begin{aligned} \sum \hat{\rho}_m^{fG_i} &= -\zeta^i RT \ln\left((\psi^{\pm})^2\,\frac{\rho_m^{fG_s}(\rho_m^{fG_s} + \frac{\phi}{1-\phi}\,\rho_m^{sG_{fc}})}{(\rho_m^{F_s})^2}\right) \\ \text{with}\quad \psi^{\pm} &= \frac{\gamma^{fG_\pm}}{\gamma^{F_\pm}} = \left(\frac{\gamma^{fG_+}\gamma^{fG_-}}{\gamma^{F_+}\gamma^{F_-}}\right)^{1/2}\,, \end{aligned} \tag{5.19}$$

where the charge-neutrality conditions (5.10) and (5.11) have been used. For reasons of convenience, the average activity coefficient $\gamma^{\alpha_\pm}$ has been introduced, whereas $\psi^{\pm}$ is defined in analogy to ψ^w (3.19) and accounts here for the activity of mobile ions in both phases.

It is worth mentioning that the driving force for mass exchange (5.14) represents the case of unconstrained swelling, which is valid for low degrees of polymer saturation as mentioned previously. To this end, it has been a priori assumed that the local change in polymer volume does not alter the total stress state. As a consequence, the chemical potential difference does not incorporate a mechanical interaction between polymer and solid skeleton. On the contrary, it should be mentioned for the sake of completeness, that mechanically-dependent mass exchange is accounted for growth theories frequently used in the field of biomechanics, cf. [11, 72] for further details.

A comparison between the chemo-physically motivated driving forces for water and ion transfer with the general result obtained from the evaluation of the entropy inequality (4.69) leads to

$$\hat{\rho}^{fG_w} = -\zeta_F^{fG_w}\,(\underbrace{\Delta\mu_{mix}^w + \Delta\mu_{elast}^w + \Delta\mu_{ion}^w}_{=\Delta\mu^w})\,, \tag{5.20}$$

$$\hat{\rho}^{fG_i} = -\zeta_F^{fG_i}\Big(\underbrace{\Delta\mu_{ion}^i}_{=\Delta\mu^i} + \underbrace{\frac{F}{M_m^i}(\lambda_e^G\, z^{G_i} - \lambda_e^F\, z^{F_i})}_{=\Delta\mu_e^i}\Big)\,, \tag{5.21}$$

where $\Delta\mu_e^i$ represents the driving force imposed by the charge neutrality condition and acts therefore only on charged species. The second order velocity terms in $\Delta K_F^{fG_j}$ have been neglected according to the previously mentioned assumptions. Note that the molar-based chemical potentials are related to its mass-based counterpart through $\mu_m^{\alpha_j} = \mu^{\alpha_j}/M_m^j$. Finally, the driving forces are correlated to the partial derivatives of the Helmholtz free energy densities through:

$$\Delta\mu_{mix}^w + \Delta\mu_{elast}^w = \frac{\partial\Psi^{sG}}{\partial q}\,, \tag{5.22}$$

$$\Delta\mu_{ion}^w = \mu^{fG_w} - \mu^{F_w} = \frac{\partial\Psi_{ion}^{fG}}{\partial c^{fG_w}} - \frac{\partial\Psi_{ion}^{F}}{\partial c^{F_w}}\,, \tag{5.23}$$

$$\Delta\mu_{ion}^i = \mu^{fG_i} - \mu^{F_i} = \frac{\partial\Psi_{ion}^{fG}}{\partial c^{fG_i}} - \frac{\partial\Psi_{ion}^{F}}{\partial c^{F_i}}\,. \tag{5.24}$$

Negative values for the total chemical potential difference $\Delta\mu^j + \Delta\mu_e^j$ lead to absorption of species j by the hydrogel, while positive chemical potential differences invert the process. Thus, the chemical potentials are related to the direction of mass transfer by

$$\Delta\mu^j + \Delta\mu_e^j \leq 0 \rightarrow \hat{\rho}^{fG_j} \geq 0 \quad (\text{gain})\,; \qquad \Delta\mu^j + \Delta\mu_e^j \geq 0 \rightarrow \hat{\rho}^{fG_j} \leq 0 \quad (\text{loss})\,. \tag{5.25}$$

Due to the fact that the driving force for the phase transition is expressed through a (chemical) potential, reversibility of the phase transition process is implicitly provided in the model. In the further course of this work, it will also be shown experimentally that reversibility holds for the studied hydrogel material.

Dynamics of inter-phase mass exchange In the past, the swelling equilibrium of charged hydrogels was extensively studied under different environmental conditions, however, the rate of swelling and shrinking is still a topic of ongoing research. Bertrand *et al.* [27] observed that the dynamics of hydrogel swelling depends in extension to environmental stimuli, for instance temperature and ion concentration, also on the shape and size of the specimen. By assuming that swelling is an exclusively diffusion-driven process on the molecular level, Tanaka & Fillmore [144] calculated the diffusion coefficient of a spherical gel network. According to their study, the diffusion coefficient is defined as the ratio between the longitudinal bulk modulus of the network and the friction coefficient between the network and the absorbed solution. They observed that a characteristic swelling time is proportional to the square of the final radius. Li & Tanaka [92] gained more insights in the swelling dynamics by additionally investigating non-spherical hydrogels. They showed experimentally and theoretically that solvent uptake by a hydrogel is in general driven by a non-Fickian type of diffusion. This is due to the fact that diffusion naturally induces a volumetric deformation, however, in case of non-zero shear modulus, solvent uptake by an arbitrary shaped hydrogel causes deviatoric deformations. Furthermore, their theory is able to explain that the shear modulus of the network, which minimizes the deviatoric deformation, reduces the diffusion of solvent by coupling deformation and diffusion. Note that the non-Fickian diffusion phenomenon in hydrogels was later investigated by various researchers [17, 82]. However,

the results made by Tanaka & Fillmore [144] are still valid due to the fact that the deviatoric strain energy is minimized automatically by solvent uptake in case of spherical hydrogels.

In a spatially-resolved hydrogel model, solvent crosses the phase boundary water-gel and is subsequently transported through the polymer network. According to various experimental studies, it was found that the fluid flow relative to the cross-linked polymer network is governed by a Darcy-type law [27, 50, 63]. Herein, the permeability of the hydrogel is related to the friction coefficient between solvent and polymer chains. It is furthermore reported by Grattoni *et al.* [63] and Tokita & Tanaka [148], that the friction coefficient depends on the polymer volume fraction ϕ through a power-law relation. Following Bertrand *et al.* [27] and Engelsberg & Barros [50], a swelling-dependent permeability function for the polymer network is typically adopted

$$k^{sG}(\phi) = k_0^{sG} \frac{1-\phi}{\phi^{\,\beta}}\,, \tag{5.26}$$

where β and k_0^{sG} are characteristic model parameters. According to the literature, values for β ranging between 1.5 and 1.85 depending on the gel type and environmental stimuli, are suggested [27, 50, 63, 148]. The swelling-dependent permeability function states basically that the polymer network is more permeable at higher fluid saturations.

However, in the upscaled model discussed in this contribution, the geometry of the hydrogel particles are no longer spatially-resolved, thus, the dynamics of the microscopic transport process are merged into the macroscopic transfer coefficient

$$\zeta^j = \frac{\Gamma^j}{RT} \quad \text{with} \quad \Gamma^j(\phi) = \Gamma_0^j \frac{1-\phi}{\phi^{\,\beta}}\,. \tag{5.27}$$

Herein, a density production function for Γ^j in analogy to (5.26) has been postulated. The swelling-dependent part is triggered through the scaling exponent β, while the density production coefficient Γ_0^j is assumed to be independent of the hydrogel's fluid saturation. The postulated expression for Γ^j reflects that the resistance to mass exchange decreases with increasing fluid saturation within the hydrogel.

Incorporating the polymer volume fraction ϕ in the transfer dynamics is an approach of enriching a macroscopic process (inter-phase mass transfer) by a microscopic-motivated constitutive law. In this study, β is chosen to 1.9, which leads to a good agreement with the experimental results, while a more detailed analysis is carried out in section 5.4.

5.2 Experimental setup

The absorption and desorption characteristics of a SAP granulate have been captured through experimental investigations. The basis of the tested SAP granulate used in this study (product name: C 4080 G, manufacturer: Evonik) is a cross-linked sodium polyacrylate (cf. Figure 5.3). It is a an anionic polyelectrolyte with negatively charged carboxylic groups. According to the particle size distribution (PSD) provided by the

(a) Dry SAP granulate **(b)** Swollen SAP particles

Figure 5.3: *The tested SAP material is a dry granulate in the initial state (a). The particles absorbing water and transform to a hydrogel, while the swollen particles agglomerate and are weakly connected through van-der-Waals forces (b).*

manufacturer, a minimum of 90% of the dry granulate is in the range between $100 - 500\,\mu$m, while maximum 5% are beyond the intervals on each side.

In the following, three different experimental tests are described for examining both the equilibrium state of swelling and the rate of mass exchange. Throughout the experimental investigations, the current state of swelling is quantified by the mass-based degree of swelling q.

5.2.1 Absorption tests

The experimental procedure starts by weighting a small amount of the dry SAP granulate (approx. 0.1 g) and equally distributing it on a laboratory test sieve with a mesh width of $100\,\mu$m. The mesh width has been chosen sufficiently small such that the dry SAP granulate is not able to pass the sieve. Note that the number of tested SAP particles is high enough to represent the PSD of the granulate. Next, the sieve loaded with the SAP particles is inserted in a test fluid to induce the water absorption. The experimental setup is schematically illustrated in Figure 5.4.

In contrast to standardized absorption tests in soil mechanics [48], the approach introduced in this contribution takes into account that the tested material is fully immersed within the aqueous fluid. In this study, demineralized water with NaCl concentrations in the range between $0.0\,\mathrm{g/l}$ and $10.0\,\mathrm{g/l}$ have been used as test fluids, which are equivalent to mass fractions ranging from $0.0\,\mathrm{m}\%$ to $1.0\,\mathrm{m}\%$. At discrete points in time, the sieve is extracted from the test fluid and the current weight of the loaded sieve is measured. Note in passing that a reproducible drying procedure of the sieve has been used to guarantee a precise measurement of the degree of swelling. After measuring the current weight, the sieve is reinserted in the test fluid for the next time span. The degree of swelling is measured within the first 1080 s at 9 points in time for each absorption test.

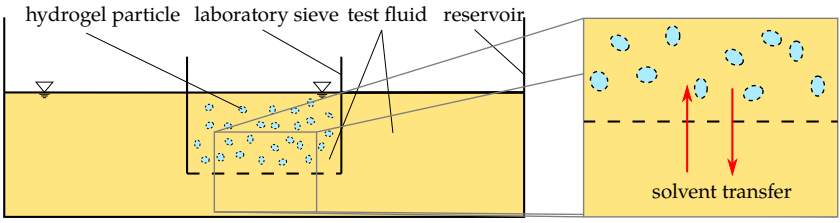

Figure 5.4: *Schematic view of the experimental setup for measuring the degree of swelling. A laboratory test sieve loaded with SAP particles is immersed in a test fluid with defined salt concentration. The weight of the hydrogel particles is measured over time to calculate the degree of swelling.*

5.2.2 Desorption tests

In contrast to the absorption tests, starting point for the desorption experiments is a granulate of maximum swollen SAP particles, i. e. swollen SAPs in demineralized water to the highest possible degree of swelling. In analogy to the absorption tests, the SAPs are inserted in NaCl solutions, while mass desorption in terms of the degree of swelling is again recorded at the same predefined points in time. For statistical purposes, the absorption as well as desorption tests have been repeated at least three times for each concentration.

5.2.3 Semi-cyclic tests

A semi-cyclic test is a sequence of multiple absorption and desorption regimes. This idea is realized by measuring the degree of swelling over time, while the ion concentration in the pore fluid follows a stair-case function. Therein, the ion concentration is held constant for a given time interval. Depending on the current concentration, the SAP particles are subjected to absorption or desorption. More specific, step functions for the concentration profiles are applied, which can be analytically expressed through

$$\rho^{F_s}(t) = \sum_{i=1}^{n} \tilde{\rho}_i^{F_s} \xi_{A_i}(t). \tag{5.28}$$

Herein, A_i denotes the i-th time interval corresponding to the i-th concentration $\tilde{\rho}_i^{F_s}$, while n is the number of defined intervals. The indicator function $\xi_{A_i}(t)$ is given with respect to the interval A_i as

$$\xi_{A_i}(t) = \begin{cases} 1 & t \in A_i \\ 0 & t \notin A_i \end{cases}. \tag{5.29}$$

Figure 5.5 illustrates the stair-case profile in an exemplary fashion for three intervals in terms of the salt mass fraction c^{F_s}.

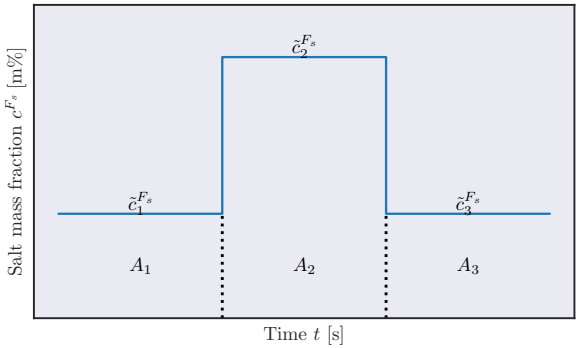

Figure 5.5: *Stair-case mass fraction profile according to* (5.28).

5.3 Experimental results

5.3.1 Absorption and desorption tests

The results for the absorption and desorption experiments are illustrated in Figure 5.6 for various NaCl concentrations. In order to visualize the high mass exchange rates, a logarithmic time scale has been chosen for both plots. The absorption and desorption curves indicate that the degree of swelling reaches an equilibrium value towards the end of the investigated time interval. To this end, the Equilibrium Degree of Swelling (EDS) q^∞ has been pragmatically defined as $q^\infty = q(t = 1080\,\mathrm{s})$, which seems to be a reasonable approximation according to the experimental findings. It should be highlighted that in the left plot of Figure 5.6 the water absorption behavior for an initially dry SAP granulate is recorded. Due to this fact, water absorption for all tested ion concentrations starts from a non-equilibrium condition. On the other hand, the results from the water desorption tests according to the testing setup described in chapter 5.2 are illustrated in the right plot in Figure 5.6. The water desorption occurs immediately after the swollen SAP particles come into contact with the saline bath solution. In contrast to the absorption experiments, the initial degree of swelling at $t = 0\,\mathrm{s}$ corresponds to the EDS for $c^{F_s} = 0.0\,\mathrm{m\%}$. However, the experimental desorption results for all tested concentrations are starting from the same initial condition.

It will be later shown in connection with the semi-cyclic tests that the dynamics of mass exchange is influenced by the initial conditions. To this end, the absorption and desorption experiments are used to investigate the EDS with respect to the external ion concentration. In case of demineralized water ($c^{F_s} = 0.0\,\mathrm{m\%}$), the EDS reaches a value of approximately $q = 270$. This value states the maximum degree of swelling for the tested SAP. It can be seen that the degree of swelling reduces dramatically by increasing the NaCl concentration in the external bath. To this end, the lowest NaCl mass fraction which has been tested, $c^{F_s} = 0.05\,\mathrm{m\%}$, reduces the EDS by 50% to $q = 135$. In gen-

eral, the results are highly sensitive with respect to deviations of the NaCl fractions in the range between 0.0 m% and 0.5 m%. On the contrary, the EDS shows only a slight reduction between 0.5 m% - 1.0 m%, which indicates a weak sensitivity in this regime.

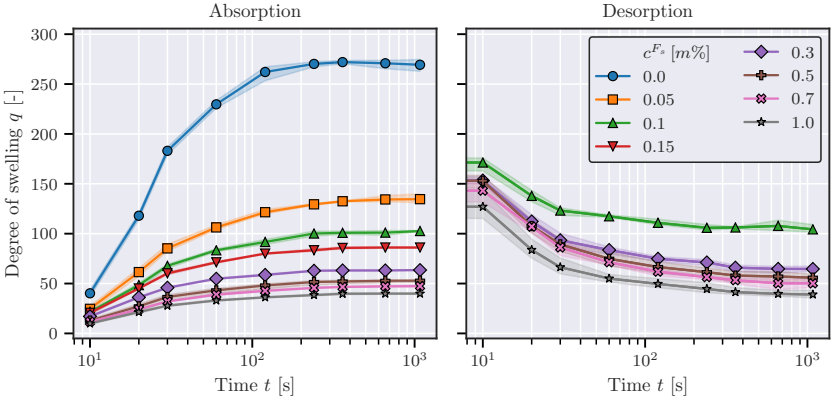

Figure 5.6: *The degree of swelling is measured over time for different NaCl concentrations to record the dynamics of mass exchange. Each marker indicates the mean value of at least three repeated measurements, while the shaded bands surrounding the bold lines represent the estimated confidence intervals with respect to the measured data points. The absorption experiments for each concentration are carried out for an initially dry SAP granulate, i. e. $q = 1$ (left). On the contrary, the desorption dynamics are investigated for initially swollen SAP particles (right). Note in passing that the initial degrees of swelling at $t = 0$ can not be illustrated due to the logarithmic time scale.*

In addition, to evaluate the reversibility of the mass exchange, the EDS values have been extracted from both test setups and have been plotted over the NaCl concentration (cf. Figure 5.7). It can be deduced that for the same ion concentrations in the test fluid, the EDS for absorption and desorption are identical in consideration of statistical deviations. To this end, the reversibility assumption is ensured for the tested hydrogel material. Since the EDS values have been experimentally recorded for a large number of ion concentrations, the experimental data can be fitted easily to an empirical function (cf. Figure 5.7). Here, the data is well represented through the rational algebraic function

$$q^{\infty}(c^{F_s}) = \frac{a_{q^\infty}\, c^{F_s} + b_{q^\infty}}{(c^{F_s})^2 + c_{q^\infty}\, c^{F_s} + d_{q^\infty}} \quad \text{with} \quad a_{q^\infty} = 9.552 \cdot 10^{-1}; \tag{5.30}$$
$$b_{q^\infty} = 1.385 \cdot 10^{-3}; \quad c_{q^\infty} = 1.689 \cdot 10^{-2}; \quad d_{q^\infty} = 5.144 \cdot 10^{-6}\,.$$

In the following course of this contribution, (5.30) is used to predict the EDS in order to compare it to the simulated results. Note that the absorption dynamics of SAPs with respect to the surrounding fluid chemistry were previously investigated for instance by Schröfl *et al.* [128]. However, a study with respect to the reversible absorption-desorption behavior was beyond the scope of their experimental investigation.

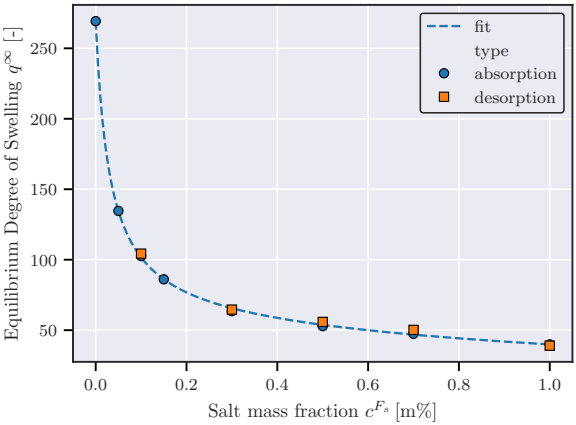

Figure 5.7: *Comparison between absorption and desorption EDS for different external NaCl concentrations. The bold line represents the empirical function* (5.30).

5.3.2 Semi-cyclic tests

It has been previously discussed that the initial conditions used in the absorption as well as desorption experiments can be viewed as very specific, i. e. absorption starts always from the dry state, while desorption is exclusively investigated for an equilibrium swollen SAP granulate in demineralized water. However, to gain insights in the dynamics of mass exchange, absorption and desorption cycles need to be performed for various initial conditions. Semi-cyclic absorption-desorption experiments are carried out to fulfill this demand.

The results corresponding to the semi-cyclic experiments are examined for three distinct concentration profiles and have been respectively illustrated in Figure 5.8. Each of the three experiments starts with an equilibrium initial condition. In order to ensure this requirement, the tested SAP granulate was immersed in a solution of fixed ion concentration for 1080 s, before the actual semi-cyclic experiment starts. For convenience, the dashed red lines in Figure 5.8 show the EDS with respect to the tested ion concentrations calculated by equation (5.30). It is worth mentioning in this context, that the measured equilibrium values are in good agreement to their calculated counterparts.

Next, the recorded data from the semi-cyclic experiments are prepared for analyzing the rate of mass exchange. Therefore, the data points represented by Figure 5.8 are subdivided into time intervals with constant external salt concentrations. For the sake of clarity, the data points corresponding to a particular time interval are illustrated by the same markers. According to the semi-cyclic experiments, each of the subdivided data sets starts more or less from an EDS (initial condition) corresponding to the pre-

vious constant salt concentration. To this end, these sequences can be viewed as individual absorption and desorption experiments, depending on their initial conditions. For the purpose of investigating the influence of the initial conditions on the rate of mass exchange, the subdivided data sets referring to the same ion concentration are plotted together. The results are consequently illustrated in Figure 5.9a, 5.10a, 5.11a and 5.12a. In Figure 5.9a the SAPs are immersed into demineralized water, while the markers are used to distinguish between the different initial conditions. More specific, the blue (circles) markers illustrate the absorption of SAP particles in demineralized water, which are previously swollen to equilibrium in a solution of $c^{F_s} = 0.1\,\mathrm{m}\%$. In analogy, the red (squares) and yellow (triangles) markers belong to initially swollen SAP particles in saline solutions of $c^{F_s} = 0.5\,\mathrm{m}\%$ and $c^{F_s} = 1.0\,\mathrm{m}\%$, respectively. Independently of the initial conditions, i. e. the EDS corresponding to the ion concentration in the previous time period, the tested SAPs are converging approximately to the same degree of swelling. The experimental results given in 5.10a, 5.11a and 5.12a can be interpreted in analogy, while the time-dependent absorption and desorption in $c^{F_s} = 0.1\,\mathrm{m}\%$, $c^{F_s} = 0.5\,\mathrm{m}\%$ and $c^{F_s} = 1.0\,\mathrm{m}\%$ is respectively investigated. Note that absorption is observed when the ion concentration in the previous time span was higher than the current ion concentration, while desorption takes place in the opposite case.

It can deduced that the mass desorption rate is generally faster in comparison to its absorption counterpart. This tendency will be later explained against the background of microstructural processes during mass exchange.

Furthermore, it should be pointed out that in case of demineralized water (Figure 5.9a), the initial degrees of swelling are far away from their equilibrium value of $q^{\infty} = 270$, especially for $q_0(c^{F_s} = 1.0\,\mathrm{m}\%)$. The measured degree of swelling in this case reveals that q at $t = 1000\,\mathrm{s}$ is slightly below the expected EDS of $q^{\infty} = 270$. Therefore, this most likely indicates that the tested time interval is too short to perfectly capture the EDS for relatively low initial degrees of swelling.

In summary, the presented subdivided data sets contain information about the equilibrium swelling state as well as for the dynamics of mass exchange for different initial conditions. In the following, the model parameters will be adapted to the subdivided data in order to mimic absorption and desorption processes in a reliable fashion.

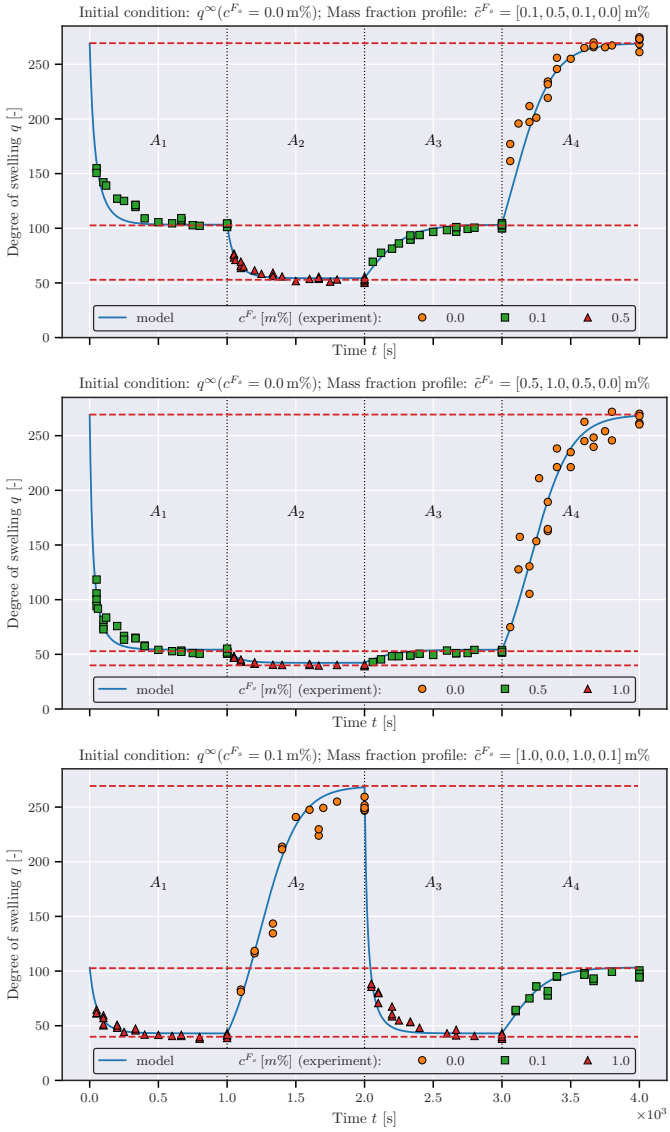

Figure 5.8: *A comparison of the simulated and experimental degree of swelling q for three different concentration profiles $\rho^{F_s}(t)$ are shown. The concentration profiles are represented by the general analytic expression of a step function* (5.28)*. Therein, the time intervals A_i for the indicator functions ξ_{A_i} are specified to the right-open intervals $A_i = \{t \in \mathbb{R} \mid (i-1)\cdot 10^3\mathrm{s} \leq t < i \cdot 10^3\mathrm{s}\}$. For convenience, each of the three absorption-desorption profiles is characterized with a specific vector of mass fraction amplitudes $\tilde{c}^{F_s} = \tilde{\rho}^{F_s}/\rho^{FR}$. The initial conditions in the semi-cyclic experiments corresponding to equilibrium swollen SAP particles in saline solutions with fixed concentration.*

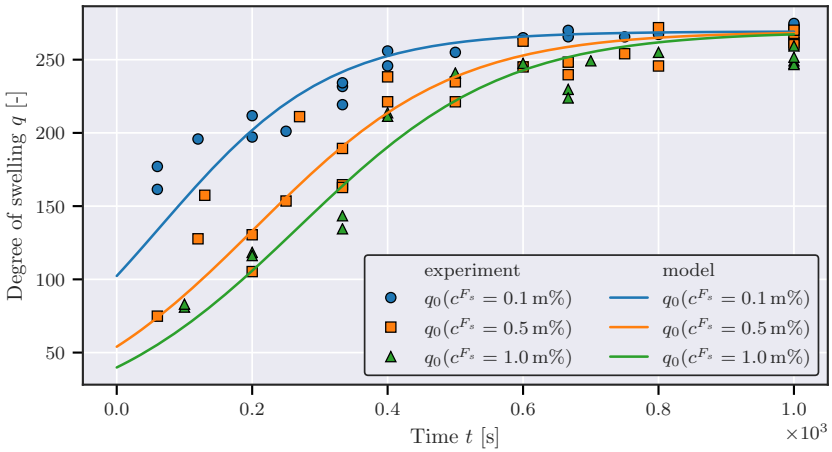

(a) Experimental degree of swelling and corresponding model prediction based on reconstructed parameters

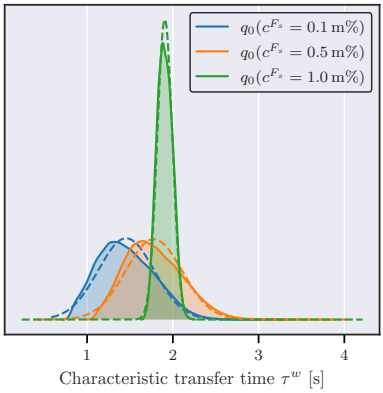

(b) Estimated distributions for the characteristic swelling time τ^w

Figure 5.9: *Experimental and numerical results for a constant salt mass fraction of* $c^{F_s} = 0.0\,\mathrm{m\%}$.

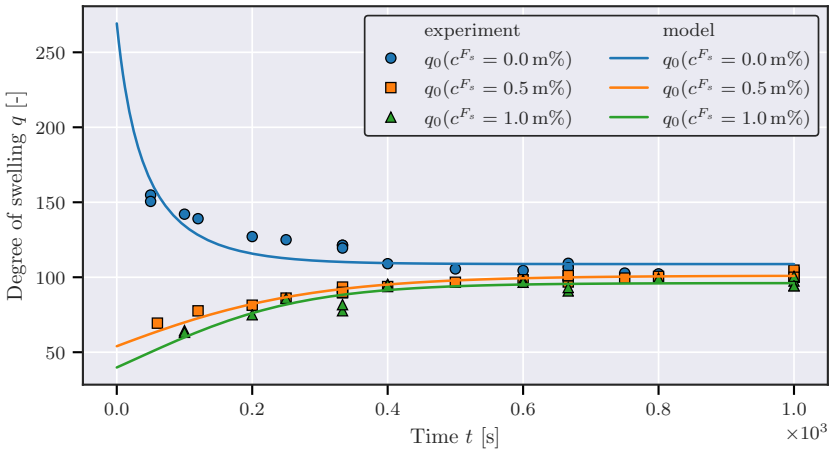

(a) Experimental degree of swelling and corresponding model prediction based on reconstructed parameters

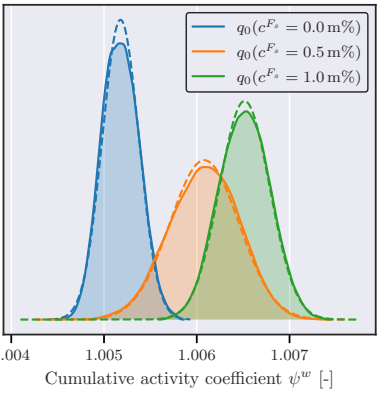

(b) Estimated distributions for the cumulative activity coefficient ψ^w

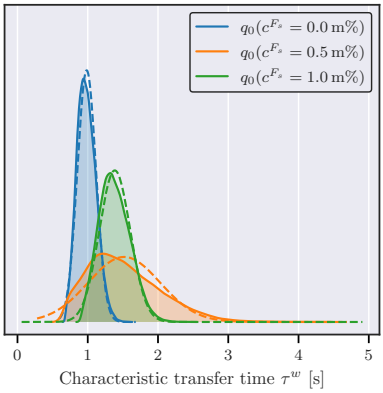

(c) Estimated distributions for the characteristic swelling time τ^w

Figure 5.10: *Experimental and numerical results for a constant salt mass fraction of* $c^{F_s} = 0.1\,\mathrm{m\%}$.

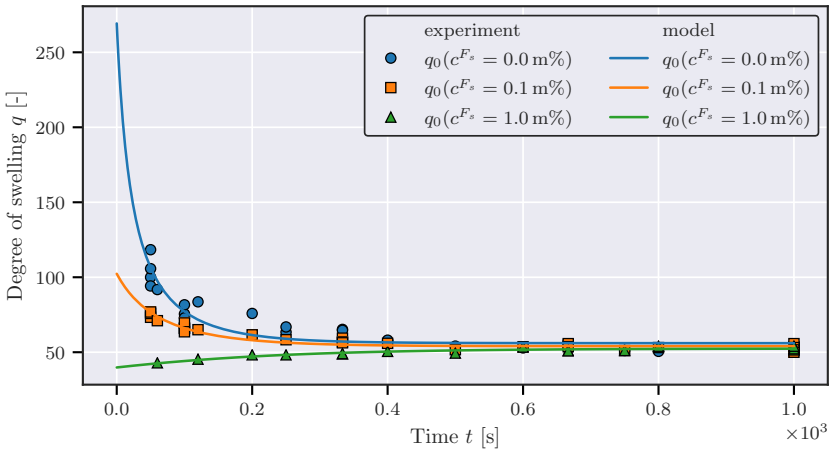

(a) Experimental degree of swelling and corresponding model prediction based on reconstructed parameters

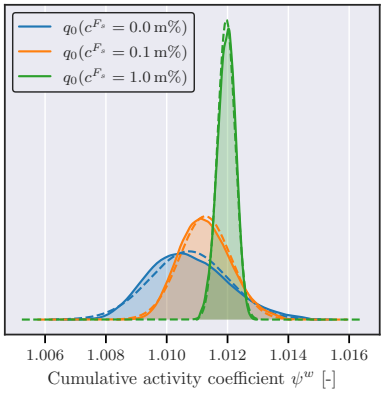

(b) Estimated distributions for the cumulative activity coefficient ψ^w

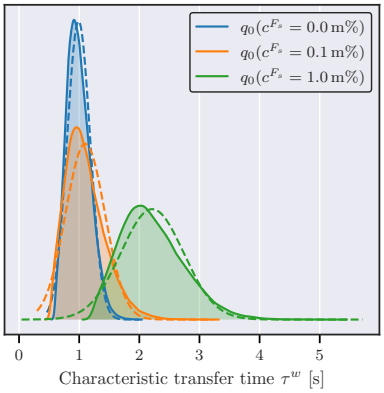

(c) Estimated distributions for the characteristic swelling time τ^w

Figure 5.11: *Experimental and numerical results for a constant salt mass fraction of* $c^{F_s} = 0.5\,\mathrm{m\%}$.

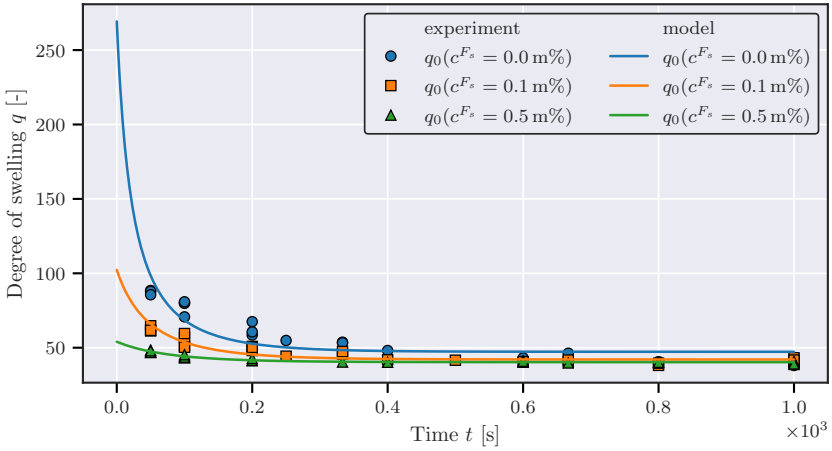

(a) Experimental degree of swelling and corresponding model prediction based on reconstructed parameters

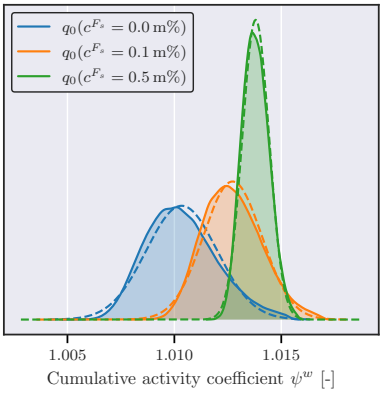

(b) Estimated distributions for the cumulative activity coefficient ψ^w

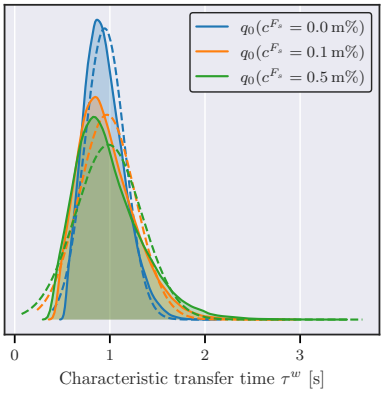

(c) Estimated distributions for the characteristic swelling time τ^w

Figure 5.12: *Experimental and numerical results for a constant salt mass fraction of* $c^{F_s} = 1.0\,\mathrm{m\%}$.

5.4 Parameter identification

5.4.1 Model assumptions with respect to the experimental data

Based on the experimental findings in the previous chapter, the reliability of the numerical model needs to be validated. In this context, the model parameters are calibrated to the experimental data from the semi-cyclic tests. Since the reversible inter-phase mass transfer is in the focus of the experimental study, the inert solid phase φ^S is dropped from the mixture model. By doing so, it is further assumed that the volume changes of the hydrogel due to mass transfer are not restricted by the pore space geometry. To this end, free swelling and de-swelling of the hydrogel are described here. Furthermore, according to the experimental setup, the volume of the water reservoir is significantly larger in comparison to the volume of the hydrogel phase. As a consequence, the absorption of aqueous solution by the SAP particles does not result in a significant change of n^F, such that the external NaCl concentration stays approximately constant. As a consequence, the evolution equation (5.12) can be dropped from the ODE system.

Without giving further details, a sensitivity analysis revealed that the degree of swelling is insensitive to changes in the transfer rate coefficient of mobile ions $\Gamma_0^{\pm}$. Note in passing that details regarding the sensitivity analysis are summarized in appendix A. Since the degree of swelling is the only experimentally observed quantity here, the dynamics of inter-phase ion exchange cannot be determined. To this end, the macroscopic hydrogel model is simplified by assuming instantaneous ($\Gamma_0^{\pm} \rightarrow \infty$) ion equilibrium between absorbed solution and pore fluid, which is also known as Donnan equilibrium [164]. As a consequence, the evolution equation in terms of absorbed salt (5.13) vanishes, such that the concentrations of positive and negative ions respectively calculate to

$$\rho_m^{fG^-} = -\frac{p_d}{2} + \sqrt{\left(\frac{p_d}{2}\right)^2 + q_d}\,, \tag{5.31}$$

$$\rho_m^{G^+} = \frac{p_d}{2} + \sqrt{\left(\frac{p_d}{2}\right)^2 + q_d}\,, \tag{5.32}$$

$$\text{with} \quad p_d = \frac{\phi}{1-\phi}\rho_m^{sG_{fc}}, \quad q_d = \left(\frac{\rho_m^{F_s}}{\psi^{\pm}}\right)^2 .$$

Further details with respect to the Donnan equilibrium have been previously discussed in chapter 3.3.1.

The time derivative of the degree of swelling q is obtained by (4.9a) and leads to

$$\partial_t(q) = \frac{1-\phi}{(\phi)^{\beta}} \frac{\Delta\mu_m^w}{RT\tau^w} \quad \text{with} \quad \tau^w = \frac{n^{sG}\rho^{sGR}}{\Gamma_0^w}\,, \tag{5.33}$$

where τ^w is the characteristic transfer time for water. Note that τ^w was previously introduced by Gajo & Loret [59] for modeling the water exchange of expansive clays.

5.4.2 Model parameters

The complete list of undetermined model parameters is given through

$$\mathcal{Q} = \{\chi, \rho_m^{sG_{fc}}, \nu, \Gamma_0^w, \beta, \psi^w, \psi^\pm\}\,, \tag{5.34}$$

where a part of these parameters cannot be uniquely identified by using the experimentally measured degree of swelling. In the following, this set will be reduced by applying reasonable assumptions.

A preliminary study showed that the mixing contribution $\Delta\mu_{mix}^w$ plays only a subordinate role in the chemical potential difference $\Delta\mu^w$ of charged hydrogels (cf. Figure 5.13). Therefore, the Flory-Huggins interaction parameter χ is here neglected from the list of model parameters.

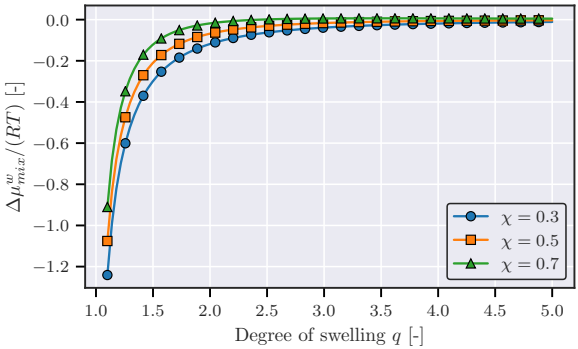

Figure 5.13: *Mixing contribution of the chemical potential difference over the degree of swelling for different values of the interaction parameter χ. The contribution has only a significant impact in the region of low swelling degrees. In contrast, high degrees of swelling are mainly driven by the ionic contribution $\Delta\mu_{ion}^w$.*

In case of demineralized water, the EDS q^∞ depends on the parameters in the chemical potential of water, namely the cross-linking density ν and the intrinsic FCD $\rho_m^{sG_{fc}}$. Motivated by the fact that the influence of the intrinsic FCD and the cross-linking density on the EDS are opposed, the dimensionless number

$$\kappa = \frac{\rho_m^{sG_{fc}}}{\nu} \tag{5.35}$$

is introduced. The amount of absorbed solution increases with increasing intrinsic FCD, while increasing the cross-linking density decreases the EDS. The dimensionless number κ is analytically calculated from the stationary condition of the chemical potential difference of water

$$\Delta\mu^w(\kappa, \nu, \psi^w = 1, q = q^\infty) = 0\,, \tag{5.36}$$

where use has been made of the assumption that in case of demineralized water, ψ^w is calibrated equal to 1. Therefore, κ is a function of ν and $q^\infty(c^{F_s} = 0.0\,\mathrm{m}\%)$, while the EDS from the experimental results, i. e. $q^\infty = 270$, is used to determine the corresponding value of κ. Note in passing that the parameter ν cannot be identified exclusively with the mass exchange data and stays therefore undetermined. In this context, Wack [159] estimated an *effective* cross-linking density through mechanical testing of hydrogels. However, this topic is beyond the scope of the current analysis. For reasons of simplicity, $\psi^\pm$ is set to 1 such that ψ^w accounts exclusively for the resulting non-ideal behavior of water in the presence of mobile ions. Finally, the set of model parameters (5.34) reduces to

$$\mathcal{Q}_{red} = \{\psi^w, \Gamma_0^w, \beta\}\,. \tag{5.37}$$

5.4.3 Metropolis-Hastings algorithm

The Metropolis-Hastings algorithm [68], a non-deterministic random walk algorithm based on a Monte-Carlo scheme, is presented in order to identify the model parameters. In this section, the procedure is first presented in a general fashion and will be subsequently applied to the specific model. Therefore, it is assumed that the model is governed by a system of ODEs, while the solution is fitted to the experimental data. The unknown model parameters are captured in the vector $\mathbf{k}$ and the corresponding solution vector of the ODE system is represented by $\mathbf{y}(t, \mathbf{k})$. The experimental data is given at discrete times, while each experiment has been repeated for statistical purposes. Finally, the measured data points are represented in the observation vector $\mathbf{d}^{obs}$. More specific, $\mathbf{d}^{obs}$ captures the degree of swelling at discrete points in time. The corresponding model prediction, i. e. the calculated degree of swelling, is denoted by $\mathbf{d}$. In general, $\mathbf{d}$ is related to the solution of the model $\mathbf{y}$ through

$$\mathbf{d} = \mathbf{g}(\mathbf{y})\,, \tag{5.38}$$

where $\mathbf{g}$ is called the *forward operator* [145]. A post processing step after solving the ODE system is usually necessary in order to relate the solution of the forward problem to the observed data points. In this particular case, observations in the experimental setting is limited to q, therefore, d is explicitly given by $d = q$. Next, a cost function has to be established in order to quantify the goodness of the corresponding set of model parameters. Therefore, the L^2 error norm (SSQ = Sum of Squares) has been chosen in order to minimize the error between the target vector $\mathbf{d}^{obs}$ and the estimated prediction $\mathbf{d}$, namely

$$SSQ = ||\mathbf{d} - \mathbf{d}^{obs}||_2^2\,. \tag{5.39}$$

Further it is assumed that the SSQ is Gaussian distributed by the probability density

$$P(\mathbf{d}^{obs}, \mathbf{q}) = \frac{1}{\sqrt{(2\pi)^{m^{obs}}\sigma^2}} \exp\left(-\frac{||\mathbf{d}(\mathbf{k}) - \mathbf{d}^{obs})||_2^2}{2\sigma^2}\right)\,, \tag{5.40}$$

where σ^2 and m^{obs} represent the mean error variance in the experimental data and the number of data points, respectively. In order to minimize (5.39), the following non-deterministic, iterative approach is followed:

1. The algorithm is initialized by choosing an initial guess for the set of parameters $\mathbf{k}_{old} = \mathbf{k}_0$. Next, the *SSQ* is calculated (5.39) by solving the forward problem and the probability density (5.40) is evaluated.

2. A new candidate for the set of model parameters is then proposed through a random variation, namely $\mathbf{k}_{new} = \mathbf{k}_{old} + \Delta\mathbf{k}$, where the i-th component of the variation is drawn from the uniform distribution $\Delta k_i \sim \mathcal{U}(-r_i, r_i)$. Herein, r_i denotes the search radius corresponding to the i-th parameter. In this approach, r_i is chosen in an adaptive manner in order to obtain an efficient algorithm, cf. appendix B. The *SSQ* (5.39) is calculated for the new candidate $\mathbf{k}_{new}$ and inserted in the probability density function (5.40). Note in passing that an alternative approach would be to draw the i-th parameter variation from a normal distribution $\Delta k_i \sim \mathcal{N}(0, \sigma_{i,pro})$, where $\sigma_{i,pro}$ is known as the standard deviation of the proposal distribution.

3. The probability ratio corresponding to the proposed and the old parameter vector is introduced upon the new candidate is accepted or rejected (Metropolis rule). To this end, the parameter set $\mathbf{k}_{new}$ is accepted if the following condition holds

$$\Theta \leq \min\left(1, \frac{P(\mathbf{d}^{obs}, \mathbf{d}(\mathbf{q}_{new}))}{P(\mathbf{d}^{obs}, \mathbf{d}(\mathbf{q}_{old}))}\right), \quad \Theta \sim \mathcal{U}(0,1)\,, \tag{5.41}$$

   where Θ is a random number between 0 and 1.

4. If the proposed parameter vector $\mathbf{k}_{new}$ leads to a lower error in comparison to $\mathbf{k}_{old}$, the probability ratio becomes larger than 1, which always results in acceptance. Note that probability ratios less then 1 are accepted upon statistics. To this end, probability ratios which are slightly lower than 1 are more likely accepted then probability ratios far away from 1. In case of acceptance, the parameter set is updated according to $\mathbf{k}_{old} = \mathbf{k}_{new}$ and the algorithm continues with step 2.

5. The algorithm stops after a predefined number of runs. A discussion about stopping criteria and chain length is carried out by Sinharay [136].

In contrast to deterministic acceptance rules, the Metropolis rule probably accepts parameter sets in some iterations, which does not improve the *SSQ* with respect to the previous step. Finally, the Metropolis-Hastings algorithm proposed in this section has the advantage that it does not converge to local extrema like many gradient-based optimization algorithms. In addition, the Metropolis-Hastings algorithm will not only be used to identify the set of best-fitting parameters, moreover, it is used to estimate probability distributions for the model parameters depending on the accuracy (standard deviation) of the experimental data.

5.4.4 Estimated model parameters

In the following, the undetermined set of model parameters (5.37) is fitted to the semicyclic data (cf. Figure 5.8) by using the previously described Metropolis-Hastings algorithm. More precisely, the subdivided time sequences of constant ion concentrations

are used as observational data. Finally, an individual parameter optimization for both equilibrium and dynamic parameters has been performed with respect to each recorded time sequence. The best-fit parameters have been respectively chosen for the simulated results illustrated in Figure 5.9a, 5.10a, 5.11a and 5.12a. A discussion concerning the optimized model parameters (5.37) is carried out in the following. Since the Metropolis-Hastings algorithm is used for the parameter reconstruction, distributions for the model parameters are obtained rather than only the best-fitting parameter set.

Equilibrium parameters: Chemical potential function The chemical potential difference $\Delta\mu^w$ depends on ψ^w and the previously calculated value of κ through (5.36). Note that ψ^w accounts for the non-ideal water activity for free and absorbed water in the presence of mobile ions in the pore fluid. Figure 5.10b, 5.11b and 5.12b respectively show the estimated probability distributions for ψ^w. Note that the shaded areas represent the Kernel Density Estimations (KDEs), while the dashed lines correspond to fitted normal distributions. Both representations are obtained from the discrete results of the Metropolis-Hastings algorithm. All distributions in the same Figure are related to a particular ion concentration in the pore fluid, but starting from different initial values for q. More detailed explanations have been presented in chapter 5.3. Furthermore, it can be easily seen that the KDEs for ψ^w are represented with high accuracy through the normal distributions for each reconstruction. Since ψ^w determines the EDS, the estimated means are correlated for the same tested ion concentration. Deviations between the mean values are consequently caused by variations in the experimental data. Recall that in case of demineralized water, ψ^w is set to 1 by definition, such that ψ^w accounts for the non-ideal behavior in the presence of mobile ions in the pore fluid. The expected values from the reconstructed distributions of ψ^w are averaged for each fixed ion concentration and fitted to an empirical function. Therefore, the following rational algebraic function is postulated

$$\begin{aligned} \psi^w(c^{F_s}) &= \frac{a_{\psi^w} c^{F_s} + b_{\psi^w}}{c^{F_s} + c_{\psi^w}} \quad \text{with} \quad a_{\psi^w} = 1.023; \\ b_{\psi^w} &= 0.190; \quad c_{\psi^w} = 0.190, \end{aligned} \tag{5.42}$$

while the result is illustrated in Figure 5.14. Since ν cannot be determined from the experiments, the estimated data as well as the fit is shown for two distinct values of ν in order to illustrate its impact. The continuous function (5.42) will be further used in the following to predict the equilibrium state with respect to c^{F_s} in the range from $0.0\,\mathrm{m}\%$ - $1.0\,\mathrm{m}\%$.

Non-equilibrium parameters: dynamics of water transfer It has been postulated that the dynamics of mass exchange is governed by the swelling-dependent transfer law (5.27) with the previously discussed model parameters Γ_0^w and β. The shape of the swelling-dependent part is determined by the exponent β. Here it is assumed that β is a constant intrinsic material property. Thus, it is set to $\beta = 1.9$ in the following analysis, which is in agreement to proposed values in the literature (cf. chapter 5.1). As a consequence, exclusively the linear scaling factor Γ_0^w in the dynamic law is optimized.

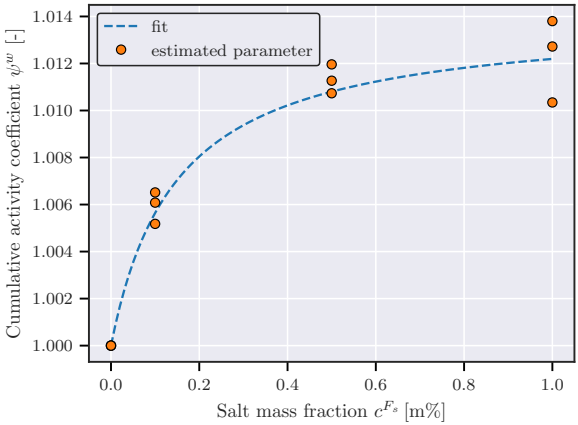

Figure 5.14: *Estimated parameter ψ^w fitted to a continuous function. Herein, a weighted least square method has been used.*

Not in passing that for convenience the results are expressed through the previously introduced characteristic swelling time τ^w, while τ^w is linked to Γ_0^w through (5.33).

Similar to the results corresponding to ψ^w, the probability distributions for τ^w are represented by Figure 5.9b, 5.10c, 5.11c and 5.12c. Again, the KDEs and fitted normal distributions in each figure correspond to the same external ion concentration. First, it can be deduced from the peaks of the estimated distributions, that the characteristic swelling times are generally shorter for desorption in comparison to absorption. For instance, this fact can be observed clearly in Figure 5.11c, where the estimated values for the desorption time are approximately $1\,\mathrm{s}$, while in contrast the estimated absorption time is approximately $2\,\mathrm{s}$. This behavior is also reflected through the corresponding model predictions. From a physical point of view, the dynamics become more comprehensible by looking again to the coupled microstructural phenomena within the hydrogel. In case of swelling, the elastic forces in the polymer network counteract the volume expansion, which is accompanied with the influx of water. In contrast, the relaxation of the reset forces within the polymer network tend to accelerate the desorption process. To this end, water will be squeezed out by the polymer network [27] and higher transfer rates, especially for high degrees of swelling, are observed on the macroscale.

Second, it is important to highlight that the individually estimated distributions for τ^w exhibit some remarkable similarities. To emphasize this fact, the estimated characteristic swelling times obtained from the normal distributions are plotted in Figure 5.15a over the number of calibration experiments. The markers are used to classify the estimated values into absorption and desorption dynamics, which are in the following denoted by τ^w_{abs} and τ^w_{des}. The parameter identification revealed a fundamental result towards the rate of mass exchange. Therefore, τ^w_{abs} and τ^w_{des} respectively deviate around

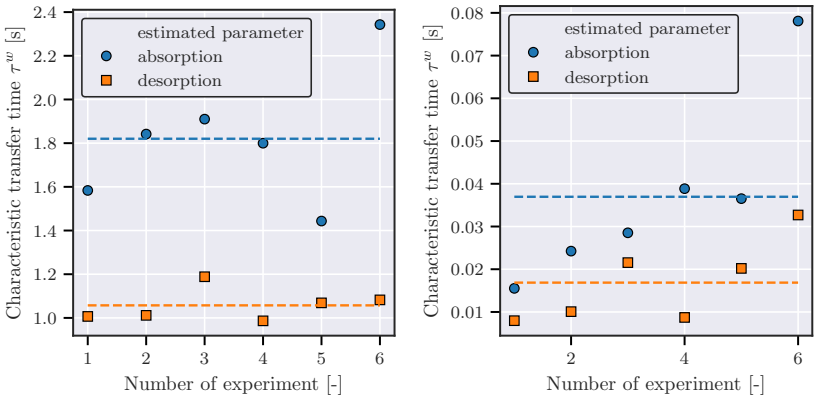

(a) $\beta = 1.9$ **(b)** $\beta = 1.0$

Figure 5.15: *The characteristic swelling time has been individually estimated for each experimental time sequence. Therefore, the model dynamics has been fitted to 6 absorption and 6 desorption experiments, while colored markers are used for distinction. The dashed lines show the mean values with respect to the estimated results.*

their mean values, which are represented by the dashed lines in Figure 5.15a. Note that the deviations for τ^w_{abs} are higher in comparison to τ^w_{des}. However, the results emphasize that τ^w is a constant rather than a function of the ion concentration.

Following this idea implies that the dynamics can be described by a swelling- and not a ion concentration-dependent part in (5.27). To this end, the individually estimated values for τ^w are substituted by their means either for absorption $\bar{\tau}^w_{abs}$ or desorption $\bar{\tau}^w_{des}$, while the external ion concentrations are not taken into account. Moreover, the constant values are assigned dynamically in the modeling approach based on

$$\tau^w = \begin{cases} \bar{\tau}^w_{abs}\,, & \text{for } \Delta\mu^w \leq 0 \\ \bar{\tau}^w_{des}\,, & \text{for } \Delta\mu^w > 0 \end{cases} \,. \tag{5.43}$$

The proposed dynamic law (5.27) in combination with the postulated constant characteristic swelling times yields to a simplified parameter reconstruction. Following this, the characteristic swelling times for absorption and desorption can be fitted to one experiment in each case, instead of examining the dynamics for different ion concentrations.

Finally, it is worth mentioning that the choice of β is crucial in this context. Choosing β arbitrary, for instance $\beta = 1$, results in a not sufficient description of the swelling-dependent part in (5.27). As a consequence, the estimated characteristic swelling times τ^w are scattered, such that the individual values deviate strongly from their mean values of absorption and desorption, respectively (cf. Figure 5.15b). A reliable prediction

of the mass exchange dynamics for neither absorption nor desorption is clearly fulfilled when the calculated mean values are used in such case.

5.4.5 Model evaluation

In the following, the derived model is evaluated in a two-step procedure. In Figure 5.8 the model prediction together with the experimental data, which are used for parameter optimization, are illustrated. In contrast to the results showed in Figure 5.9a - 5.12a, the model parameter ψ^w follows from the empirical law (5.42) and the characteristic swelling time τ^w is set to (5.43). The parameters used for the simulation are represented in Table 5.1. It is remarkable to see, that the EDS can be reproduced by the

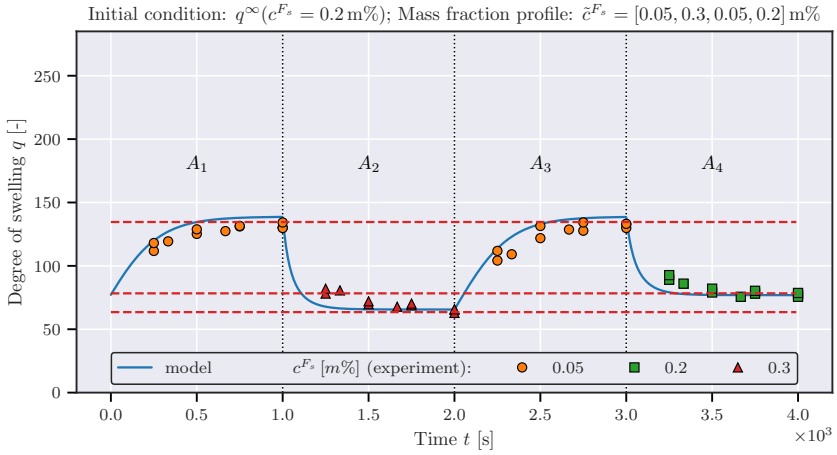

Figure 5.16: *Comparative study between model prediction and unknown experimental data. Initial condition:* $q^\infty(c^{F_s} = 0.2\,\mathrm{m\%})$*; Concentration profile:* $\tilde{c}^{F_s} = [0.05, 0.3, 0.05, 0.2]\,\mathrm{m\%}$*, cf. Figure 5.8.*

model with very high accuracy. This behavior can be observed for both absorption and desorption across the whole range of tested ion concentrations. In case of absorption, the predicted rate of mass exchange coincides with the experimental data. However, the de-swelling rate of mass exchange appears to be overestimated, while this behavior becomes clearly visible for high initial degrees of swelling, namely for desorption from the maximum swollen state. In this approach, absorption and desorption dynamics are modeled by the same swelling-dependent transfer law with constant scaling exponent β. It should be pointed out that a more sophisticated approach would probably lead to a better fit for the de-swelling dynamics, however, relating an even more complex physical-motivated transfer law to the microscopic diffusion process is challenging.

Besides evaluating the model to experimental data previously used for calibration, Figure 5.16 shows the model prediction with respect to a new semi-cyclic experiment. Note

Parameter	Value	Unit
M_m^w	18.015	g/mol
M_m^+	22.99	g/mol
M_m^-	35.45	g/mol
z^+	1	-
z^-	-1	-
z^{fc}	-1	-
ρ^{FR}	1000	kg/m^3
ρ^{sGR}	1000	kg/m^3
ρ^{fGR}	1000	kg/m^3
F	96 485.332	C/mol
R	8.314	J/(mol K)
T	293.15	K
ν	30	mol/m^3
n_0^{sG}	1×10^{-3}	-
n_0^S	0	-
$\psi^{\pm}$	1	-
β	1.9	-
κ	1.355×10^3	-
$\tilde{V}_m^w$	1.8015×10^{-5}	m^3/mol
$\bar{\tau}_{abs}^w$	1.7864	s
$\bar{\tau}_{des}^w$	1.0684	s

Table 5.1: *Material parameters and constants used for the simulation.*

that the red dashed lines are used again for convenience and indicate the expected EDS based on (5.30). Against the background that $\psi^w(c^{F_s})$ has only fitted to the values available in Figure 5.14, the predicted EDS shows a good performance throughout the experiment. In addition, the absorption dynamics is able to mimic the experimental data, however, the predicted desorption dynamics deviate again more significantly from the experimental results. More precisely, the desorption rate is overestimated in comparison to the experimental data, such that equilibrium is reached earlier. However, this result is not surprising when the previously calibrated desorption dynamics are taken into consideration, cf. Figure 5.8.

Chapter 6:
Transport and infiltration of polymer solutions in porous media

6.1 Introduction

Transport of non-Newtonian fluids through porous media has various technical applications in different fields such as chemical, groundwater and petroleum engineering [109, 150]. The specific applications ranging from modeling blood flow through the kidney in biomechanics [103] to air filtration processes [78] and deep filtration in granular porous media [97]. Besides the previous mentioned applications, polymer solutions are frequently used for polymer flooding to enhance the efficiency of oil production in low permeable reservoirs [4, 52, 77, 112, 133, 146, 161]. Herein, polymer solutions are injected into the reservoir rock to mobilize and transport the oil towards the production well, cf. Figure 6.1. Lenormand *et al.* [91] studied the principal mechanisms behind immiscible fluid displacement in porous media. In this context, viscous fingering, capillary fingering and stable displacement were correlated to the capillary number and the viscosity ratio of the two immiscible pore fluids. For negligible capillary effects, a stable displacement front can be ensured for a high viscosity contrast in favor of the injected fluid. On the contrary, viscous fingering is observed when the viscosity contrast between injected and displaced fluid is smaller than a specific threshold value. Since

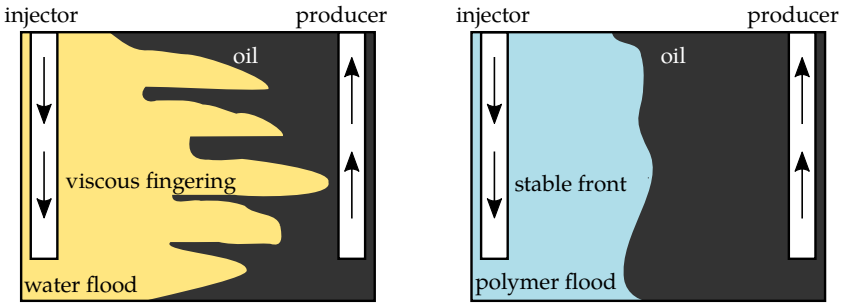

Figure 6.1: *Schematic comparison between sweep efficiency during water and polymer flooding [112]. The displacement of immiscible fluids in porous media is dominated by capillary and viscous forces. In case of negligible capillary effects, viscous fingering or stable displacement is observed with respect to the viscosity ratio of the fluids. Note that the polymer solution causes in general a higher viscosity contrast, such that a stable displacement front can be achieved in polymer flooding. For further details regarding the physical mechanisms, the interested reader is referred to the pioneering work by Lenormand et al. [91].*

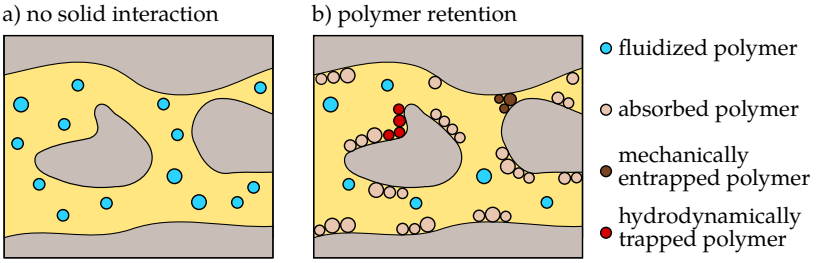

Figure 6.2: *Schematically illustrations of polymer solutions in the pore space of a porous media.*

the used polymer solutions are more viscous than pure water, a better sweep efficiency of the reservoir can be obtained by polymer flooding in comparison to conventional techniques [60].

Predicting the flow of polymer solutions through porous media, together with the accompanied interactions with the solid skeleton, is in the focus of this chapter. Figure 6.2 illustrates the interaction between the polymer gel and the solid skeleton. From a physical point of view, the fluidized polymer particles are captured through three distinct mechanisms to the solid skeleton: physio-chemical adsorption, mechanical entrapment and hydrodynamical retention. Note that further details are presented in chapter 1.

In this chapter, the transport and infiltration processes of polymer solutions through porous media are modeled. The chosen continuum mixture model is deduced from the general multi-phase mixture model, cf. Figure 4.1. The transport of the polymer solution is accounted through a generalized Darcy's law, which accounts for the non-Newtonian in situ viscosity and also for the permeability reduction due to the capture of polymer particles to the solid skeleton. The particle capture is modeled through kinetic laws in the mass balance equations. Laboratory core flooding experiments are further discussed to introduce well-established experimental settings and methods. Based on the experimental procedure, the model parameters in the proposed constitutive relations are estimated from experimental results. The ultimate goal is to obtain a calibrated model based on simple core flooding experiments, which is able to predict the very challenging task of polymer flooding on the field scale.

6.2 Multi-phase model for polymer solution flow through porous media

A continuum mixture approach for modeling polymer solution flow through a linear elastic solid skeleton φ^S is represented through the model decomposition in Figure 6.3. The polymer solution is a mixture of an aqueous pore liquid φ^F and a polymer gel φ^G. Here, φ^F is treated as the carrier fluid for the fluidized polymer particles φ^G. The

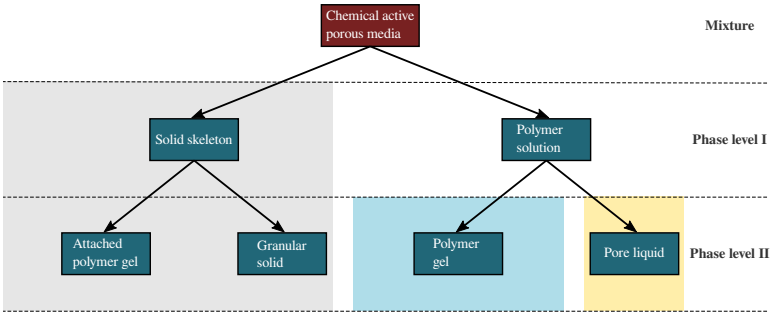

Figure 6.3: *Decomposition of the reduced transport and infiltration model.*

solution is consequently defined by

$$\varphi^L = \varphi^F \cup \varphi^G \,. \tag{6.1}$$

In addition, taking the attachment of polymer gel to the solid skeleton φ^S into account yields to

$$\varphi^S = \varphi^K \cup \varphi^A \,, \tag{6.2}$$

where φ^K denotes the intrinsic, clean solid skeleton without any accumulation, while φ^A refers to the captured particles. The captured polymer gel φ^A is subdivided into reversibly φ^A_{rev} and irreversibly φ^A_{irr} attached polymer, such that

$$\varphi^A = \varphi^A_{rev} \cup \varphi^A_{irr} \,. \tag{6.3}$$

The multi-phase model is concluded by the following representation of phases

$$\varphi = \{\varphi^S \cup \varphi^L\} \quad \Rightarrow \quad \left\{\varphi^A_{rev} \cup \varphi^A_{irr} \cup \varphi^K \cup \varphi^F \cup \varphi^G\right\},$$

while the saturation condition (2.4) yields to

$$\sum_\alpha n^\alpha = \underbrace{n^K + \underbrace{n^A_{rev} + n^A_{rev}}_{:=n^A}}_{:=n^S} + \underbrace{n^F + n^G}_{:=n^L} = 1 \,. \tag{6.4}$$

The polymer gel saturation of the solution, which denotes the volume of φ^G with respect to the volume of the solution φ^L, reads

$$s^G = \frac{n^G}{n^L} \,; \quad s^G + s^F = 1 \,. \tag{6.5}$$

In Figure 6.4, the volumetric composition of a porous media model without particle capture is compared to a model which incorporates both reversible and irreversible capture mechanisms.

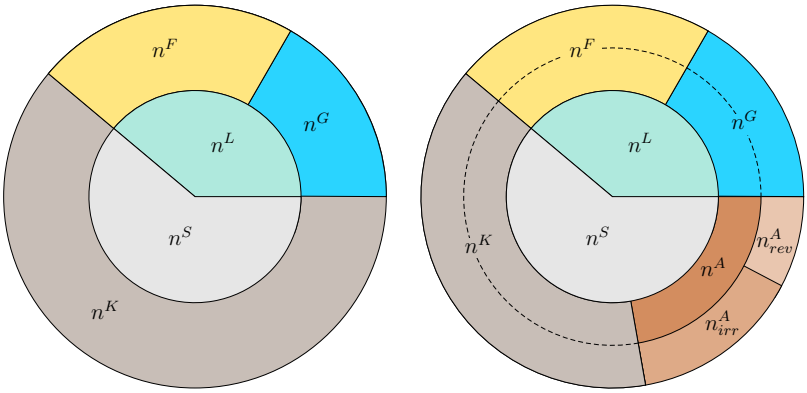

(a) No polymer retention

(b) Two-site polymer attachment mechanism: reversible and irreversible polymer attachment

Figure 6.4: *Volume fractions of porous media models with and without polymer capture.*

6.2.1 Governing equations

Volume balance equations Each phase is treated as material incompressible, such that the material time derivative of the intrinsic phase density vanishes in (2.33), namely $(\rho^{\alpha R})'_S = 0$. Furthermore, the mass balance equation (2.33) simplifies to a volume balance

$$(n^\alpha)'_S + \operatorname{div}(\mathbf{q}^\alpha) + n^\alpha \operatorname{div} \mathbf{v}_S = \hat{n}^\alpha \,, \tag{6.6}$$

where the Darcy velocity of φ^α reads $\mathbf{q}^\alpha = n^\alpha \mathbf{v}_{\alpha S}$. Note that the density production $\hat{\rho}^\alpha$ in (2.33) has been multiplicatively split into a volume production term $\hat{n}^\alpha$ times the corresponding intrinsic phase density $\rho^{\alpha R}$. More precisely, particle capture is modeled through inter-phase volume transfer between the fluidized polymer gel and the solid skeleton. Since particle capture is a priori classified into a reversible and an irreversible contribution, the total volume production due to polymer capture reads $\hat{n}^A = \hat{n}^A_{rev} + \hat{n}^A_{irr}$. Here, the solid skeleton exclusively exchanges volume with the fluidized polymer, such that the volume production of φ^G consequently calculates to $\hat{n}^G = -\hat{n}^A$. As the name suggests, reversibly captured polymer gel is in general able to detach from the solid skeleton and become part of the fluidized polymer gel again. It is assumed that the intrinsic density of captured and fluidized polymer is the same, i. e. $\rho^{AR} = \rho^{GR}$.

Linear momentum balance The linear momentum balance of the overall mixture is obtained by summing over the phases, which leads to

$$\operatorname{grad} p - \operatorname{div}(\mathbf{T}^S_E) = \hat{n}^A \rho^{GR} \mathbf{v}_{GS}, \tag{6.7}$$

where $\sum_\alpha \hat{\mathbf{p}}^\alpha = \hat{\rho}^A \mathbf{v}_G - \hat{\rho}^A \mathbf{v}_S$ and $\mathbf{T} = -p\mathbf{I} + \mathbf{T}^S_E$ have been used in the derivation.

Kinematic restrictions The captured particles by the solid skeleton exhibit by definition the same motion as the intrinsic solid, such that the following restriction holds for the phase velocities

$$\mathbf{v}_K = \mathbf{v}_{A,rev} = \mathbf{v}_{A,irr} = \mathbf{v}_S \,. \tag{6.8}$$

Specific volume balance equations Against the background of the previously introduced assumptions, the volume balances for φ^K, φ^A_{rev} and φ^A_{irr} reduce to the following set of evolution equations

$$(n^K)'_S = -n^K \mathrm{div}\, \mathbf{v}_S \,, \tag{6.9}$$
$$(n^A_{rev})'_S = \hat{n}^A_{rev} - n^A_{rev} \mathrm{div}\, \mathbf{v}_S \,, \tag{6.10}$$
$$(n^A_{irr})'_S = \hat{n}^A_{irr} - n^A_{irr} \mathrm{div}\, \mathbf{v}_S \,. \tag{6.11}$$

An evolution equation for the porosity is obtained by summing (6.9) - (6.11) , which yields to

$$(n^L)'_S = -\hat{n}^A - n^A \mathrm{div}\, \mathbf{v}_S \,. \tag{6.12}$$

The first contribution in (6.12) illustrates the porosity decrease with the ongoing particle capture, while the second terms accounts for a deformation-dependent porosity change. Next, the volume balance of the material incompressible mixture is obtained by summing (6.6) over all phases

$$\mathrm{div}\, (\mathbf{q} + \mathbf{v}_S) = 0 \,, \tag{6.13}$$

where the sum of volumetric fluxes has been substituted by the polymer solution flux $\mathbf{q}$ given by

$$\mathbf{q} = n^L \mathbf{v}_{LS} = \mathbf{q}^G + \mathbf{q}^F \,. \tag{6.14}$$

By exploiting the kinematic identity $\mathbf{v}_{\alpha S} = \mathbf{v}_{LS} + \mathbf{v}_{\alpha L}$, the filter velocities can be expressed through

$$\mathbf{q}^\alpha = s^\alpha \mathbf{q} + \Delta \mathbf{q}^\alpha \qquad \forall\, \alpha \in \{F, G\} \,, \tag{6.15}$$

while $\Delta \mathbf{q}^\alpha = n^\alpha \mathbf{v}_{\alpha L}$ is the relative flux of φ^α with respect to the polymer solution. It is worth mentioning that the filter velocity of both pore liquid and polymer gel are driven by a convective part, $s^\alpha \mathbf{q}$, and a diffusive part, $\Delta \mathbf{q}^\alpha$. In various applications, the latter one is governed by the dispersion phenomena [58]. Note that the sum of dispersion fluxes places a restriction according to

$$\sum_\alpha n^\alpha \mathbf{v}_{\alpha L} = \mathbf{0} \rightarrow \Delta \mathbf{q}^G = -\Delta \mathbf{q}^F \,. \tag{6.16}$$

In the present contribution, constitutive models for the Darcy velocity of the solution $\mathbf{q}$ and the dispersion flux of the polymer gel $\Delta \mathbf{q}^G$ are developed. To this end, (6.15) is inserted in the volume balance equation of the hydrogel (6.6), which finally leads to

$$(s^G)'_S\, n^L + \mathrm{grad}\, s^G \cdot \mathbf{q} + \mathrm{div}\, \Delta \mathbf{q}^G = \hat{n}^G (1 - s^G) \,. \tag{6.17}$$

Remark on solid velocity: The balance equations are derived for arbitrary solid velocities, however, quasi-static deformations $\mathbf{v}_S \approx \mathbf{0}$ are assumed in the following course of this work. As a consequence, the material time derivative reduces to $(\,\cdot\,)'_S = \partial(\,\cdot\,)/\partial t$, where the convective contribution $\operatorname{grad}(\,\cdot\,) \cdot \mathbf{v}_S$ has been neglected.

6.3 Constitutive modeling

6.3.1 Linear elastic solid

In case of a linear elastic solid skeleton, the effective stress tensor is given by the Hookean model

$$\mathbf{T}_E^S = \lambda_{eff} \operatorname{tr}(\boldsymbol{\varepsilon}_S)\mathbf{I} + 2\mu_{eff}\boldsymbol{\varepsilon}_S\,, \tag{6.18}$$

where λ_{eff} and μ_{eff} are the effective Lamé parameters of the solid skeleton and $\boldsymbol{\varepsilon}_S$ is the linearized version of the Green-Lagrange strain tensor $\mathbf{E}_S$, which computes to

$$\boldsymbol{\varepsilon}_S = \frac{1}{2}\left[(\operatorname{grad}\mathbf{u}_S) + (\operatorname{grad}\mathbf{u}_S)^T\right]\,. \tag{6.19}$$

The effective Young's modulus E_{eff} and the Poisson ratio ν_{eff} are calculated from the Lamé parameters to

$$E_{eff} = \frac{\mu_{eff}(3\lambda_{eff} + 2\mu_{eff})}{\lambda_{eff} + \mu_{eff}} \quad \text{and} \quad \nu_{eff} = \frac{\lambda_{eff}}{2(\lambda_{eff} + \mu_{eff})}\,. \tag{6.20}$$

Note that the previously introduced elastic material parameters denote effective quantities of the solid skeleton, which deviate in general from the intrinsic solid material with vanishing pore space.

6.3.2 Kinetic polymer capture

Particle attachment processes can be classified into equilibrium and kinetic capture. Equilibrium capture is usually modeled through isotherms, from which the amount of captured substance is linked to the thermodynamic state of the system. Since the theoretical development of the Langmuir-isotherm [87], numerous isotherms were developed to describe the uptake of substrate. Note that besides the Langmuir-isotherm, the more general Freundlich-isotherm is also a widely used candidate [83, 98, 127]. By applying any type of isotherm, it is a priori assumed that the system reaches equilibrium instantaneously. The interested reader is referred to an excellent review on adsorption-isotherms published by Foo & Hameed [57].

In contrast, kinetic or non-equilibrium particle capture is a time-dependent process. The rate of particle capture is usually expressed through the superposition of attachment and detachment rates. An equilibrium state for the amount of captured particles is reached when the competitive phenomena yield a steady-state. Note in passing that equilibrium and non-equilibrium adsorption phenomena can also occur superimposed

within a specific material. For instance, Schijven & Hassanizadeh [127] modeled the attachment of viruses to soil and accounted for both adsorption-isotherms and kinetic adsorption in their model.

General capture model The volume production terms are modeled through a multi-site kinetic model, which was proposed by Tosco & Sethi [151] in a similar way to model straining and physico-chemical attachment/detachment of iron particles in porous media. After representing the model in a general fashion, the active sites are identified as reversible and irreversible attachment.

The model can be viewed as a generalization of the classical filtration theory used by [126, 129, 153, 154] to model kinetic adsorption phenomena in porous media. The generic attachment/detachment model for the k-th active site reads

$$\hat{n}_k^A = n^L \, k_{a,k} \, \psi_{a,k} \, s^G - k_{d,k} n_k^A \,, \quad \text{with} \quad \psi_{a,k} = 1 + a_k (n_k^A)^{b_k} \,. \tag{6.21}$$

Herein, $k_{a,k}$ denotes the deposition or attachment rate, while a_k and b_k are model parameters in the k-th attachment function $\psi_{a,k}$. The latter traces back to works by Bradford *et al.* [33, 34] and are used to account for blocking and ripening phenomena induced by particle capture [3, 81]. The first term in (6.21) states that the attachment rate increases linearly with increasing polymer saturation s^G. In the limiting case, when the saturation vanishes, no further particle capture is possible, which is a meaningful result from a physical point of view. The superimposed detachment is modeled through a linear relation in terms of the volume fraction of already captured particles, while $k_{d,k}$ denotes the detachment rate. Therefore, it is ensured that particle detachment vanishes when $n_k^A = 0$. Note that irreversible capture is obtained by setting $k_{d,k} = 0$, cf. [125, 155].

Bradford *et al.* [33], Schijven & Hassanizadeh [127], Tiraferri *et al.* [147] and Yao *et al.* [166] suggested a linear relation for the attachment rate $k_{a,k}$ in terms of the Darcy velocity through

$$k_{a,k} \propto |\mathbf{q}| \Longrightarrow k_{a,k} = \lambda_{a,k} \, |\mathbf{q}| \,, \tag{6.22}$$

where $\lambda_{a,k}$ denotes the filtration coefficient, which measures the particle capture probability per unit length of the particle trajectory [167]. Note that (6.22) was originally proposed in the classical filtration theory. Furthermore, a Langmuir-type attachment function

$$\psi_{a,k} = 1 - \left(\frac{n_k^A}{n_{k,crit}^A} \right)^{b_k} \tag{6.23}$$

is applied, where $n_{k,crit}^A$ denotes the critical volume fraction of captured particles corresponding to the k-th active site. Non-linear particle capture mechanisms are obtained by choosing $b_k \neq 1$, cf. Figure 6.5.

Specific attachment model A two-site capture model is used in this contribution to account individually for *reversible* as well as *irreversible* particle capture, i. e. $k \in \{rev, irr\}$. Following the general attachment and detachment model (6.21), the volume production

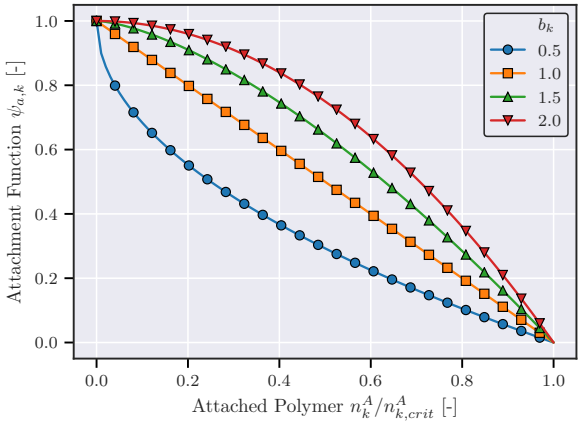

Figure 6.5: *Investigation of particle attachment function. A linear relation is obtained for* $b_k = 1$.

terms are respectively specified to

$$\hat{n}_{rev}^A = n^L k_{a,rev} \psi_{a,rev} s^G - k_{d,rev}\, n_{rev}^A \quad \text{with} \quad \psi_{a,rev} = 1 - \left(\frac{n_{rev}^A}{n_{rev,crit}^A} \right) , \tag{6.24}$$

$$\hat{n}_{irr}^A = n^L k_{a,irr} \psi_{a,irr} s^G \quad \text{with} \quad \psi_{a,irr} = 1 - \left(\frac{n_{irr}^A}{n_{irr,crit}^A} \right) . \tag{6.25}$$

Note that the vanishing detachment rate in (6.25) results in irreversible particle capture. Moreover, in the reversible case, the equilibrium amount $n_{rev,eq}^A$ is less than the critical volume fraction $n_{rev,crit}^A$ due to the influence of the detachment rate. The equilibrium volume fraction of reversibly captured polymer particles $n_{rev,eq}^A$ is connected to the critical value $n_{rev,crit}^A$ through

$$n_{rev,eq}^A = n_{rev,crit}^A \left(1 + \frac{n_{rev,crit}^A k_{d,rev}}{n^L s^G k_{a,rev}} \right)^{-1} , \tag{6.26}$$

which has been derived based on the equilibrium condition $\hat{n}_{rev}^A = 0$ in (6.24). Note that $n_{irr,eq}^A = n_{irr,crit}^A$ holds in the irreversible case.

Remark on inter-phase mass exchange due to polymer attachment: The evaluation of the entropy inequality dictates a thermodynamic-consistent expression for the mass transfer $\hat{\rho}^A$ given by (4.71), which reduces to

$$\hat{\rho}^A \propto - \frac{\partial \Psi^K}{\partial W} , \tag{6.27}$$

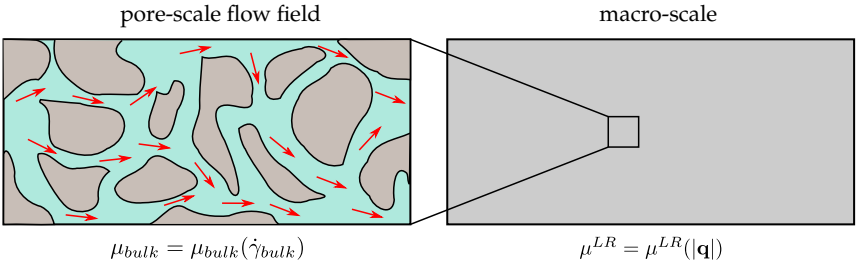

Figure 6.6: *On the pore-scale, the polymer solution shows a shear rate-dependent viscosity. The shear rate is exclusively a pore-scale quantity, which is related to the actual flow field. The upscaled effective viscosity on the macroscale is formulated in terms of the Darcy velocity, cf. [26]. Linking the effective to the bulk viscosity is a crucial step in the multi-phase modeling approach.*

under the assumption of negligible second order velocity terms. Since the linear relation $W \propto n^A = \sum_k n_k^A$ results from the incompressibility condition, the above equation can be finally rewritten to

$$\hat{n}_k^A \propto -\frac{\partial \Psi^K}{\partial n_k^A} \quad \forall k \in \{rev, irr\}\,. \tag{6.28}$$

The specific kinetic particle capture rates (6.24) and (6.25) are phenomenologically-motivated. However, the proposed kinetic laws satisfy the entropy inequality expressed through (6.28).

6.3.3 Convective and diffusive transport

Seepage flow Under the assumption of laminar flow, the friction force $\operatorname{div} \mathbf{T}_E^L$ in the linear momentum balance of the polymer solution (2.38) has an insignificant impact in comparison to the viscous momentum production $\hat{\mathbf{p}}^L$ and is therefore neglected. A thermodynamic-consistent expression for the seepage velocity $\mathbf{v}_{LS}$ under quasi-static conditions is finally obtained by (4.64).

Seepage flow of Newtonian fluids through porous media are on the macroscale usually modeled by Darcy's law, which presents a linear relationship between the flux and the applied pressure gradient. However, many polymer solutions exhibit a non-Newtonian rheology, i. e. the fluid shows an intrinsic shear rate-dependent viscosity. The functional dependency of the bulk viscosity $\mu_{bulk} = \mu_{bulk}(\dot{\gamma}_{bulk})$ is usually modeled through analytic expressions in terms of the shear rate $\dot{\gamma}_{bulk}$. For instance, shear-thickening and shear-thinning behavior can be respectively modeled through the power-law fluid model (Ostwald-de-Waele model), while more complex behavior can be described through the Carreau or Cross model. Furthermore, the inherent model parameters are usually estimated through rheometer experiments. In this context, the interested reader is referred to a comprehensive review regarding non-Newtonian fluid models published by Sochi [140].

Against the background of non-Newtonian fluids, a generalized Darcy's law, which is consistent with the mathematical representation of the classical expression, is postulated by

$$\mathbf{q} = n^L \mathbf{v}_{LS} = -M^L \operatorname{grad} p \quad \text{with} \quad M^L = \frac{k^S}{\mu^{LR}}, \tag{6.29}$$

where an isotropic mobility M^L has been assumed in the derivation. Note that inertia as well as body forces have been neglected throughout the derivation. Herein, k^S and μ^{LR} represent the intrinsic permeability and the effective polymer solution viscosity on the Darcy-scale, respectively. In the classical case of Newtonian fluids, the effective viscosity matches the constant bulk viscosity, i. e. $\mu^{LR} = \mu_{bulk}$. However, for non-Newtonian fluids, the shear rate-dependent viscosity can not be directly formulated on the macroscale since the shear rate is a pore-scale quantity, cf. Figure 6.6. Therefore, the effective viscosity is formulated as a function of the Darcy velocity, i. e. $\mu^{LR} = \mu^{LR}(|\mathbf{q}|)$ [26]. In order to carry out simulations on the macroscale, a crucial step is to find an appropriate relation between the bulk and the effective viscosity.

Here, it is assumed that the effective and the bulk viscosity are governed by the same functional constitutive model, while the effective viscosity is reformulated to $\mu^{LR} = \mu^{LR}(\dot{\gamma}_{pm}(|\mathbf{q}|))$. Moreover, $\dot{\gamma}_{pm}$ denotes the porous media shear rate, i. e. the effective shear rate expected within the pore space [150, 151, 171]. The porous media shear rate can be correlated to the Darcy velocity through a semi-analytic approach based on capillary bundle models, cf. [40]. According to this approach, Cannella *et al.* [37] derived a constitutive relation between the effective porous media shear rate and the Darcy velocity. In the derivation, a power-law model was used for the rheology of the bulk viscosity. Note that details concerning the derivation are explained in the appendix C. The following linear simplification proposed by Zamani *et al.* [170] is used in the further course of this work

$$\dot{\gamma}_{pm} = \alpha_{pm} \frac{|\mathbf{q}|}{\sqrt{k^S n^L}}, \tag{6.30}$$

where α_{pm} denotes an empirical parameter, often referred to as shift factor. This parameter accounts for the deviation between the bulk viscosity observed in rheometer experiments and the in situ viscosity for polymer solutions flowing through porous media [99, 170]. Note that α_{pm} is a complex parameter depending on both the porous media geometry and the solution rheology.

Dispersive transport In addition, the relative transport of polymer gel $\Delta\mathbf{q}^G$ in (6.17) is modeled through a Fickian-type model

$$\Delta\mathbf{q}^G = -D^G \operatorname{grad} s^G, \tag{6.31}$$

where D^G denotes the isotropic dispersion coefficient of the polymer gel. In polymer flooding, the transport of polymer gel is typically convection-dominated, while a discussion is carried out in section 6.5.

Remark on the dissipative contribution due to convective and dispersive transport: Note that (6.31) is postulated from a phenomenological point of view, however, it can be shown that the Fickian-type dispersion model satisfies the dissipation inequality. Starting point of the derivation is the dissipation in the material induced by the independent seepage velocities

$$- \mathbf{v}_{FS} \cdot \left[\hat{\mathbf{p}}^F - p \operatorname{grad} n^F\right] - \mathbf{v}_{GS} \cdot \left[\hat{\mathbf{p}}^G - p \operatorname{grad} n^G\right] \geq 0\,, \tag{6.32}$$

which can be reformulated to

$$- \mathbf{v}_{LS} \cdot \left[\hat{\mathbf{p}}^L - p \operatorname{grad} n^L\right] - \mathbf{v}_{FL} \cdot \left[\hat{\mathbf{p}}^F - p \operatorname{grad} n^F\right] - \mathbf{v}_{GL} \cdot \left[\hat{\mathbf{p}}^G - p \operatorname{grad} n^G\right] \geq 0\,, \tag{6.33}$$

where $\hat{\mathbf{p}}^L = \hat{\mathbf{p}}^F + \hat{\mathbf{p}}^G$ has been used in the derivation. Next, the inter-phase momentum interaction terms are postulated by

$$\hat{\mathbf{p}}^F = p \operatorname{grad} n^F - \mathbf{R}^F \cdot \mathbf{v}_{LS} - \mathbf{R}^{FL} \cdot \mathbf{v}_{FL}\,, \tag{6.34}$$

$$\hat{\mathbf{p}}^G = p \operatorname{grad} n^G - \mathbf{R}^G \cdot \mathbf{v}_{LS} - \mathbf{R}^{GL} \cdot \mathbf{v}_{GL}\,, \tag{6.35}$$

while $\mathbf{R}^\alpha$ and $\mathbf{R}^{\alpha L}$ denote positive-definite, second-order resistance tensors for seepage and dispersive flow, respectively. Furthermore, the following thermodynamic admissible coupling between the resistance tensors is applied

$$\mathbf{R}^\alpha = s^\alpha \mathbf{R}^L \quad \text{and} \quad \mathbf{R}^{\alpha L} = s^\alpha \mathbf{R}^{GS} \quad \forall \alpha \in \{F, G\}\,. \tag{6.36}$$

Herein, $\mathbf{R}^L$ and $\mathbf{R}^{GS}$ are again second-order tensors. As a consequence, the momentum interaction of the polymer solution reduces to

$$\hat{\mathbf{p}}^L = p \operatorname{grad} n^L - \mathbf{R}^L \cdot \mathbf{v}_{LS}\,, \tag{6.37}$$

while the kinematic restriction (6.16) has been exploited in the derivation. Finally, the dissipation inequality (6.33) can be subdivided in a seepage and a dispersion contribution through

$$-\mathbf{v}_{LS} \cdot \left[-\mathbf{R}^L \cdot \mathbf{v}_{LS}\right] \geq 0\,, \tag{6.38}$$

$$-\mathbf{v}_{FL} \cdot \left[-\mathbf{R}^{FL} \cdot \mathbf{v}_{FL}\right] - \mathbf{v}_{GL} \cdot \left[-\mathbf{R}^{GL} \cdot \mathbf{v}_{GL}\right] \geq 0\,, \tag{6.39}$$

while (6.38) satisfies the entropy inequality. In addition, substituting the Fickian-type approach for the dispersion velocities

$$\mathbf{v}_{FL} = -(\mathbf{R}^{FL})^{-1} \cdot \operatorname{grad} s^F\,, \tag{6.40}$$

$$\mathbf{v}_{GL} = -(\mathbf{R}^{GL})^{-1} \cdot \operatorname{grad} s^G \tag{6.41}$$

in (6.39) satisfies the kinematic restriction (6.16) as well as the dissipation inequality.

6.3.4 Permeability damage

In addition to the non-Newtonian viscosity model, another non-linearity arises in (6.29) due to the permeability evolution. Therefore, the permeability of the solid skeleton $k^S(n^A_{rev}, n^A_{irr})$ is affected through particle attachment and detachment. The decrease of k^S is in the literature known as permeability damage [18, 19, 167]. An empirical function in terms of the volume fractions of captured polymer, previously used by Bedrikovetsky *et al.* [18], is applied here

$$k^S(n^A_{rev}, n^A_{irr}) = \frac{k^S_0}{1 + \beta_{rev} n^A_{rev} + \beta_{irr} n^A_{irr}} \,. \tag{6.42}$$

Herein, β_{rev} and β_{irr} are the formation damage coefficients due to the reversible and irreversible capture mechanism, respectively, while k^S_0 is the intrinsic permeability of the solid skeleton without any captured particles.

Remark on difference between permeability damage function and Kozeny-Carman equation: The semi-empirical Kozeny-Carman equation is widely used for estimating the permeability of granular materials, cf. [38]. To this end, the permeability can be expressed through the porosity by

$$k^S = k^S_0 \left[\frac{(n^L)^3}{(1-n^L)^2}\right] \left[\frac{(1-n^L_0)^2}{(n^L_0)^3}\right] , \qquad \text{with} \quad k^S_0 = \frac{d^2_{eff}}{C_{KC}} \frac{(n^L_0)^3}{(1-n^L_0)^2} \,, \tag{6.43}$$

where C_{KC} denotes the Kozeny-Carman constant and d_{eff} is the effective particle diameter of the granular solid matrix. Herein, C_{KC} is usually assumed to be 5 in case of spherical solid particles. Figure 6.7 shows a comparison between the permeability evolution according to the Kozeny-Carman model (6.43) and the permeability damage function (6.42), while both permeabilities are normalized by k^S_0. Note in passing that the effective particle diameter does not have an influence on the normalized permeability.

6.3.5 Effective dynamic viscosity

Modeling the in situ rheology of polymer viscosities in porous media is a very challenging task since the characteristic behavior depends generally on the effective shear rate behavior as well as on the polymer concentration. In the following, a few prominent viscosity models are presented, which are frequently used to model the effective viscosity of non-Newtonian polymer solutions. Note that the choice is limited here to generalized Newtonian fluid models (time-independent), which can be mathematically represented through

$$\tau_{eff} = \mu^{LR}(\dot{\gamma}_{pm})\dot{\gamma}_{pm} \,, \tag{6.44}$$

where τ_{eff} denotes the effective shear stress.

A simple generalization of the Newtonian fluid model is obtained by the Power Model (PM)

$$\mu^{LR}_{PM}(\dot{\gamma}_{pm}) = K_{PM} \mu^{FR}(\dot{\gamma}_{pm})^{n_{PM}-1} \,. \tag{6.45}$$

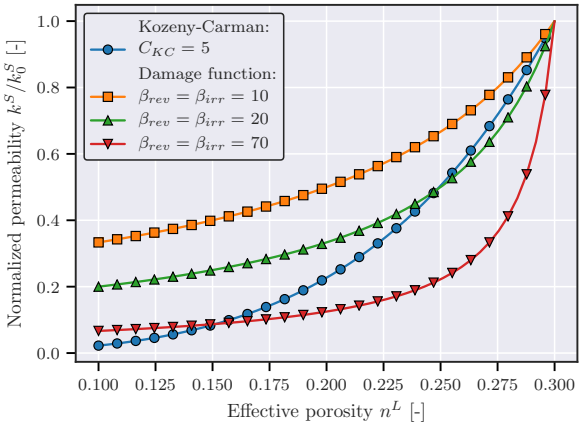

Figure 6.7: *Permeability evolution with respect to the effective porosity n^L. The Kozeny-Carman model is compared to the permeability damage function (6.42), while the permeability has been normalized by k_0^S. Note that k_0^S corresponds to the initial permeability at $n_0^L = 0.3$.*

Herein, K_{PM} and n_{PM} are model parameters and μ^{FR} has been additionally introduced to relate the solution viscosity to the carrier fluid φ^F. The model represents shear-thickening for $n_{PM} > 1$ and shear-thinning for $n_{PM} < 1$, while $n_{PM} = 1$ denotes the Newtonian case. The effective viscosity is plotted over the shear rate in Figure 6.8 (left).

However, it is well-known that most polymer solutions exhibit Newtonian behavior within low and high shear rate regimes, while at moderate shear rates the same fluids show a shear-thinning (pseudoplastic) behavior [5, 122, 169]. From a microscopic point of view, this behavior can be explained by the fact that with increasing shear rate, weak bonds within the polymer solution are destroyed [41, 96]. At high shear rates, many dilute polymer solution converge again to a Newtonian viscosity [96]. This more complex solution rheology can be for instance represented through the Carreau Model (CM)

$$\mu_{CM}^{LR}(\dot{\gamma}_{pm}) = \mu_\infty + \frac{\mu_0 - \mu_\infty}{[1 + (\lambda_{CM}\,\dot{\gamma}_{pm})^2]^{(1-n_{CM})/2}}\,, \tag{6.46}$$

where μ_0 and μ_∞ denote respectively the plateau viscosities for the Newtonian regimes at low and high shear rates, while λ_{CM} and n_{CM} are additional model parameters, which are influencing the shape of the viscosity function with increasing shear rate.

It was experimentally observed that the rheology of polymer solutions in porous media deviate from the expected shear-thinning behavior determined in rheometer experiments [5, 110, 169]. In contrast to the expected rheology for purely shear-thinning fluids, the viscosity of the polymer solution flowing through a porous matrix increases at high shear rates. This behavior is frequently explained by the fact that at high shear rates the

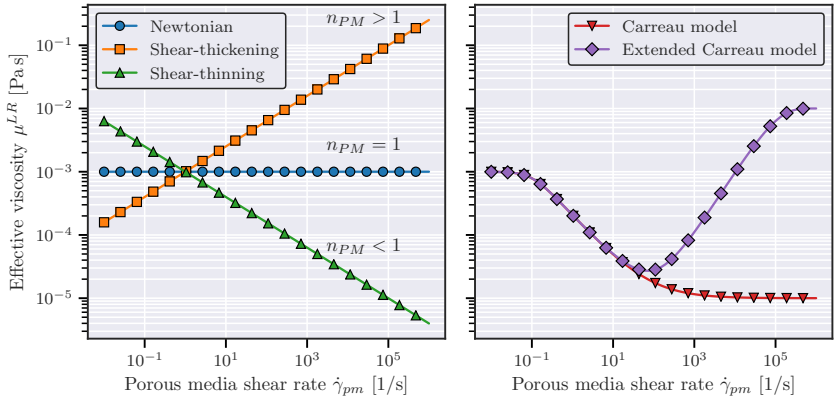

Figure 6.8: *Comparison between Power Model , Carreau Model and Extended Carreau Model. The effective viscosity is plotted over the porous media shear rate. The Power Model is able to describe shear-thickening, shear-thinning as well as Newtonian behavior depending on the exponent n_{PM} (left). The Carreau Model shows purely shear-thinning behavior, while the Extended Carreau Model is able to mimic a shear-thickening effect at high shear rates (right).*

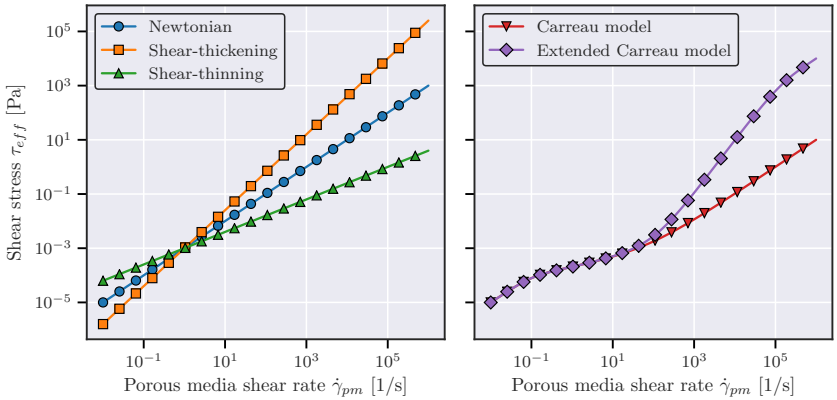

Figure 6.9: *The effective shear stress $\tau_{eff} = \mu^{LR}(\dot{\gamma}_{pm})\dot{\gamma}_{pm}$ is plotted over the porous media shear rate for the viscosity models illustrated in Figure 6.8.*

extension becomes more dominant than the shear rate [140]. The Carreau Model (6.46) as well as the Power Model (6.45) cannot sufficiently represent the effective rheology over a large shear rate regime in closed form. To overcome this drawback, an extension to the Carreau Model was proposed by Delshad *et al.* [46] and most recently by Azad

& Trivedi [15]. According to [46], the Extended Carreau Model (ECM) reads

$$\mu_{ECM}^{LR}(\dot{\gamma}_{pm}) = \mu_\infty + \frac{\mu_0 - \mu_\infty}{[1 + (\lambda_{CM}\dot{\gamma}_{pm})^2]^{(1-n_{CM})/2}} + \mu_{ECM}[1 - \exp(-\beta_{ECM}N_{deb})]^{n_{ECM}-1}\,, \tag{6.47}$$

where μ_{ECM}, n_{ECM} and β_{ECM} denote the extensional parameters, while N_{deb} is the Deborah number. Since N_{deb} increases with shear rate, the second term models the shear-thickening behavior at high shear rates. A comparison between the Carreau Model and the Extended Carreau Model is illustrated in the right plot in Figure 6.8.

Remark on generalized Darcy-type law: Note that the generalized Darcy-type law (6.29) was initially derived for laminar flow conditions. However, modeling shear-thickening at high shear rates, which is equivalent to high Darcy velocities (cf. (6.30)), probably requires one to account for inertia terms in (6.29). In this context, the interested reader is referred to the work by Tosco *et al.* [150], in which a generalized Darcy-Forchheimer equation was systematically derived for non-Newtonian fluid flow through porous media. The effective shear-thickening behavior observed on the macroscale at high flow rates was correlated to non-linear inertia terms.

Remark on concentration-dependent viscosity models: The mobility of fluidized polymer particles become more restricted at higher polymer concentrations, such that the inter-particle forces result in an increased flow resistance of polymer solutions on the macroscale [41]. In this context, Delshad *et al.* [47] proposed an empirical concentration-dependent viscosity model at zero shear rate, i. e. a constitutive law for μ_0. They calibrated a polynomial expression in terms of the concentration to rheometer experiments. Note that Tosco & Sethi [151] used a similar approach to estimate the effective zero shear viscosity of iron particle suspensions in porous media. In order to fully characterize the shear rate- and concentration-dependent behavior of a specific polymer solution requires experimental investigations of a large range of shear rates and concentrations.

6.4 Initial Boundary Value Problem (IBVP)

Weak forms of the governing equations are derived for the purpose of implementation in a finite element code. To this end, the strong forms for the

- linear momentum balance of the mixture (6.7),
- volume balance of the mixture (6.13),
- and the volume balance of the mobile hydrogel phase (6.17)

are multiplied by test functions and integrated over the domain Ω, thus

$$\int_{\Omega} \left[\operatorname{div}\left(\mathbf{T}_E^S - p\mathbf{I}\right) \cdot \operatorname{grad} \delta\mathbf{u}_S - \hat{n}^A \rho^{GR} \mathbf{v}_{GS}\, \delta\mathbf{u}_S\right] \mathrm{d}v = \int_{\Gamma_{\mathbf{u}_s}} \bar{\mathbf{t}} \cdot \mathbf{n}\, \delta\mathbf{u}_S \,\mathrm{d}a \tag{6.48}$$

$$\int_{\Omega} \left[\mathbf{q} \cdot \operatorname{grad} \delta p \; - \operatorname{div} \mathbf{v}_S\, \delta p\right] \mathrm{d}v = \int_{\Gamma_p} \bar{q}\, \delta p \,\mathrm{d}a\,, \tag{6.49}$$

$$\begin{aligned} &\int_{\Omega} \left[\left(-(s^G)'_S\, n^L - (1-s^G)\hat{n}^A - \operatorname{grad} s^G \cdot \mathbf{q}\right) \delta s^G + \Delta\mathbf{q}^G \cdot \operatorname{grad} \delta s^G\right] \mathrm{d}v \\ &= \int_{\Gamma_{sG}} \Delta\bar{q}^G \delta s^G \mathrm{d}a\,. \end{aligned} \tag{6.50}$$

Herein, $\delta\mathbf{u}_S$, δp and δs^G respectively denote the test functions corresponding to the primary variables, i. e. the solid displacement $\mathbf{u}_S$, the hydraulic pressure p and the gel saturation s^G. Closure of the problem requires boundary and initial conditions. Therefore, the following initial conditions are prescribed for the primary variables

$$\mathbf{u}_S = \mathbf{u}_{S,0}\,, \qquad p = p_0\,, \qquad s^G = s_0^G\,, \qquad \forall \mathbf{x} \in \Omega_0 \times t_0\,. \tag{6.51}$$

The boundary of the domain Γ is given as union of the Dirichlet boundary Γ_D and Neumann boundary Γ_N, i. e. $\Gamma = \Gamma_D \cup \Gamma_N$. Furthermore, Dirichlet boundary conditions, or boundary conditions of first type, prescribe the values of the primary variables, while Neumann boundary conditions, or boundary conditions of second type, prescribe the derivatives of the primary variables. More specific, $\Gamma_{\mathbf{u}_s}$, Γ_p and Γ_{sG} correspond to the Neumann boundaries of the displacement, pressure and saturation field, respectively. According to this, the following set of boundary conditions are applied to the Dirichlet and Neumann boundaries

$$p = \bar{p}, \qquad s^G = \bar{s}^G, \qquad \mathbf{u}_S = \bar{\mathbf{u}}_S, \qquad \forall \mathbf{x} \in \Gamma_D \times t, \tag{6.52}$$

$$\bar{q} = \mathbf{q} \cdot \mathbf{n} \qquad \Delta\bar{q}^G = \Delta\mathbf{q}^G \cdot \mathbf{n}, \qquad \bar{\mathbf{t}} = \mathbf{T} \cdot \mathbf{n}, \qquad \forall \mathbf{x} \in \Gamma_N \times t\,. \tag{6.53}$$

Herein, $\bar{q}$, $\Delta\bar{q}^G$ and $\bar{\mathbf{t}}$ are the polymer solution volume flux, the dispersive volume flux of the gel and the total traction vector of the mixture, respectively, while $\mathbf{n}$ denotes the outward oriented normal vector. For adapting the balance equations in the finite element code, the weak formulations are discretized in space by using the Galerkin method (weighted residual) and in time by means of a fully implicit scheme. A suitable time integration algorithm is adapted to solve the global system iteratively.

Moreover, under the assumption of quasi-static solid deformations, the balance equations (6.9)-(6.11) reduce to the local ODE system

$$\partial_t(n^K) = 0 \rightarrow n^K = n_0^K\,, \tag{6.54}$$

$$\partial_t(n^A_{rev}) = \hat{n}^A_{rev}\,, \tag{6.55}$$

$$\partial_t(n^A_{irr}) = \hat{n}^A_{irr}\,, \tag{6.56}$$

which has to be solved at each time step in every integration point. Note that (6.54) does not evolve in time and is therefore initially fulfilled. The initial conditions for the reversibly n^A_{rev} and irreversibly n^A_{irr} captured particles are set to

$$n^A_{rev} = n^A_{rev,0} \quad \text{and} \quad n^A_{irr} = n^A_{irr,0} \quad \forall \mathbf{x} \in \Omega_0 \times t_0 \,. \tag{6.57}$$

Finally, the primary variables corresponding to the system's governing equations are summarized by

$$\mathbf{u}_S,\ p,\ s^G,\ n^A_{rev},\ n^A_{irr} \,. \tag{6.58}$$

6.5 Application to core flooding

6.5.1 Laboratory flooding experiments

Laboratory core flooding experiments need to be carried out as a first step towards the successful design of flooding applications at the field scale. In this context, the rate of polymer propagation through a well-defined porous media is observed in a small-scale laboratory setup, while the results are usually directly upscaled to field experiments. It was frequently addressed in the literature that the transport of a polymer solution depends highly on the interaction with the porous skeleton. More precisely, the retention behavior is coupled to an evolution in hydraulic permeability as well as the flow rate-dependent polymer solution rheology have a tremendous influence on the transport [1, 4, 6, 46, 47, 52, 62, 77, 88, 112, 161–163]. In the following, results of laboratory core flooding experiments carried out by Al-Hajri *et al.* [7] will be used to calibrate the postulated constitutive models in the continuum-based modeling approach.

A key point of the experimental investigation is the quantitative characterization of the hydrodynamic retention phenomena. To this end, the polymer retention with respect to different injection flow rates are tested. Note in passing that experimental studies investigating the influence of flow rate on retention are rather rare, however, some additional laboratory results are published by Zhang & Seright [173] and Idahosa *et al.* [77]. In the following, the experimental setup and procedure described in Al-Hajri *et al.* [7] is summarized for convenience, while the interested reader is referred to their paper for further details.

Polymer and brine A brine solution mixed with low molecular weight sulfonated polyacrylamide polymers (AN 113 VLM) is used for the polymer flooding experiments. The brine has a concentration of 5000 ppm of sodium chloride (NaCl), while the polymer concentration in the solution is 1000 ppm. Brine mixed with polymer (polymer solution) as well as pure brine are used for the experimental procedure. The composition of brine and polymer solution are the same for each experiment.

Porous media The polymer solution flows through a cylindrical Bentheimer sandstone core, while its physical properties are summarized in Table 6.1. The porosity of

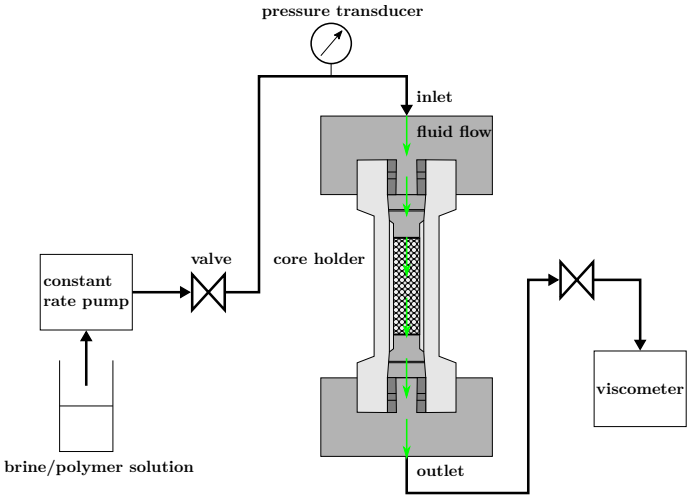

Figure 6.10: *Schematic view of experimental setup used to determine the polymer retention [7].*

the core is 19.5% and the permeability is 1991 mD (milli Darcy[1]). The same core is used for all experiments. Note that the apparent density of the core as well as the intrinsic density of the solid are calculated from the remaining properties.

Parameter	Value	Unit
length	7.6	cm
weight	169	g
porosity	0.195	-
permeability	1991	mD
pore volume	17.2	cm^3
cross section	11.6	cm^2
intrinsic density of solid	2381	kg/m^3
apparent density of core	1917	kg/m^3

Table 6.1: *Physical properties of the sandstone core used in the experimental retention tests carried out by Al-Hajri et al. [7].*

Experimental setup The experimental setup used by Al-Hajri *et al.* [7] to determine the polymer retention is given in Figure 6.10. The core flooding experiments are flow rate controlled, while the volumetric flow rate Q, which measures the injected fluid volume per unit time, is held constant. Therefore, the number of injected pore volumes (Pore Volumes Injected (PVI)) to the core is defined by $PVI = Qt/PV$, where PV is

[1] 1 Darcy = $9.869233 \times 10^{-13}\,\mathrm{m}^2$

the pore volume of the sample (PV = 17.2 cm^3) and t is the injection time. In most core flooding experiments PVI is used instead of the time for a better interpretation of the results, especially when the results of different flow rates are compared. Here, the transport and infiltration of the polymer solution corresponding to four volumetric flow rates are investigated, namely 1.0, 3.0, 5.0 and 8.0 ml/min. The polymer concentration is controlled at the inlet and follows the double-polymer bank method, which is explained in detail within the next section. Moreover, the differential pressure between inlet and outlet is logged during the experiment and the polymer saturation at the outlet is measured through ultraviolet-visible spectroscopy [73, 162].

6.5.2 Double-polymer bank method

Dynamic adsorption The double-polymer bank method, proposed by Lotsch *et al.* [102], is an experimental core flooding procedure in which a defined volume of a polymer solution is injected in two consecutive steps. After the first polymer injection, the core is flooded with a brine solution.

The double-polymer bank methods is a widely applied measuring technique to estimate the polymer retention in porous media, while the amount of reversible and irreversible retention can be distinguished. Figure 6.11 illustrates the method in an exemplary fashion by showing the polymer concentration at the inlet and outlet over the injected pore volume. Note that the polymer saturation has been normalized by the concentration of the injected polymer solution, i. e. $\bar{s}^G_{in,max}$. The concentration at the outlet denotes the breakthrough curve and reveals information towards the retention behavior.

The experiment starts with the injection of pure brine until the core is fully saturated. Next, a predefined number of pore volumes of the polymer solution is injected. After the first polymer bank, the core is again flushed with brine in order to clear the core from any not adsorbed polymer particles. The polymer molecules, which are still attached or trapped after flushing are consequently irreversibly captured. In analogy to the first bank, a predefined volume of the polymer solution is injected, followed by flushing the core from the reversible polymer.

Reversible and irreversible polymer capture Two breakthrough curves for the same injection flow rate corresponding to the double-polymer bank method are illustrated in Figure 6.12. Since the core is flushed with brine between the breakthrough curves, all reversible polymer is removed from the pore space. Therefore, the area between the first (A) and second breakthrough curve (B) is a measure of the amount of irreversibly retained polymer. The breakthrough curves in Figure 6.12 indicate that a certain amount of polymer is irreversibly retained during the first injection, such that less polymer is captured by the porous media during the second injection. As a consequence, the amount of injected pore volumes to reach the inlet concentration is decreased, which is represented by the shift between the breakthrough curves. To put it in other words, polymer retention slows down the propagation of the concentration front during injection. In case of purely reversible retention, the breakthrough curves A and B are

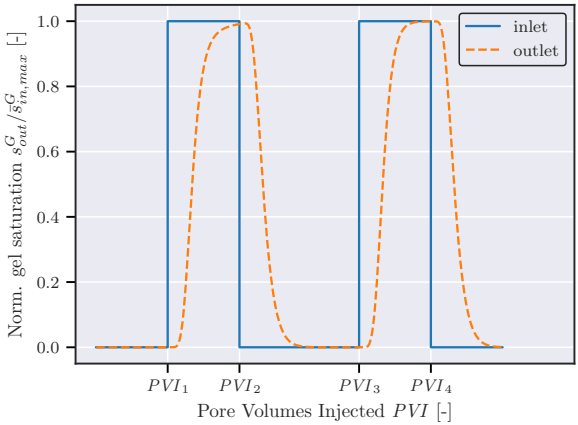

Figure 6.11: *Inlet and outlet polymer concentration in the dynamic double-polymer bank method plotted over the amount of injected pore volumes. The concentrations are normalized by the polymer concentration in the polymer solution, i. e.* $\bar{s}^G_{in,max} = 10^{-3}$. *The polymer concentration at the inlet is controlled during the experiment, while the concentration at the outlet is measured, cf. Figure 6.10.*

identical.

In the following, the amount of hydrodynamic retained polymer corresponding to a specific (high) flow rate is related to the amount of retained polymers under static conditions. According to the literature [7, 77, 173], it is assumed that static retention conditions also apply for low injection flow rates. In the presented study, Al-Hajri *et al.* [7] assumed static conditions up to $Q_{static} = 1.0\,\mathrm{ml/min}$.

Figure 6.13 illustrates the method proposed by Zhang & Seright [173] to determine hydrodynamic retention, i. e. the flow rate-depended retention. In the beginning, the double-polymer bank method is carried out at a sufficient low injection flow rate Q_{static}. Subsequently, the double-polymer bank method is applied to the same core, but now with a higher injection rate, i. e. $Q > Q_{static}$.

The area between the breakthrough curves A and B corresponding to the high injection flow rate denotes the amount of irreversible hydrodynamic retention, cf. Figure 6.13. A measure for reversible hydrodynamic retention is given by the area between B and C. To this end, hydrodynamic retention is measured relative to static retention. In case of flow rate-independent attachment, the breakthrough curves recorded at high flow rates (A and B) are matching the static breakthrough curve (C).

Experimental procedure In the experimental study carried out by Al-Hajri *et al.* [7], static retention is investigated by applying the double-polymer bank method at 1.0 ml/min. It is a priori assumed that hydrodynamic retention has no significant impact at such low flow rate.

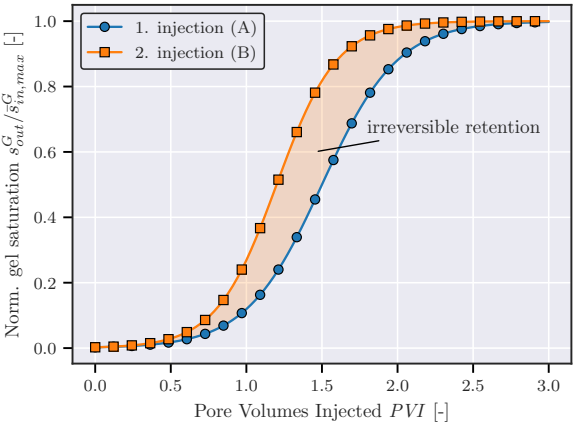

Figure 6.12: *Determine the amount of irreversible retention from the breakthrough curves corresponding to the dynamic double-polymer bank method.*

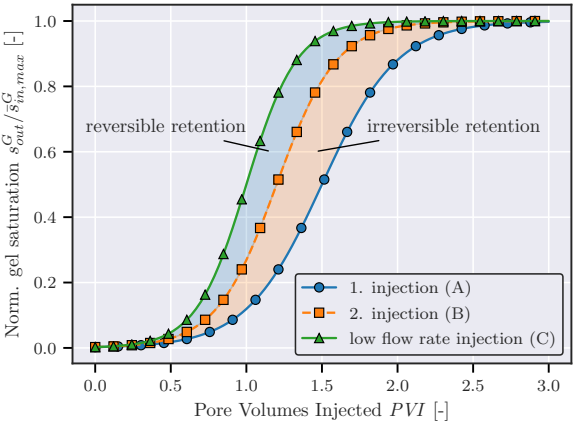

Figure 6.13: *Determine the amount of flow rate-dependent retention, i. e. hydrodynamic retention, by using the method proposed by Zhang & Seright [173].*

The experimental determination of the flow rate-dependent polymer retention is determined for the same sandstone core, which has been previously investigated for static retention. In this context, the double-polymer bank method is applied subsequently with flow rates of 3.0, 5.0 and 8.0 ml/min, while the breakthrough curves are recorded in each test run.

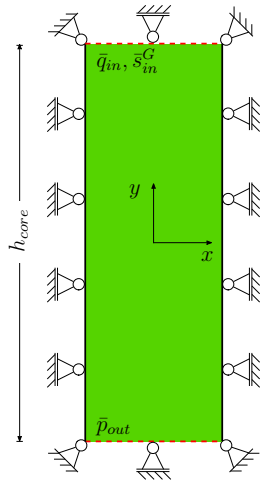

Figure 6.14: *The geometry and boundary conditions for the IBVP corresponding to the 1D core flooding experiment. Fixed displacements normal to the outer boundaries are applied. The injection flow rate is controlled at the top boundary, while the pressure is set at the bottom ($\bar{p}_{out} = 0$). Additionally, the gel saturation is controlled at the inlet to match the experimental setting.*

Numerical realization The 1D polymer transport through the sandstone core is simulated by the IBVP specified in Figure 6.14. Dirichlet boundary conditions for the displacement field are prescribed on all boundaries. More precisely, normal displacements are set to zero in order to simulate the core holder in the experimental setting. In addition, undrained boundary conditions, i. e. homogeneous Neumann boundary conditions, for the pressure field, are set to all domain boundaries except for the injection and outflow boundaries at top and bottom (dashed lines), respectively. The injection flow rate $\bar{q}_{in}$ and polymer saturation $\bar{s}^G_{in}$ are controlled at the injection boundary, while at the outflow boundary only the pressure $\bar{p}_{out} = 0$ is controlled. Following the double-polymer bank method, the injection flow rate $\bar{q}_{in}$ is analytically described through the step-function (cf. Figure 6.11)

$$\bar{s}^G_{in} = \begin{cases} 0, & \text{for } PVI \leq PVI_1 \\ \bar{s}^G_{in,max}, & \text{for } PVI_1 < PVI \leq PVI_2 \\ 0, & \text{for } PVI_2 < PVI \leq PVI_3 \\ \bar{s}^G_{in,max}, & \text{for } PVI_3 < PVI \leq PVI_4 \\ 0, & \text{for } PVI > PVI_4 \end{cases} . \tag{6.59}$$

Moreover, the injection flow rate is given by

$$\bar{q}_{in} = \frac{Q}{A_{cross}} , \tag{6.60}$$

while A_{cross} denotes the cross section area of the core, cf. Table 6.1. Furthermore, the following set of initial conditions is applied to the primary variables

$$\mathbf{u}_{S,0} = \mathbf{0}\,, \quad s_0^G = 0\,, \quad p_0 = 0\,, \quad n_{rev,0}^A = 0\,, \quad \forall \mathbf{x} \in \Omega_0 \times t_0\,. \tag{6.61}$$

Note that the initial amount of irreversibly attached polymer $n_{irr,0}^A$ depends on the case of retention test, i. e. static or dynamic. Therefore, $n_{irr,0}^A$ vanishes in case of the static retention at low injection flow rate (double-polymer bank method for polymer-free core). However, the hydrodynamic retention tests are obtained at the same core after the static retention has been determined. To this end, the initial amount of irreversible adsorbed polymer starts at $n_{irr,0}^A = \bar{n}_{irr,0}^A$, which corresponds to the amount after the static retention test.

The material properties and parameters for the simulation are summarized in Table 6.2, while the elastic parameters for the sandstone E_{eff} and ν_{eff} as well as the dispersion coefficient D^G of the polymer gel in an aqueous carrier fluid are estimated from the literature, cf. Lake [86] and Sorbie [141].

The polymer solution mobility in Darcy's law is given by $M^L = k_0^S/\mu^{LR}$, while its specific value does not influence the polymer solution velocity for flux controlled boundary conditions. In the further course of this work, the effective viscosity and permeability are fitted to the experimental data.

The generalized Darcy's law applied in this modeling approach is derived under the assumption of laminar flow. Therefore, the Reynolds number Re is introduced through

$$Re = \frac{\rho^{LR} d_{grain} Q}{\mu^{LR} A_{cross}} \tag{6.62}$$

to justify the laminar flow-assumption in the following. Herein, d_{grain} denotes the medium grain size diameter of the porous skeleton and is here used as the specific length scale. Typical values for d_{grain} ranging from 0.2–0.33 mm for Bentheimer sandstones, cf. Peksa *et al.* [114]. For all tested injection rates Q, $Re \ll 1$ holds, such that the laminar flow assumption is valid. More precisely, the Reynolds number is in the regime 0.287×10^{-2}–2.30×10^{-2}, where $d_{grain} = 0.2\,\mathrm{mm}$ and $\mu^{LR} = 1.0\,\mathrm{mPa\,s}$ have been assumed in the derivation.

Moreover, a second dimensionless number is introduced to analyze the mass transport through the porous matrix. The Péclet number Pe relates the convective to the diffusive transport through

$$Pe = \frac{d_{grain} Q}{D^G A_{cross}}. \tag{6.63}$$

Herein, the specific length scale has been again chosen to the medium grain size diameter, while the diffusive process is identified with the dispersion coefficient of the polymer gel. According to Sorbie [141], very low values for the dispersion coefficient are reported, i. e. $D^G = 5 \times 10^{-12}\,\mathrm{m^2/s}$. To this end, the Péclet number is in the range between 575–4598, which indicates that the polymer transport is strongly convection-dominated.

Description	Symbol	Value	Unit
intrinsic solid density	ρ^{SR}	2381	kg/m^3
intrinsic fluid density	ρ^{FR}	1000	kg/m^3
intrinsic polymer gel density	ρ^{GR}	1000	kg/m^3
effective dispersion viscosity	μ^{LR}	1.0	mPa s
intrinsic permeability	k_0^S	1991	mD
dispersion coefficient of polymer gel	D^G	5×10^{-12}	m^2/s
initial porosity	n_0^L	0.195	-
Young's modulus	E_{eff}	20	GPa
Poisson ratio	ν_{eff}	0.3	-
length of domain	h_{core}	7.6	cm
start 1. polymer bank	PVI_1	3	-
end 1. polymer bank	PVI_2	6	-
start 2. polymer bank	PVI_3	18	-
end 2. polymer bank	PVI_4	21	-

Table 6.2: *Material properties used in the core flooding simulation.*

Note that a streamline upwind scheme has been applied to the convection-diffusion-reaction equation (6.50) for numerical stabilization. Following this approach, additional diffusion in the direction of the convection velocity $\mathbf{q}$ has been introduced. More precisely, the following integral expression

$$\int_\Omega -\frac{\tilde{D}^G}{|\mathbf{q}|^2}(\mathbf{q}\cdot\operatorname{grad}\delta s^G)(\mathbf{q}\cdot\operatorname{grad} s^G)\mathrm{d}v \tag{6.64}$$

is added to the l.h.s of (6.50). Herein, $\tilde{D}^G$ denotes the artificial isotropic dispersion coefficient. In analogy to the analytic solution of a 1D convection-diffusion problem, the artificial diffusion $\tilde{D}^G$ is expressed through the computational Péclet number $\tilde{P}e$ through

$$\tilde{D}^G = \min\{1, \frac{\tilde{P}e}{3}\}\tilde{P}e\, D^G \quad \text{with} \quad \tilde{P}e = \frac{\max\{q_1h_1, q_2h_2, q_3h_3\}}{2D^G}\,. \tag{6.65}$$

Note that $\{q_1, q_2, q_3\}$ and $\{h_1, h_2, h_3\}$ are the components of the Darcy velocity $\mathbf{q}$ and the local finite element dimensions, respectively. To this end, $\tilde{P}e$ is a mesh-dependent quantity, which is not directly correlated to the physical-motivated Péclet number Pe.

Further details regarding the implementation of stabilization methods in the finite element method are well documented by Koch [84], while a comprehensive description of the mathematical background was intensively discussed by Kuzmin [85].

6.6 Parameter identification to laboratory results

In the following, the continuum-based attachment model is fitted to the results of the laboratory study carried out by Al-Hajri *et al.* [7]. The objective is twofold. On the one

hand, the applicability of the proposed modeling approach is tested, while on the other hand, functional dependencies of the model parameters with respect to the flow rate are investigated. The latter one is necessary for generalization of the results, i. e. to predict the adsorption behavior for various flow rates.

The undetermined model parameters are fitted to the experimental results by using the Nelder-Mead algorithm. The optimization workflow is illustrated in Figure 6.15. The workflow starts by initializing the boundary and initial conditions as well as the fitting parameters. Based on the current parameter set, a core flooding simulation is carried out and the numerical breakthrough curves are extracted from the simulation results. Next, a cost function is formulated, which measures the mean squared error between the simulated and the experimentally obtained breakthrough curves. The goal of the algorithm is to find the parameter set, which minimizes the cost function. Here, the Nelder-Mead algorithm [61] is used for the optimization. Note in passing that the Nelder-Mead algorithm is implemented in the open-source library SciPy, a Python library for scientific computing, cf. [157].

6.6.1 Irreversible retention for low flow rate injection

The breakthrough curves corresponding to Q_{static} are given in Figure 6.16. Before the first polymer front is injected, the core is fully saturated with brine solution and no polymer is attached to the solid skeleton. It can be deduced from the area between the breakthrough curves that a small amount of injected polymer is irreversibly attached, such that the injection concentration is reached earlier for the second bank. The breakthrough curves are fitted with the previously described two-site capture model (cf. (6.24) and (6.25)), while model parameters therein are optimized to

$$n^A_{irr,eq} = 1.73 \times 10^{-5}\,, \qquad k_{a,irr} = 1.30 \times 10^{-4}\,\mathrm{s}^{-1}\,,$$
$$n^A_{rev,eq} = 1.75 \times 10^{-5}\,, \qquad k_{a,rev} = 1.46 \times 10^{-2}\,\mathrm{s}^{-1}\,.$$

Since the output concentration is exclusively measured during the injection of polymer, no information of the dynamics of the detachment is accessible from the experimental results. As a consequence, the detachment coefficient $k_{d,rev}$ is left undetermined. However, the double-polymer bank method requires that all reversibly captured polymers are flushed from the core before the second polymer front will be injected. To this end, the detachment coefficient has been chosen to $k_{d,rev} = 1 \times 10^{-2}\,\mathrm{s}^{-1}$, which satisfies the requirement according to the experiment.

6.6.2 Flow rate-dependent retention

The double-polymer bank method is carried out for four different injection rates in order to investigate the flow rate-dependent retention. The breakthrough curves corresponding to 3.0, 5.0 and 8.0 ml/min are respectively given by Figure 6.17a, 6.17b and 6.17c. The amount of reversibly captured polymer increases with increasing flow rate, such that hydrodynamic retention has been proven experimentally for the tested setup.

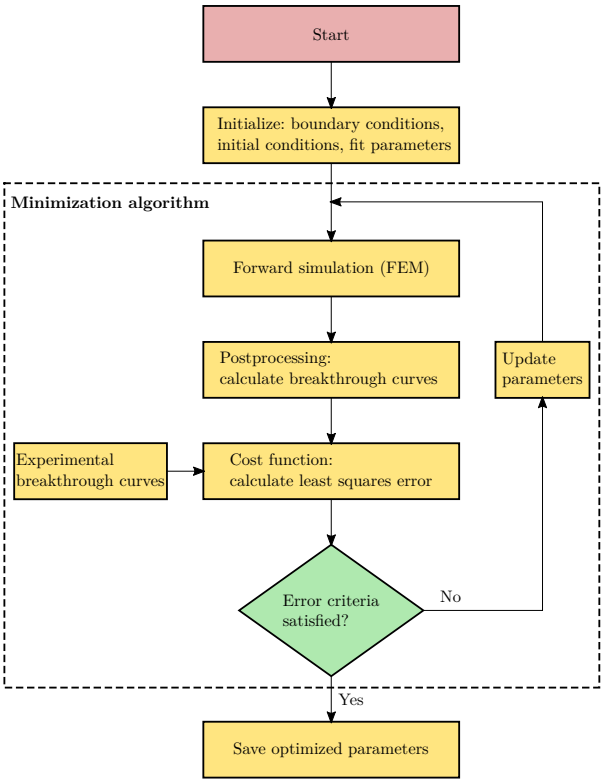

Figure 6.15: *Flowchart for parameter optimization workflow. The model parameters, which are minimizing the cost function, are searched. Here, the cost function is minimized by using the Nelder-Mead algorithm, cf. [61].*

Note that before investigating the hydrodynamic retention for the higher flow rates (3.0, 5.0 and 8.0 ml/min), the same core was subjected to the double-polymer bank method at Q_{static}. Therefore, it is assumed that the adsorption process was terminated before the hydrodynamic retention tests are carried out.

As expected from a previous study by Zhang & Seright [173], hydrodynamic retention turns out to be reversible, such that the first and second breakthrough curves of the same flow rate are identical. To this end, the breakthrough curves corresponding to the second high flow rate injections are not explicitly illustrated in Figure 6.17a, 6.17b and 6.17c. In case of modeling the flow rate-dependent retention, use has been made of the fact that the amount of irreversibly captured polymer during the low flow rate test is constant for the subsequent hydrodynamic retention tests. Consequently, only the

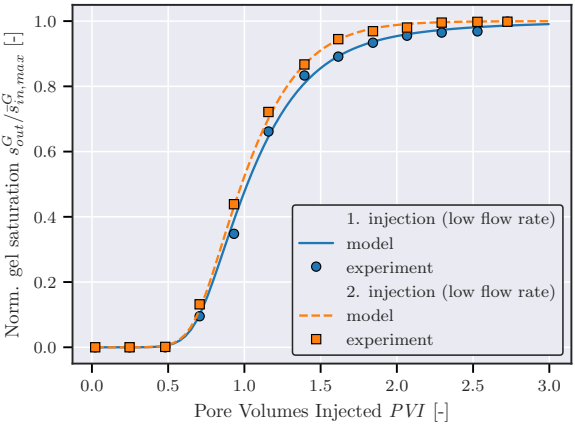

Figure 6.16: *Breakthrough curves corresponding to dynamic retention for low flow rate ($Q_{static} = 1.0$ ml/min). The markers indicate the experimental breakthrough curves, while the lines denote the simulated results from the continuum model. The volumetric injection flow rate $\bar{q}_{in} = 1.44 \times 10^{-5}$ m/s is used as boundary condition.*

Q [ml/min]	$k_{a,rev}$[s^{-1}]	$k_{d,rev}$ [s^{-1}]	$n^A_{rev,eq}$ [-]	$k_{a,irr}$ [s^{-1}]	$n^A_{irr,eq}$ [-][1]
1.0	1.46×10^{-2}	1.0×10^{-2}	1.75×10^{-5}	1.30×10^{-4}	1.73×10^{-5}
3.0	2.01×10^{-2}	1.0×10^{-2}	3.60×10^{-5}	1.30×10^{-4}	1.73×10^{-5}
5.0	6.70×10^{-3}	1.0×10^{-2}	4.27×10^{-5}	1.30×10^{-4}	1.73×10^{-5}
8.0	6.67×10^{-3}	1.0×10^{-2}	7.15×10^{-5}	1.30×10^{-4}	1.73×10^{-5}

Table 6.3: *Best fit parameters in continuum-based capture model. The irreversibly captured polymer is a priori assumed to be flow rate-independent.*

model parameters $n^A_{rev,crit}$ and $k_{a,rev}$, which are associated with the reversible polymer capture, need to be identified for the polymer injection at 3.0, 5.0 and 8.0 ml/min. Note that the reversible detachment rate is again set to $k_{d,rev} = 1 \times 10^{-2}\,\mathrm{s}^{-1}$. The optimized parameters for each individual injection rate are summarized in Table 6.3.

A linear relation between the volume fraction of reversible attached polymers $n^A_{rev,eq}$ and the injection flow rate can be deduced from the optimized parameters, cf. Figure 6.18a. In addition, a more sophisticated correlation for the reversible attachment rate is shown in Figure 6.18b. Here, the values for $k_{a,rev}$ are normalized by the absolute Darcy velocity $|\mathbf{q}|$ and fitted to an exponential function. Hydrodynamic polymer attachment is a velocity-dependent capture mechanisms which is active at higher velocities. To this end, a threshold velocity $|\mathbf{q}_{static}| = 1.47 \times 10^{-5}\,\mathrm{m/s}$ is defined at which the equilibrium amount of reversible attached polymer becomes a function of the Darcy velocity. Note that $|\mathbf{q}_{static}|$ corresponds through (6.60) to $Q_{static} = 1.0\,\mathrm{ml/min}$. Therefore, the follow-

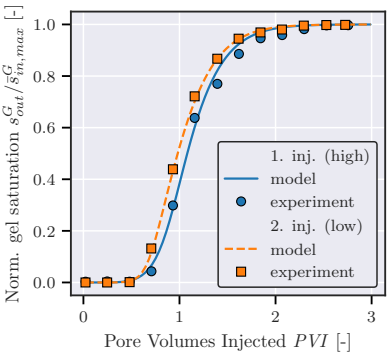

(a) $Q = 3.0\,\mathrm{ml/min}$ (experiment), $\bar{q}_{in} = 4.31 \times 10^{-5}\,\mathrm{m/s}$ (boundary condition in simulation)

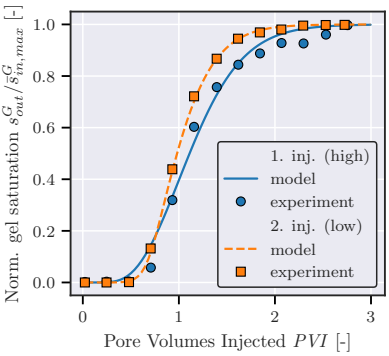

(b) $Q = 5.0\,\mathrm{ml/min}$ (experiment), $\bar{q}_{in} = 7.18 \times 10^{-5}\,\mathrm{m/s}$ (boundary condition in simulation)

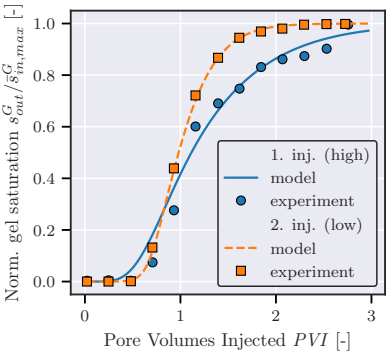

(c) $Q = 8.0\,\mathrm{ml/min}$ (experiment), $\bar{q}_{in} = 1.15 \times 10^{-4}\,\mathrm{m/s}$ (boundary condition in simulation)

Figure 6.17: *Breakthrough curves corresponding to hydrodynamic retention for various flow rates. The amount of reversibly captured polymer can be estimated from the area between the curves. The dashed curve is obtained from the low flow rate injection and is here given as reference. Note that the amount of captured polymer increases with flow rate. Experimental results in Al-Hajri et al. [7] revealed that the hydrodynamic retention is completely reversible.*

ing split-wise functions are fitted to the experimental results:

$$n^A_{rev,eq} = \begin{cases} a_{n^A_{rev,eq}} + b_{n^A_{rev,eq}} \, |\mathbf{q}_{static}| \,, & \text{for } |\mathbf{q}| \leq |\mathbf{q}_{static}| \\ a_{n^A_{rev,eq}} + b_{n^A_{rev,eq}} \, |\mathbf{q}| \,, & \text{for } |\mathbf{q}| > |\mathbf{q}_{static}| \end{cases} \tag{6.66}$$

$$\text{with} \quad a_{n^A_{rev,eq}} = 1.04 \times 10^{-5}; \quad b_{n^A_{rev,eq}} = 5.04 \times 10^{-1} \,,$$

$$k_{a,rev} = \begin{cases} a_{k_{a,rev}} \, |\mathbf{q}_{static}| \exp(b_{k_{a,rev}} \, |\mathbf{q}_{static}|), & \text{for } |\mathbf{q}| \leq |\mathbf{q}_{static}| \\ a_{k_{a,rev}} \, |\mathbf{q}| \exp(b_{k_{a,rev}} \, |\mathbf{q}|), & \text{for } |\mathbf{q}| > |\mathbf{q}_{static}| \end{cases} \tag{6.67}$$

$$\text{with} \quad a_{k_{a,rev}} = 1578.43; \quad b_{k_{a,rev}} = -30923.41 \,.$$

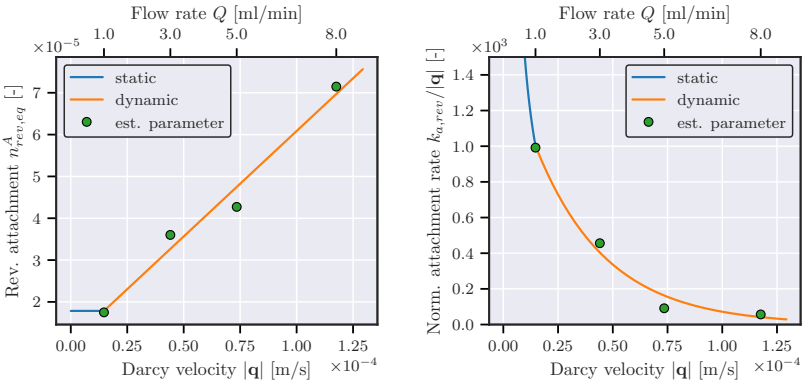

(a) Maximum volume fraction of reversible attached polymer

(b) Attachment rate of reversible polymer

Figure 6.18: *Parameters corresponding to reversible attachment plotted over the Darcy velocity.*

Finally, the analytic functions for $n^A_{rev,eq}$ and $k_{a,rev}$ allow one to predict the hydrodynamic retention behavior for flow rates, which differs from the ones used in the laboratory study.

6.6.3 Permeability reduction

The attachment of polymer results in a decrease in permeability. In this context, the Residual Resistance Factor (RRF) is typically used as a measure of the effective permeability damage due to polymer injection. Therefore, the RRF relates the brine mobility before polymer injection to the brine mobility after the core has been flooded by a polymer solution. To this end, the RRF is defined through

$$RRF = \frac{\Delta p_{post}/Q_{post}}{\Delta p_{pre}/Q_{pre}}\,, \tag{6.68}$$

where Δp_{pre} and Q_{pre} are the differential pressure and the corresponding flow rate measured during brine injection before polymer flooding, while in analogy, Δp_{post} and Q_{post} denote the differential pressure and induced flow rate for brine injection after polymer flooding. In this study, the flow rate is constant, while the pressure drop is measured. According to the laboratory study by Al-Hajri *et al.* [7], $RRF = 1.05$ was obtained. This means that the irreversible retention results also in an irreversible permeability reduction. Using the previously introduced empirical permeability damage function (6.42) leads to

$$RRF = \frac{k_0^S}{k^S} = 1 + \beta_{irr} n^A_{irr,eq} \rightarrow \beta_{irr} = \frac{RRF - 1}{n^A_{irr,eq}}\,, \tag{6.69}$$

such that the permeability damage coefficient evaluates to $\beta_{irr} = 2887$. Not that the permeability reduction does not change with flow rate since hydrodynamic retention is completely reversible.

6.6.4 In situ rheology of polymer solution in porous media

The Resistance Factor (RF) is used to investigate the influence of the polymer solution's in situ rheology on the flow behavior. The RF is defined as the mobility of brine before polymer injection divided by the mobility of injected polymer solution [172], namely

$$RF = \frac{\Delta p_{polymer}/Q_{polymer}}{\Delta p_{pre}/Q_{pre}} = \frac{\Delta p_{polymer}}{\Delta p_{pre}}\,, \tag{6.70}$$

where $\Delta p_{polymer}$ and $Q_{polymer}$ are respectively the pressure drop and corresponding flow rate during the injection of polymer. The RF can be rewritten by using the generalized Darcy's law to

$$RF = \frac{k_0^S}{k^S}\frac{\mu^{LR}}{\mu^{FR}} \rightarrow \mu^{LR} = \frac{k^S}{k_0^S}\mu^{FR}RF = \frac{\mu^{FR}}{1+\beta_{rev}n_{rev}^A + \beta_{irr}n_{irr}^A}RF\,, \tag{6.71}$$

where the in situ viscosity μ^{LR} becomes finally a function of RF. The permeability evolution during polymer injection in (6.71) is again modeled through the permeability damage function (6.42). The influence of irreversible and reversible captured polymer on the permeability is assumed to be equal, such that the formation damage coefficients evaluate to the previous identified value $\beta_{rev} = \beta_{irr} = 2887$. Next, RF is calculated from the measured pressure drops corresponding to the injected flow rates. The results are summarized in Table 6.5. The increase of RF with increasing flow rate indicates an effective shear-thickening behavior of the polymer solution (cf. (6.71)). Note that RF is obtained for quasi-static flow conditions.

A modified Carreau model (6.47) is usually applied to describe the effective non-Newtonian rheology of polymer solutions in porous media. However, the measured RF indicates a purely shear-thickening behavior (in situ) of the complex fluid in the range of the tested injection flow rates. To this end, the fluid is effectively modeled through the Power Model (6.45), where the fitting parameters evaluate to $K_{PM}^* = 1.433$ and $n_{PM}^* = 1.232$. The constitutive relation between the porous media shear rate and the Darcy velocity (6.30) are applied. The Viscosity Increase Factor (VIF) is obtained by normalizing the polymer solution viscosity μ^{LR} by the brine viscosity μ^{FR}, i. e. the viscosity of the carrier fluid. In Figure 6.19, the VIF is plotted over the porous media shear rate. The model is in good agreement to the measured RF from the recorded pressure drops.

The constitutive models for permeability and solution viscosity have been successfully fitted to the RRF and the RF. The core flooding experiments were exclusively carried out with a single polymer concentration, such that a concentration-dependent rheology model can not be calibrated here. However, it is a priori known that the polymer solution viscosity reduces to the carrier fluid's viscosity for $s^G = 0$ and reaches the calibrated results for $s^G/\bar{s}_{in,max}^G = 1$. Based on this admissible conditions, a linear

Description	Symbol	Value	Unit
reversible damage coefficient	β_{rev}	2887.16	-
irreversible damage coefficient	β_{irr}	2887.16	-
1. viscosity parameter	K^*_{PM}	1.43	-
2. viscosity parameter	n^*_{PM}	1.23	-
shift factor	α_{pm}	1	-
irreversible attachment rate	$k_{a,irr}$	1.73×10^{-5}	s^{-1}
irreversible detachment rate	$k_{d,irr}$	0	s^{-1}
irreversible volume fraction (eq.)	$n^A_{irr,eq}$	1.3×10^{-4}	-
reversible detachment rate	$k_{d,rev}$	10^{-2}	s^{-1}

Table 6.4: *Constant parameters in effective viscosity model μ^{LR}_{PM}, permeability damage function k^S and polymer attachment model $\hat{n}^A$.*

Q [ml/min]	|q| [m/s]	$\dot{\gamma}_{pm}$ [1/s]^2	RF [-]
1.0	1.47×10^{-5}	24.91	3.26
3.0	4.41×10^{-5}	76.52	4.56
5.0	7.35×10^{-5}	128.60	5.37
8.0	1.18×10^{-4}	212.93	6.12

Table 6.5: *Experimentally obtained resistance factor (RF) by Al-Hajri et al. [7].*

concentration-dependent model in terms of the power-law parameters is postulated by

$$K_{PM} = (K^*_{PM} - 1)\frac{s^G}{\bar{s}^G_{in,max}} + 1 \quad \text{and} \quad n_{PM} = (n^*_{PM} - 1)\frac{s^G}{\bar{s}^G_{in,max}} + 1\,, \tag{6.72}$$

where K^*_{PM} and n^*_{PM} are the calibrated parameters. The concentration- and shear rate-dependent VIF is finally shown in Figure 6.20, while the different curves indicate the inter- and extrapolation between the calibrated viscosity model and the Newtonian carrier model. For reasons of clarity, the estimated parameters of the viscosity model and the permeability damage function are summarized in Table 6.4.

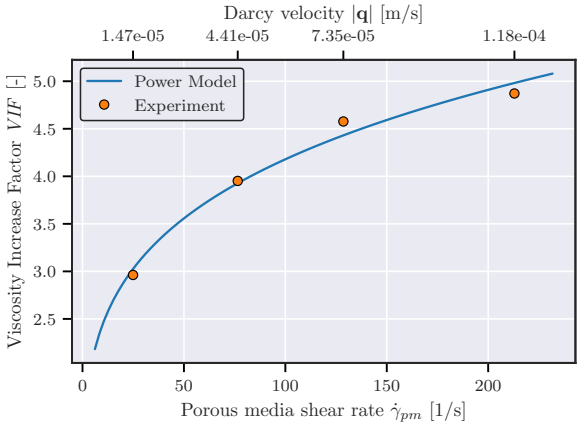

Figure 6.19: *VIF obtained from the RF corresponding to different injection flow rates. The bold line corresponds to the fitted Power Model.*

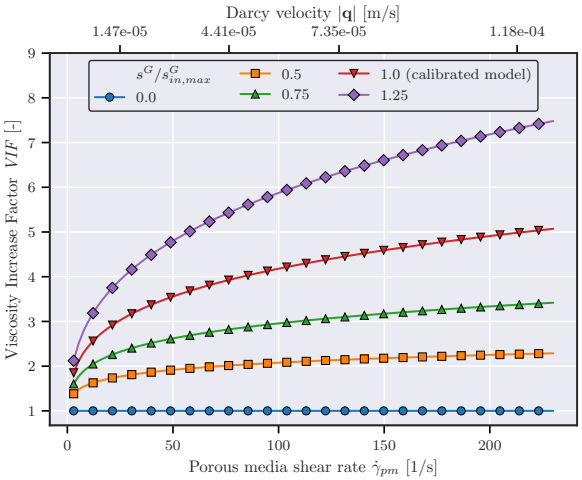

Figure 6.20: *Concentration- and shear-rate-dependent VIF. The concentration-dependent behavior results from inter- and extrapolation between the calibrated model and the expected Newtonian rheology of the carrier fluid φ^F, i. e. pure brine solution.*

6.7 Numerical example of calibrated model

In the previous section, the developed continuum model was successfully used to simulate the experimental results obtained from core flooding tests. In this context, the constitutive models accounting for polymer retention, permeability damage and effective polymer solution viscosity were calibrated. Moreover, the estimated model parameters were carefully investigated, such that further constitutive formulations were deduced.

The 1D core flooding IBVP (cf. Figure 6.14) was sufficient for calibration purposes, however, the geometry together with the applied boundary conditions induced a homogeneous velocity distribution, such that the model capabilities with respect to the expected non-Newtonian rheology could not be properly investigated.

In contrast to the 1D simulations, a more sophisticated polymer injection simulation is carried out in this section. Therefore, the geometry, boundary conditions and the applied mesh for the 2D IBVP studied in this section are shown in Figure 6.21. The simulation domain represents a squared plate with uniformly distributed circular holes.

Again, the multi-phase model is governed by the weak forms (6.48)-(6.50) and the local volume balance equations (6.10) and (6.11). To this end, the coupled set of balance equations needs to be solved for the primary variables (6.58). Finally, the problem formulation is closed by applying the constitutive relations from the previous section:

- linear elastic solid stress tensor $\mathbf{T}_E^S$ (6.18),
- filter velocity $\mathbf{q}$ modeled through the generalized Darcy's law (6.29),
- Power Model for effective polymer solution viscosity (6.45),
- saturation-dependent viscosity parameters (6.72),
- porous media shear rate (6.30),
- permeability damage function (6.42),
- reversible and irreversible particle attachment rates (6.24) and (6.25),
- velocity-dependent reversible attachment (hydrodynamic retention) through functional dependencies (6.66) and (6.67) in (6.24),
- streamline upwind stabilization approach (6.64) in (6.50).

Note that the remaining material and model parameters are chosen in accordance to Table 6.6, which mainly correspond to the core flooding simulations from the previous section.

Furthermore, the following set of initial conditions is applied to the primary variables

$$\mathbf{u}_{S,0} = \mathbf{0}\,, \quad s_0^G = 0\,, \quad p_0 = 0\,, \quad n_{rev,0}^A = 0\,, \quad n_{irr,0}^A = 0\,, \quad \forall \mathbf{x} \in \Omega_0 \times t_0\,. \tag{6.73}$$

Dirichlet boundary conditions for the displacement field are prescribed on the outer domain boundaries. More precisely, normal displacements are set to zero. In addition, undrained boundary conditions, i. e. homogeneous Neumann boundary conditions for the pressure field, are set to all domain boundaries, except for the injection and outflow boundaries at top and bottom (dashed lines), respectively. The pressure and polymer saturation are controlled at the injection boundary (Dirichlet boundary conditions), while at the outflow boundary only the pressure is controlled. Since the outflow pressure is set to $\bar{p}_{out} = 0$, the pressure difference is in the following equal to the injection pressure $\bar{p}_{in}$. The injection pressure increases linearly through the ramp function

$$\bar{p}_{in} = \begin{cases} \frac{\bar{p}_{in,max}\, t}{t^*}, & \text{for } t \leq t^* \\ \bar{p}_{in,max}, & \text{for } t > t^* \end{cases} \tag{6.74}$$

until the plateau value $\bar{p}_{in,max}$ is reached at the threshold time t^*, while the polymer saturation at the injection boundary follows the step-function

$$\bar{s}^G_{in} = \begin{cases} 0, & \text{for } t \leq t^* \\ \bar{s}^G_{in,max}, & \text{for } t > t^* \end{cases} . \tag{6.75}$$

Note in passing that the ramp function for the injection pressure is used for numerical stabilization. In the further course of this section, the results at times $t \geq t^*$ are exclusively discussed.

The asymmetric boundary conditions as well as the regularly distorted domain induce an inhomogeneous flow field, which in turn interacts with the velocity-dependent non-Newtonian polymer solution rheology.

The transport and infiltration of polymer solutions are simulated for injection pressures $\bar{p}_{in,max}$ ranging between 50 to 200 kPa, while the simulation time is set to 5×10^4 s for each individual simulation. Note that for $t \leq t^*$ no polymer is injected due to the procedure mentioned above.

Next, the results corresponding to the finite element solution are illustrated and discussed. For convenience, the time t has been shifted by $-t^*$ in the further course of the analysis, while only results corresponding to constant injection pressures are analyzed.

A comparison between snapshots of the saturation distribution over the domain are shown in Figure 6.22 for various injection pressures at different times. The injection pressure increases from left to right, while the time increases from top to bottom. On a qualitative level, the saturation front's velocity increases with increasing injection pressure as expected from fluid flow governed by Darcy's law. However, the transport of the polymer solution is here modeled through a modified Darcy's law, which shows an implicit relation through the velocity-dependent effective viscosity. Therefore, the propagation of the saturation front depends on both, the pressure gradient and the effective viscosity.

The velocity- as well as the saturation-dependent solution viscosity distributions are illustrated in Figure 6.23. Note that the snapshots are arranged in accordance to the snapshots in Figure 6.22. It can be deduced in a qualitative sense, that the viscosity increases locally simultaneously to the propagation of the polymer front. Besides this,

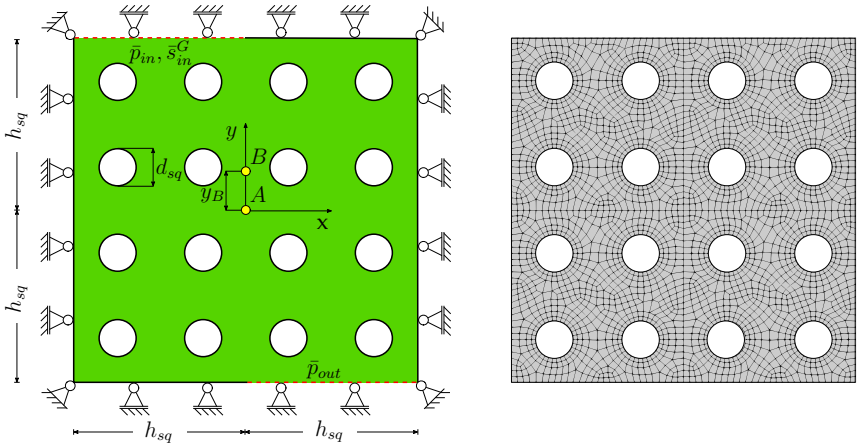

Figure 6.21: *The geometry and boundary conditions for the problem under consideration are illustrated on the left. Fixed displacements normal to the outer boundaries are applied. Pressure boundary conditions at the top and bottom are prescribed, while the gel saturation is additionally controlled at the top (only at dashed line). The time-dependent evolution of the saturation and pressure will be later analyzed for two spatial positions, which are indicated by the points A and B. On the right, the spatially discretized finite element mesh is shown.*

higher viscosities occur at spatial positions at which the flow field is geometrically distorted, i. e. when the flow is channeled through narrow areas.

Due to the asymmetric boundary conditions and the distorted geometry, the absolute polymer solution velocity varies throughout the domain. To emphasize this point, the velocity field is illustrated in Figure 6.24 for a constant injection pressure of $\bar{p}_{in} = 150\,\text{kPa}$, while snapshots at $0.1\,\text{h}$, $1.5\,\text{h}$, $2.9\,\text{h}$ and $7.1\,\text{h}$ are presented to show the decrease in velocity with increasing injected polymer. Note that a quasi-static distribution is reached when the polymer saturation front is fully propagated through the domain, cf. Figure 6.22. By plotting the saturation and viscosity over time at fixed points on the domain, the coupling effects of the model can be analyzed in a more quantitative way. The spatial positions of the points A and B under consideration are illustrated in Figure 6.21. It is expected with respect to Figure 6.24, that the velocity evolution at the different points distinguishes significantly from each other. The temporal evolution of the polymer saturation and the VIF are plotted in Figure 6.25 for injection pressures ranging between 50 to 200 kPa. Shear-thickening is observed simultaneously to the arrival of the polymer saturation front. As expected, the saturation front is faster for higher injection pressures. However, the saturation curves are not shifted proportional to the injection pressures, which is caused by the non-Newtonian rheology. More precisely, the applied Power Model (cf. (6.45)) dictates a purely shear-thickening behavior for increasing shear rates, such that the shift of the breakthrough curves becomes smaller

Description	Symbol	Value	Unit
injection saturation	$\bar{s}^G_{in,max}$	10^{-3}	-
vector of injection pressures	$\bar{\mathbf{p}}_{in,max}$	[50,100,150,200]^T	kPa
outlet pressure	$\bar{p}_{out}$	0	Pa
threshold time	t^*	5.0×10^3	s
simulation time	t_{max}	5.0×10^4	s
domain geometry	h_{sq}	1.0	m
domain geometry	d_{sq}	0.22	m
distance to point B	y_B	0.23	m
initial intrinsic permeability	k_0^S	1991	mD
initial porosity	n_0^L	0.195	-
intrinsic solid density	ρ^{SR}	2381	kg/m^3
intrinsic fluid density	ρ^{FR}	1000	kg/m^3
intrinsic polymer gel density	ρ^{GR}	1000	kg/m^3
effective carrier fluid viscosity	μ^{FR}	1.0	mPa s
dispersion coefficient of polymer gel	D^G	$5{\times}10^{-12}$	m^2/s
Young's modulus	E_{eff}	20	GPa
Poisson ratio	ν_{eff}	0.3	-
reversible damage coefficient	β_{rev}	2887.16	-
irreversible damage coefficient	β_{irr}	2887.16	-
1. viscosity parameter	K^*_{PM}	1.43	-
2. viscosity parameter	n^*_{PM}	1.23	-
shift factor	α_{pm}	1	-
irreversible attachment rate	$k_{a,irr}$	1.73×10^{-5}	s^{-1}
irreversible detachment rate	$k_{d,irr}$	0	s^{-1}
irreversible volume fraction (eq.)	$n^A_{irr,eq}$	1.3×10^{-4}	-
reversible detachment rate	$k_{d,rev}$	10^{-2}	s^{-1}

Table 6.6: *Material parameters and constants used for the simulation.*

at higher applied injection pressures. As a practical consequence, in order to double the saturation front's velocity, requires more than twice as much of the injection pressure. A closer look at Figure 6.25 reveals that the viscosity evolution can be divided into three distinct regimes, which are caused by the superposition of the saturation- and velocity-dependent effects:

1. The viscosity increases due to an increase in polymer saturation, while at the same time the polymer solution velocity slows down as a consequence of increasing flow resistance.

2. When the local polymer saturation reaches the injected saturation, the viscosity starts to decrease due to the decreasing local velocity.

3. The viscosity reaches a constant plateau, when the velocity field equilibrates to a steady-state. From this point onwards, the polymer saturation throughout the domain is constant in time, such that the flow resistance does not change anymore.

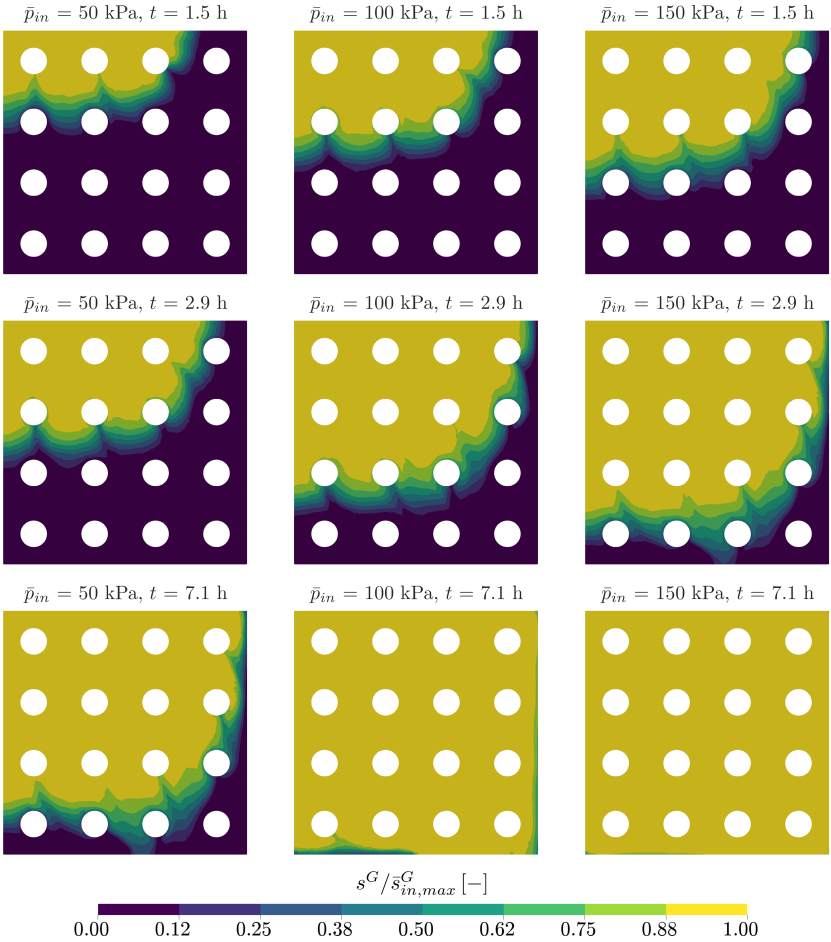

Figure 6.22: *Snapshots of the gel saturation for different points in time and various injection pressures.*

Note in passing, that the permeability evolution to the flow resistance has here only a negligible influence on the flow resistance.

The temporal evolution of the saturation and the viscosity are qualitatively the same in point A and B. Due to the spatial locations of the specific points, the saturation front reaches the points at different times. In addition, the VIFs are shifted for point B to higher values in comparison to the results at A, which is in accordance to the velocity distribution at these specific points.

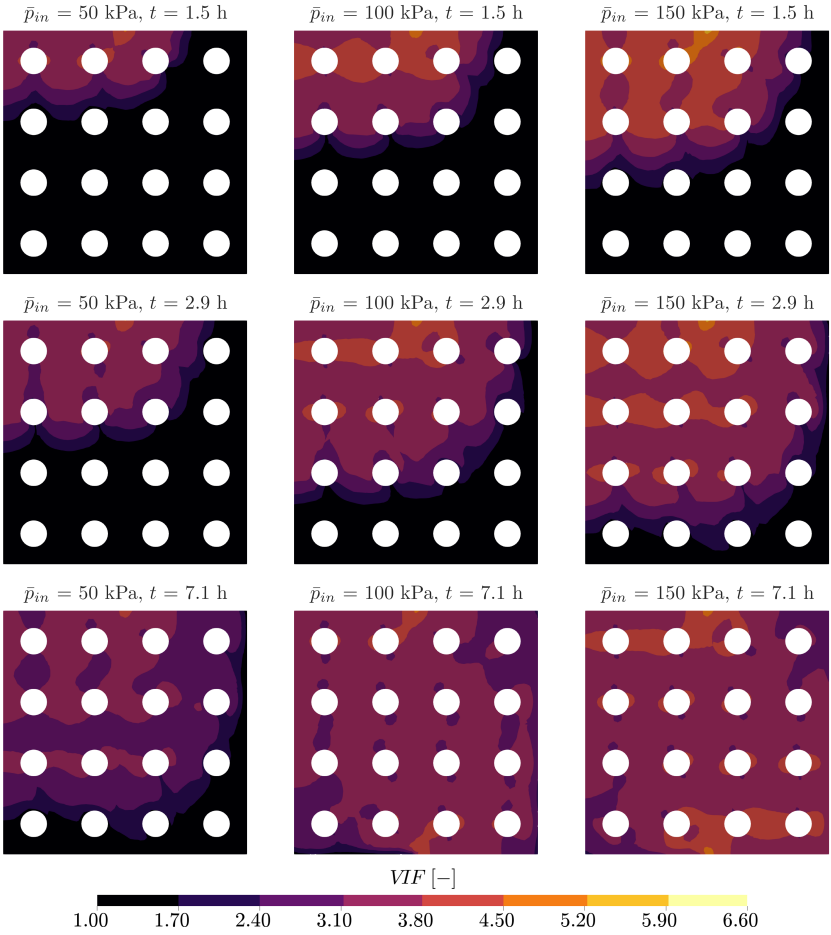

Figure 6.23: *Snapshots of the VIF for different points in time and various injection pressures. The value pairs of the injection pressure and the injection time correspond to the ones used in Figure 6.22.*

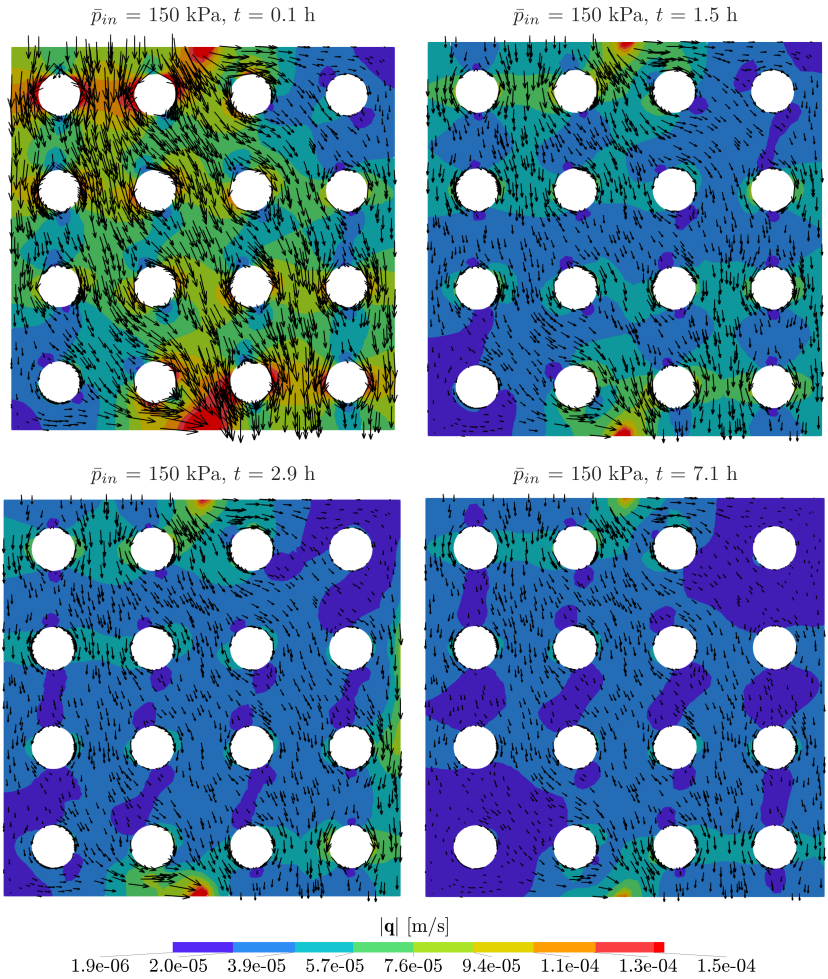

Figure 6.24: *The temporal evolution of the velocity distribution is illustrated through four different snapshots, while the injection pressure is constant. The color map shows the absolute Darcy velocity, while the flow field is additionally visualized with the aid of the velocity vectors. Note that the arrows are scaled by the magnitude of the velocity vectors.*

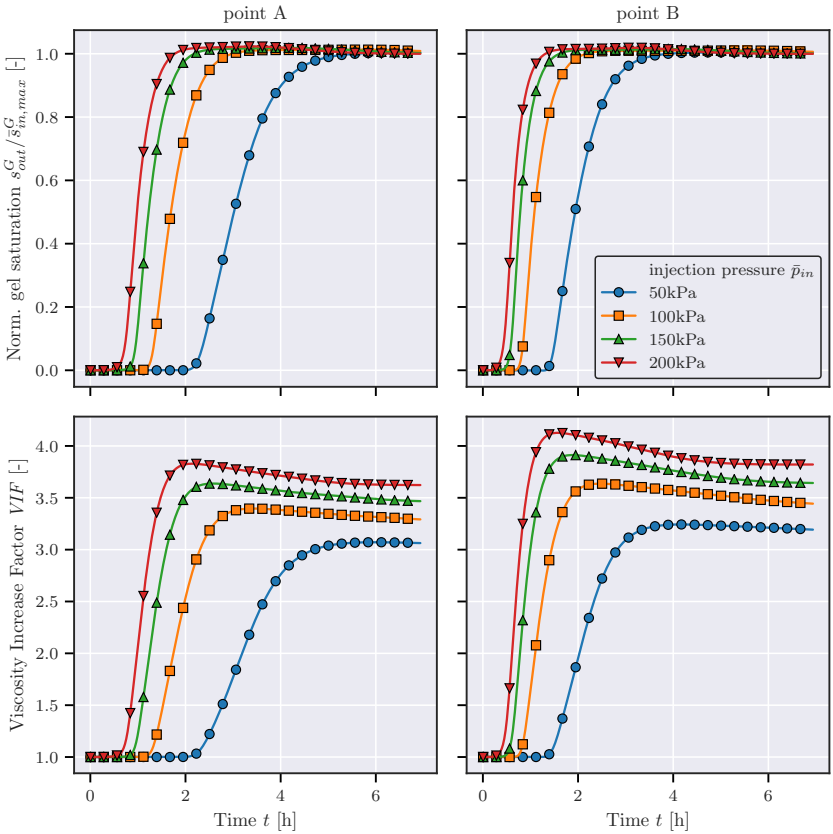

Figure 6.25: *The local evolution of the gel saturation and the pressure at the points A and B are compared, cf. 6.21.*

Chapter 7:
Summary and outlook

7.1 Summary

In this manuscript, a multi-phase model for a porous media saturated with a pore liquid and a polymer gel was developed. The polymer gel within the pore space was able to interact through two distinct mechanisms with the pore liquid and solid skeleton. In particular, the polymer gel within the pore space was able to attach and detach to the solid skeleton. Furthermore, absorption and desorption of pore liquid by the polymer gel was additionally incorporated in the model description. The aim of the thesis was to formulate a general model, which accounts for both mass exchange processes simultaneously. However, depending on the specific application under consideration, the superimposed interactions can also be investigated independently from each other.

In this manuscript, the multi-phase material was formulated through a continuum-based mixture theory – the Hybrid Mixture Theory (HMT). The HMT presented an excellent framework for modeling both types of mass interactions through appropriate exchange terms in the corresponding macroscopic mass balance equations. Therefore, the developed model incorporated the model capabilities in a superimposed fashion.

On the one hand, absorption/desorption of pore liquid by polymers was motivated by the use of Superabsorbent Polymers (SAPs) as chemical admixture in concrete constructions. SAPs are charged hydrogels, which can reversibly absorb large amounts of aqueous pore fluid and are used to control the free pore water content in the mixture. On the other hand, attachment/detachment of polymers to the solid skeleton occurs in polymer flooding, a well-established Enhanced Oil Recovery (EOR) technique. Herein, a polymer solution composed of polymer gel and pore liquid is injected into a reservoir rock. During the infiltration, the polymer gel partially attaches to the solid skeleton. In order to combine both interactions of the polymer gel in a generalized model description, the polymer gel was modeled as a charged hydrogel, which additionally formed a polymer solution with the pore liquid.

The modeling of absorption and desorption of charged hydrogels required an extension of the classical continuum mechanical balance equations by the conservation of electrical charges. For reasons of clarity, the thermodynamic fundamentals of charged hydrogels were introduced in a separate chapter, cf. chapter 3. In this course, the hydrogel was modeled as a two-phase material composed of a charged polymer network and an absorbed electrolyte. Fixed charges are attached to the polymer chains, while mobile ions are distributed in the absorbed solution. It was assumed that the charges of the overall polymer gel are neutralized. Absorption/desorption of pore liquid by the polymer gel was identified with the chemical potential difference. The driving force was decomposed into a mixing, elastic and an ionic contribution. The first two stemmed from the theory of elastic gels, while the letter one is given by the Donnan theory for

electrolytic solutions. Chemical potential differences with respect to liquid exchange were derived from the proposed two-phase material, which was identified as the driving force for absorption/desorption.

In chapter 4, the general HMT model was adapted to the model requirements. Since the developed model incorporates all requirements in a superimposed fashion, the model was termed master model. First, the porous media model was decomposed into phases and species according to the microstructure and the expected material behavior. More precisely, phases were defined across specific modeling layers (phase levels) to gain a systematic model description. The model's complexity was increased by each additional layer. On phase level I, the mixture was viewed as a porous skeleton filled with a polymer solution. On the next level, the polymer solution was further resolved into a polymer gel and a pore liquid, while the solid skeleton was composed of a granular matrix and an attached polymer gel. On phase level III, the attached and fluidized polymer gel were respectively decomposed into polymer chains and absorbed solution. Species were further introduced in the mixture model according to the charged hydrogel model presented in chapter 3.

Constitutive dependencies with respect to the expected material behavior were postulated and the entropy inequality of the overall material was evaluated. Besides constitutive equations for the partial stress tensors and the chemical potential differences, near-equilibrium results for the seepage and diffusion velocities as well as for the density production terms were obtained. The seepage and diffusion velocities were similar to Darcy's law of fluid flow through porous media and Fick's law of diffusion, respectively. The driving forces for the density production terms were given by electrochemical potential differences. In addition, the driving forces for mass exchange were superimposed by the change in Helmholtz free energy with respect to the amount of absorbed and attached mass.

In chapter 5 and 6, two model variants were derived from the master model to investigate absorption/desorption and attachment/detachment processes isolated from each other. In this context, the postulated constitutive functions were calibrated to experimental findings.

Therefore, a constitutive model predicting reversible pore liquid absorption was investigated in chapter 5. The effect of a salt concentration on the mass exchange behavior was incorporated in the constitutive model. In accordance to the results obtained from the evaluation of the entropy inequality, mass exchange terms between pore liquid and polymer gel were specified. Following this, the driving force for mass exchange was expressed through a consistent formulation, which implicitly assumed the reversibility of the absorption process. Experimental results revealed that this modeling assumption was valid for the tested SAPs. In addition to the driving force for mass exchange, a constitutive model for the transfer dynamics was developed based on microstructural processes within the hydrogel. As a consequence, the rate of mass exchange was linked to a widely accepted swelling-dependent permeability function for hydrogels. The dynamics of mass transfer depends therefore on the current state of swelling. A Monte-Carlo method was used to identify the set of unknown model parameters with respect to experimental data. On the one hand, the equilibrium degree of swelling is

exclusively governed by the cumulative water activity coefficient, which turned out to be a function of the salt concentration in the pore fluid. On the other hand, the mass exchange rate respectively depends on constant characteristic absorption and desorption times, which are not influenced by the presence of salt in the pore fluid. Finally, the derived constitutive model was able to mimic the experimental data very well. It is worth mentioning that through the detailed investigation of microstructural processes, the dynamics of water transfer was modeled in a reliable fashion with a minimum amount of fitting parameters.

In chapter 6, the transport and infiltration of a polymer solution through a porous material was investigated on the continuum scale. Again, the multi-phase model represented a systematical reduction of the master model. Inter-phase mass exchange terms were incorporated in the mass balance equations to account for polymer capture by the solid matrix. Special attention was paid to the modeling of the kinetic particle capture process, while the capture mechanisms were derived and finally classified into reversible as well as irreversible polymer capture. Furthermore, the non-Newtonian in situ rheology of the polymer solution was addressed by using adequate effective viscosity models (generalized Newtonian models). In addition, an effective permeability function was incorporated, which relates a permeability damage to the amount of captured polymer. The parameters in the proposed constitutive models were calibrated by experimental results from core flooding experiments reported in the literature. The breakthrough curves and the measured pressure drops showed that the model was in accordance to the experimental results. The calibrated material model was finally applied to a more complex boundary value problem to study the coupled constitutive models against the background of heterogeneous seepage velocity distributions.

7.2 Outlook

Up to now, the developed master model accounts for absorption/desorption and attachment/detachment processes within the pore space of a porous media. These processes were effectively modeled through mass exchange terms on the macroscale. The two types of mass exchange were developed independently and were superimposed in the modeling framework. However, experimental investigations of simultaneous absorption and attachment processes in porous media are not yet carried out to the author's knowledge. Model improvements and extensions are in the following related to the two model variants discussed in chapter 5 and 6.

In case of SAP enhanced concrete mixtures, the evolution of the cement phase over time is essential for predicting the hardening process of the mixture. In the modeling approach presented in this thesis, the desorption of pore liquid by the hydrogel phase was modeled, however, the model did not account explicitly for a cement phase and the potential coupling with the embedded SAPs. To this end, the hydration of a cement phase needs to be accounted for, while appropriate mass exchange terms between the pore liquid and the cement phase have to be developed in accordance to experimental findings.

The mechanical behavior of SAP modified concrete constructions needs to be addressed properly for the development of real constructions. Furthermore, experimental studies showed that the desorption of pore fluid by SAPs leads to air-filled voids in the pore space. The developed model was fully-saturated, such that the model needs to be extended by a gaseous phase. In the model derivation was assumed that mass exchange terms were not coupled to the solid deformation of the porous skeleton. However, for a high polymer saturation in the pore space, the free swelling hypothesis of SAPs would be no longer valid. In this case, the mass exchange needs to be coupled to the kinematics of the solid skeleton. Similar approaches were derived by Ristinmaa *et al.* [119] for a multi-phase material based on the HMT. Herein, the deformation gradient was decomposed into a purely mechanical and a growth part, while only the first contribution represents a mass-conserving deformation.

In addition, the model variant presented in chapter 6, which was used for simulating polymer flooding, can be also extended in various manners. Linking the in situ viscosity of the non-Newtonian polymer solution to the bulk viscosity is a very challenging but crucial task. In the present manuscript, constitutive models for the generalized Newtonian viscosity and permeability were calibrated to experimental results. However, the macroscopic behavior of the viscosity with respect to changes in permeability and polymer concentration were not evident. To this end, an extensive experimental characterization of the in situ rheology with respect to both porous media and solution properties are of great interest from a modeling point of view.

Appendix A: Sensitivity analysis

A sensitivity analysis is a powerful tool to quantify how strong parameter variations influence the system's output, here, the cost function. Therefore, a sensitivity analysis is often used to identify the driving forces which are mainly responsible for the system's behavior. As a result, the identified phenomena, which has a non-significant effect to the model's output are then neglected to simplify complex models [64]. The sensitivity coefficient s_{ij} measures the change in the system's output $y_i(t)$ due to variations in the model parameter k_j. Large values for the sensitivity imply a large change of the output due to a small variation of the parameter, while low sensitivities indicate a weak dependency between the (chosen) output and the parameter under consideration. Finally, the first-order sensitivity coefficient defined by Varma *et al.* [156] reads

$$s_{ij} = \frac{\partial}{\partial k_j} \int_{t_0}^{t} y_i(t) \, \mathrm{d}t \,, \tag{A.1}$$

where $y_i(t)$ is here the i-th continuous solution to a ODE system. The sensitivity definition given above measures changes in the solution vector integrated over time. More specific, the sensitivity of the degree of swelling due to variations in the model parameters (5.37) is in the focus of this analysis. To this end, the sensitivity definition used in this contribution reads

$$s_j = \frac{\partial}{\partial k_j} \int_{t_0}^{t} q(t) \, \mathrm{d}t \,. \tag{A.2}$$

A numerical approximation of (A.2) has been obtained by applying the centered difference approximation according to

$$s_j = \frac{k_j}{2\Delta k_j} \int_{t_0}^{t} \frac{q(t, k_j - \Delta k_j) - q(t, k_j + \Delta k_j)}{q(t, k_j)} \mathrm{d}t \,. \tag{A.3}$$

where Δk_j denotes the perturbation of the parameter k_j. Note in passing that the above equation has been normalized, such that the sensitivity is a dimensionless quantity.

Appendix B:
Adaptive Metropolis-Hastings algorithm

The vector of search radii $\mathbf{r}$ in the proposal step of the Metropolis-Hastings algorithm influences the acceptance ratio significantly and therefore the efficiency of the algorithm. Large acceptance ratios (too small $\mathbf{r}$) indicate a slow movement in the parameter space, while in contrast a low acceptance ratio (too large $\mathbf{r}$) results in a stagnation of the Metropolis-Hastings algorithm. To this end, an optimal step size guarantees an efficient exploration of the parameter space by accepting a sufficient number of proposed moves. According to Tarantola [145], an acceptance ratio of 30–50% is desired to obtain the previous requirements. To meet this requirement, the acceptance ratio is adapted during the run of the Metropolis-Hastings algorithm, while the following steps are implemented in addition to the proposed scheme in chapter 5.4.3:

1. Start with an arbitrary choice for $\mathbf{r}$ and run a fixed number of loops, while recording the accepted parameters.
2. Calculate the standard deviations $\boldsymbol{\sigma}_{ac}$ from the vector of accepted parameters.
3. Determine the current acceptance ratio of the previous interval, which relates basically the accepted loops to the number of loops within the interval.
4. Next, the search radius is substituted by $\mathbf{r} = \alpha_r \boldsymbol{\sigma}_{ac}$. Furthermore, α_r scales the vector-valued step size in an adaptive fashion, such that the desired acceptance ratio is reached throughout the algorithm runs. Initially α_r is set to 1.
5. The step size is adapted by updating α_r, when the acceptance ratio is not in the desired regime.
6. Run again a fixed number of loops and continue with step 3.

The basic idea of the proposed adaptive scheme is to introduce a proper scaling between the variations of the model parameters. This scaling should reflect somehow the sensitivity of the parameters with respect to the cost function. It turns out that the vector of standard deviations calculated with respect to a sufficient number of accepted loops tunes the parameter variation vector $\Delta\mathbf{k}$ pretty well.

Appendix C:
From pipe flow to Darcy-scale

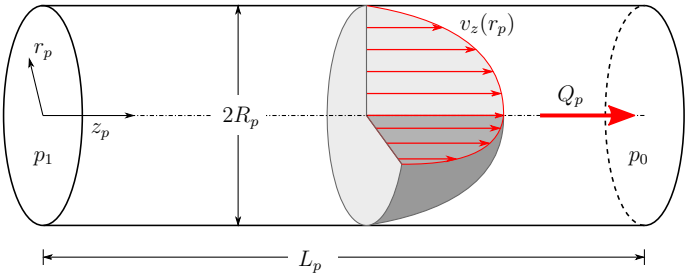

Figure C.1: *Fluid flow driven by a constant pressure gradient $\Delta p/L_p$ through a cylindrical pipe with radius R_p and length L_p. The pressure difference Δp is given by $p_0 - p_1$, while $p_1 > p_0$ is here assumed. Note that a cylindrical coordinate system (r_p, z_p) is used for the mathematical description.*

In the following derivation, an analytic approach for modeling non-Newtonian fluid flow through porous media is presented. Starting point is the analytical derivation of the volumetric flow rate Q_p through a single pipe. Next, the results are upscaled to a porous media by using the effective media theory. Finally, a porous media shear rate $\dot{\gamma}_{pm}$ can be expressed in terms of the Darcy velocity. The first part of the derivation is mainly taken from the textbook by Rütten [120], while the second part, the upscaling to the Darcy-scale, was already published by Cannella *et al.* [37].

Pipe flow Fluid flow through a straight, cylindrical pipe with radius R_p and length L_p is driven through a constant pressure gradient $\Delta p/L_p$, cf. Figure C.1. It is further assumed that the flow is laminar, stationary and fully developed. According to the assumptions, the velocity field reduces to one component, namely $v_z(r_p)$, which denotes the velocity in axial direction. The balance of linear momentum in axial direction yields to a relation for the shear stress τ_{rz} through

$$\frac{2}{r_p}\tau_{rz}(r_p) = \frac{\partial p(z_p)}{\partial z_p}\,, \tag{C.1}$$

where the pressure gradient reduces to

$$\frac{\partial p(z_p)}{\partial z_p} = \frac{\Delta p}{L_p}\,. \tag{C.2}$$

To this end, the shear stress is directly linked to the pressure gradient by

$$\tau_{rz} = \frac{\Delta p\, r_p}{2L_p}\,. \tag{C.3}$$

The volumetric flow rate for an arbitrary fluid rheology calculates to

$$Q_p = 2\,\pi \int_0^{R_p} r_p v_z(r_p) \mathrm{d}r_p\,, \tag{C.4}$$

which can be rewritten in terms of the shear rate $\dot{\gamma}_p$ to

$$Q_p = -\pi \int_0^{R_p} r_p^2 \dot{\gamma}_p \mathrm{d}r_p\,. \tag{C.5}$$

Note that the shear rate is related to the velocity field through

$$\dot{\gamma}_p = \frac{\mathrm{d}v_z(r_p)}{\mathrm{d}r_p}\,. \tag{C.6}$$

In the derivation of (C.5), the identity

$$\int_0^{R_p} r_p v_z(r_p) \mathrm{d}r_p = \left[\frac{1}{2} r_p^2 v_z(r_p)\right]_0^{R_p} - \int_0^{R_p} \frac{1}{2} r_p^2 \frac{\mathrm{d}v_z(r_p)}{\mathrm{d}r_p} \mathrm{d}r_p \tag{C.7}$$

has been exploited, which stems from the partial integration

$$\frac{\mathrm{d}}{\mathrm{d}r_p}\left(\frac{1}{2} r_p^2 v_z(r_p)\right) = r_p v_z(r_p) + \frac{1}{2} r_p^2 \frac{\mathrm{d}v_z(r_p)}{\mathrm{d}r_p}\,. \tag{C.8}$$

The first term on the r.h.s of (C.7) vanishes due to the no-slip boundary condition at the wall, i. e. $v_z(r_p = R_p) = 0$.

Substituting the power-law fluid model $\tau_{rz} = C_{PM}\dot{\gamma}_p^{n_{PM}}$ in (C.3) and insert the result in (C.5) yields after integration over the radius to the flow rate

$$Q_{p,PM} = \frac{\pi n_{PM}}{3n_{PM}+1}\left(\frac{\Delta p}{2C_{PM}\,L_p}\right)^{1/n_{PM}} R^{(3n_{PM}+1)/n_{PM}}. \tag{C.9}$$

Herein, n_{PM} and C_{PM} are model parameters of the power-law fluid model. For $n_{PM} = 1$ and $C_{PM} = \mu_{newton}$, the well-known Hagen-Poiseuille equation is obtained by

$$Q_{p,newton} = \frac{\pi R_p^4}{8\mu_{newton}} \frac{\Delta p}{L_p}\,. \tag{C.10}$$

Herein, μ_{newton} denotes the constant viscosity of a Newtonian fluid. An effective viscosity is calculated by comparing the Newtonian (C.10) to the non-Newtonian case (C.9) and assuming the same volumetric flow, i. e. $Q_{p,PM} = Q_{p,newton}$. To this end, the effective viscosity becomes

$$\mu_{p,eff} = C_{PM}\frac{3n_{PM}+1}{4n_{PM}}\left(\frac{R_p \Delta p}{2L_p C_{PM}}\right)^{(n_{PM}-1)/n_{PM}}. \tag{C.11}$$

Since the effective viscosity has to satisfy $\mu_{p,eff} = C_{PM}\dot{\gamma}_{p,eff}^{n_{PM}-1}$, the effective shear rate computes to

$$\dot{\gamma}_{p,eff} = \left(\frac{3n_{PM}+1}{4n_{PM}}\right)^{1/(n-1)}\left(\frac{\Delta p R_p}{2L_p C_{PM}}\right)^{1/n}. \tag{C.12}$$

Darcy-scale The results based on the pipe flow are now upscaled to the Darcy-scale by using the effective media theory, cf. [37]. In this approach, the porous media model is treated as a set of parallel capillary tubes, such that an equivalent tube radius R_{eq} can be defined. In general, R_{eq} is a function of the macroscopic properties of the porous media: the effective porosity n^L, intrinsic permeability k^S and the tortuosity Ψ_{tor}. The (absolute) Darcy velocity of the tube model $|\mathbf{q}|$, i. e. the surface specific discharge, is obtained from the volumetric flow rate through

$$|\mathbf{q}| = \frac{Q_p}{A_{eq}} n^L \quad \text{with} \quad A_{eq} = \pi R_{eq}^2 \,. \tag{C.13}$$

Herein, A_{eq} denotes the pipe's equivalent cross sectional area. Inserting the volumetric flow rate of the power-law fluid (C.9) in (C.13) and substituting the tube radius by the equivalent tube radius of the porous media results in the following relation for the Darcy velocity

$$|\mathbf{q}| = \frac{n_{PM} n^L}{3n_{PM}+1} \left(\frac{\Delta p}{2 C_{PM} L_p} \right)^{1/n_{PM}} R_{eq}^{(n_{PM}+1)/n_{PM}} \,. \tag{C.14}$$

In case of a Newtonian fluid ($n_{PM} = 1, C_{PM} = \mu_{newton}$), $|\mathbf{q}|$ has to reduce to the classical Darcy's law. Therefore, $R_{eq} = \sqrt{8k^S/n^L}$ yields to the well-known relationship. Following Cannella *et al.* [37], the equivalent tube radius is in the following defined through

$$R_{eq} = \sqrt{\frac{8k^S \Psi_{tor}}{n^L}} \,. \tag{C.15}$$

Finally, the Darcy velocity for non-Newtonian fluid flow becomes

$$|\mathbf{q}| = \frac{n_{PM} n^L}{3n_{PM}+1} \left(\frac{8k^S \Psi_{tor}}{n^L} \right)^{(n_{PM}+1)/2} \left(\frac{\Delta p}{2 C_{PM} L_p} \right)^{1/n_{PM}} \,. \tag{C.16}$$

Substituting the equivalent radius (C.15) and the Darcy velocity (C.16) in (C.12) yields to the porous media shear rate

$$\dot{\gamma}_{pm} = \frac{4}{\sqrt{8\Psi_{tor}}} \left(\frac{3n_{PM}+1}{4n_{PM}} \right)^{n_{PM}/(n_{PM}-1)} \frac{|\mathbf{q}|}{\sqrt{k^S n^L}} \tag{C.17}$$

Zamani *et al.* [170] simplified the relationship between Darcy velocity and porous media shear rate to a linear expression

$$\dot{\gamma}_{pm} = \alpha_{pm} \frac{|\mathbf{q}|}{\sqrt{k^S n^L}} \,. \tag{C.18}$$

Herein, α_{pm} is in general an empirical parameter, while the above equation is equivalent to the analytical solution by choosing

$$\alpha_{pm} = \sqrt{\frac{2}{\Psi_{tor}}} \left(\frac{3n_{PM}+1}{4n_{PM}} \right)^{n_{PM}/(n_{PM}-1)} \,. \tag{C.19}$$

Bibliography

[1] Abidin, A.; Puspasari, T. & Nugroho, W.: Polymers for enhanced oil recovery technology. *Procedia Chemistry: International Conference on Innovation in Polymer Science and Technology* **4** (2012), 11–16.

[2] Acartürk, A. Y.: *Simulation of charged hydrated porous materials*. Ph.D. thesis, University of Stuttgart (2009).

[3] Adamczyk, Z.; Siwek, B.; Zembala, M. & Belouschek, P.: Kinetics of localized adsorption of colloid particles. *Advances in Colloid and Interface Science* **48** (1994), 151–280.

[4] Agi, A.; Junin, R.; Gbonhinbor, J. & Onyekonwu, M.: Natural polymer flow behaviour in porous media for enhanced oil recovery applications: a review. *Journal of Petroleum Exploration and Production Technology* **8** (2018), 1349–1362.

[5] Akbari, S.; Mahmood, S.; Ghaedi, H. & Al-Hajri, S.: A new empirical model for viscosity of sulfonated polyacrylamide polymers. *Polymers* **11** (2019).

[6] Al-Hajri, S.; Mahmood, S. M.; Abdulelah, H. & Akbari, S.: An overview on polymer retention in porous media. *Energies* **11** (2018).

[7] Al-Hajri, S.; Mahmood, S. M.; Abdulrahman, A.; Abdulelah, H.; Akbari, S. & Saraih, N.: An experimental study on hydrodynamic retention of low and high molecular weight sulfonated polyacrylamide polymer. *Polymers* **11** (2019).

[8] Alexandersson, M.; Askfelt, H. & Ristinmaa, M.: Triphasic model of heat and moisture transport with internal mass exchange in paperboard. *Transport in Porous Media* **112** (2016), 381–408.

[9] Alexandersson, M. & Ristinmaa, M.: Multiphase transport model of swelling cellulose based materials with variable hydrophobicity. *International Journal of Engineering Science* **141** (2019), 112–140.

[10] Ambrosi, D. & Mollica, F.: On the mechanics of a growing tumor. *International Journal of Engineering Science* **40** (2002), 1297–1316.

[11] Ambrosi, D. & Preziosi, L.: On the closure of mass balance models for tumor growth. *Mathematical Models and Methods in Applied Sciences* **12** (2002), 737–754.

[12] Askfelt, H.; Alexandersson, M. & Ristinmaa, M.: Transient transport of heat, mass, and momentum in paperboard including dynamic phase change of water. *International Journal of Engineering Science* **109** (2016), 54–72.

[13] Assmann, A.: *Physical properties of concrete modified with superabsorbent polymers*. Ph.D. thesis, University of Stuttgart (2013).

[14] Atkin, R. J. & Craine, R. E.: Continuum theories of mixtures: Basic theory and historical development. *The Quarterly Journal of Mechanics and Applied Mathematics* **29** (1976), 209–244.

[15] Azad, M. S. & Trivedi, J. J.: Novel viscoelastic model for predicting the synthetic polymer's viscoelastic behavior in porous media using direct extensional rheological measurements. *Fuel* **235** (2019), 218–226.

[16] Baehr, H. D. & Kabelac, S.: *Thermodynamik; Grundlagen und technische Anwendungen*. Springer, Berlin, Heidelberg 2012.

[17] Barati, A.; Norouzi, H.; Sharafoddinzadeh, S. & Davarnejad, R.: Swelling kinetics and modeling of cationic and methacrylamide-based hydrogels. *World Applied Sciences Journal* **11** (2010), 1336–1341.

[18] Bedrikovetsky, P.; Siqueira, F. D.; Furtado, C. A. & Souza, A. L. S.: Modified particle detachment model for colloidal transport in porous media. *Transport in Porous Media* **86** (2011), 353–383.

[19] Bedrikovetsky, P.; Zeinijahromi, A.; Siqueira, F. D.; Furtado, C. A. & de Souza, A. L. S.: Particle detachment under velocity alternation during suspension transport in porous media. *Transport in Porous Media* **91** (2012), 173–197.

[20] Bennethum, L. S. & Cushman, J. H.: Multiscale, hybrid mixture theory for swelling systems - I: Balance laws. *International Journal of Engineering Science* **34** (1996), 125–145.

[21] Bennethum, L. S. & Cushman, J. H.: Multiscale, hybrid mixture theory for swelling systems - II: Constitutive theory. *International Journal of Engineering Science* **34** (1996), 147–169.

[22] Bennethum, L. S. & Cushman, J. H.: Multicomponent, multiphase thermodynamics of swelling porous media with electroquasistatics: I. Macroscale field equations. *Transport in Porous Media* **47** (2002), 337–362.

[23] Bennethum, L. S. & Cushman, J. H.: Multicomponent, multiphase thermodynamics of swelling porous media with electroquasistatics: II. Constitutive theory. *Transport in Porous Media* **47** (2002), 309–336.

[24] Bennethum, L. S.; Murad, M. A. & Cushman, J. H.: Macroscale thermodynamics and the chemical potential for swelling porous media. *Transport in Porous Media* **39** (2000), 187–225.

[25] Bennethum, L. S. & Weinstein, T.: Three pressures in porous media. *Transport in Porous Media* **54** (2004), 1–34.

[26] Berg, S. & van Wunnik, J.: Shear rate determination from pore-scale flow fields. *Transport in Porous Media* **117** (2017), 229–246.

[27] Bertrand, T.; Peixinho, J.; Mukhopadhyay, S. & MacMinn, C.: Dynamics of swelling and drying in a spherical gel. *Physical Review Applied* **6** (2016).

[28] Beushausen, H.; Gillmer, M. & Alexander, M.: The influence of superabsorbent polymers on strength and durability properties of blended cement mortars. *Cement and Concrete Composites* **52** (2014), 73–80.

[29] Bird, R. B.: Transport phenomena . *Applied Mechanics Reviews* **55** (2002).

[30] de Boer, R.: Highlights in the historical development of porous media theory: toward a consistent macroscopic theory. *Applied Mechanics Reviews* **49** (1996), 201–262.

[31] de Boer, R.: *Theory of Porous Media*. Springer-Verlag, Berlin 2000.

[32] Bowen, R. M.: *Continuum Physics, Vol. III*, Academic Press, New York 1976, chap. Theory of Mixtures. pp. 1–127.

[33] Bradford, S. A.; Simunek, J.; Bettahar, M.; van Genuchten, M. T. & Yates, S. R.: Modeling colloid attachment, straining, and exclusion in saturated porous media. *Environmental Science & Technology* **37** (2003), 2242–2250.

[34] Bradford, S. A.; Simunek, J.; Bettahar, M.; van Genuchten, M. T. & Yates, S. R.: Significance of straining in colloid deposition: Evidence and implications. *Water Resources Research* **42** (2006).

[35] Byrne, H.: Modelling solid tumour growth using the theory of mixtures. *Mathematical Medicine and Biology* **20** (2003), 341–366.

[36] Cai, S. & Suo, Z.: Mechanics and chemical thermodynamics of phase transition in temperature-sensitive hydrogels. *Journal of the Mechanics and Physics of Solids* **59** (2011), 2259–2278.

[37] Cannella, W. J.; Huh, C. & Seright, R. S.: Prediction of xanthan rheology in porous media. *Society of Petroleum Engineers* (1988).

[38] Carrier, W. D.: Goodbye, hazen; hello, kozeny-carman. *Journal of Geotechnical and Geoenvironmental Engineering* (2003).

[39] Choi, B.; Park, K.; Choi, J. & Lee, K.: New approach for modeling of polymer retention mechanisms - mechanical entrapment and adsorption **2014** (2014), 1–5.

[40] Christopher, R. H. & Middleman, S.: Power-law flow through a packed tube. *Industrial & Engineering Chemistry Fundamentals* **4** (1965), 422–426.

[41] Comba, S.; Dalmazzo, D.; Santagata, E. & Sethi, R.: Rheological characterization of xanthan suspensions of nanoscale iron for injection in porous media. *Journal of Hazardous Materials* **185** (2011), 598–605.

[42] Craeye, B.; Geirnaert, M. & Schutter, G. D.: Super absorbing polymers as an internal curing agent for mitigation of early-age cracking of high-performance concrete bridge decks. *Construction and Building Materials* **25** (2011), 1–13.

[43] Czupryna, S.: Improvements in superabsorbent water blocking materials for new power cable applications. In *International Conference on Power Insulated Cables*, 2007.

[44] Dang, T. Q. C.; Chen, Z.; Nguyen, T. B. N. & Bae, W.: Investigation of isotherm polymer adsorption in porous media. *Petroleum Science and Technology* **32** (2014), 1626–1640.

[45] Dawson, R. & Lantz: Inaccessible pore volume in polymer flooding. *SPE Journal* **24** (1972), 448–452.

[46] Delshad, M.; Kim, D. H.; Magbagbeola, O. A.; Huh, C.; Pope, G. A. & Tarahom, F.: Mechanistic interpretation and utilization of viscoelastic behavior of polymer solutions for improved polymer-flood efficiency. In *Society of Petroleum Engineers, Improved Oil Recovery Symposium, Tulsa, Oklahoma, USA*, 2008.

[47] Delshad, M.; Pope, G. & Sepehrnoori, K.: A compositional simulator for modeling surfactant enhanced aquifer remediation, 1 formulation. *Journal of Contaminant Hydrology* **23** (1996), 303–327.

[48] DIN 18132: Soil, testing procedures and testing equipment – Determination of water absorption (2012).

[49] Ehlers, W. & Bluhm, J.: Foundations of multiphasic and porous materials. *Porous Media: Theory, Experiments and Numerical Applications* (2002), 3–86.

[50] Engelsberg, M. & Barros, W.: Free-evolution kinetics in a high-swelling polymeric hydrogel. *Physical Review E* **88** (2013), 1–7.

[51] English, A. E.; Tanaka, T. & Edelman, E. R.: Equilibrium and non-equilibrium phase transitions in copolymer polyelectrolyte hydrogels. *Journal of Chemical Physics* **107** (1997), 1645–1654.

[52] Ferreira, V. H. S. & Moreno, R. B. Z. L.: Modeling and simulation of laboratory-scale polymer flooding. *International Journal of Engineering and Technology* (2016), 24–33.

[53] Flory, P. J.: Thermodynamics of high polymer solutions. *Journal of Chemical Physics* **10** (1942), 51–61.

[54] Flory, P. J.: *Principles of polymer chemistry*. Cornell University Press, Ithaca, New York 1953.

[55] Flory, P. J. & Rehner, J.: Statistical mechanics of cross-linked polymer networks I. Rubberlike elasticity. *Journal of Chemical Physics* **11** (1943), 512–520.

[56] Flory, P. J. & Rehner, J.: Statistical mechanics of cross-linked polymer networks II. Swelling. *Journal of Chemical Physics* **11** (1943), 521–526.

[57] Foo, K. & Hameed, B.: Insights into the modeling of adsorption isotherm systems. *Chemical Engineering Journal* **156** (2010), 2–10.

[58] Gabbanelli, S. C.; Grattoni, C. A. & Bidner, M. S.: Miscible flow through porous media with dispersion and adsorption. *Advances in Water Resources* **10** (1987), 149–158.

[59] Gajo, A. & Loret, B.: Finite element simulations of chemo-mechanical coupling in elastic-plastic homoionic expansive clays. *Computer Methods in Applied Mechanics and Engineering* **192** (2003), 3489–3530.

[60] Gao, C.: Viscosity of partially hydrolyzed polyacrylamide under shearing and heat. *Journal of Petroleum Exploration and Production Technology* **3** (2013), 203–206.

[61] Gao, F. & Han, L.: Implementing the nelder-mead simplex algorithm with adaptive parameters. *Computational Optimization and Applications* **51** (2012), 259–277.

[62] Gbadamosi, A. O.; Junin, R.; Manan, M. A.; Agi, A. & Yusuff, A. S.: An overview of chemical enhanced oil recovery: recent advances and prospects. *International Nano Letters* **9** (2019), 171–202.

[63] Grattoni, C. A.; Al-Sharji, H. H.; Yang, C.; Muggeridge, A. H. & Zimmerman, R. W.: Rheology and permeability of crosslinked polyacrylamide gel. *Journal of Colloid and Interface Science* **240** (2001), 601–607.

[64] Gunawan, R.; Cao, Y.; Petzold, L. & Doyle, F. J.: Sensitivity analysis of discrete and stochastic systems. *Biophysical Journal* **88** (2005), 2530–2540.

[65] Hasholt, M. T.; Jensen, O. M.; Kovler, K. & Zhutovsky, S.: Can superabsorent polymers mitigate autogenous shrinkage of internally cured concrete without compromising the strength? *Construction and Building Materials* **31** (2012), 226–230.

[66] Hassanizadeh, M. & Gray, W. G.: General conservation equations for multi-phase systems: 1. averaging procedure. *Advances in Water Resources* **2** (1979), 131–144.

[67] Hassanizadeh, M. & Gray, W. G.: General conservation equations for multi-phase systems: 2. mass, momenta, energy, and entropy equations. *Advances in Water Resources* **2** (1979), 191–203.

[68] Hastings, W. K.: Monte Carlo sampling methods using Markov chains and their applications. *Biometrika* **57** (1970), 97–109.

[69] Hatzignatiou, D. G.; Norris, U. L. & Stavland, A.: Core-scale simulation of polymer flow through porous media. *Journal of Petroleum Science and Engineering* **108** (2013), 137–150.

[70] Horkay, F.; Tasaki, I. & Basser, P. J.: Osmotic swelling of polyacrylate hydrogels in physiological salt solutions. *Biomacromolecules* **1** (2000), 84–90.

[71] Huggins, M. L.: Solutions of long chain compounds. *The Journal of Chemical Physics* **9** (1941), 440–440.

[72] Humphrey, J. D. & Rajagopal, K. R.: A constrained mixture model for growth and remodeling of soft tissues. *Mathematical Models and Methods in Applied Sciences* (2002), 407–430.

[73] Hunt, J.; Young, T.; Green, D. & Willhite, G.: Size-exclusion chromatography in the measurement of concentration and molecular weight of some eor polymers. *Society of Petroleum Engineers* (1988), 835–841.

[74] Huyghe, J. & Janssen, J.: Quadriphasic mechanics of swelling incompressible porous media. *International Journal of Engineering Science* **35** (1997), 793–802.

[75] Huyghe, J. M.: General theory of mixtures. physical and chemistry of mixtures and swelling. In *Coupled and multiphysics phenomena*, 2015, pp. 43–67.

[76] Huyghe, J. M. & Janssen, J. D.: Thermo-chemo-electro-mechanical formulation of saturated charged porous solids. *Transport in Porous Media* **34** (1999), 129–141.

[77] Idahosa, P.; Oluyemi, G.; Oyeneyin, M. & Prabhu, R.: Rate-dependent polymer adsorption in porous media. *Journal of Petroleum Science and Engineering* **143** (2016), 65–71.

[78] Innocentini, M. D. M.; Salvini, V. R.; Pandolfelli, V. C. & Coury, J. R.: Assessment of forchheimer's equation to predict the permeability of ceramic foams. *Journal of the American Ceramic Society* **82** (1999), 1945–1948.

[79] Jensen, O. M. & Hansen, P. F.: Water-entrained cement-based materials: I. principles and theoretical background. *Cement and Concrete Research* **31** (2001), 647–654.

[80] Jensen, O. M. & Hansen, P. F.: Water-entrained cement-based materials: Ii. experimental observations. *Cement and Concrete Research* **32** (2002), 973–978.

[81] Johnson, P. R. & Elimelech, M.: Dynamics of colloid deposition in porous media: Blocking based on random sequential adsorption. *Langmuir* **11** (1995), 801–812.

[82] Karadag, E.; Üzüm, Ö. B. & Saraydin, D.: Swelling equilibria and dye adsorption studies of chemically crosslinked superabsorbent acrylamide/maleic acid hydrogels. *European Polymer Journal* **38** (2002), 2133–2141.

[83] Kinniburgh, D. G.: General purpose adsorption isotherms. *Environmental Science & Technology* **20** (1986), 895–904.

[84] Koch, D.: *Thermomechanical Modelling of Non-isothermal Porous Materials with Applications to Enhanced Geothermal Systems*. Ph.D. thesis, University of Stuttgart (2016).

[85] Kuzmin, D.: *A Guide to Numerical Methods for Transport Equations*. Friedrich-Alexander-Universität Erlangen-Nürnberg 2010.

[86] Lake, L.: *Petroleum Engineering Handbook*. Richardson, TX: Society of Petroleum Engineers 2007.

[87] Langmuir, I.: The adsorption of gases on plane surfaces of glass, mica and platinum. *Journal of the American Chemical Society* **40** (1918), 1361–1403.

[88] Lashgari, H.; Pope, G.; Balhoff, M. & Tagavifar, M.: New and improved physical property models for chemical flooding simulators. In *SPE Reservoir Simulation Conference, Galveston, Texas, USA*, 2019.

[89] Lee, H. X. D.; Wong, H. S. & Buenfeld, N. R.: Potential of superabsorbent polymer for self-sealing cracks in concrete. *Advances in Applied Ceramics* **109** (2010), 296–302.

[90] Lei, X.; Wong, H.; Fabbri, A.; Limam, A. & Cheng, Y.: A thermo-chemo-electro-mechanical framework of unsaturated expansive clays. *Computers and Geotechnics* **62** (2014), 175–192.

[91] Lenormand, R.; Touboul, E. & Zarcone, C.: Numerical models and experiments on immiscible displacements in porous media. *Journal of Fluid Mechanics* **189** (1988), 165–187.

[92] Li, Y. & Tanaka, T.: Kinetics of swelling and shrinking of gels. *The Journal of Chemical Physics* **92** (1990), 1365–1371.

[93] Lin, G.; Chang, S.; Kuo, C.-H.; Magda, J. & Solzbacher, F.: Free swelling and confined smart hydrogels for applications in chemomechanical sensors for physiological monitoring. *Sensors and Actuators B: Chemical* **136** (2009), 186–195.

[94] Liu, I.-S.: Method of lagrange multipliers for exploitation of the entropy principle. *Archive for Rational Mechanics and Analysis* (1972), 131–148.

[95] Liu, I.-S. & Müller, I.: Thermodynamics of mixtures of fluids. *Rational Thermodynamics, Editor: C. A. Truesdell* (1984), 264–285.

[96] Liu, M.; Cheng, R. & Qian, R.: Effect of solution concentration on the gelation of aqueous polyvinyl alcohol solution. *Journal of Polymer Science Part B: Polymer Physics* **33** (1995), 1731–1735.

[97] Liu, S. & Masliyah, J. H.: On non-newtonian fluid flow in ducts and porous media. *Chemical Engineering Science* **53** (1998), 1175–1201.

[98] Liu, Y.: Some consideration on the langmuir isotherm equation. *Colloids and Surfaces A: Physicochemical and Engineering Aspects* **274** (2006), 34–36.

[99] Lopez, X.; Valvatne, P. H. & Blunt, M. J.: Predictive network modeling of single-phase non-newtonian flow in porous media. *Journal of Colloid and Interface Science* **264** (2003), 256–265.

[100] Loret, B.; Gajo, A. & Simões, F. M.: A note on the dissipation due to generalized diffusion with electro-chemo-mechanical couplings in heteroionic clays. *European Journal of Mechanics - A/Solids* **23** (2004), 763–782.

[101] Loret, B.; Hueckel, T. & Gajo, A.: Chemo-mechanical coupling in saturated porous media: elastic–plastic behaviour of homoionic expansive clays. *International Journal of Solids and Structures* **39** (2002), 2773–2806.

[102] Lotsch, T.; Muller, T. & Pusch, G.: The effect of inaccessible pore volume on polymer coreflood experiments. In *SPE Oilfield and Geothermal Chemistry Symposium, Phoenix, Arizona, USA*, 1985.

[103] Mattson, D. L.; Lu, S.; Roman, R. J. & Cowley, A. W.: Relationship between renal perfusion pressure and blood flow in different regions of the kidney. *American Journal of Physiology-Regulatory, Integrative and Comparative Physiology* **264** (1993), 78–83.

[104] Mechtcherine, G. M. S. C. e. a., V.: Effect of internal curing by using superabsorbent polymers (sap) on autogenous shrinkage and other properties of a high-performance fine-grained concrete: results of a rilem round-robin test. *Materials and Structures* **47** (2014), 541–562.

[105] Mechtcherine, V.: Use of superabsorbent polymers (SAP) as concrete additive. *RILEM Technical Letters* **1** (2016), 81–87.

[106] Mechtcherine, V. & Reinhardt, H.-W. (eds.): *Application of Super Absorbent Polymers (SAP) in Concrete Construction*. Springer Netherlands 2012.

[107] Mechtcherine, V.; Secrieru, E. & Schröfl, C.: Effect of superabsorbent polymers (SAPs) on rheological properties of fresh cement-based mortars - development of yield stress and plastic viscosity over time. *Cement and Concrete Research* **67** (2015), 52–65.

[108] Mönnig, S.: *Superabsorbing additions in concrete: applications, modelling and comparison of different internal water sources*. Ph.D. thesis, University of Stuttgart (2009).

[109] Morais, A.; Seybold, H.; Herrmann, H. & Andrade, J.: Non-newtonian fluid flow through three-dimensional disordered porous media. *Physical review letters* **103** (2009).

[110] Najafabadi, N. F.; Delshad, M.; Han, C. & Sepehrnoori, K.: Formulations for a three-phase, fully implicit, parallel, eos compositional surfactant-polymer flooding simulator. *Journal of Petroleum Science and Engineering* **86-87** (2012), 257–271.

[111] Nestle, N.; Kühn, A.; Friedemann, K.; Horch, C.; Stallmach, F. & Herth, G.: Water balance and pore structure development in cementitious materials in internal curing with modified superabsorbent polymer studied by NMR. *Microporous and Mesoporous Materials* **125** (2009), 51–57.

[112] Olajire, A. A.: Review of asp eor (alkaline surfactant polymer enhanced oil recovery) technology in the petroleum industry: Prospects and challenges. *Energy* **77** (2014), 963–982.

[113] Pefferkorn, E.; Nabzar, L. & Garroy, A.: Adsorption of polyacrylamide to na kaolinite: Correlation between clay structure and surface properties. *Journal of Colloid and Interface Science* **106** (1985), 94–103.

[114] Peksa, A. E.; Wolf, K.-H. A. & Zitha, P. L.: Bentheimer sandstone revisited for experimental purposes. *Marine and Petroleum Geology* **67** (2015), 701–719.

[115] Perrin, C. L.; Tardy, P. M.; Sorbie, K. S. & Crawshaw, J. C.: Experimental and modeling study of newtonian and non-newtonian fluid flow in pore network micromodels. *Journal of Colloid and Interface Science* **295** (2006), 542–550.

[116] Pierce, D. M.; Unterberger, M. J.; Trobin, W.; Ricken, T. & Holzapfel, G. A.: A microstructurally based continuum model of cartilage viscoelasticity and permeability incorporating measured statistical fiber orientations. *Biomechanics and Modeling in Mechanobiology* **15** (2016), 229–244.

[117] Pourjavadi, A.; Fakoorpoor, S. M.; Hosseini, P. & Khaloo, A.: Interactions between superabsorbent polymers and cement-based composites incorporating colloidal silica nanoparticles. *Cement and Concrete Composites* **37** (2013), 196–204.

[118] Ricken, T. & Bluhm, J.: Remodeling and growth of living tissue: a multiphase theory. *Archive of Applied Mechanics* **80** (2009), 453–465.

[119] Ristinmaa, M.; Ottosen, N. & Johannesson, B.: Mixture theory for a thermoelastoplastic porous solid considering fluid flow and internal mass exchange. *International Journal of Engineering Science* **49** (2011), 1185–1203.

[120] Rütten, M.: *Verallgemeinerte newtonsche Fluide: Thermische und viskose Strömungseigenschaften*. Springer, Berlin, Heidelberg 2019.

[121] Safronov, A. P.; Adamova, L. V.; Blokhina, A. S.; Kamalov, I. A. & Shabadrov, P. A.: Flory-huggins parameters for weakly crosslinked hydrogels of poly(acrylic acid) and poly(methacrylic acid) with various degrees of ionization. *Polymer Science Series A* **57** (2015), 33–42.

[122] Santoso, R. K.; Fauzi, I.; Hidayat, M.; Swadesi, B.; Aslam, B. M. & Marhaendrajana, T.: Study of non-newtonian fluid flow in porous media at core scale using analytical approach. *Geosystem Engineering* **21** (2018), 21–30.

[123] Sauerwein, M. & Steeb, H.: A modified effective stress principle for chemical active multiphase materials with internal mass exchange. *Geomechanics for Energy and the Environment* **15** (2018), 19–34.

[124] Sauerwein, M. & Steeb, H.: Modeling of dynamic hydrogel swelling within the pore space of a porous medium. *International Journal of Engineering Science* **155** (2020).

[125] Schaufler, A.: *Multi-physical simulations: transport and infiltration of suspensions in granular porous media*. Ph.D. thesis, Ruhr University Bochum (2015).

[126] Schaufler, A.; Becker, C. & Steeb, H.: Infiltration processes in cohesionless soils. *ZAMM - Journal of Applied Mathematics and Mechanics / Zeitschrift für Angewandte Mathematik und Mechanik* **93** (2012), 138–146.

[127] Schijven, J. F. & Hassanizadeh, S. M.: Removal of viruses by soil passage: Overview of modeling, processes, and parameters. *Critical Reviews in Environmental Science and Technology* **30** (2000), 49–127.

[128] Schröfl, C.; Mechtcherine, V. & Gorges, M.: Relation between the molecular structure and the efficiency of superabsorbent polymers (SAP) as concrete admixture to mitigate autogenous shrinkage. *Cement and Concrete Research* **42** (2012), 865–873.

[129] Schröfl, C.; Mechtcherine, V.; Vontobel, P.; Hovind, J. & Lehmann, E.: Sorption kinetics of superabsorbent polymers (SAPs) in fresh portland cement-based pastes visualized and quantified by neutron radiography and correlated to the progress of cement hydration. *Cement and Concrete Research* **75** (2015), 1–13.

[130] Secrieru, E.; Mechtcherine, V.; Schröfl, C. & Borin, D.: Rheological characterisation and prediction of pumpability of strain-hardening cement-based-composites (shcc) with and without addition of superabsorbent polymers (sap) at various temperatures. *Construction and Building Materials* **112** (2016), 581–594.

[131] Shah, B. N.; Willhite, G. P. & Green, D. W.: Water-soluble polymer adsorption from saline solutions. In *International Symposium on Oilfield and Geothermal Chemistry, Phoenix, Arizona, USA*, 1985.

[132] Shen, D.; Wang, T.; Chen, Y.; Wang, M. & Jiang, G.: Effect of internal curing with super absorbent polymers on the relative humidity of early-age concrete. *Construction and Building Materials* **99** (2015), 246–253.

[133] Sheng, J. J.: Chapter 3 - polymer flooding-fundamentals and field cases. In Sheng, J. J. (ed.): *Enhanced Oil Recovery Field Case Studies*. Gulf Professional Publishing, Boston 2013, pp. 63–82.

[134] Singh, P. P.; Cushman, J. H. & Maier, D. E.: Multiscale fluid transport theory for swelling biopolymers. *Chemical Engineering Science* **58** (2003), 2409–2419.

[135] Singh, P. P.; Cushman, J. H. & Maier, D. E.: Three scale thermomechanical theory for swelling biopolymeric systems. *Chemical Engineering Science* **58** (2003), 4017–4035.

[136] Sinharay, S.: Assessing convergence of the markov chain monte carlo algorithms: A review. *ETS Research Report Series* (2003), 1–52.

[137] Snoeck, D.: Superabsorbent polymers to seal and heal cracks in cementitious materials. *RILEM Technical Letters* **3** (2018), 32–38.

[138] Snoeck, D.; Jensen, O. & Belie, N. D.: The influence of superabsorbent polymers on the autogenous shrinkage properties of cement pastes with supplementary cementitious materials. *Cement and Concrete Research* **74** (2015), 59–67.

[139] Snoeck, D.; Steuperaert, S.; Tittelboom, K. V.; Dubruel, P. & Belie, N. D.: Visualization of water penetration in cementitious materials with superabsorbent polymers by means of neutron radiography. *Cement and Concrete Research* **42** (2012), 1113–1121.

[140] Sochi, T.: Non-newtonian flow in porous media. *Polymer* **51** (2010), 5007–5023.

[141] Sorbie, K.: *Polymer Improved Oil Recovery*. Blackie and Son, Glasgow 1991.

[142] Stavland, A.; Jonsbraten, H.; Lohne, A.; Moen, A. & Giske, N. H.: Polymer flooding - flow properties in porous media versus rheological parameters. In *SPE EUROPEC/EAGE Annual Conference and Exhibition, Barcelona, Spain*, 2010.

[143] Steeb, H. & Diebels, S.: A thermodynamic-consistent model describing growth and remodeling phenomena. *Computational Materials Science* **28** (2003), 597–607.

[144] Tanaka, T. & Fillmore, D. J.: Kinetics of swelling of gels. *Journal of Chemical Physics* **70** (1979), 1214–1218.

[145] Tarantola, A.: *Inverse Problem Theory and Methods for Model Parameter Estimation*. SIAM 2004.

[146] Taylor, K. C. & Nasr-El-Din, H. A.: Water-soluble hydrophobically associating polymers for improved oil recovery: A literature review. *Journal of Petroleum Science and Engineering* **19** (1998), 265–280.

[147] Tiraferri, A.; Tosco, T. & Sethi, R.: Transport and retention of microparticles in packed sand columns at low and intermediate ionic strengths: experiments and mathematical modeling. *Environmental Earth Sciences* **63** (2011), 847–859.

[148] Tokita, M. & Tanaka, T.: Friction coefficient of polymer networks of gels. *The Journal of Chemical Physics* **95** (1991), 4613–4619.

[149] Tosco, T.; Bosch, J.; Meckenstock, R. U. & Sethi, R.: Transport of ferrihydrite nanoparticles in saturated porous media: Role of ionic strength and flow rate. *Environmental Science & Technology* **46** (2012), 4008–4015.

[150] Tosco, T.; Marchisio, D. L.; Lince, F. & Sethi, R.: Extension of the darcy–forchheimer law for shear-thinning fluids and validation via pore-scale flow simulations. *Transport in Porous Media* **96** (2013), 1–20.

[151] Tosco, T. & Sethi, R.: Transport of non-newtonian suspensions of highly concentrated micro- and nanoscale iron particles in porous media: A modeling approach. *Environmental Science & Technology* **44** (2010), 9062–9068.

[152] Truesdell, C. & Toupin, R. A.: The classical field theories. In Flügge, S. (ed.): *Handbuch der Physik, Vol. III/1*. Springer-Verlag, Berlin-Göttingen-Heidelberg 1960, pp. 226–902.

[153] Tufenkji, N.; Redman, J. A. & Elimelech, M.: Interpreting deposition patterns of microbial particles in laboratory-scale column experiments. *Environmental Science & Technology* **37** (2003), 616–623.

[154] Vardoulakis, I.; Papanastasiou, P. & Stavropoulou, M.: Sand erosion in axial flow conditions. *Transport in Porous Media* **45** (2001), 267–280.

[155] Vardoulakis, I.; Stavropoulou, M. & Papanastasiou, P.: Hydro-mechanical aspects of the sand production problem. *Transport in Porous Media* **22** (1996), 225–244.

[156] Varma, A.; Morbidelli, M. & Wu, H.: *Parametric Sensitivity in Chemical Systems*. Cambridge University Press 1999.

[157] Varoquaux, G.; Haenel, V.; de Buyl, P.; Ingold, G.-L. & Gouillart, E.: *Scipy lecture notes, Edition 2020.1*. www.scipy-lectures.org.

[158] Viejo, I.; Esteves, L. P.; Laspalas, M. & Bielsa, J. M.: Numerical modelling of porous cement-based materials by superabsorbent polymers. *Cement and Concrete Research* **90** (2016), 184–193.

[159] Wack, H.: *Zum Quellungsdruck von polymeren Hydrogelen*. Ph.D. thesis, University Duisburg-Essen (2006).

[160] Wack, H. & Ulbricht, M.: Gel blocking effects during the swelling of polymeric hydrogels. In *Proceedings of the First International Conference on Self Healing Materials*, 2007.

[161] Wang, W.; Liu, Y. & Gu, Y.: Application of a novel polymer system in chemical enhanced oil recovery (eor). *Colloid and Polymer Science* **281** (2003), 1046–1054.

[162] Wei, B.; Romero-Zerón, L. & Rodrigue, D.: Mechanical properties and flow behavior of polymers for enhanced oil recovery. *Journal of Macromolecular Science, Part B* **53** (2014), 625–644.

[163] Wever, D.; Picchioni, F. & Broekhuis, A.: Polymers for enhanced oil recovery: A paradigm for structure-property relationship in aqueous solution. *Progress in Polymer Science* **36** (2011), 1558–1628.

[164] Wilson, W.; Huyghe, J. M. & van Donkelaar, C. C.: Depth-dependent compressive equilibrium properties of articular cartilage explained by its composition. *Biomechanics and Modeling in Mechanobiology* **6** (2006), 43–53.

[165] Yang, Q.-S.; Ma, L.-H. & Shang, J.-J.: The chemo-mechanical coupling behavior of hydrogels incorporating entanglements of polymer chains. *International Journal of Solids and Structures* **50** (2013), 2437–2448.

[166] Yao, K. M.; Habibian, M. T. & O'Melia, C. R.: Water and waste water filtration: concepts and applications. *Environmental Science & Technology* **5** (1971), 1105–1112.

[167] You, Z.; Yang, Y.; Badalyan, A.; Bedrikovetsky, P. & Hand, M.: Mathematical modelling of fines migration in geothermal reservoirs. *Geothermics* **59** (2016), 123–133.

[168] Yu, C.; Huyghe, J. M. & Malakpoor, K.: 2D mixed hybrid FEM of lanir model. *Procedia IUTAM* **12** (2015), 93–104.

[169] Zamani, N.; Bondino, I.; Kaufmann, R. & Skauge, A.: Effect of porous media properties on the onset of polymer extensional viscosity. *Journal of Petroleum Science and Engineering* **133** (2015), 483–495.

[170] Zamani, N.; Bondino, I.; Kaufmann, R. & Skauge, A.: Computation of polymer in-situ rheology using direct numerical simulation. *Journal of Petroleum Science and Engineering* **159** (2017), 92–102.

[171] Zamani, N.; Kaufmann, R.; Kosinski, P. & Skauge, A.: Mechanisms of non-newtonian polymer flow through porous media using navier-stokes approach. *Journal of Dispersion Science and Technology* **36** (2015), 310–325.

[172] Zhang, G.: *New insights into polymer retention in porous media*. Ph.D. thesis, New Mexico Institute of Mining and Technology (2013).

[173] Zhang, G. & Seright, R.: Hydrodynamic retention and rheology of EOR polymers in porous media. In *SPE International Symposium on Oilfield Chemistry, Woodlands, Texas, USA*, 2015.

[174] Zhu, Q.; Barney, C. W. & Erk, K. A.: Effect of ionic crosslinking on the swelling and mechanical response of model superabsorbent polymer hydrogels for internally cured concrete. *Materials and Structures* **48** (2014), 2261–2276.

List of Figures

List of Tables

Curriculum Vitae

Personal data:

Name:	Malte Ferry Sauerwein
Date of birth:	November 29, 1990
Place of birth:	Bochum, Germany
Nationality:	German
Parents:	Andreas Sauerwein and Sibylle Baehr-Sauerwein
Siblings:	Gerrit Sauerwein

Education:

1997 – 2001	elementary school "Köllerholz Grundschule", Bochum, Germany
2001 – 2010	secondary school "Theodor-Körner-Schule" (Gymnasium), Bochum, Germany
2010	degree: "Allgemeine Hochschulreife" (high school diploma)
10/2010 – 10/2015	studies in mechannical engineering at the Ruhr-University Bochum, Germany major subject: "Angewandte Mechanik"
10/2015	degree: "Master of Science"
09/2014 – 01/2015	study abroad at the Texas A&M (DAAD scholarship) College Station, Texas, USA

Professional occupation:

11/2015 – 11/2016	teaching assistant and research associate at the Institute of Mechanics at the Ruhr-University Bochum, Germany
12/2016 – 12/2020	teaching assistant and research associate at the Institute of Applied Mechanics (Civil Engineering) at the University of Stuttgart, Germany
since 01/2021	Data Science Consultant Wipro Technologies GmbH

Institute of Applied Mechanics (IAM)
Chair for Continuum Mechanics

The use of polymers in fluid-saturated porous media has increased in relevance during the last years. Polymers, which exist in the pore space of a solid skeleton, are able to interact with the pore fluid as well as with the solid. The interactions cause changes in the macroscopic behavior, while especially transport and transfer processes within the pore space are affected. The precise knowledge of these processes over time is a key factor for developing innovative applications in petroleum engineering but also for innovative building materials.

Therefore, the aim of this thesis is to develop a multi-phase model for simulating the coupled processes in such kind of material. With such model, the physical behavior of water-soluble polymers in petroleum engineering and the swelling behavior of hydrogels in polymer-enhanced building materials can be predicted over time. The coupled processes are simulated by solving the system's governing equations in a finite element framework and are validated through experimental results.

ISBN 978-3-937399-55-3